THE UNIVERSITY
of EDINBURGH

Anatomical and functional investigation of the deep medial entorhinal cortex

Klára Zsófia Gerlei

THE UNIVERSITY *of* EDINBURGH

Doctor of Philosophy (PhD)

Biomedical Sciences

The University of Edinburgh

2019

Abstract

Spatial computations are thought to be processed in the hippocampal-entorhinal network and involve neurons with spatially selective firing properties. The deep medial entorhinal cortex (MEC) consists of molecularly distinct sublayers with distinct connectivity. One of these layers, layer 5b (L5b) receives input both from the hippocampal *cornu ammonis* 1 (CA1) area and the superficial MEC, regions that have abundant spatially selective cells. Extracellular recordings from rats found grid and conjunctive cells in the deep MEC, while other studies suggest that deep MEC neurons are silent. Based on its position in the circuit and the presence of spatial cells, I hypothesized that L5b plays a role in spatial cognition. To test this hypothesis, I first investigated approaches to target L5b cells with genetic precision and characterized transgenic mouse lines. I found a mouse line that had tTA expression sufficiently specific to L5b, and used this line to investigate the anatomy and firing properties of L5b cells. I developed an analysis pipeline to automate the analysis of extracellular recordings using MountainSort, and evaluated opto-tagging of genetically defined cells in an open field arena. I successfully opto-tagged one genetically defined deep layer cell and a small number of cells that receive input from genetically defined deep layer cells. My analysis of the firing properties of deep MEC cells recorded from mice indicates that grid and head-direction properties are similar to what was reported in the rat. My results support the idea that deep layers of MEC have a powerful influence on more superficial layers and suggest how cells in this area may contribute to spatial behaviours.

Lay summary

To understand the biological basis of cognition it will be critical to bridge the gap between how brain cells code information and their function. Investigation of cognitive processes of the brain that have a clear behavioural readout will be important to address this goal. Spatial navigation is a cognitive process whose behavioural outcome is the current and future location of the animal. This clear outcome makes spatial navigation a good focus for investigation of cognition.

Self-localization can be defined as knowing one's current position in the environment, relative to landmarks. Both self-localization and navigation are essential for the survival of animals including humans. My thesis is about a group of cells that reside in a part of the brain called the medial entorhinal cortex (MEC). The MEC can be divided into layers orientated parallel to the surface of the brain. While much previous work has focussed on layers close to the brain surface, my focus is on the less well understood deep MEC. I performed experiments to investigate the connectivity of a specific population of neurons in the deep MEC and investigated the role of this area in navigation.

Investigating specific groups of cells in the brain is challenging as nearby cell populations are difficult to distinguish from one another. Genetically altered mouse lines can be used to overcome this difficulty. In these mice a specific group of cells is genetically altered in ways that enable them to be labelled and manipulated. I identified a mouse line that allows specific access to a subpopulation of deep MEC cells. In an initial set of experiments, I investigated the connectivity between these cells and other brain regions and confirmed that they are connected to cells in superficial layers of the MEC. I next wanted to know how these cells are activated during behaviour. I set up computational pipelines that automate detection and analysis of neuronal activity that I recorded from behaving mice. I used the mouse line that labels cells in the deep MEC in subsequent experiments to identify these cells and to control their activity. My results support the idea that deep layers of the MEC have a powerful influence on superficial layers and suggest how cells in this area may contribute to spatial behaviours.

Acknowledgements

I would like to thank Matt Nolan for his support and guidance throughout my PhD and for being a great supervisor. His insight into my research questions and critical attention to my project were invaluable during my PhD. I am also grateful to Emma Wood, Ian Duguid and Iris Oren for being on my thesis committee and for their advice and support on my project and thesis. I would like to thank Matt Nolan, Gülşen Sürmeli, Daniel Marcu, Brianna Vandrey, Tímea Tóth and Gábor Gerlei for proofreading parts or the whole of this thesis and giving me feedback. I am indebted to Gülşen Sürmeli for teaching me immunohistochemistry, for her advice and ideas on experimental planning, as well as having eternal patience when explaining molecular biology. I thank Sarah Tennant and Alfredo González-Sulser for teaching me the VR task and the related surgical procedures as well as for helpful discussions. I would like to thank Sarah for taking care of my mice on some weekends. Setting up the open field exploration experiment, programming, and in general working with Elizabeth Allison was the most fun and at the same time most productive part of my PhD. I would also like to thank her for teaching me how to build microdrives and implant them in the brain. I was fortunate to collaborate with excellent students, technicians and postdocs. I would like to thank Saishree Badrinarayanan, Oliver Shipston-Sharman, Zuohang Wu and Martyna Rakowska for patching cells in more than a 100 mice I injected. I also thank Derek Garden, Christina Brown and Li-Wen Huang for supervising them and patching even more cells. I would like to thank Christina Brown for organizing and analysing this data. I am grateful to Cristina Martinez-Gonzalez, Holly Stevens and Martyna Rakowska for staining and imaging and being very nice to work with. I also thank Brianna Vandrey for letting me use her favourite place cell. I also thank the whole Nolan lab and members of the Duguid, Rochefort, Wood and Oren labs and Patrick Spooner for being supportive colleagues. I thank the Impact and BRR facilities. I also thank Sacha Nelson and Dr Yasuyuki Shima for sending me p038 sperm. I would also like to thank Dr Steve Ramirez for advice on viruses, Dr Jeremy Magland for help with setting up MountainSort and Dr Yiannis Papastathopoulos for explaining statistics and fitting models to my data. I also thank my family and friends for supporting me throughout my PhD both intellectually and emotionally. My parents for listening to my problems and providing cake, programming and musical training when I needed it the most, both of my grandmothers and my grandfather for their interest in my work and for their support, as well as for their help with cooking on the phone. I would like to thank my grandmother Terézia Komáromy and Sarah Tennant for painting the deep MEC for my PhD thesis. I would specifically like to thank my friends Tímea Tóth, Pál András Papp, Máté Szabó, Stella Kouloulia and Ester Varhaug for their support. Finally, I would like to thank Daniel Marcu for all his support, patience and scientific advice.

This thesis is dedicated to the memory of my grandmother, Terézia Komáromy.

Declaration

I declare that this thesis has been composed by me and that the work included is my own except where explicitly stated otherwise and that this work has not been submitted for any other degree or professional qualification.

Chapter II: Histology and imaging for some of the experiments on the p038 line were done by Martyna Rakowska, Cristina Martinez-Gonzalez, and Holly Stevens as indicated in the text. Cell counting for the Ctip2 analysis was performed by Cristina Martinez-Gonzalez.

Chapter III: I set up the open field exploration task in collaboration with Elizabeth Allison. Parts of the work done by Elizabeth alone are clearly marked in the text. The MATLAB analysis was written by Elizabeth Allison and previous students and postdocs in Emma Wood's lab.

Chapters IV and V: Histology and imaging for the opto-tagging experiment was performed by Holly Stevens. The R code used for the two sample Watson test was implemented by Matt Nolan.

Appendix: The virtual reality based location estimation task was designed and built by Lukas Fischer and Sarah Tennant.

Contents

Chapter I

1 Introduction

How can we understand relationships between neural codes, circuitry and ultimately cognition? Higher-level cognitive processes rely on pre-processed information from lower order brain regions and have a mixture of firing correlates that are often difficult to interpret in experiments. A powerful approach to overcome this difficulty is to investigate cortices that have a clear behavioural readout. With clear behavioural outcomes and associated neural spiking correlates, investigation of cognitive processes may become more tractable and advances in understanding more easily achieved.

Spatial cognition includes processes by which animals determine their location and use this information for planning and navigation. Knowing one's position in the environment is essential for the survival of animals including humans. Spatial cognitive processes are needed for finding food, running away from predators and finding a mate. Normally, navigation is a process continuously executed that happens automatically. When the ability to navigate is compromised, for example by neurodegeneration, it has devastating consequences for the individual (Lithfous, Dufour, and Després 2013), such as reduced mobility and autonomy (Claessen and van der Ham 2017). The outcome of successful spatial navigation, the position of an animal at a desired location, is easily measurable. It is therefore a good focus for investigating mechanisms for cognition.

Based on the spatially selective firing patterns of neurons recorded in the hippocampus, O'Keefe and Nadel (1978) hypothesized that hippocampal neurons store cognitive maps of the environment. Further experiments found several types of spatial cells in the medial entorhinal cortex (MEC) and hippocampus (Fyhn et al. 2004; Taube, Muller, and Ranck 1990b; J O'Keefe and Dostrovsky 1971). My thesis focusses on a group of cells that reside in the deep layers of the MEC and receive

spatially selective input from multiple brain regions. I performed experiments to investigate the connectivity between these cells and other brain regions that contain spatially selective neurons. I also investigated the role of these cells in navigation. The overall aim of my thesis was to take a step towards understanding cognition by deciphering a component of the circuitry underlying spatial cognition.

My aim in the introduction is to define concepts relevant to my thesis, rather than giving a comprehensive literature review on spatial navigation. First, I will discuss some of the main spatial navigation strategies, with a focus on cognitive maps. Then, I will review spatially selective cells in the entorhinal-hippocampal circuit, and the organization of spatial firing in the deep MEC. To introduce the anatomical structure of the deep MEC, I will give a brief overview on its intrinsic and extrinsic connectivity. Afterwards, I will describe the possible predicted functions of the deep MEC. I will introduce experimental paradigms I used to investigate spatial navigation. Finally, I will outline the aims of my thesis.

1.1 Spatial navigation strategies

Mammals can navigate using a number of different strategies. These include beaconing, which uses sensory cues, path integration, which uses information about speed and direction of movement, and triangulation, which integrates information from far away cues (Geva-Sagiv et al. 2015). More complex strategies that rely on internal cognitive maps have also been proposed. In this section, I will review some of the main navigation strategies, namely beaconing, path integration and navigation based on an internal cognitive map.

1.1.1 Beaconing and piloting

A landmark based strategy, beaconing is carried out when animals navigate towards a sensory cue (Geva-Sagiv et al. 2015). This could be visual, auditory, or olfactory (Figure 1.1B). One example of this behaviour was described by Buchler & Childs (1981), who showed that big brown bats orient towards the sound of frogs coming from the swamp, possibly to direct themselves towards the highest concentration of insects in the air when they are hungry. The bats also oriented towards artificially broadcast sounds.

A related strategy, piloting, is when animals use cues near the goal to find the goal relative to these cues. Piloting was put in conflict with beaconing by Redhead et al. (1997). In their experiments, rats were trained to find a submerged platform with a beacon attached to it. Some rats had additional 'piloting' beacons added to the environment, identical to the beacon at the platform. On probe trials, when all beacons were removed, the rats that had ambiguous piloting beacons on training sessions were more successful at finding the platform. These results showed that learning the location of the target platform was influenced by the combination of available piloting and beaconing cues.

Beaconing has been investigated in rodents using several experimental strategies. Alyan and Jander (1994) studied visual beaconing in female mice where the animals learned to retrieve their pups from the centre of an arena. They tested how homing behaviour is affected in experienced mice when distal cues are rotated. Animals made mistakes when distal cues were rotated, which suggests that they relied on distal visual cues during navigation. To test whether rats can use their own smell as an olfactory cue, Wallace et al. (2002) used scented strings that rats had to follow for food rewards. They found that rats were able to track odours including the smell of other rats and their own smell. More recently, Tennant et al. (2018) designed a behavioural task where olfactory cues were removed successfully and visual beaconing was tested in isolation. In this task, mice navigated in a virtual environment towards a beacon on a linear corridor. Overall, experimental data suggests that rodents use beaconing navigation in several behaviours.

Several groups investigated the neural mechanisms underlying beaconing navigation by lesioning brain structures. For example, experiments where the hippocampus was lesioned in a water maze task where animals navigated using beacons to find a hidden platform suggest that the hippocampus is required for recognizing beacons and performing beaconed navigation (Clark, Zola, and Squire 2000). Cue response plus maze experiments established that lesioning the lateral dorsal striatum, a brain region that plays a role in forming habits, impairs visual cue-based navigation permanently (Ferbinteanu 2016). Hippocampal lesions in the same task did not cause a navigation deficit (Ferbinteanu 2016). These results suggest that the involvement of the hippocampus in beaconing navigation might be dependent on experimental conditions.

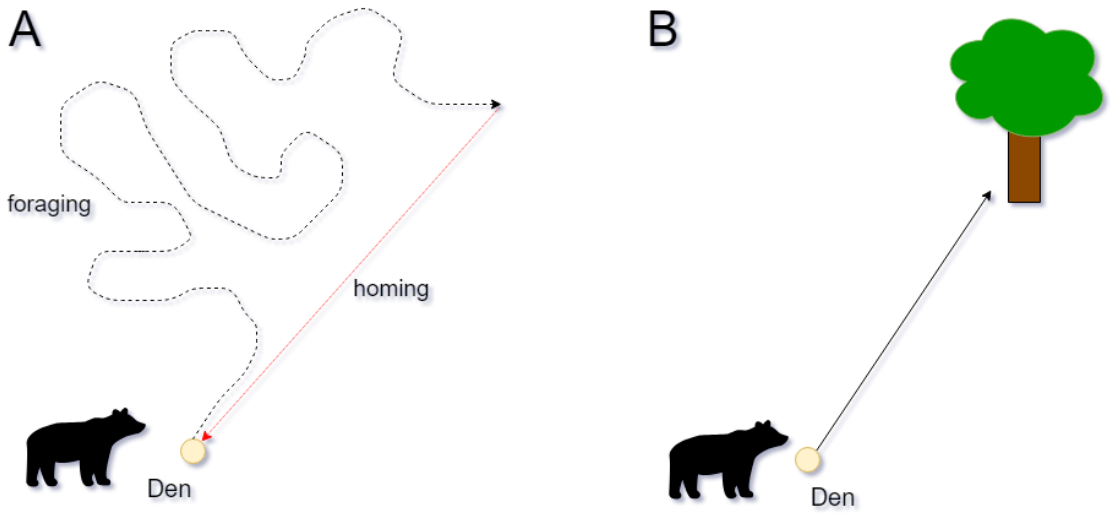

Figure 1.1. Path integration (A) and beaconing (B) navigation. Path integration (A) relies on an internally generated representation of space based on self-motion. Beaconing navigation (B) relies on landmarks, such as visual, auditory and olfactory cues.

1.1.2 Path integration

In his *Origin of certain instincts on how animals find their way home*, Darwin (1873) compared homing behaviour to how natives navigate on the frozen sea in Siberia. Darwin called this ability of keeping track of one's position 'dead reckoning'. He proposed that this strategy is based not only on vision but also on the sense of muscular movement, postulating path integration. One of the first observations to suggest this behaviour existed in rodents was reported by Lashley (1929). He noticed that some of his experimental rats ripped the cover off the maze after learning a task, and ran straight to the reward (Tolman 1948).

Path integration was experimentally demonstrated in mammals by Mittelstaedt & Mittelstaedt (1980) who rotated a platform to test how the gerbil's path to its nest is affected when retrieving her pups. Path integration (Figure 1.1A) is a navigation strategy that relies on self-motion cues rather than external landmarks. This mechanism may rely on an internal representation of space. Path integration in itself is error-prone, but combined with other strategies, such as using landmarks, the 'path integrator' can be reset for more precise location estimation (Etienne and Jeffery 2004). Path integration can be broken down to a linear and angular component to compute the distance travelled and direction, respectively.

Linear and angular path integration have been investigated in rodents using real world and virtual reality-based tasks. Séguinot et al. (1993) led golden hamsters to a feeding place from their nest in a way that they took detours in an arena. When hamsters finished eating, they went directly back to the location of the nest, even when they were rotated while eating and the nest was removed. This experiment demonstrated that the hamster was able to derive the linear components of its route from the nest to the feeding place and calculate a 'homing vector' based on self-motion. More recent studies investigated path integration on a molecular level in mice performing homing tasks. Allen et al. (2014) found path integration to be impaired in mice lacking GluA1-containing AMPA receptors. Path integration was also impaired when NMDA glutamate receptors were removed from the retro-hippocampal region (Gil et al. 2018). Tennant et al. (2018) designed a virtual reality based task to test linear path integration and beaconing strategies. They found that stellate cells, a group of cells in the MEC, are needed for learning the task. It was not tested by Tennant et al. (2018) whether the hippocampus or other brain areas are required for performing the path integration task, but the hippocampus is likely to play a role in representing features of the task (Sarel et al. 2017; Buzsáki and Tingley 2018).

1.1.3 Cognitive maps

Observations by Lashley (1929) and his own rodent experiments inspired Tolman (1948) to develop the concept of an internal cognitive map. This theory suggests that as animals navigate, the brain constructs a mental map of the environment. One of the earliest experiments to support this idea was performed by Blodgett (1929), where he trained food-deprived rats to find a goal location in a maze that had blind-alley entrances. Another two groups of food-deprived rats were not rewarded at the goal location, but fed in their home cages 2 hours later. The rats were trained once a day. The rewarded group learned the location of the food box and entered fewer and fewer blind-alleys. The non-rewarded groups did not learn the task and entered bling-alleys. After the first few days (on day 3 for one group and day 7 for the other group), the non-rewarded groups received a reward for the first time. On subsequent days, these groups immediately showed a high performance and found the goal location quickly, suggesting that they learned about the maze on non-rewarded trials. Similar experiments by Tolman (1948) confirmed that animals are able to learn where blind-alleys are without the reinforcement of a reward. Tolman hypothesized that animals are able to do this by constructing a mental map of the maze while exploring.

Cognitive map-based navigation relies both on self-motion cues and distal landmarks, enabling finding places without crossing familiar areas (Geva-Sagiv et al. 2015).

An example of the investigation of cognitive maps in mammals comes from Tsoar et al. (2011). They displaced Egyptian fruit bats and found that the bats were able to return either to their home cave or to a specific familiar fruit tree. Displacing them far away from home ruled out beaconing and path integration strategies but did not rule out the use of olfactory cues, celestial patterns and magnetic gradients (Holland et al. 2008). However, the straight flights the bats took suggested the use of distal visual cues and the existence of a large scale cognitive map of the environment similar to what was suggested in bees and migrating song birds (Cochran, Mouritsen, and Wikelski 2004; Menzel et al. 2005). Experiments performed on pigeons suggest that another likely homing strategy to consider in cognitive map based navigation experiments is learned road-following (Lipp et al. 2004).

1.1.4 Challenges of investigating spatial navigation

The difficulty of designing experimental paradigms to uncover the mechanisms behind navigation comes from the fact that in real world environments animals are able to use multiple strategies, and may even switch between strategies. For instance, in experiments that aim to investigate path integration, all sensory cues, such as odours, sounds and visual cues need to be removed to ensure that animals rely on proprioceptive cues exclusively. This is technically challenging. Approaches such as virtual reality-based tasks may help overcome these challenges to dissect different navigation strategies.

Classic rodent tests of spatial cognition such as the radial maze (Olton and Samuelson 1976) and water maze (Morris 1981) are solvable through multiple strategies. Animals can potentially use distal visual cues from the room, olfactory cues, auditory cues or path integration. It is difficult to eliminate all cues from the environment that are not included in the design of the experiment. These experiments are also limited in their throughput. For example, because environments need to be cleaned or reorganized between trials the number of trials per day is limited. Another limitation of real world environments is that the size of the environment is restricted based on the size of the experimental rooms as well as the length of wires if neuronal activity is recorded. Virtual reality-based tasks (Tennant et al. 2018; Kautzky and

Thurley 2016) may address these problems by allowing the experimenter to design and manipulate the environment while the animal is head-fixed (Appendix C).

1.2 Neurons in the entorhinal-hippocampal circuit represent space

Spatially selective firing means that a single neuron's action potentials correlate with a spatial aspect of the animal's behaviour such as the animal's location, head-direction or the speed of the animal's movement. Such correlation can be demonstrated by implanting microelectrodes in the brain of a live animal and recording neural activity while the animal explores an enclosure. Spatially selective cells were first discovered in the hippocampus (J O'Keefe and Dostrovsky 1971; Taube, Muller, and Ranck 1990c) then in the entorhinal cortex (Hafting et al. 2005; Fyhn et al. 2004), a structure adjacent and heavily connected to the hippocampus. Several spatial firing patterns were found in the hippocampal-entorhinal circuit. I will give an overview of most spatially selective cell types in this section.

Place cells are neurons that fire selectively at either a single location or multiple locations (Fenton et al. 2008) in the environment (Figure 1.2A). Different place cells fire at different locations, and the combination of active place cells is unique for each location (John O'Keefe and Nadel 1978). Ensemble recordings in the rat hippocampus demonstrated that it is possible to predict the animal's location based on the firing of the cells. Firing properties that predict the animal's position confirm that place cells code the location of the animal (Wilson and McNaughton 1993). Individual place cells are part of multiple independent representations of space (Moser, Rowland, and Moser 2015) and were shown to change their firing when the environment or task is changed (Muller and Kubie 1987). Furthermore, manipulating proximal and distal cues revealed that different place cells code individual local and distal cues and that they can change their firing when the cues are changed (Shapiro, Tanila, and Eichenbaum 1997).

Border cells (Figure 1.2B) and boundary vector cells, neurons that fire relative to the sides of the enclosure, were found in all layers of the entorhinal cortex as well as in the subiculum (Lever et al. 2009; Solstad et al. 2008). Stretching the environment does not alter which sides the border cells fire close to. Border cells are a sparse population, around 10 % of MEC neurons. They are thought to be important in anchoring the firing fields of other spatially selective cells (Solstad et al. 2008). Border

cells might also be important in representing the geometric properties of the environment (Dumont and Taube 2015). Interestingly, before the first experimental observations of border cells, their existence was predicted by computational models that aimed to account for effects of environmental manipulations on place cell firing (Hartley et al. 2000; Barry and Burgess 2007).

Head-direction cells (Figure 1.2C) were discovered in the postsubiculum of freely moving rats (Taube, Muller, and Ranck 1990a). These neurons fire depending on the direction the animal is facing. Their firing is not dependent on other factors such as the animal's location or behaviour. Head-direction cells are sensitive to the rotation of salient cues and rotate their firing fields along with rotated cues (Taube, Muller, and Ranck 1990a). Furthermore, head-direction cells were shown to give coherent responses to cue rotation on a population level when there is a conflict between proximal and distal cues (Yoganarasimha, Yu, and Knierim 2006). A possible role of head direction cells is to maintain the direction the animal is heading, and therefore they could be considered to function as an internal 'compass' (Dumont and Taube 2015). Head-direction cells were later found in multiple brain regions, including the MEC (Sargolini et al. 2006).

Grid cells are spatially selective cells that reside in the medial entorhinal cortex (MEC). They have a hexagonal firing pattern that spans the whole environment (Figure 1.2D). The symmetry of this hexagonal firing pattern is influenced by environmental geometry (Krupic et al. 2013; Krupic et al. 2015). Strikingly, the scale of grid firing is anatomically organized within the MEC with more dorsal parts having grid cell modules that have shorter physical distances between firing peaks in the enclosure, and more ventral parts with longer distances (Brun et al. 2008). Grid cells, similarly to head-direction cells, react to cue rotations on a population level and rotate their firing fields when salient cues are rotated (Hafting et al. 2005). Due to their firing pattern, grid cells are theorized to be involved in path integration (Hafting et al. 2005). Grid cells are found in all layers of the MEC. Some of these cells, called conjunctive cells, in addition to having a hexagonal firing pattern, are also sensitive to the head-direction of the animal (Sargolini et al. 2006).

The hippocampal-entorhinal loop is not only involved in spatial navigation, but also plays a role in other memory-related processes (Squire 1992). To test whether spatial patterns might correlate with other cognitive tasks, Aronov et al. (2017) trained rats to use a joystick to manipulate sound frequency and stop at a specific frequency for a

reward. Recordings during this task showed that a population of neurons represented the entire task, including cells that were sensitive to certain frequencies and cells that had multiple firing fields. Aronov et al. (2017) recorded the same cells in an open field exploration task and found that the neurons representing the sound task overlapped with the grid cell and place cell populations. Moreover, in addition to spatial and auditory space, grid cells represent visual space and fire based on the position of visual gaze on an image (Killian, Jutras, and Buffalo 2012). Strikingly, in experiments where features of cartoon birds were varied, grid cells represented these parameters, suggesting that grid cells might be capable of supporting more abstract non-spatial cognitive processes (Constantinescu, OReilly, and Behrens 2016). These results support the hypothesis that spatially selective cells in the hippocampal-entorhinal system may be representing a variety of cognitive functions in addition to spatial navigation (Buzsáki and Moser 2013; Schiller et al. 2015; Constantinescu, OReilly, and Behrens 2016).

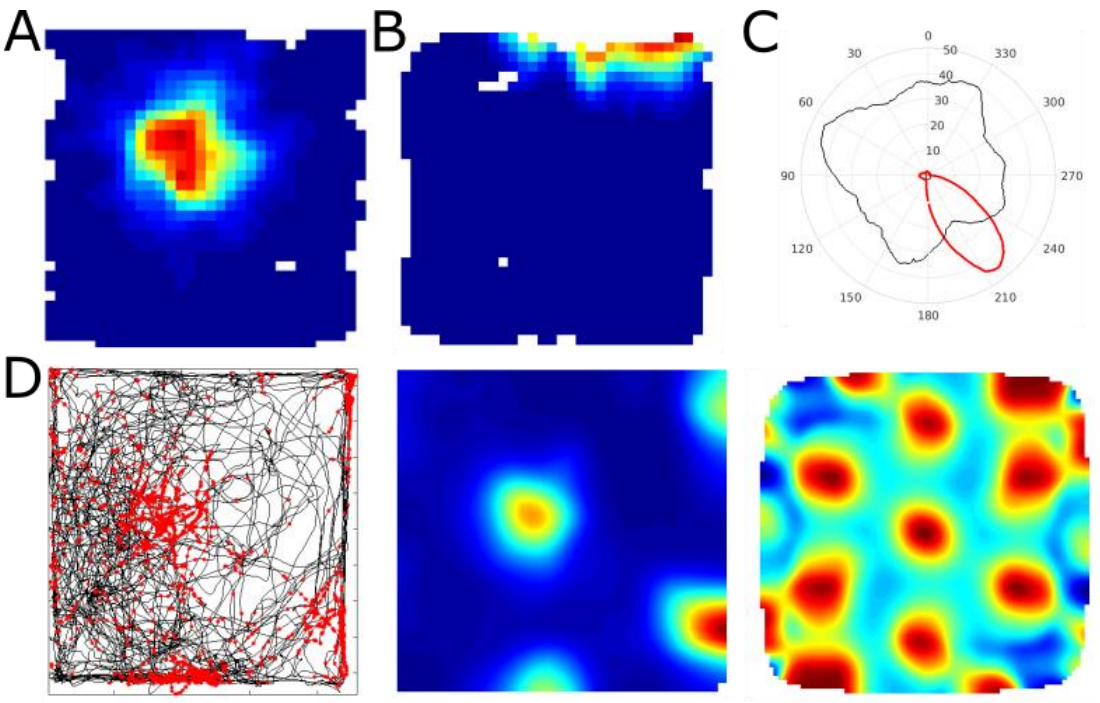

Figure 1.2. Firing fields of spatially selective cell types. Firing field rate maps of a place cell (A) and a place cell with border-like properties (B). Polar histogram of head-direction for head-direction cell (C). Head direction plots were made by plotting a smoothed (10 degree window) polar histogram of the animal's head direction from the whole session (black, normalized value) and during when the cell fired (red, in Hz). Firing events (red dots) on the trajectory of the animal (black line), firing rate map and autocorrelation matrix for rate map of grid cell (D). Firing rate maps were calculated by summing the number of spikes in each location and dividing that by the time the animal spent there and then smoothing the surface with a Gaussian centred on each location bin (Leutgeb et al. 2007). White pixels on rate maps were not visited by the animal. A and B were recorded by Brianna Vandrey and are shown with permission.

How do spatial cells contribute to behaviours? The correlation between spatial and non-spatial cognitive tasks and neuronal firing in the hippocampus and entorhinal cortex suggest that the recorded neurons might play a role in the computation of both cognitive processes. Lesions of the entorhinal cortex (e.g. Davis, Gimenez, & Therrien, 2001) were shown to cause impaired sensory integration and spatial learning. More specific manipulation of entorhinal cells revealed that mice lacking GluA1-containing AMPA receptors have impaired path integration as well as impaired grid cell spatial periodicity (Allen et al. 2014). Furthermore, Gil et al. (2018) disrupted grid cell firing by removing NMDA glutamate receptors from the retro-hippocampal region and found path integration to be impaired. Strikingly, other spatial cells appeared not to be affected in this study, further suggesting the importance of grid cells in path integration. The above results suggest that spatial cells in the MEC are

involved in spatial cognition, but the underlying neuronal mechanism of these computations or how the spatial firing patterns arise is not yet known.

1.2.1 Organization of spatial firing in the deep MEC

Spatially selective cells have been reported to be found in all principal layers of the MEC. Both deep and superficial layers have grid cells (Fyhn et al. 2004; Hafting et al. 2005; Sargolini et al. 2006). The deep MEC, in addition to having grid cells, has conjunctive and head-direction cells (Sargolini et al. 2006). The presence of such spatially selective cells indicates that the deep MEC might play an important role in spatial cognition. However, *in vivo* research was primarily focussed on the superficial layers of the MEC and there is very little data on the deep layers. Extracellular and juxtacellular recordings were performed in the deep MEC of the rat (Sargolini et al. 2006; Burgalossi, von Heimendahl, and Brecht 2014; Burgalossi et al. 2011). Here, I will summarize the main findings of these papers.

Neuronal activity in the dorsal deep MEC was first recorded by Sargolini et al (2006) in rats that explored a 2D environment. In contrast to layer 2 of the MEC that was dominated by pure grid cells, they found that grid cells colocalized with head-direction cells and conjunctive cells. They found that head-direction cells recorded in the deep MEC were similar to the ones in the hippocampus, and had a maximum firing rate of about 40 Hz when the animal was facing the direction to which the cell was sensitive. Simultaneously recorded head-direction cells were found to have widely distributed firing directions, and were usually encountered together with grid cells. The population of grid and head-direction cells overlapped, with some grid cells having head-direction sensitivity, and some head-direction cells having grid properties. Importantly, entorhinal cells gave coherent responses to manipulations of the environment. For instance, rotating a polarizing cue on the wall of the environment resulted in the rotation of the firing fields of the recorded cells by the same angle.

In contrast to the data from Sargolini et al. (2006), which was recorded with tetrodes, juxtacellular recordings suggest that cells in the deep layers of the MEC have very low firing rate (Burgalossi et al. 2011). To test whether the low firing rate (Burgalossi et al. 2011) of deep entorhinal neurons is modulated by novelty, Burgalossi et al. (2014) performed juxtacellular recordings on rats that explored both familiar and novel environments. They found that deep MEC activity was very low in both conditions, and that the majority of cells they recorded were silent (19 out of 37 cells). These

results indicate that encoding is sparser in the deep MEC than previously suggested (Sargolini et al. 2006). Sparse coding was theorized to be used to encode information in the cortex (Field 1994). In a system that uses sparse coding, information is represented with a minimum number of active units in a distributed manner. All cells respond to a given input with the same probability, but they all have a low response probability for a single input (Field 1994). Low firing rates both in novel and familiar environments may suggest that sparse coding is a general feature of the deep MEC (Burgalossi, von Heimendahl, and Brecht 2014).

Elements of the above two studies are inconsistent. A possible reason for this is that they may have included molecularly different cell types. Due to the methods applied in the papers, we do not know the molecular identity of the recorded cells. In extracellular recordings, it is not possible to identify the molecular identity of the recorded cells without combining recordings with genetic methods. Juxtacellular recordings are extremely laborious, but could in principle access molecular identity of deep MEC cells by performing immunostaining after recording. However, this was not done by Burgalossi et al. (2014). Furthermore, since both studies were done in rats, there is no information available in mice.

One of the difficulties of investigating firing properties of small structures like the deep MEC is that hitting the layer with electrodes and then confirming the location of the electrodes is challenging. Relative to previous studies, specific targeting could be improved by using transgenic animals to genetically target and identify deep MEC cells. Transgenic animals that have transgenic expression restricted to a sublayer of the deep MEC could be injected with viruses that infect transgenic cells selectively. Viruses that make cells light sensitive (Liske et al. 2013; Kohara et al. 2014) could be used for identification by recording activity from cells that respond to light stimuli. Another challenge when extracellular recordings are performed is that cells with low firing rates are difficult to separate from other cells. It is possible that this issue could be addressed by improved spike sorting methods.

1.3 The position of the deep MEC in the entorhinal-hippocampal loop

The suggestion that the hippocampus and the MEC may be functionally related was made by Ramón y Cajal (1902), based on the extensive connectivity between the two structures. Further research refined this idea, and now we consider the MEC to be a

structure that processes information between the hippocampus and various cortical areas (Burwell and Amaral 1998; Witter et al. 2017). One step to understanding how this information is processed is to map the connectivity between various cell types within the layers of the MEC. Investigating the anatomical organization of structures provides invaluable insight into potential function, since it reveals which parts are able to communicate. In the next section, I will give an overview of the intrinsic and extrinsic connectivity of the deep MEC.

1.3.1 The deep MEC is subdivided

Based on the morphology of the cells, the deep MEC was divided into layer 5a (L5a) and layer 5b (L5b). Neurons in L5a are pyramidal cells with relatively large cell bodies, positioned next to the lamina dissecans. L5b cells have smaller cell bodies and are densely packed, and have a more uniform soma size relative to L5a (Canto et al. 2012a; Sürmeli et al. 2015). In addition to morphology, comprehensive analysis of gene expression markers from *in situ* hybridization images suggested that L5 comprises of distinct sublayers (Ramsden et al. 2015). To find out the molecular identity of deep MEC cells, Sürmeli et al. (2015) performed immunohistochemistry staining (Figure 1.3) to label L5b cells with Ctip2, and L5a cells with Etv1 (Er81) markers. This experiment confirmed that layer 5 of the deep MEC is subdivided into molecularly different sublayers.

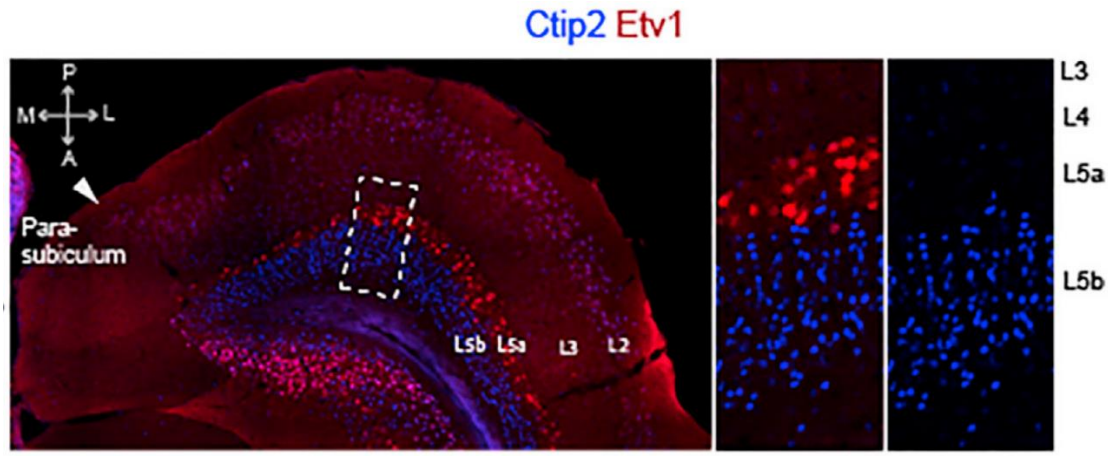

Figure 1.3. The deep MEC is subdivided. Horizontal section of the medial entorhinal cortex stained with Ctip2 (blue), Etv1 (red). A zoomed in image on the right shows how L5a and L5b can be distinguesed by Etv1 and Ctip2 staining. Etv1 and Ctip2 stained cells are clearly separated into two bands, labelling L5a and L5b. Figure by Sürmeli et al (2015) used with permission.

1.3.2 Extrinsic connectivity

Initially, the deep MEC was thought to function as a relay between the hippocampus and cortical areas, while the superficial layers were though to provide input to the hippocampus (Burwell and Amaral 1998). Sürmeli et al (2015) investigated inputs to L5 by labelling synaptic terminals of potential upstream neurons and by optogenetically activating potential input pathways. They found that L5b, but not L5a, receives input from L2 stellate cells and from the hippocampus (Figure 1.4). Recent trans-synaptic tracing experiments in the rat suggest that information flows the opposite way as well, and L5b cells project to L5a as well as to superficial layers (Ohara et al. 2018).

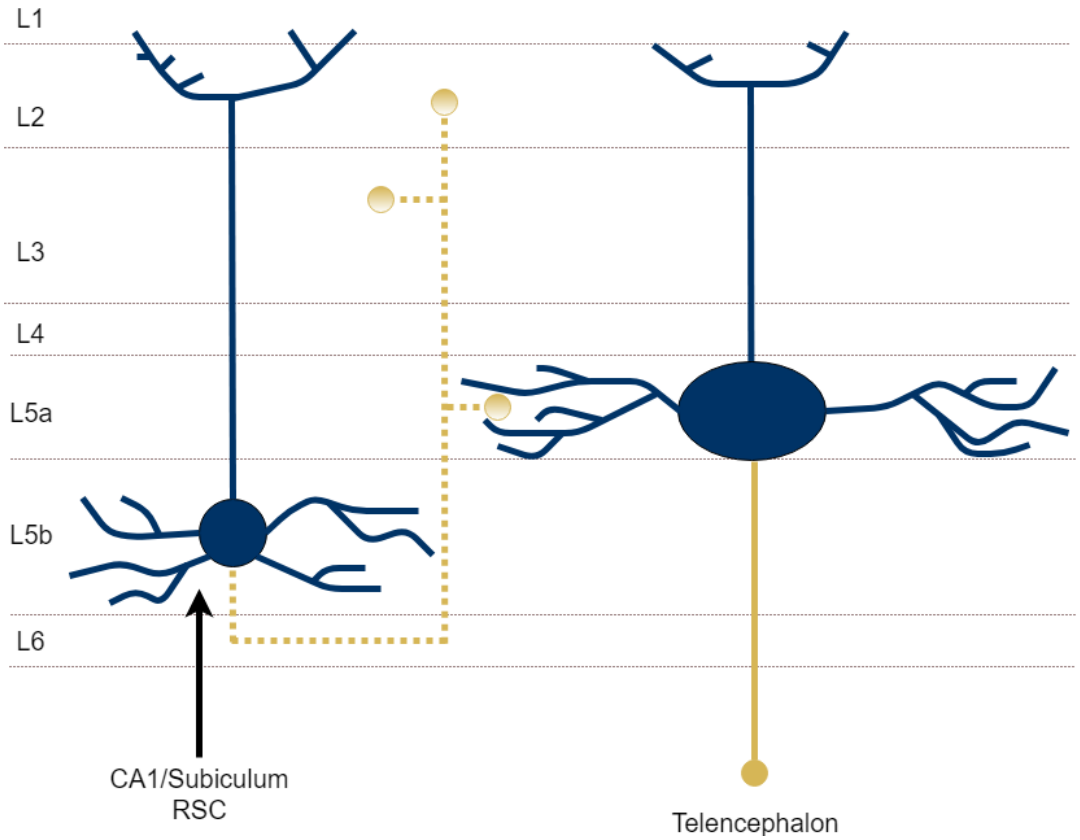

Figure 1.4. Extrinsic connectivity of the deep MEC. L5b cells receive input from L2 stellate cells, CA1, and the retrosplenial cortex (RSC), and project to L5a, L3 and L2. L5a cells project to the telencephalon (Sürmeli et al. 2015; Witter et al. 2017; Canto, Wouterlood, and Witter 2008).

By injecting retrograde tracers into various cortical areas, Sürmeli et al. found extensive intratelencephalic projections originating from L5a, but not from L5b. The deep MEC was suggested to receive input from frontal and cingulate cortices (see review by Witter et al., 2017), as well as from the retrosplenial cortex (Czajkowski et al. 2013). The retrosplenial cortex was shown to almost exclusively innervate L5 cells within the MEC (Wyass and Van Groen 1992; Vertes 2004; Jones and Witter 2007). Some of the cells innervated by the retrosplenial cortex had axons in the superficial MEC, which suggests that the cells that receive input from the retrosplenial cortex are in L5b (Witter et al. 2017).

The presence of such extensive connectivity between deep MEC cells and other cell groups of the hippocampal-entorhinal complex that are known to have spatially selective cells among them suggests that the deep MEC might play a role in spatial computations. More specifically, based on its position in the circuit, L5b could be receiving input from place cells (CA1), and grid cells (L2 of the MEC) simultaneously,

as well as head-direction input from the retrosplenial cortex. However, the connectivity between specific spatially selective cell types and the functional relevance of these connections remains to be investigated *in vivo*.

1.4 Predicted role in navigation

Based on its position in the hippocampal-entorhinal loop, the deep MEC is well-placed to play a role in spatial cognitive processes. The presence of spatially selective cells in the deep MEC, such as head-direction cells and conjunctive cells further supports this hypothesis. However, computation in the deep MEC received little attention. So far, two classes of models have been suggested, and I will outline them both.

Tocker et al. (2015) measured noise correlations between 508 pairs of simultaneously recorded grid cells. They found highly correlated noise with a 0 ms time lag in grid cells that belonged to the same module, which suggests that these cells receive common input. Based on their correlation measurements, they introduced a model in which conjunctive cells in the deep MEC form an attractor network and send organized feed-forward projections to the superficial MEC, activating pure grid cells. In this model, superficial grid cell 'activity bumps' did not receive velocity input, but they followed activity bumps in the deep MEC. Overall, Tocker et al. suggest that the deep MEC computes path integration, while the superficial MEC computes the absolute position of the animal.

Egorov et al. (2002) demonstrated that L5 MEC neurons respond to stimulation in combination with bath application of cholinergic agent carbachol with a Ca^{2+} dependent plateau, which leads to graded persistent firing (Frank and Brown 2003). Graded persistent firing means that the cells are able to fire for a prolonged period after stimulation, and that their firing frequency depends on the input stimulation. Such graded activity could potentially store information in the individual cells, making it possible to make associations between events that happen at different times (Frank and Brown 2003). *In vitro* models were proposed (Fransén et al. 2006) to describe this working memory mechanism, but there are no *in vivo* studies that investigate persistent activity in the deep MEC.

The function of the deep MEC is not yet known. Possible functions include computing path integration and playing a role in working memory (Tocker, Barak, and Derdikman 2015b; Fransén et al. 2006). To test whether L5 plays a role in path integration,

experiments need to be done on animals that perform path integration. Neuronal activity could be recorded and manipulated to reveal whether L5 cells are needed for path integration and to find out their firing patterns during the task. To complete the models describing persistent activity, *in vivo* experiments are needed to (1) demonstrate that persistent activity is present in live animals and (2) find out the molecular identity and spatial firing properties of these cells. Furthermore, it would be important to distinguish between L5a and L5b due to their different connectivity.

The entorhinal grid system is hypothesized to be involved in path integration because of the periodic firing patterns of grid cells (Hafting et al. 2005; Fyhn et al. 2004) and impaired location estimation when entorhinal cells are manupulated (Allen et al. 2014; Tennant et al. 2018). Two major groups of models were proposed to predict possible mechanisms for path integration by the grid system. Continuous attractor network models predict that local recurrent network activity creates an 'activity bump' that is controlled by head-direction and velocity inputs (Mcnaughton et al. 2006; Guanella, Kiper, and Verschure 2007; Shipston-Sharman, Solanka, and Nolan 2016). Oscillatory interference models propose that the head-direction and speed of the animal is coded in the membrane potential oscialltions of individual grid cells (Giocomo, Moser, and Moser 2011). It is an open question whether the predictions of these models are correct. An alternative hypothesis is that the grid system is a high capacity code (Klukas, Lewis, and Fiete 2019; Fiete, Burak, and Brookings 2008; Mathis, Herz, and Stemmler 2012) that is able to represent many environements and cognitive spaces and implement error correction, but does not necessarily perform path integration. To test these ideas and establish the role of deep MEC grid cells specifically, more *in vivo* experiments are needed where entorhinal activity is recorded.

1.5 Experimental paradigms to investigate spatial navigation

What do we need to do to understand what the deep MEC does? One way to address this question is to record and manipulate the activity of deep MEC neurons in behaving animals. Since the deep MEC is a relatively small structure, genetic tools are needed to target it selectively. Here, I will discuss some methods that can address this question and possible ways to combine them, highlighting the aspects I focussed on in the experimental work described later in my thesis.

1.5.1 Identifying action potentials fired by single neurons in behaving animals

Understanding how neural computations work in behaving animals requires us to decode the communication between neurons. Neurons send information to each other by firing action potentials, which causes electrical potential changes in the extracellular space. To record these action potentials, we can place electrodes in the brain and measure changes in the extracellular electric potential. This signal will contain low frequency local field oscillations that arise from synchronized multi-unit activity, as well as action potentials from the cells close enough (< 50 µm) to the recording electrode tips (Rey, Pedreira, and Quian Quiroga 2015). We may record multiple neurons with this method, but without analysing the data, we cannot know which firing event belongs to which cell. Identifying which action potentials correspond to which cell is paramount, since cells close to each other can have different properties and play different roles (Rey, Pedreira, and Quian Quiroga 2015).

Spike sorting is a technique that enables identification of action potentials fired by a single neuron. This is possible because the detected shape of action potentials is different for different cells. The shape of the firing event is determined by the expression pattern of ion channels on the cell membrane (Bean 2007) and the distance of the cell from the recording site. When a neuron's membrane potential becomes depolarized, voltage gated ion channels open, and sodium ions enter the cell, which further depolarizes the cell. As the membrane depolarizes, further potassium channels open and the cell returns to its resting potential (Hodgkin and Huxley 1952). Depending on the number, sensitivity and type of ion channels that influence the kinetics of this process, the shape of the action potential will be different. For instance, GABA-releasing interneurons tend to have narrower action potentials compared to glutamatergic pyramidal cells (McCormick et al. 1985). In addition to the differences due to the intrinsic properties of the cells, the amplitude and shape of the action potentials detected will differ depending on the position of the tip of the recording electrode relative to the cell's soma and dendrites (Gold et al. 2006). Thus, it may be possible to sort action potentials fired from identical cell types, since the position of the cells will be different relative to the electrode.

In practice, spike sorting neuronal data poses a number of challenges. One challenge is that electrodes record signals from multiple neurons, some of which are far from the recording tips and so will be recorded with very low amplitude. If two or more cells have synchronized activity and fire simultaneously or very close in time, their

waveforms will overlap on the recorded signal, and may not be possible to separate (Ekanadham, Tranchina, and Simoncelli 2014; Franke et al. 2010). In addition, noise can arise from the movement of the animal or due to external sources. Furthermore, electrodes can drift during recordings. Several groups attempted to develop spike sorting techniques to address these challenges and separate single units in a fast, objective and reproducible way.

In one of the main approaches, clustering is based on various features of the waveforms. Such features can be the amplitude, the width of the spike or principal components (Lewicki 1998; Einevoll et al. 2013; Marre et al. 2012). These algorithms include manual steps. Other groups implemented semi-automatic spike sorting algorithms, where users only need to curate the output and merge or split clusters (Hill, Mehta, and Kleinfeld 2015; S N Kadir, Goodman, and Harris 2017; Rossant et al. 2016). Still, manual curation results in errors and is prone to bias (Wood et al. 2004).

Recently, Chung et al. (2017) developed a fully automated spike sorting algorithm called MountainSort, which has a similar or lower error rate compared to manual methods. MountainSort sorts neuronal spikes into clusters based on their density in a low-dimensional feature space. There are two main assumptions MountainSort relies on about clusters in feature space. The first assumption made is that all clusters arise from a unimodal density function, meaning that if we project a cluster to any line, it will have only one peak. The second assumption is that any two clusters can be separated by a hyperplane, and near the hyperplane the density of spikes will be lower (J. E. Chung et al. 2017). The main advantage of this pipeline is that it removes manual intervention, and therefore makes spike sorting fully reproducible. However, it does not address the problems of overlapping spikes or electrode drift.

1.5.2 In vivo optogenetic identification of neurons

Spike sorting is a powerful tool to identify action potentials fired by single neurons, but alone it cannot reveal a neuron's anatomical or molecular identity. Optogenetic strategies (Zemelman et al. 2002; Boyden et al. 2005) have been used to identify a genetically modified neurons that express opsins (Buetfering, Allen, and Monyer 2014; Kravitz, Owen, and Kreitzer 2013; Lima et al. 2009; Pi et al. 2014). This can be achieved by injecting mice that express Cre or tTA in specific cell populations with viruses that express opsins conditionally on the presence of Cre/tTA expressing cells.

In this way, the cells expressing Cre/tTA become light responsive. With this strategy, action potentials are triggered or inhibited (Rowland et al. 2018) in opsin expressing cells by shining a light. It is then possible to deduce that the cells that respond to light stimulation belong to the genetically altered population (Roux et al. 2013). In principle, this approach sounds straightforward, but there are a number of issues to consider.

One of the technical difficulties of identifying directly activated light responsive neurons is that stimulation may activate multiple neurons simultaneously, causing them to fire at the same time. High intensity stimulation can also cause photoelectric artefacts that distort spike waveforms. Additionally, high intensity stimulation can cause the tissue to heat up, which might damage cells, or increase firing in cells that do not express opsins (Stujenske, Spellman, and Gordon 2017). To address these problems, low light intensity stimulation can be applied *via* optic fibres mounted very close (< 40 µm) to the recording electrodes (Roux et al. 2013). However, low light intensity stimulation will make responses less reliable, increasing the number of false negatives. Another potential approach for identifying single light responsive neurons is to infect neurons sparsely to reduce multi-unit responses.

To evaluate whether stimulated cells are light responsive, a statistically robust method is needed. To reduce the number of false negatives in experiments where low intensity stimulation is used to perform opto-tagging, Kvitsiani et al (2013) developed a statistically based unsupervised method to detect neurons directly activated by light. In their Stimulus-Associated spike Latency Test (SALT), they test the null hypothesis that light stimulation does not change firing latencies. This analysis is done by measuring the distance between the distribution of spike latencies after light stimulation and a baseline distribution using a modified version of the Jensen-Shannon divergence (Endres and Schindelin 2003). The advantage of this analysis is that it does not use any arbitrary thresholds or time windows, providing an objective method to test whether neurons are light responsive. Overall, this approach reduces false positives caused by high firing rates, and false negatives in case of unreliable responses at low intensity stimulation, increasing the data yield of experiments.

1.6 Aims of this thesis

Based on the presence of spatially selective cells, spatial cognition is hypothesized to be computed in the entorhinal-hippocampal loop (John O'Keefe and Nadel 1978). The

deep MEC is a part of this circuitry and has spatially selective neurons including grid cells and head-direction cells (Sargolini et al. 2006). *In vivo* juxtacellular recordings from the deep MEC of rats found that deep MEC cells have very low firing rates (Burgalossi, von Heimendahl, and Brecht 2014), which is not in agreement with extracellular results from rats by Sargolini et al. (2006). Two distinct sublayers were identified in L5 of the MEC in mice, with one of the sublayers, L5b, receiving input from areas rich in spatially selective cells (Sürmeli et al. 2015). Stellate cells in L2 of the MEC, a part of the brain with the highest number of grid cells (Hafting et al. 2005; Fyhn et al. 2004, Sarolini et al. 2006), were shown to project to L5b of the MEC. Additionally, CA1 of the hippocampus, an area rich in place cells (J O'Keefe and Dostrovsky 1971) was shown to send information to L5b (Sürmeli et al. 2015). However, the projection targets of L5b cells are not yet known, and the function of L5b neurons has never been tested. Based on the above findings I hypothesized that L5b of the MEC plays a role in spatial cognition by integrating the spatial input it receives.

The overall aim of my thesis was to investigate the function of cells in the deep MEC in mice. In the first results chapter (Chapter II), my primary aim was to identify and anatomically characterize a transgenic mouse line that has specific transgenic expression in L5b. I selected lines from online databases based on gene expression patterns and performed experiments to test specificity in viral injections. I identified a mouse line that had transgenic expression restricted to a small subpopulation of L5b neurons, and characterized this transgenic population using immunolabeling. My secondary aim in Chapter II was to identify projection targets of L5b cells. More specifically, I set out to test whether L5b cells project to the thalamus and superficial layers of the MEC.

In Chapter III, my main aim was to implement and test an automated spike sorting pipeline using MountainSort (Chung et al. 2017) to analyse electrophysiology data from mice exploring an open field arena and during optogenetic stimulation. I set out to test different parameters and processing strategies to maximize the number of correctly detected units in my data. Setting up an automated spike sorting pipeline was motivated by analyses described in the Appendix where I tested more manual spike sorting approaches. Further, I needed to implement an environment that can accept input from multiple users, perform all data processing without user intervention and then save results to the lab's permanent storage.

To investigate firing properties of L5b cells, my aim in Chapter IV was to record neuronal activity in mice that explore an open field arena and identify recorded cells in L5b. I used the mouse line identified in Chapter II to gain genetic access to a small subpopulation of L5b cells and injected a channelrhodopsin virus that selectively infected the transgenic population. To identify infected cells, I performed opto-tagging stimulation at the end of each exploration session. Using the analysis pipeline presented in Chapter III, I was able to identify light responsive cells. This analysis allowed me to characterize the firing fields of identified cells in the open field. I hypothesized that identified L5b cells would include spatially selective cells such as grid cells and conjunctive cells.

In Chapter V, I set out to (1) compare the population of MEC cells I recorded in mice (data presented in Chapter IV as well) to existing extracellular and juxtacellular results from rats and (2) further analyse head-direction properties within the firing fields of grid cells. To compare my population of recorded neurons from the mouse to results reported by Sargolini et al. (2006) and by Burgalossi et al. (2014) from the rat, I analysed grid and head-direction scores as well as firing rates of cells in deep and superficial layers of the MEC. I hypothesized to find similar results in mice compared to what was reported in rats. Finally, I performed analyses to investigate head-direction firing within individual grid fields. I tested the hypothesis that individual firing fields of a grid cell code different head-directions.

Overall, my thesis will present an investigation of anatomical and firing properties of L5b neurons of the MEC.

Dorsal deep medial entorhinal cortex by Sarah Tennant.

Chapter II

2 Targeting the deep MEC and dissecting connectivity

2.1 Introduction

Designing experiments that specifically test the function of deep MEC layers requires molecular targeting strategies to be identified and characterized. Circuitry in the deep layers of the MEC has been investigated using classical anatomical methods (Canto, Wouterlood, and Witter 2008; Sürmeli et al. 2015; Ohara et al. 2018), while electrophysiological recordings in behaving animals have indicated that some deep MEC neurons have spatial firing fields (Sargolini et al. 2006). Whereas mouse lines that give genetic access to stellate cells in superficial layers of MEC has benefited investigation of the connectivity and function of superficial layers (Sürmeli et al. 2015; Tennant et al. 2018), lines targeting specific neuronal populations in the deep layers of the MEC have not yet been characterised. The main goal of this chapter is to identify and characterise lines suitable for this purpose.

Layer 5 (L5) of the deep MEC was subdivided into two sublayers based on the morphology of cells (Canto and Witter 2012a), but it was only shown recently that these two sublayers have different molecular markers and projections in the mouse (Sürmeli et al. 2015). Immunolabeling against the transcription factor Etv1 labelled 66.8 % of cells in L5a, the more superficial sublayer next to the lamina dissecans. In

the deeper sublayer, L5b, Ctip2 immunolabeling marked 85.8 % of neurons (Sürmeli et al. 2015). It was shown that L5a has extensive intra-telencephalic projections and L5b receives projections from the dorsal hippocampus and superficial entorhinal stellate cells (Sürmeli et al. 2015). L5b cells that responded to optogenetic activation of L2 stellate cells were mostly pyramidal, had small cell bodies and their basal dendrites were mostly restricted to L5b. The basal dendrites of responsive L5b cells extended in all directions within the sublayer. In contrast, L5a basal dendrites were found to extend along the medial-lateral axis, mostly restricted to L5a. Further, retrograde tracers injected into anterior and lateral thalamic nuclei resulted in sparse expression in L5b, suggesting that L5b cells might project to the thalamus (Sürmeli et al. 2015). Such striking difference in connectivity suggests that these adjacent layers might play different roles. Trans-synaptic tracer experiments in the rat demonstrated that L5b MEC innervate neurons in L5a, L2 and L3 (Ohara et al. 2018). These results suggest that L5b neurons might mediate hippocampal output (from CA1 and subiculum) to telencephalic areas *via* L5a and send feedback to the superficial MEC through the hippocampal loop (Ohara et al. 2018). However, the identity of projection targets of L5b neurons is not yet known and the two sublayers have never been selectively targeted *in vivo* and their function remains to be described.

One of the challenges of investigating the function of specific brain regions is that without genetic access to the cells of interest, manipulations, such as lesions, will affect adjacent areas and therefore confound findings and make behavioural results hard to interpret. Thus, to address hypotheses proposed in my thesis and investigate the role of L5b of the deep MEC in spatial computation by manipulating its activity specifically without affecting L5a or L6, I needed to find genetic tools that give

sufficiently specific access to L5b cells. My primary aim in this chapter was to identify methods to selectively access L5b of the MEC in mice.

To be able to selectively target the deep MEC and manipulate cellular activity without affecting adjacent parts of the brain, I had to find a transgenic mouse line with genetic access specific to L5. Based on the gene expression analysis done by Ramsden et al. (2015), I searched the Allen Brain Atlas (http://www.brain-map.org/), GENSAT (Gene Expression Nervous System Atlas, http://www.gensat.org), and the literature for all molecular markers that were found to be present in the deep MEC. I selected three potential candidates, the rasgrp, trib2CreER and p038 lines. The rasgrp and trib2CreER lines express Cre under the control of the rasgrp1 (RAS guanyl releasing protein 1) and the endogenous tribbles homolog 2 promoters, respectively.

In the trib2CreER mouse line, on the Trib2-2A-CreERT2-D knockin/knockout allele, exon 2 of the tribbles homolog 2 was replaced by a CreER fusion gene, and an in-frame F2A peptide cleavage signal. This modification abolishes Trib2 gene function and expresses CreERT2 from the Trib2 promoter elements. CreER is a tamoxifen-dependent Cre recombinase (Feil, Valtcheva, and Feil 2009). In the absence of tamoxifen the enzyme has reduced activity. When tamoxifen is injected in these mice, it binds to the CreER fusion protein, and allows it to excise DNA specifically at LoxP sites.

The p038 mouse line (Figure 2.1) was generated using a tet-transactivator dependent enhancer in a study that aimed to generate transgenic lines with restricted expression (Shima et al. 2016). The tet-enhancer probe was incorporated into the PiggyBac transposon system to deliver the tet enhancer trap probe. The enhancer probe constructs use the tet-off system and incorporate a tet-responsive element driving mCitrine reporter expression. tTA positive cells have endogenous mCitrine reporter

expression. The rationale behind capturing distal enhancers to generate transgenic lines, rather than using BAC transgenesis to recapitulate expression of marker genes, is that higher specificity can be achieved using enhancers. Shima el al. (2016) generated more than 200 such lines using this method, with some, such as the p038 mouse line having remarkably restricted expression patterns.

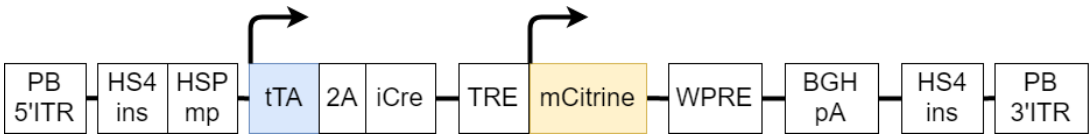

Figure 2.1. p038 mouse line. PiggyBac constructs containing tTa and Cre. HSPmp: minimal promoter from Hspa1a, tTA: tet transactivator, TRE: tet response element, WPRE: woodchuck hepatitis virus post-transcriptional regulatory element, 2A: FMDV-2A sequence, BGHpA: poly-adenylation signal from bovine growth hormone, HS4ins: insulator sequence from DNase hyper sensitive site in the chicken β-globin gene, PB- 5'ITR and PB-3'ITR: PiggyBac inverted terminal repeat (Shima et al. 2016).

I assessed the specificity of the selected lines by injecting viruses that selectively label transgenic cells. For lines where labelled cells were present in L5b and adjacent structures had no or little expression, I quantified specificity by counting cells. To confirm that the transgenic cells are in L5b of the deep MEC, and quantify the extent of expression within the layer, I performed immunohistochemistry staining experiments to explore overlaps between the transgenic cell populations and molecular markers. To evaluate the feasibility of experiments where all transgenic cells are manipulated, I mapped transgenic cells in the whole brain.

My secondary aim was to establish whether L5b neurons made long range connections to other parts of the brain or their output is restricted to neurons in the MEC. I did this by characterizing L5b specific lines anatomically by mapping their connectivity with other regions. To do this, I injected tracers and viruses in potential target areas, and assessed expression patterns. Mapping connectivity was important to evaluate whether the transgenic subpopulation has the expected connectivity or is

a specialized subset of L5b cells. Characterizing lines to this extent informed the experimental design of my subsequent experiments.

2.2 Methods

2.2.1 Ethical statement

All procedures were performed under a UK Home Office project license (PC198F2A0) in accordance with The University of Edinburgh Animal Welfare committee's guidelines. All procedures complied with the Animals (Scientific Procedures) Act, 1986, and were approved by the Named Veterinary Surgeon.

2.2.2 Animals

Rasgrp1 (Tg(Rasgrp1-Cre)PO1Gsat/Mmucd, Stock No: 034811-UCD) mice were obtained from MMRRC (Mutant Mouse Resource & Research Centers supported by NIH). This line was generated using BAC (bacterial artificial chromosome) engineering. An intron containing a cassette expressing Cre recombinase was inserted, followed by a polyadenylation sequence, to terminate transcription, into a BAC vector at the ATG codon (BAC address: RP23-73I19). A BAC vector was then used to generate the transgenic line. When injected intracranially with AAVs (adeno-associated virus) that express transgenes conditionally on the presence of Cre, only cells that express Cre should express the transgene.

Trib2-CreER (Trib2-2A-CreERT2-D) mice (Figure 2.2) were obtained from The Jackson Laboratory (Stock No. 022865, Trib2-2A-CreERT2-D). Cre expression was induced by injecting 20 mg / ml (75 mg / kg of body weight) tamoxifen (Sigma-Aldrich, 10540- 29- 1) dissolved in 0.1 ml corn oil (Sigma-Aldrich, 8001-30-7) solution intraperitoneally for three consecutive days, 10 days after intracranial Cre-dependent AAV viral injections. Mice were perfused 10 days after the last tamoxifen injection.

The p038 mouse line (Shima et al. 2016) was obtained from Sacha Nelson's lab (Brandeis University), and re-derived at the University of Edinburgh.

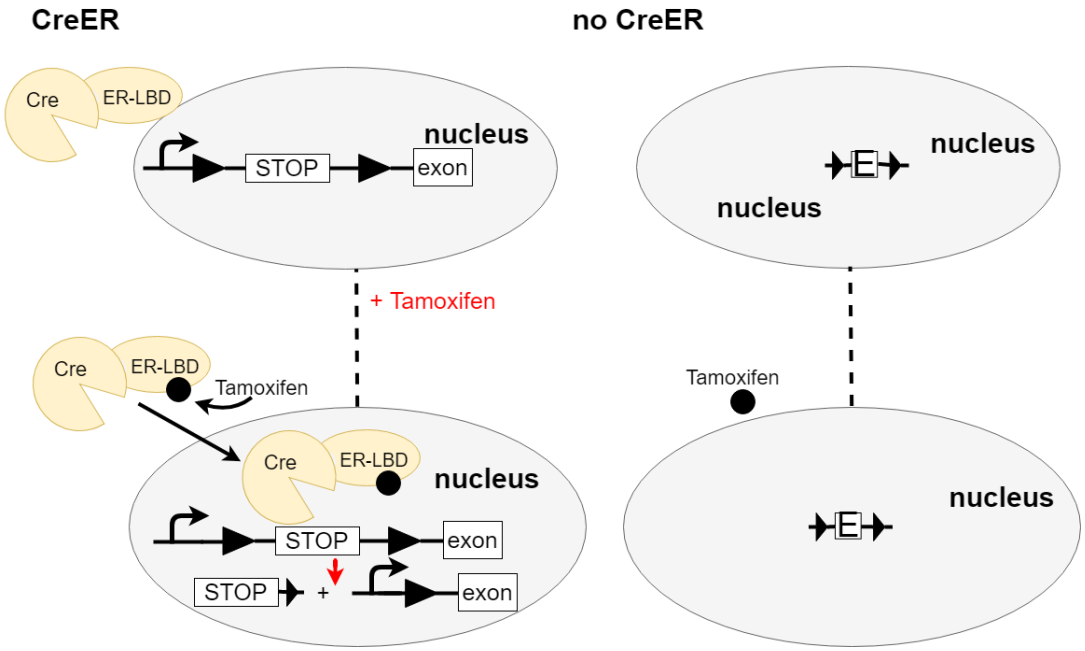

Figure 2.2. CreER recombinase system. Cell that expresses CreER (left) and cell in the same animal that does not express CreER (right). The loxP (triangle)-flanked stop codon is excised in cells that express tamoxifen dependent CreER recombinase, so the exon will be expressed. CreER recombinase is Cre fused to a mutated ligand-binding domain (LBD) of the estrogen receptor (ER). Without tamoxifen, CreER stays in the cytoplasm. When tamoxifen is present, and it binds to the LBD, the recombinase is translocated to the nucleus, where it can recombine its loxP flanked DNA. This means that cells that express CreER will express Cre in the presence of tamoxifen only (Feil, Valtcheva, and Feil 2009).

2.2.3 Injection of viruses and dyes

To inject viruses (Table 2.1) and retrograde tracers to the medial entorhinal cortex or to the thalamus I performed stereotaxic surgeries in a designated room. I induced inhalation anaesthesia using 5 % isoflurane / 95% oxygen and sustained at 1 - 2 % isoflurane / 98 – 99 % oxygen throughout the procedure (1 L / minute). I shaved the head (WAHL Pocket Pro Trimmer, Cat.: 34452P) and wiped the skin with concentrated Betadine. I covered the eyes with Viscotears to protect vision. I made an incision at the midline from between the eyes to between the ears.

For injections targeting the deep MEC, I disconnected the muscles above the structure using a spatula and a forceps and removed connective tissue. I straightened the head by measuring the depth of the skull both medio-laterally and rostro-caudally using a micropipette. To do this, I set the stereotax to zero on Bregma and measured the depth of the skull 2 mm lateral relative to Bregma on both sides and adjusted the head using the stereotax until the depth was the same (with 0.02 mm precision) on the two sides. I repeated this between Bregma and Lambda to straighten the skull along its rostro-caudal axis. I alternated between the above two adjustments until the head was completely straight. I also ensured that Lambda was not shifted laterally relative to Bregma.

For deep MEC injections, I made a craniotomy using a hand drill +/- 3.4 mm lateral from Lambda, on the fissure. For injections targeting the thalamus, I made a craniotomy at +/- 0.75 mm lateral and 0.75 mm posterior to Bregma. I used a glass pipette to inject 100 - 500 nl of virus or fast blue (Polysciences, 17740-1).

For targeting the deep MEC, I injected at 3.4 mm lateral to Bregma at 1.8, 2.2, and 2.6 mm deep. For the antero-dorsal nucleus of the thalamus, I injected 0.7 mm lateral and 0.7 mm posterior from Bregma at 2.9 and 3.0 mm deep. To target the lateral-dorsal nucleus of the thalamus, I injected at 0.8 mm lateral, 0.8 mm posterior to Bregma, at 2.8 and 2.9 mm deep. I waited for 3 minutes after each injection site. The volume and concentration of the injected viruses was based on previous experiments performed in the lab mostly by Gulsen Surmeli.

At the end of the surgery, I made sure that the skull was clean and dry, and used surgical glue (Vetbond Tissue Adhesive) to seal the incision. I used a pipette tip to put glue on the inside of the skin at the sides of the incision, lifting the skin from the bone with a forceps to avoid the skin getting stuck to the bone.

Mice were left to recover on a heat mat for about 20 minutes, moved back to the holding room and fed Vetergesic jelly (0.5 mg/kg of body weight buprenorphine in raspberry jelly) 12 hours after surgery.

Table 2.1. Overview of viruses. Promoter, serotype, and inserted gene.

	Promoter	**Serotype**	**Gene / insert name**	**Catalogue number and article**
AAV-fl-GFP	CMV	2	eGFP	Addgene: 49055, Edward Boyden, unpublished
AAV2-fl-ChR2(H134R)-mCherry	AmpR	2	Channelrhodopsin 2-mCherry	Addgene: 18916, (Atasoy et al. 2008)
AAV/hSyn-DIO-hM4D-mCherry	human Synapsin 1	2	hM4D(Gi)-mCherry	Vector Core UNC, No stock number, Addgene: 44362, (H. Zhu and Roth 2014)
AAV-pCAG-fl-tdTomato	pCAG	2	tdTomato	UNC vector core, Addgene: 51503, (Oh et al. 2014)
pAAV-Ef1a-DIO hChR2(E123T/T159C)-mCherry	Ef1a	2	mCherry	UNC vector core, Addgene: 35510, (Mattis et al. 2012)
AAV9-tre-ChR2-mCherry	Tre	9	mCherry	UMass Vector Core, (Ramirez et al. 2013)
AAV-pCAG-fl-tdTomato	pCAG	2	tdTomato	UNC vector core

2.2.4 Perfusion

I intracardially perfused the animals 2 to 10 weeks after the viral injection. Mice were anesthetized using isoflurane and injected with 0.1 ml of pentobarbital intraperitoneally. Once the animal was no longer responsive to pinch tests and had no eye-reflex, I intracardially perfused PBS (phosphate buffered saline, Thermo Fisher Scientific, 7001104410, 10 times diluted with distilled water) for 2 minutes, then with 4% PFA (paraformaldehyde, Sigma Aldrich, 30525-89-4) in 1 M PB (phosphate buffer, Sigma Aldrich, P7994) for 4 minutes at a 10 mL / minute flow rate.

I left the brains in 4 % PFA in 1 M PB for 16 hours, then transferred them to 30 % sucrose (Sigma Aldrich, S0389) in PBS until they sank.

2.2.5 Histology

Brains were sectioned along the sagittal plane using a freezing microtome at 50-60 µm thickness and kept in PBS-T (0.3 % triton in PBS, Sigma Andrich) before immunohistochemical staining.

For staining against Ctip2, heat retrieval was required before blocking. Brain slices were first incubated in an 80°C water bath in 10 mM citrate buffer (sodium citrate buffer, pH = 6.0, adjusted with citric acid). In initial experiments the incubation time was 3 hours, which was gradually reduced to 30 minutes in later experiments. Sections were left at room temperature to cool down for 30 minutes after the water bath. The rest of the staining protocol was similar for all antibodies used and only concentrations differed.

For all staining protocols, sections were blocked in 5 % NGS (normal goat serum) in 0.3 % PBS-T to prevent unspecific binding of antibodies for two hours. Primary antibodies were incubated overnight at 4°C. A series of antibody concentrations were

tested in initial experiments. Optimised concentrations were 1:1000 for rat monoclonal anti-Ctip2 (rat monoclonal [25B6] to Ctip2, Abcam, ab18465), 1:2000 for rabbit anti-calbindin (SWANT, CB38), 1:10000 for chicken anti GFP (Abcam, ab13970), 1:3000 for parvalbumin (SWANT PV235), and 1:10000 for Etv1 (from Thomas Jessell). Slices were washed in PBS the next day three times for 15-20 minutes. Secondary antibodies were incubated either for 6 hours at room temperature, or overnight at 4°C, diluted 1:800 in PBST. Neurotrace (Invitrogen N21483, and N21482) was used in some experiments either 1:500 or 1:1000 in PBST together with the secondary antibodies. Sections were washed in PBS three times for 15-20 minutes, and then mounted on slides (Fischer Scientific, MNJ-150-030U) in Mowiol (home-made, 4.8 g Mowiol, 12 g of glycerol and 1.25 g of 1,4-diazabicyclo[2.2.2]octane (DABCO) in 12ml ddH_2O and 24 ml of 0.2 M TrisHCl (pH 8.5)). Slices were cover-slipped (cover glass VWR, 631-0880) and left to dry at 4°C overnight.

2.2.6 Imaging

Sections were imaged using a Nikon A1 confocal microscope. 4 x, 10 x, and 20 x air objectives were used in all experiments (pinhole = 1 airy unit).

2.2.7 Analysis

To quantify the proportion of p038 positive cells relative to the Ctip2 population, manual cell counting was done. For this analysis, cells were counted on a single medial-lateral level (3.4 mm relative to the midline) in a selected region near the dorsal border of the MEC using ImageJ (Schindelin et al. 2012). Cell counting for the Ctip2 analysis was done by Cristina Martinez-Gonzalez.

2.3 Results

2.3.1 Evaluation of mouse lines for genetic access to the deep MEC

To identify mouse lines that might allow selective manipulation of L5b cells, I performed experiments to test the specificity of the trib2CreER, rasgrp and p038 lines. I injected AAVs that express fluorescent reporters conditionally on the presence of tTA or Cre and evaluated whether infected cells were located in L5b. In mouse lines where viral injections revealed L5b specific expression, I proceeded with characterizing the molecular identity of the infected cells.

To what extent is Cre expression in the trib2CreER line specific to L5b of the MEC?

To test whether Cre activity is specific to L5b of the MEC in the trib2CreER line, I injected mice with Cre-dependent viruses in stereotaxic surgeries, and induced Cre activity by injecting tamoxifen 1.5 weeks after the surgery. I removed brains from the mice 10 days after the last tamoxifen injection and assessed specificity of viral expression by staining for molecular markers of the deep MEC.

In the first set of tests, I injected 5 trib2CreER mice (3 females and 2 males) with AAV2-fl-GFP (Table 2.1, 200-350 nL/hemisphere) that was made in the lab. The injected volume was based on previous experiments performed in the lab. The Cre positive cells infected by the virus expressed GFP. By comparing GFP expression with labelling by layer specific molecular markers, I was able to determine whether the expression was selective to L5b. To find out the identity of the labelled cells, I stained with antibodies against Ctip2 to label L5b cells, and with antibodies against Etv1 to label L5a cells (Figure 2.3). As reported previously (Sürmeli et al. 2015), Ctip2 antibodies labelled a band of cells in the deep MEC. Expression of GFP overlapped with these cells, but was also observed in Ctip2 negative cells in more superficial

layers. I also stained some slices against Etv1 and parvalbumin to test whether infected cells have parvalbumin positive interneurons among them (Figure 2.4). I did not observe cells that were positive for both Etv1 and parvalbumin. However, the Etv1 staining did not label L5a as clearly as expected. A small number of GFP positive cells expressed parvalbumin, but I did not quantify this due to the general lack of specificity of the viral infection for L5b (Figure 2.4). Together, these data indicate that Cre-dependent expression of GFP in trib2CreER mice is not specific to L5b as GFP expressing cells were consistently observed in the superficial MEC. These results indicate that either Cre expression in the trib2CreER line is not specific to L5b, or that the AAV2-fl-GFP virus was not Cre specific. To resolve this, I decided to test different reporter viruses.

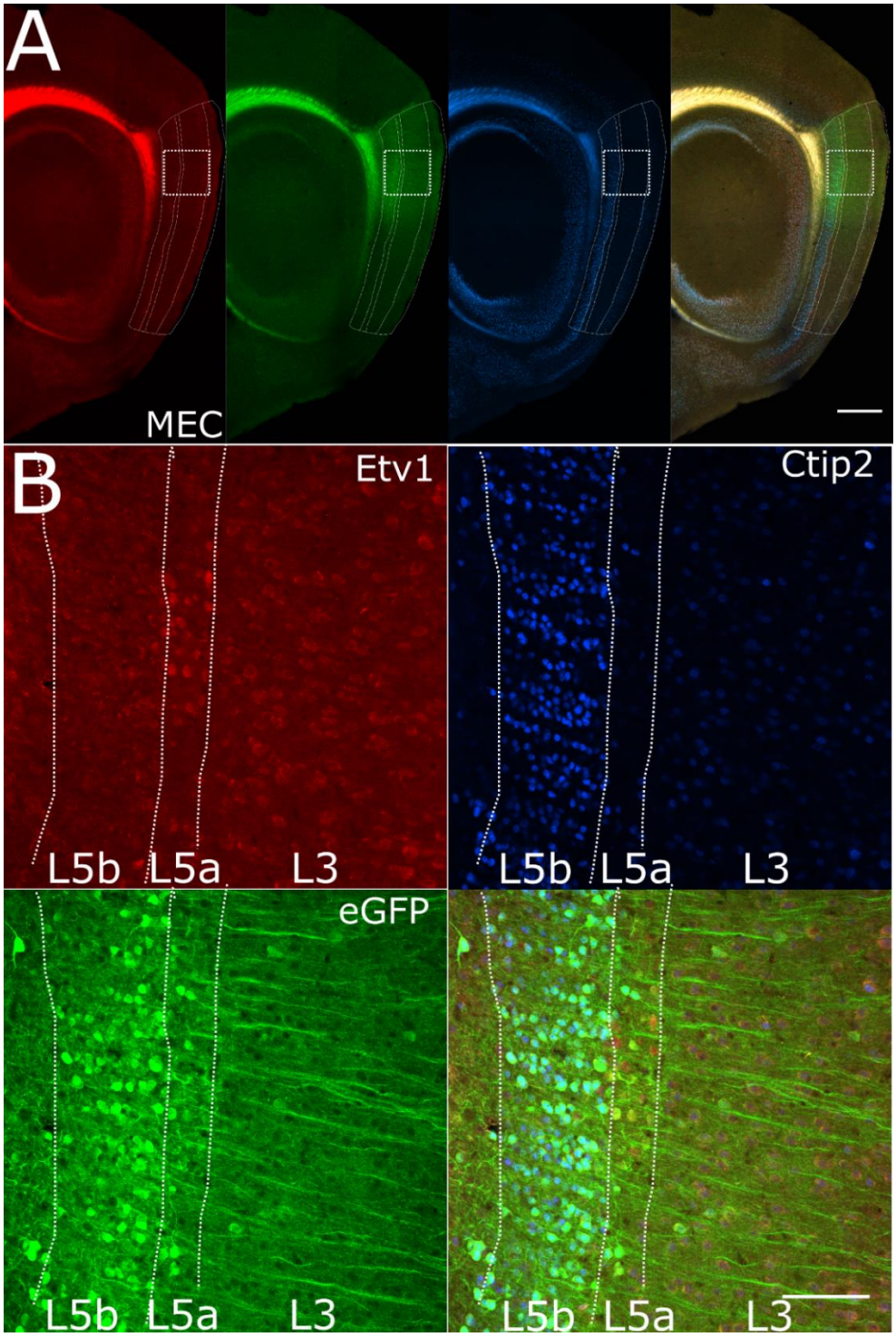

Figure 2.3. AAV2-fl-GFP infection is not specific to L5b but colocalized with Ctip2 in some cells. Ctip2 positive cells in L5b (blue) overlap with GFP labelled cells, but GFP labelled cells are also present in L5a and the superficial MEC. Confocal images of AAV2-fl-GFP injections to L5b of trib2CreER mouse stained against Ctip2 and Etv1. Ctip2 (blue), eGFP (green), Etv1 (red). A. Low magnification confocal images obtained using a 4 x objective (scale bar = 500 µm). B. High magnification confocal images obtained using a 20 x objective (scale bar = 100 µm).

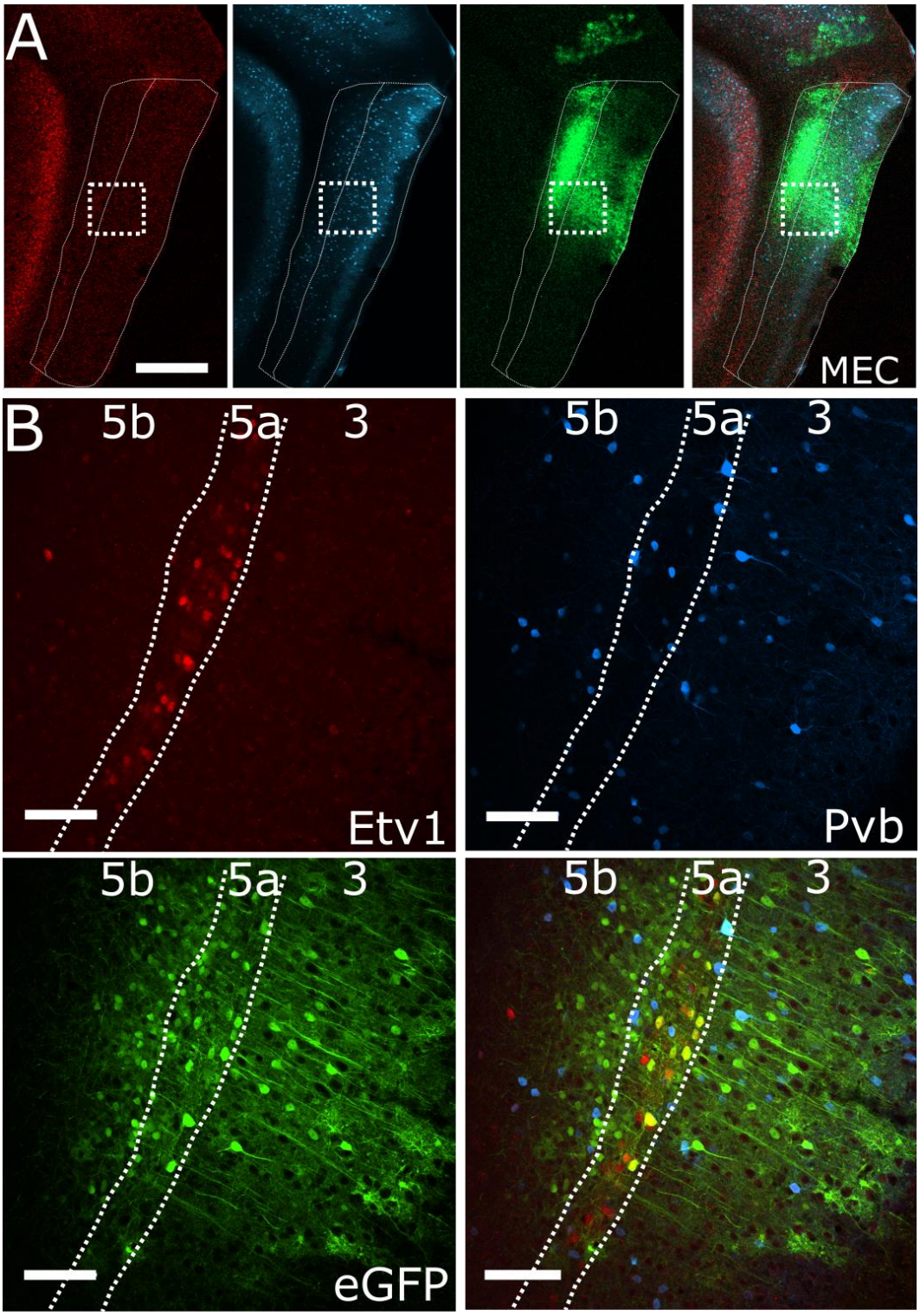

Figure 2.4. AAV2-fl-GFP infection is not specific to L5b but colocalized with parvalbumin in some cells. GFP labelled (green) cells were present in L5b, L5a and L3 of the MEC. Confocal images of AAV2-fl-GFP injections to L5b of trib2CreER mouse stained against parvalbumin and Etv1. Etv1 (red), parvalbumin (blue) and eGFP (green). A. Low magnification confocal images obtained using a 4x objective (scale bar = 500 µm). B. High magnification confocal images obtained using a 20 x objective (scale bar = 100 µm).

To test specificity with a different virus, I injected 10 mice (4 females and 6 males) with AAV2-fl-ChR2(H134R)-mCherry (Table 2.1, 200-230 nL/hemisphere). The injected volume was based on previous experiments performed in the lab. I used this virus, because the animals were used in *in vitro* experiments to investigate MEC connectivity by undergraduate students. I identified layers of the MEC based on the morphology of cells and evaluated the specificity of mCherry expression by comparing mCherry expression with cortex wide labelling of neuronal cell bodies with Neurotrace.

The initial tamoxifen doses were based on experiments performed on Wfs1 mice (Sürmeli et al. 2015). To test whether different tamoxifen concentrations improve specificity, I compared the mCherry expression in 2 mice injected with 0.1 mL of 20 mg/mL tamoxifen with 2 mice injected with 0.1 mL of 2 mg/mL tamoxifen. I found that the 2 mice injected with 20 mg/mL of tamoxifen showed deep MEC specific expression of mCherry (Figure 2.5). Mice injected with the lower concentration had no expression.

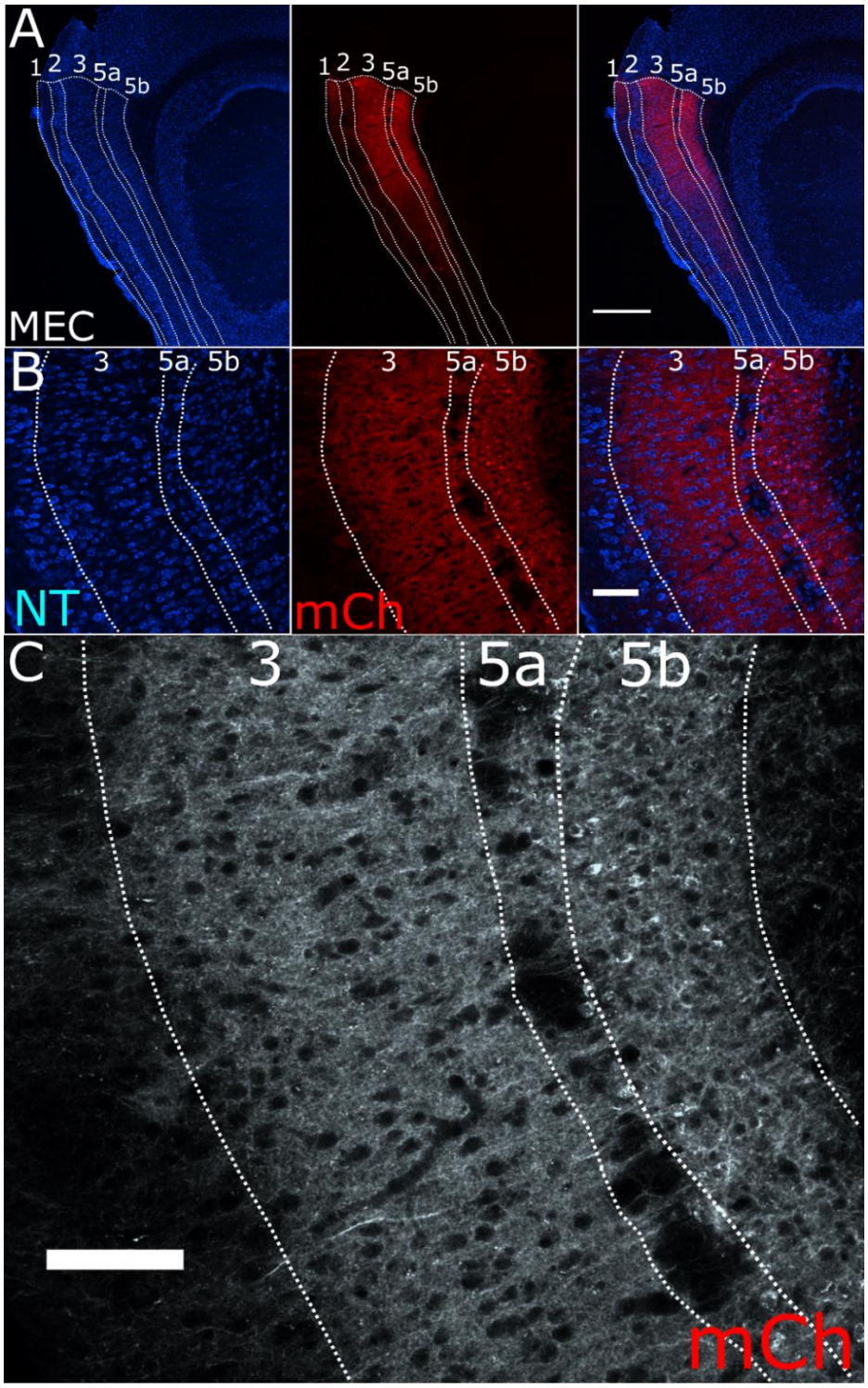

Figure 2.5. AAV2-fl-ChR2-mCherry expression is specific to L5b in trib2CreER mice. mCherry labelled (red) cells bodies were only present in L5b of the MEC. The projections of these labelled cells were visible in the superficial MEC. 10x (A, scale bar = 500 µm) and 20x (B and C, scale bar = 100 µm) confocal images of trib2CreER mice injected with fl-ChR2-mCherry (red) stained with Neurotrace (blue), and 20x image of mCherry expression in grey (C).

Since the results from the AAV2-fl-GFP, and AAV2-fl-ChR2-mCherry injections were inconsistent, to test the virus that I planned to use for a behavioural experiment to transiently silence L5b cells in path integration, I injected AAV/hSyn-DIO-hM4D-mCherry (Table 2.1). I injected 2 mice with the undiluted virus, 1 with a 5 x dilution, and 3 with 50 x dilution (50 nL/injection site, z = -2.0 mm, -1.9 mm, -1.8 mm from surface, 3.5 mm lateral from the midline, between fissure and transverse sinus). I decided to inject such a small volume to reduce the spread of the virus and avoid infecting superficial MEC neurons.

I found that the two mice injected with the undiluted virus had strong mCherry expression in the deep MEC and perirhinal cortex (Figure 2.6). The four mice injected with the lower concentrations had very faint or no expression. The expression appeared to be specific to L5b based on the organisation of cell bodies labelled with neurotrace. I was not able to confirm this with labelling using antibodies against Ctip2, because the heat retrieval step of the staining against Ctip2 caused the endogenous mCherry signal to disappear.

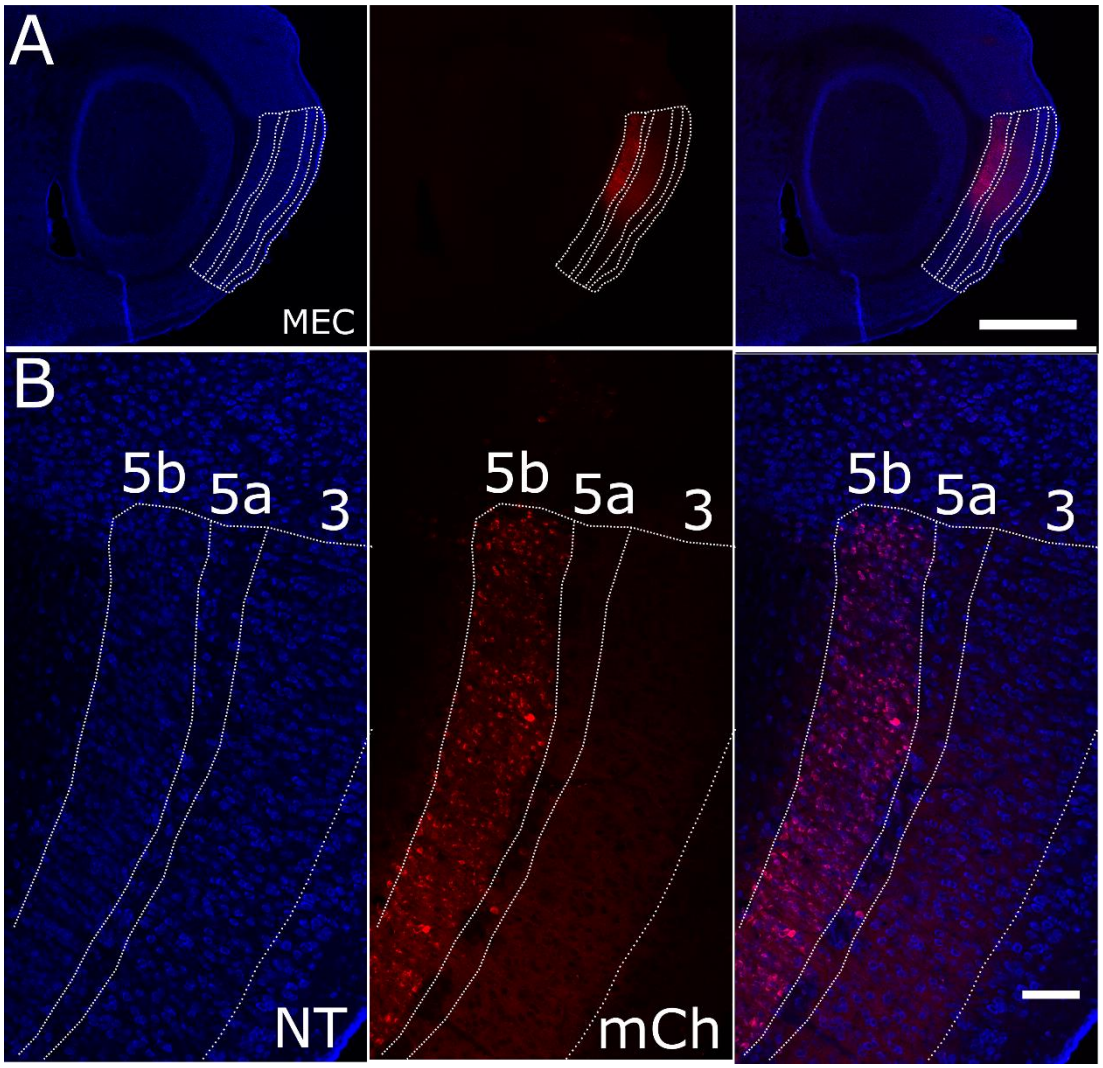

Figure 2.6. AAV/hSyn-DIO-hM4D-mCherry expression is specific to L5b in trib2CreER mice. mCherry labelled cell bodies (red) were only present in L5b of the MEC. Confocal images of sagittal sections stained with Neurotrace (blue). Endogenous mCherry signal from virus is shown in red at (A) 10x (Scale bar = 1000 µm.) (B) at 20x magnifications (Scale bar = 100 µm.).

To validate AAV/hSyn-DIO-hM4Di-mCherry for silencing the deep MEC in behaving mice, which I anticipated would require a wider dorsal-ventral spread of transfection, I injected 2 more animals with the undiluted virus, and one more with 1:50 dilution. I increased the number of injection sites and the volume of the virus relative to the previous test and injected at 1.5 mm, 2.0 mm, 2.5 mm, and 3.0 mm from the surface (200 nL/site). In this experiment, mice injected with the undiluted virus had infected cells in the superficial MEC as well as in L5b (Figure 2.7), while the 1:50 diluted injection had no expression.

Together these experiments gave inconsistent labelling with the trib2CreEr mice; labelling with AAV2-fl-ChR2(H134R)-mCherry virus appeared specific to L5b, labelling with AAV2-fl-GFP virus appeared to include other layers, and labelling with rAAV2/hSyn-DIO-hM4D-mCherry was either specific or not-specific depending on the experimental conditions (Table 2.1, Table 2.2). I therefore decided to explore the rasgrp and p038 lines as alternative for targeting neurons in deep layers of MEC.

Table 2.2. Summary of viral injection experiments in trib2CreER mice.

Virus / experiment	number of animals	age at surgery (weeks)	gender	tamoxifen concentration (mg / kg)	labelling
AAV2-fl-GFP	5	10.9, SD = 0.3	3f 2m	75	deep and superficial MEC
AAV2-fl-ChR2(H134R)-mCherry	2	9.1, SD = 0.1	2f	75	**deep MEC and perirhinal cortex**
AAV2-fl-ChR2(H134R)-mCherry	2	9.2, SD = 0.07	1m 1f	7.5	no labelled cells
rAAV2/hSyn-DIO-hM4D-mCherry	2	8.3, SD = 0	2f	75	**deep MEC**
rAAV2/hSyn-DIO-hM4D-mCherry	2	6.7, SD = 0	2m	75	superficial and deep MEC
rAAV2/hSyn-DIO-hM4D-mCherry (diluted 1:5)	1	8.7	f	75	no labelled cells
rAAV2/hSyn-DIO-hM4D-mCherry (diluted 1:50)	3	7.9, SD = 0.8	2m 1f	75	no labelled cells
rAAV2/hSyn-DIO-hM4D-mCherry	4	8.0, SD = 0	3m 1f	75	superficial and deep MEC

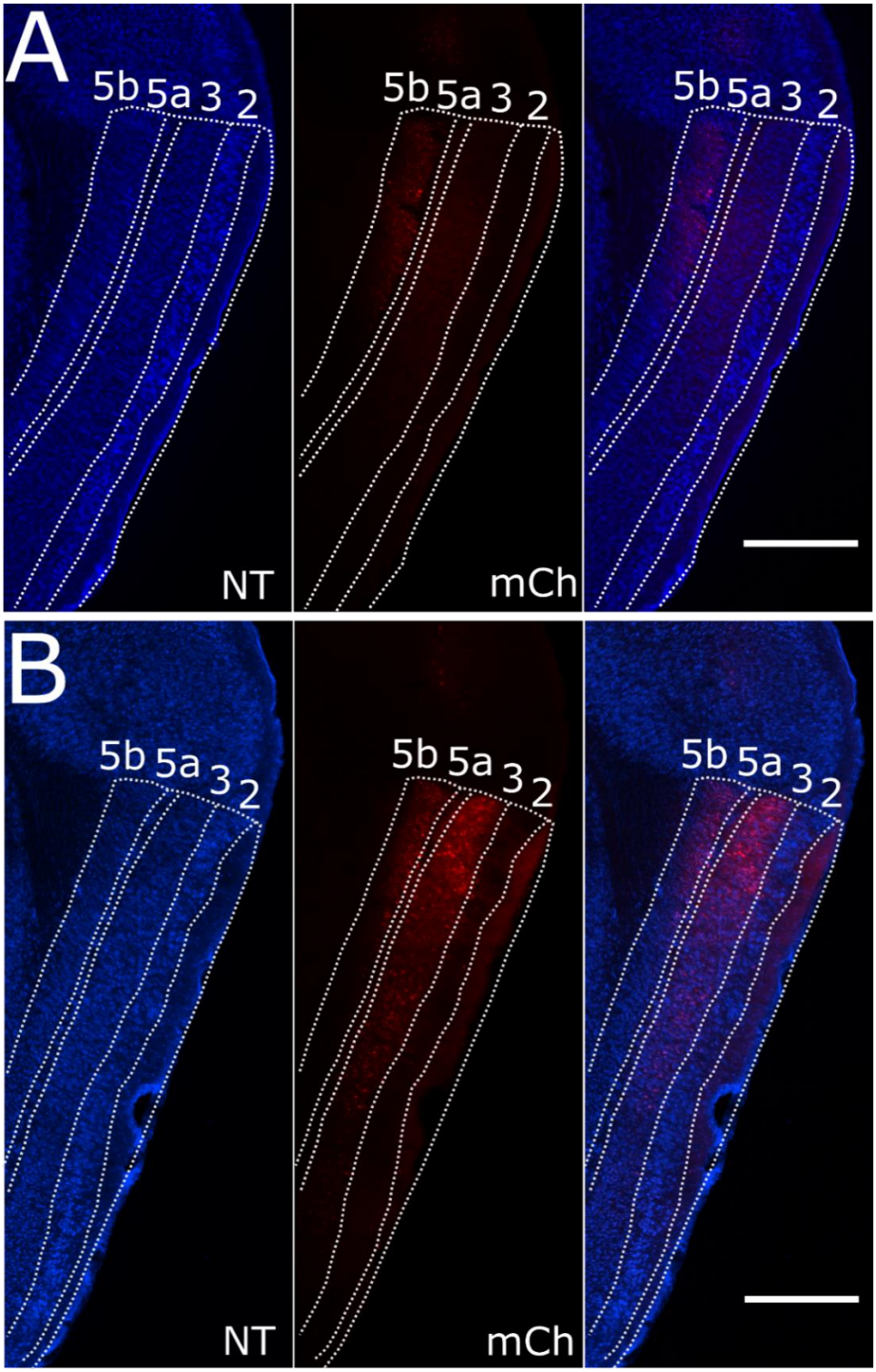

Figure 2.7. AAV/hSyn-DIO-hM4D-mCherry infection is not specific to L5b of the MEC in trib2CreER mice. mCherry labelled (red) cell bodies were present in the superficial and deep layers of the MEC. AAV/hSyn-DIO-hM4Di-mCherry (red) in trib2CreER sagittal sections stained with Neurotrace (blue), right (A) and left (B) hemispheres of the same animal. (Scale bars = 500 µm.)

Is Cre expression specific to L5b in the rasgrp line?

To test whether Cre expression is specific to L5b in the rasgrp line, I injected two 7 weeks old male mice with AAV-pCAG-fl-tdTomato in the deep MEC. Following these injections I observed tdTomato expression in layer 2 as well as in layer 5 and possibly layer 6 of the MEC (Figure 2.8). Because of the Cre expression I observed in the superficial MEC, I decided not to further characterize the line.

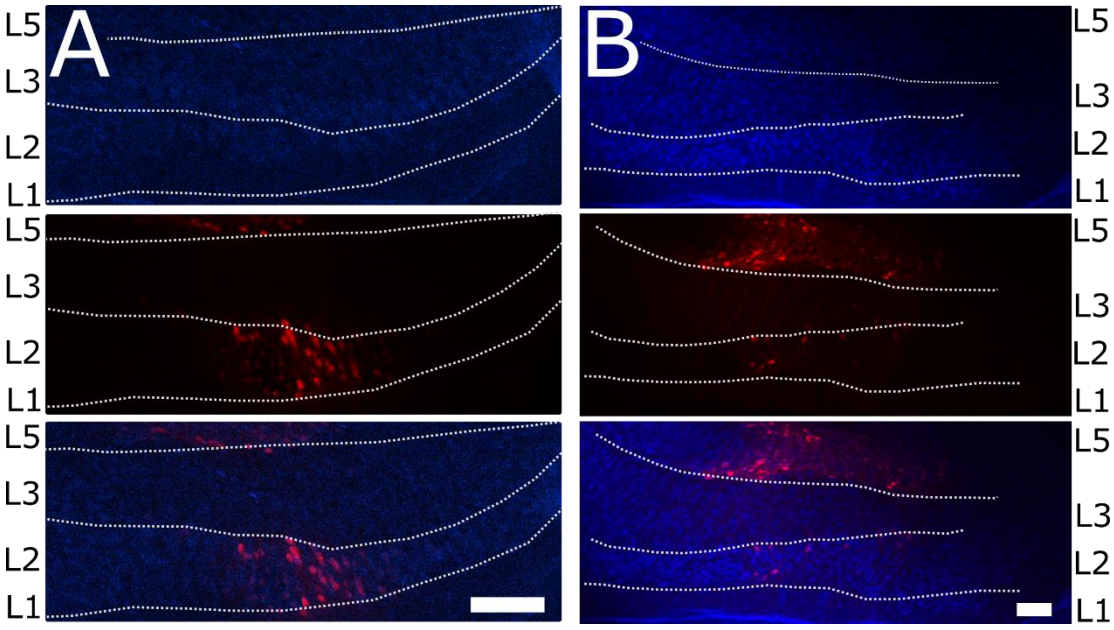

Figure 2.8. AAV-pCAG-lf-tdTomato expression is not specific to L5b in rasgrp mice. mCherry labelled cell bodies were present in the deep and superficial layers of the MEC. Two (A and B) rasgrp mice injected in the deep MEC with AAV-pCAG-fl-tdTomato (red) and stained with Neurotrace (blue). (Scale bar = 100 µm.) Histology and imaging was performed by Cristina Martinez-Gonzalez.

Is Cre or tTA expression specific to L5b in the p038 line?

In p038 mice a subset of neurons in the MEC express mCitrine (Figure 2.9). Neurons labelled with mCitrine are located in L5b of the MEC, the retrosplenial cortex and the parasubiculum. In p038 mice the inserted cassette expresses both Cre and tTA. The aim of my first set of experiments was to test whether the mCitrine expression pattern is captured by either Cre- or tTA-dependent reporters.

To test Cre specificity, I injected two p038 positive mice with AAV2-fl-ChR2-mCherry in the deep MEC. I found that cells in layer 2 of the MEC were labelled with mCherry (Figure 2.9A). I evaluated Cre-dependent expression in a further 3 mice injected with pAAV-Ef1a-DIO-hChR2(E123T/T159C)-mCherry. I again found infected cells both in the deep and superficial layers of the MEC. I therefore concluded that Cre expression does not replicate the mCitrine expression and is not specific to L5b in the p038 line (Figure 2.9A).

To test whether tTA expression is specific to the mCitrine positive L5b cells, I injected AAV9-tre-ChR2-mCherry in two mice. I found that mCherry expression was restricted to mCitrine positive L5b cells in the MEC, although the level of expression was relatively low (Figure 2.9B). Projections of mCherry labelled cells were visible in the superficial MEC with some projections reaching layer 1. Additionally, I observed a small number of mCherry labelled mCitrine negative cells in the hippocampus. I used this virus to access the p038 population in Chapter IV.

Based on these results, I decided to characterize the p038 line in more detail. My goal was to evaluate its suitability for experiments targeting L5b.

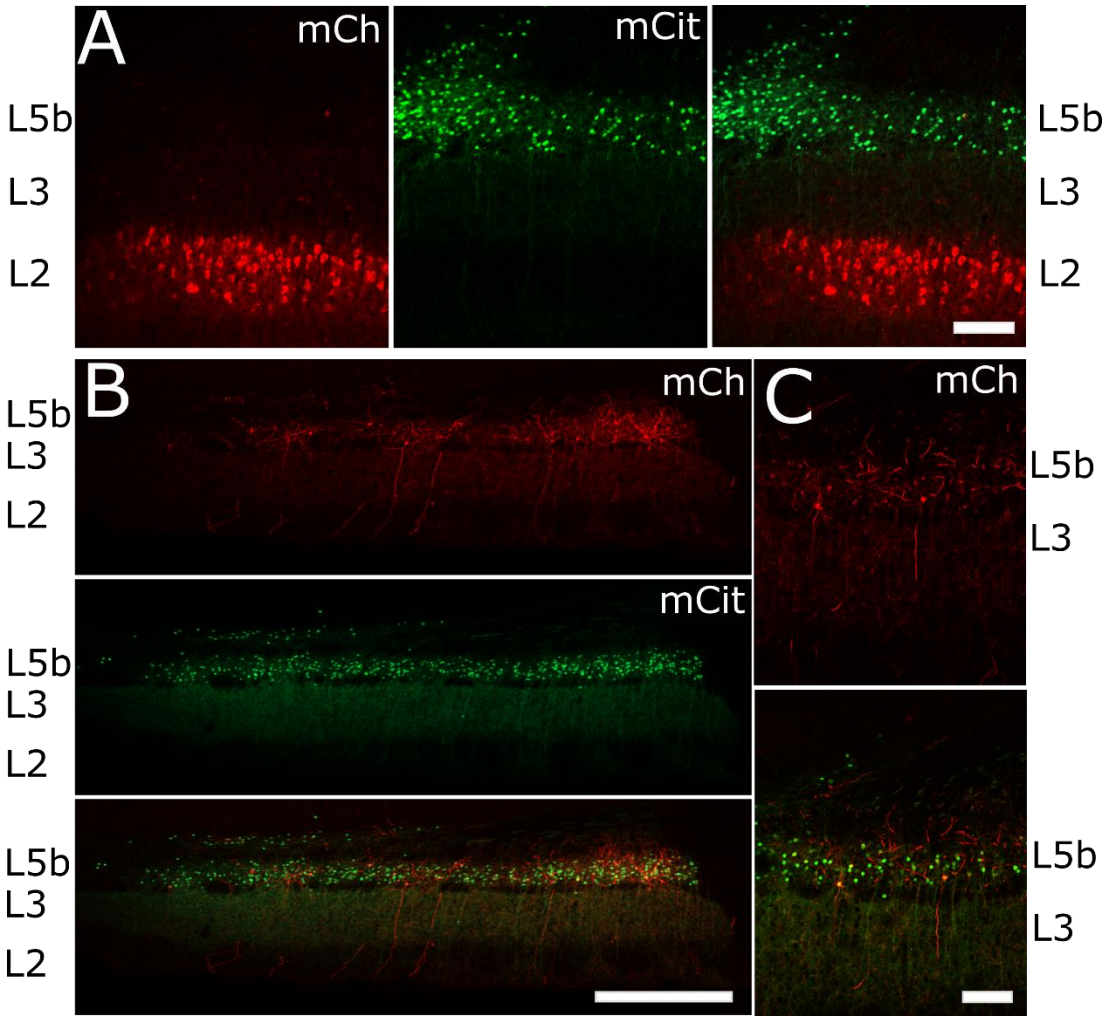

Figure 2.9. Cre and tTA expression in p038 mice. Cre-dependent viral injections labelled superficial MEC cells, suggesting that Cre expression is not specific to the deep MEC in p038 mice. tTA dependent viral injections labelled mCitrine labelled deep MEC cells and no superficial MEC cells, which suggests that tTA expression is specific to the deep MEC in p038 mice. Confocal image (10x) of a sagittal section of MEC of a p038 mouse injected with fl-ChR2-mCherry (A) and p038 mouse injected with tre-ChR2-mCherry (B and C). Endogenous mCitrine fluorescence in p038 positive cells in green, infected cells are red. (Scale bar = 100 µm on A and C and 500 µm on B.)

2.3.2 Characterizing the p038 mouse line

To design experiments using the p038 line, I first needed to characterize the specificity and extent of transgenic expression to understand the limitations of using the line. To find out what proportion of Ctip2 positive L5b cells the p038 line can give access to, I decided to count the number of tTA positive cells in the deep MEC relative to Ctip2 positive cells. Additionally, I investigated whether mCitrine positive cells and their projections are present in any parts of the brain apart from the deep MEC. The endogenous mCitrine fluorescence present in tTA positive p038 cells allowed me to carefully characterize expression patterns without performing viral injections.

Pattern of mCitrine expression in p038 mice

Published images of the endogenous mCitrine expression in p038 mice (Shima et al. 2016) suggested that expression is highly specific to the deep MEC. To test whether tTA expression is specific to the deep MEC, and to explore projections of tTA positive cells, together with Martyna Rakowska, we imaged the whole brain of two p038 mice to map the endogenous mCitrine expression. We observed p038 positive cell bodies throughout the medial-lateral extent of the deep MEC. Other areas with mCitrine positive cell bodies included the parasubiculum, subiculum, and retrosplenial cortex (Figure 2.10). We did not observe mCitrine signal in the lateral entorhinal cortex (LEC). Non-somatic mCitrine signal was present in the thalamus, the lateral part of the hippocampus and superficial MEC (Figure 2.10 and Figure 2.11). In the latter two structures this likely reflects axonal labelling, whereas in the MEC it could result from dendritic or axonal signals.

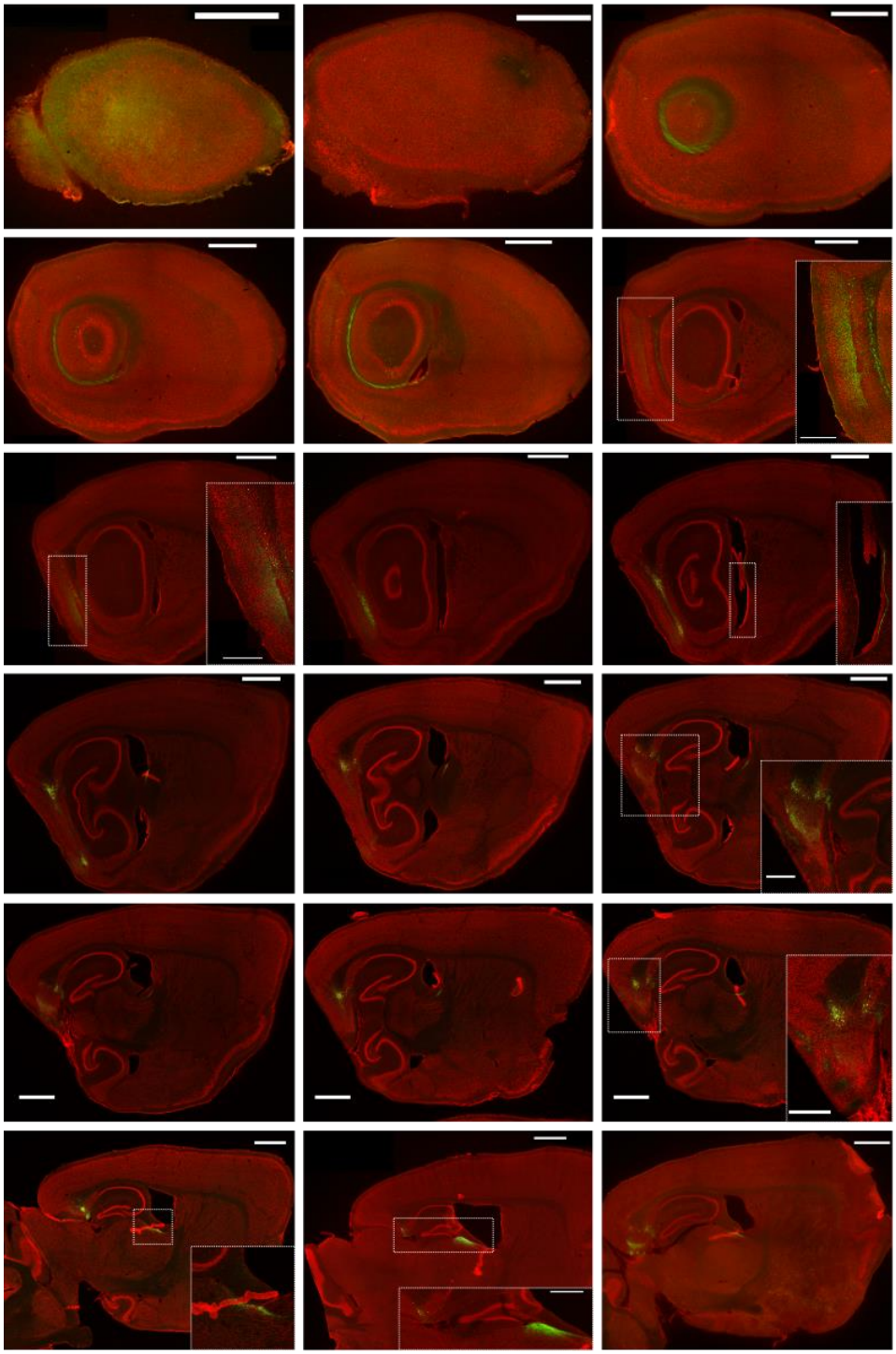

Figure 2.10. Endogenous mCitrine expression in p038 mouse. mCitrine labelled cell bodies were mainly located in the deep MEC, parasubiculum and retrosplenial cortex of p038 mice. Sagittal sections stained with Neurotrace 640/660 (red) imaged on Nikon A1 confocal microscope. tTA positive cells express mCitrine (green) endogenously. The 18 images showing the whole sagittal section were taken using a 4x objective (scale bar = 1000 µm), and the images in boxes with 20x (scale bar = 500 µm). Histology and imaging was performed with Martyna Rakowska.

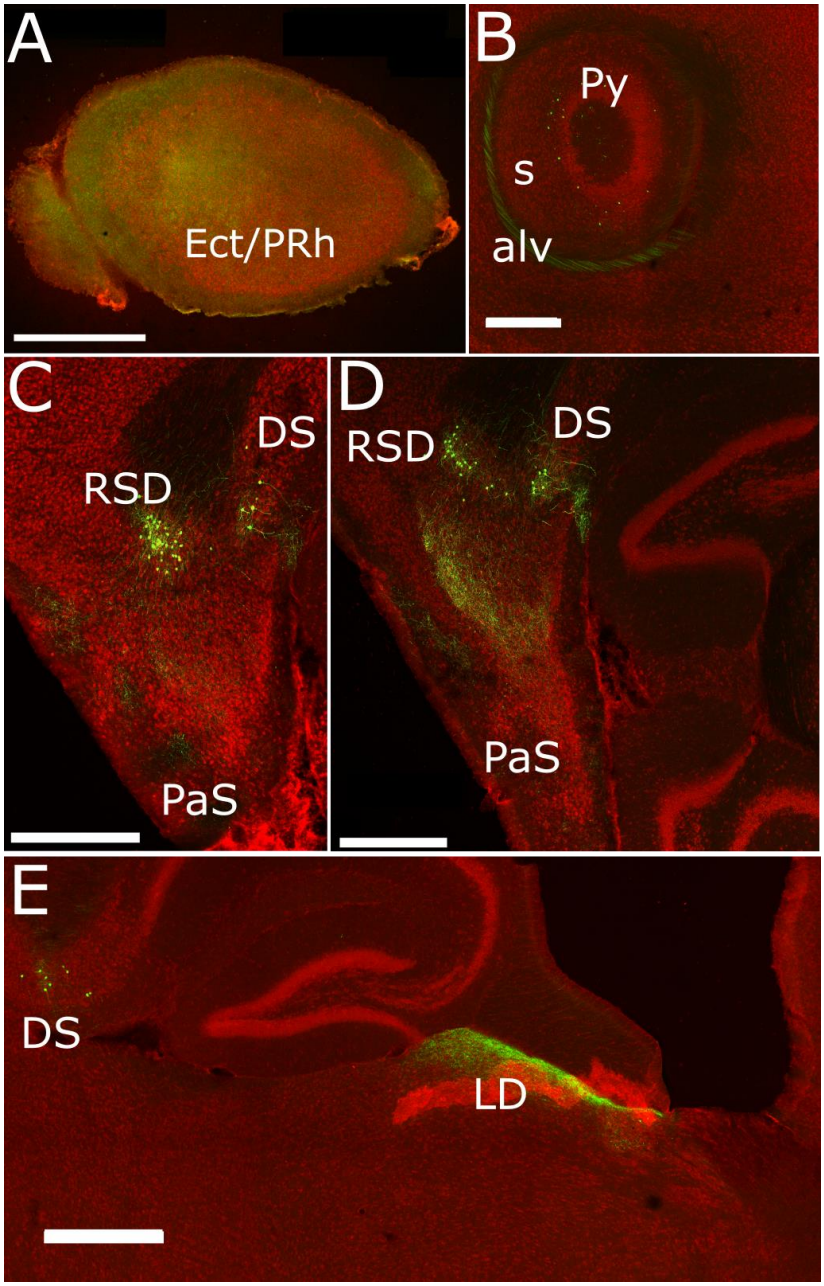

Figure 2.11. mCitrine expression outside the MEC in p038 mice. Projections of mCitrine labelled cell bodies were present in superficial layers of the MEC, the thalamus and the lateral part of the hippocampus. Sagittal sections labelled with Neurotrace 640/660 (red) imaged on Nikon A1 confocal microscope. tTA positive cells express mCitrine (green) endogenously. Projections on sections lateral relative to the hippocampus in ectorhinal (Ect) and perirhinal (PRh) cortex (A). Cell bodies in the pyramidal layer (Py) of the hippocampus and projections passing through the alveus of the hippocampus (B). Cell bodies in the retrosplenial dysgranular cortex (RSD) and dorsal subiculum (DS) and spatially organized projections in the parasubiculum (PaS) (C and D). Cell bodies in the dorsal subiculum (DS) and projections in the lateral dorsal (LD) nucleus of the thalamus (E). Histology and imaging was performed with Martyna Rakowska.

Correspondence between mCitrine expression and Ctip2 labelling in p038 mice

Identifying L5a and L5b cells based on morphology can be somewhat ambiguous. Therefore, to test if mCitrine positive cells in the MEC are a subpopulation of Ctip2 positive cells and whether they overlap with other cell populations, we compared mCitrine labelling with labelling from antibodies against Ctip2, to identify L5b neurons, and calbindin, to identify superficial pyramidal neurons and populations of interneurons in deeper layers. To quantify the proportion of Ctip2 cells that are mCitrine positive, we analysed sagittal sections from three mice. I found that 13.1 % (SD = 3.8) of Ctip2 positive cells were mCitrine positive. The mCitrine population did not overlap with the cells stained with calbindin (Figure 2.12). Only 0.3 % of mCitrine labelled cells was Ctip2 negative. These data indicate that the p038 line gives genetic access, through expression of tTA, to a subpopulation of Ctip2 positive cells in layer 5b of the MEC.

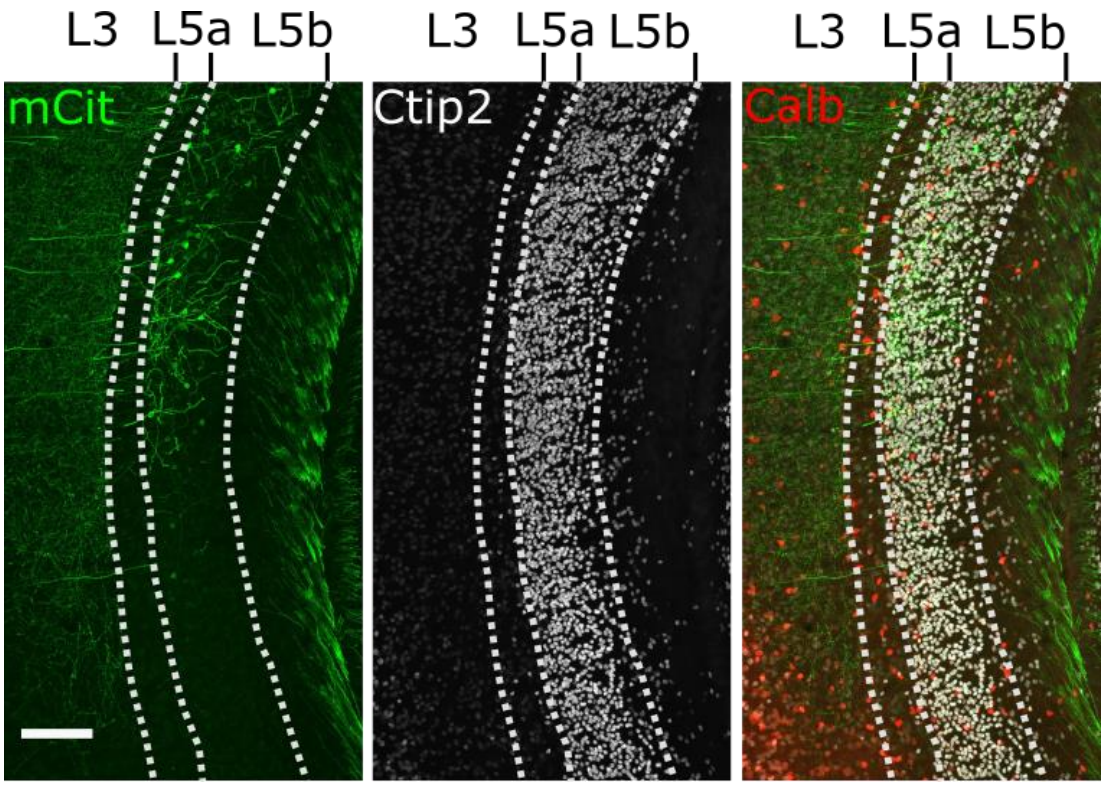

Figure 2.12. p038 cells are Ctip2 positive. The p038 line labels 13% of Ctip2 positive L5b cells. Sagittal section of p038 mouse (x 4) stained with anti-GFP (green), Ctip2 (white), and calbindin (red). Histology, imaging and cell counting was performed by Cristina Martinez-Gonzalez.

Projections of p038 cells appear to avoid calbindin islands in the superficial MEC

The non-somatic mCitrine labelling in the MEC of p038 mice was non-uniform (Figure 2.13). In layer 5a I found patches of dense labelling separated by larger patches in which labelling was absent. In layer 3 labelling was dense and relatively uniform, while in layer 2 labelling was more sparse and patchy. To test whether the architecture of mCitrine labelling in layer 2 of the MEC is related to the position of calbindin positive islands (Fujimaru and Kosaka 1996), I stained sagittal sections from p038 mice with antibodies against calbindin. On slices where calbindin islands were clearly present, mCitrine labelling was nearly absent in areas with high calbindin expression (Figure 2.13).

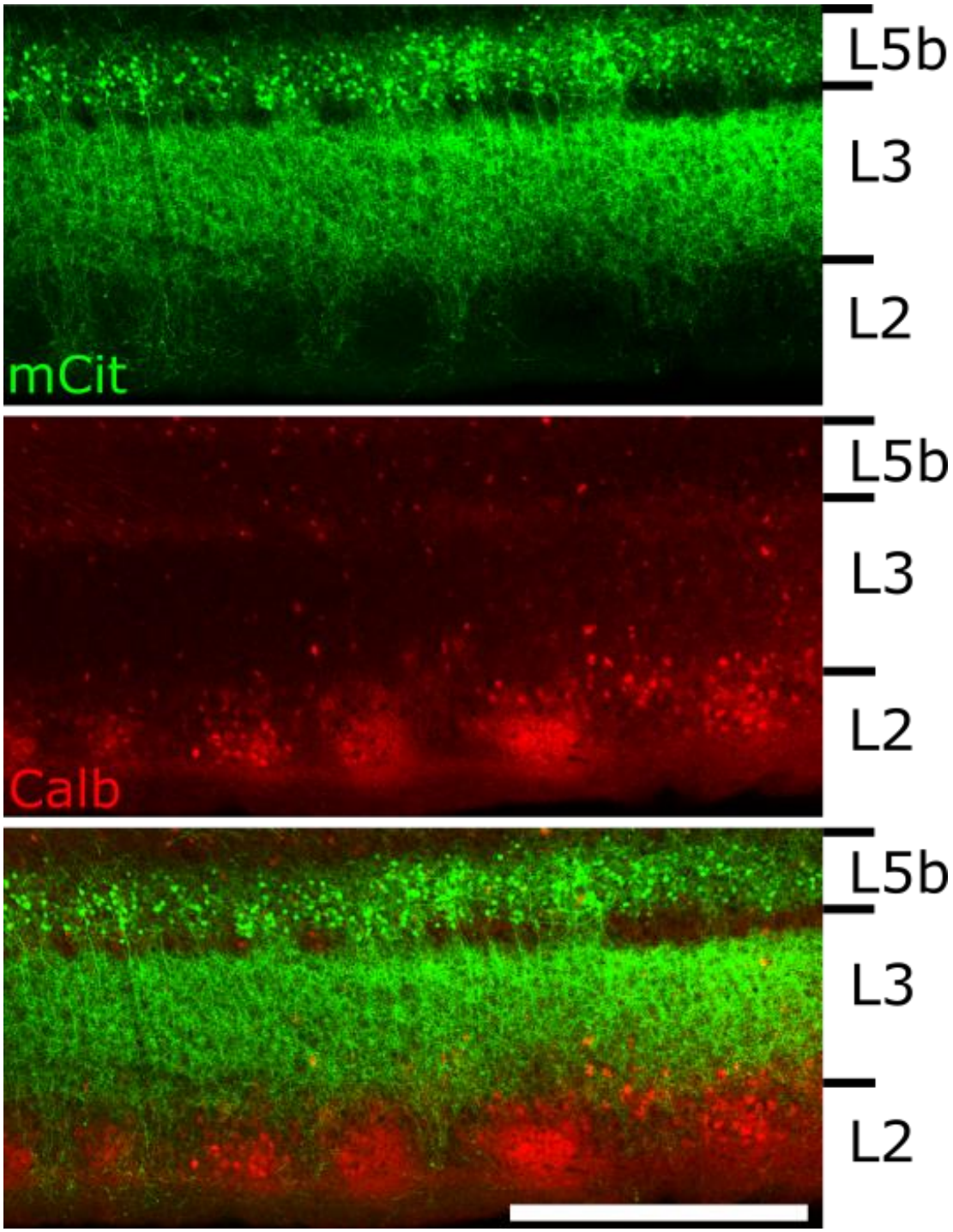

Figure 2.13. Projections of p038 cells (green) avoid calbindin islands (red) in the superficial MEC. Sagittal section of p038 mouse stained with calbindin (red). Endogenous mCitrine expression is green. (Scale bar = 500 µm.) Histology and imaging was performed together with Martyna Rakowska.

2.3.3 Does the deep MEC project to the thalamus?

The abundance of endogenous mCitrine terminals in the thalamus suggests that mCitrine positive cells in L5b of the MEC might project to the thalamus (Figure 2.10 and Figure 2.11). Alternatively, these projections could arise from the more sparsely labelled mCitrine positive cell bodies labelled in other areas. To investigate whether deep MEC cells project to the thalamus, I performed a set of experiments where I injected fast blue, a retrograde tracer, in p038 mice targeting the anterodorsal (AD) and lateral-dorsal (LD) nuclei of the thalamus. Because cells that project to the injection site would be labelled with fast blue, I could therefore test whether they are located in the deep MEC and if so whether they are also positive for mCitrine.

I targeted injections of fast blue to the thalamus of 23 p038 mice (13 females and 10 males) bilaterally (age at surgery was 11.74 weeks, SD = 3.5 weeks). I observed fast blue throughout LD in two mice, and throughout AD in two mice. In 15 hemispheres, I only hit the edge of LD. Fast blue and mCitrine labelling overlapped in these animals. I did not hit the target areas in the remaining 4 animals. In the two mice in which the fast blue was through LD, in one of the mice where the fast blue was through AD and in further 4 mice where the fast blue was in parts of LD, I found fast blue positive cell bodies in the dorsal border of the deep MEC and parasubiculum (Figure 2.14). In the other mouse where there was fast blue throughout AD, I did not find labelled cells in the MEC (Figure 2.15). There was very little overlap between the p038 and fast blue population. In some animals (n = 6), my fast blue injection also hit the fornix or the dentate gyrus and labelled cells in the superficial MEC (Figure 2.14 and Figure 2.15).

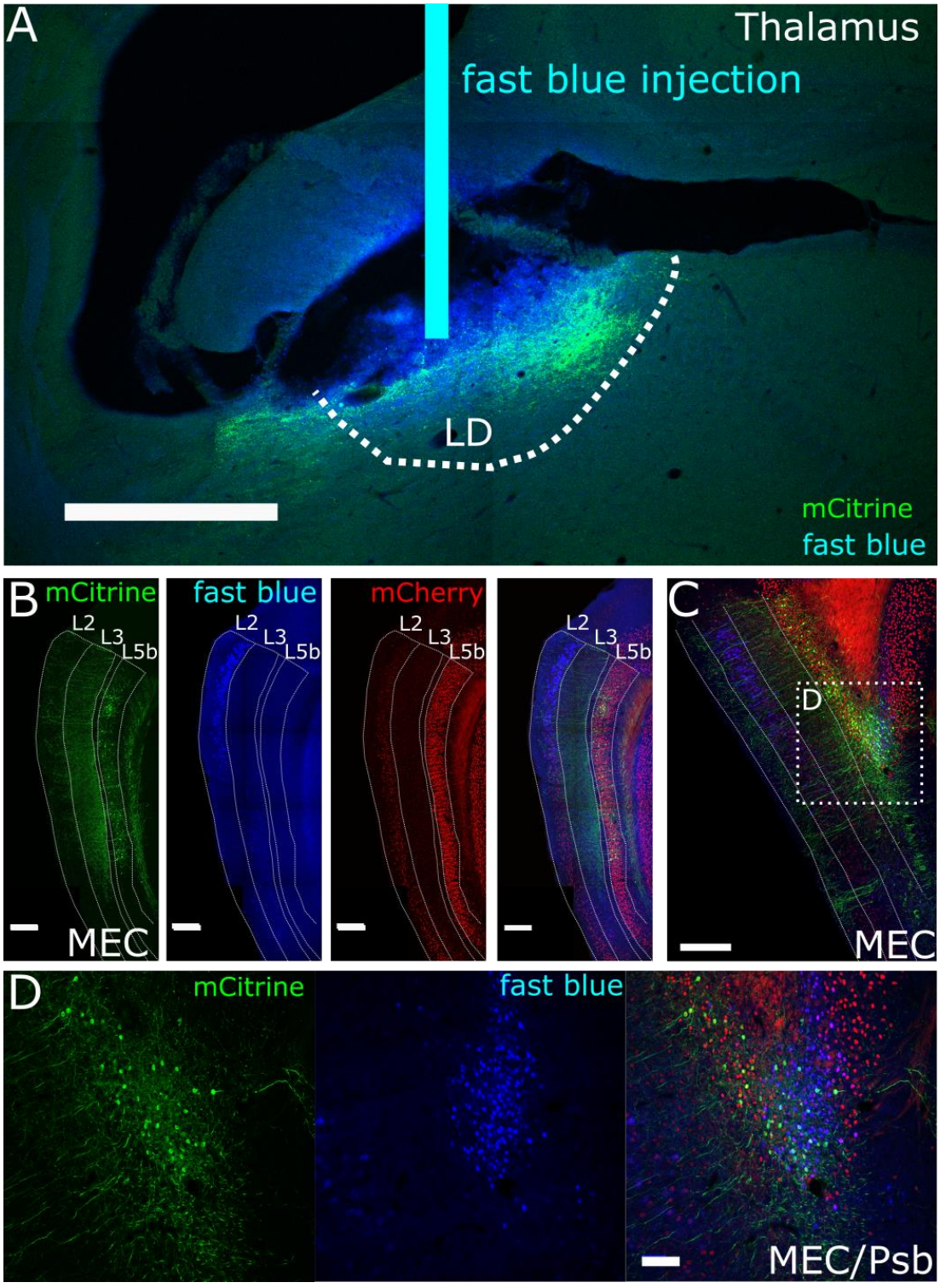

Figure 2.14. Fast blue injection in the LD nucleus of the thalamus labels cell bodies in the dorsal border of the deep MEC. Fast blue was injected in the LD nucleus of the thalamus (A). Sparse expression of fast blue positive cells in the lateral (B) and medial (C and D) part of the MEC or in parasubiculum. (Scale bar = 100 µm). Histology and imaging was performed by Cristina Martinez-Gonzalez.

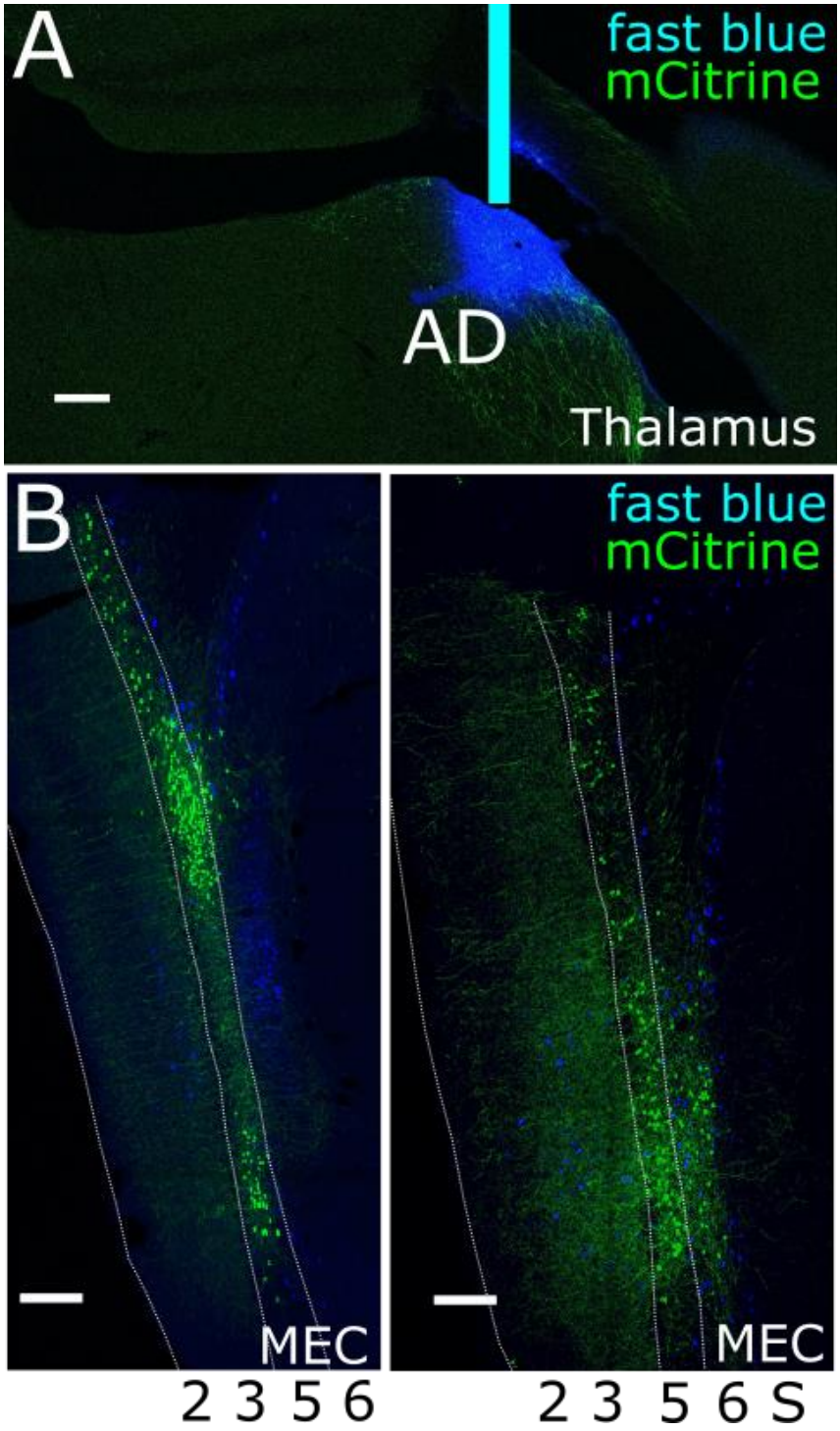

Figure 2.15. Fast blue injection in the AD nucleus of the thalamus labels cell bodies in L5b and L6 of the deep MEC. (A) Fast blue injection site in the AD nucleus, and sparse expression of fast blue labelled cells in the MEC (B). Endogenous mCitrine is green, fast blue is blue (Scale bar = 100 µm, 10x magnification.) Histology and imaging was performed by Cristina Martinez-Gonzalez.

Since Cre expression was present in the deep MEC in rasgrp mice, I also examined whether Cre positive L5b cells are among the cells that project to the thalamus. I injected fast blue and AAV-pCAG-fl-tdTomato in the LD and AD nucleus of nine 12.5 weeks old (SD = 0.98 weeks) rasgrp mice (6 females and 3 males) unilaterally. In animals where I hit the nuclei (n = 2), labelling was sparse in the deep MEC, and numerous cell bodies got labelled in other cortical areas (Figure 2.16).

Together, these experiments fail to find overlap between neurons in layer 5b of the MEC in p038 or rasgrp mice and neurons retrogradely labelled from the thalamus. Thus, axonal labelling in the thalamus of p038 mice likely arises from neuronal populations outside of the MEC.

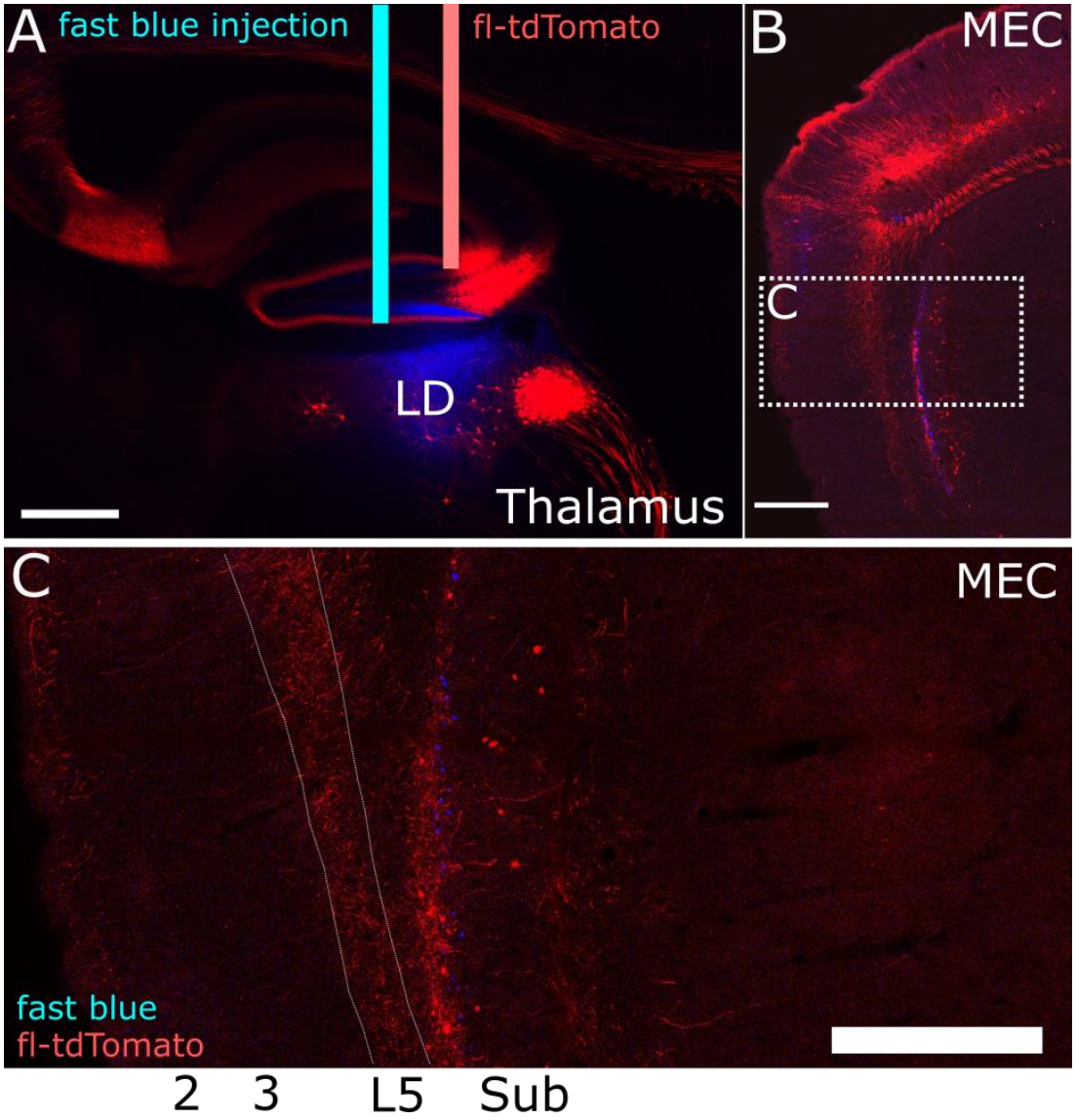

Figure 2.16. Fast blue and AAV-fl-tdTomato injection in thalamus labels cells in cortical areas. (A) Injection sites in thalamus targeting AD (fast blue), and LD (fl-tdTomato) in rasgrp mouse. (B and C) Fast blue (blue) and fl-tdTomato (red) expressing cells in the MEC (L5) and subiculum (Sub). (Scale bar = 400 µm.) Histology and imaging was performed by Cristina Martinez-Gonzalez.

2.4 Discussion

I found that expression of tTA, but not Cre is specific to L5b of the MEC in p038 mice. A subpopulation of approximately 13 % of Ctip2 positive L5b cells of p038 mice is labelled by tTA-dependent expression of mCitrine. Projections of tTA positive L5b cells in p038 mice avoid calbindin islands in the superficial MEC and that L5b tTA positive cells do not project to the thalamus. Viral reporter injections revealed labelled neurons in superficial layers of the MEC in rasgrp and trib2CreER lines, which indicates that they are not suitable for specifically targeting cells in L5b. In this discussion, I will evaluate the advantages and limitations of using p038 mice in behavioural experiments, and propose further tests to map the anatomical organization of L5b of the deep MEC.

2.4.1 Genetic access to L5b of the deep MEC

My results suggest that transgenic cells in p038 mice can be labelled by tTA-dependent reporters. However, viral reporter labelling was sparser than the mCitrine population, even though the virus has spread throughout the deep MEC. The difference in viral and endogenous labelling could indicate that the virus did not infect all mCitrine positive cells that it reached, or that detectable expression of viral reporter genes require multiple copies of the viral reporter, which would be achievable in fewer cells. Surprisingly, mCitrine negative cells that expressed the viral reporter were found in the hippocampus of both test animals. This suggests that the virus has either spread to that area or was retrogradely transported *via* the axons near the injection site. It is unclear how viral transgenes would be expressed in the absence of the mCitrine reporter. A possible way to reduce expression in the hippocampus and increase expression in the deep MEC might be to use a virus with a different concentration or serotype.

Could other mouse lines give genetic access to a higher proportion of Ctip2 positive L5b cells compared to the p038 line? The results of my viral reporter injection experiments in trib2CreER mice were inconsistent and sometimes yielded labelling specific to L5b while in other mice superficial cells were labelled. In some animals I observed specific labelling in one hemisphere but not in the other. A possible explanation for variable specificity across animals and hemispheres could be that the injection was more precise in mice where L5b cells were labelled specifically. In animals with highly specific labelling, a high proportion of Ctip2 positive cells appeared to be labelled. Experiments using the trib2CreER line to access L5b neurons would need to carefully assess the specificity of labelling for each experimental animal and use low volumes of viruses in very precise injections. Viral reporter injections in rasgrp mice revealed labelling in the superficial MEC. Further, labelled cells in the deep MEC appeared to be mostly in L5a and L6. Similarly to the trib2CreER mice, it is possible that more precise targeting and different volumes and concentrations of injected viruses could restrict the labelling to more specific deep MEC populations.

2.4.2 Anatomical organization of the deep MEC

Axonal targets of L5b neurons were recently shown to include L5a, L3 and L2 in a study using trans-synaptic tracing approaches in the rat (Ohara et al. 2018). The dendritic architecture of L5b cells and their relationship to other elements of MEC circuits has only been briefly explored in previous studies (Canto and Witter 2012b; Quilichini, Sirota, and Buzsáki 2010). Both *in vitro* and *in vivo* studies found that L5 neurons project to the superficial MEC (Canto and Witter 2012b; Quilichini, Sirota, and Buzsáki 2010). However, whether these projections are anatomically organized, whether they originate from L5a and / or L5b, and whether they target molecularly distinct populations is not yet known. Projections of mCitrine labelled cells in p038

mice appeared to avoid calbindin islands in the superficial MEC. To quantify this observation, more data could be collected and the correlation between calbindin and p038 expression could be analysed in L2. To investigate whether this projection pattern is specific to tTA positive cells in p038 mice or applies to more L5b neurons, tTA positive and negative cells could be recorded and filled with a dye *in vitro* to compare their projections and intrinsic properties (Martínez, Rahsepar, and White 2017; Sürmeli et al. 2015). Patch clamp recordings would also reveal whether there are any morphological and electrophysiological differences between tTA positive p038 and other Ctip2 positive L5b cells. Differences in projections and morphology would be relevant, since it is possible that p038 cells are a functionally distinct subpopulation of L5b cells, playing different roles in spatial computations carried out by the MEC.

A previous study found some evidence for projections from the deep layers of the MEC to the thalamus (Sürmeli et al. 2015), but these projections were not found when axonal targets of L5b were systematically investigated in the rat (Ohara et al. 2018). Retrograde tracer injections in my experiments targeting the LD nucleus of the thalamus labelled cells near the dorsal border of the deep MEC, mostly in the parasubiculum, but not in more ventral parts. Injections targeting the AD thalamic nucleus labelled cells in the subiculum and possibly in L6 of the MEC, but not in L5b. However, in most injected animals I either did not hit the target nuclei or did not find labelled MEC cells. A potential reason for not finding labelled cell bodies could be that not all MEC sections were processed, so labelled cells may have been discarded. A possible way to ensure that all labelled cells are found in future experiments could be to use clearing methods and image the whole brain (K. Chung et al. 2013; Renier et al. 2014).

2.4.3 Limitations and advantages of using the p038 mouse line in future experiments

What sorts of experimental questions is the p038 line useful in addressing? I will consider its possible uses in experiments to test necessity and sufficiency of L5b cells in behaviours, to identify firing patterns of L5b cells *in vivo*, and to establish connectivity of L5b cells through ex-vivo and anatomical experiments.

A possible use of lines giving genetic access to specific cell populations is in testing necessity of these cells for behaviours. This is achieved through coupling of the cell-specific marker to genetically encoded tools that either transiently or permanently inactivate the targeted neurons. Because the p038 mouse line gives access to only 13 % of Ctip2 positive L5b cells, it appears unlikely to be well suited for this purpose. This is because even if L5b is important in navigation, silencing the p038 population might not be sufficient to test this since other L5b cells might be able to compensate. On the other hand, if p038 cells are not a random subpopulation, but one with a specialized task, it might be useful to test their function separately.

What is the function of the p038 population in spatial cognition? To test the role of the p038 population, they could be silenced or activated in spatial behaviours. Transgenic crosses could allow all p038 positive cells to be manipulated (see Appendix), more than what viral injections can give access to. Mapping p038 positive cells in the whole brain revealed that expression is present in areas outside the deep MEC. These areas included the retrosplenial cortex, parasubiculum and parts of the hippocampus, which are thought to be involved in spatial cognition. Therefore, experiments using transgenic crosses where all p038 cells are manipulated would not yield results specific to the role of the deep MEC in spatial cognition. Experiments using viral injections to access the p038 population would also need to consider cells potentially infected in areas outside the deep MEC and validate specificity.

How does firing of L5b neurons relate to behaviour? A further possible use of the p038 line could be for identification of neurons recorded extracellularly during behaviour. This could be achieved through opto-tagging strategies (see Chapter IV). For example, by injecting a tTA-dependent channelrhodopsin virus, we can make p038 cells light responsive. Combining optogenetic stimulation with extracellular recordings makes it possible to identify responsive cells by opto-tagging them. Sparse expression is advantageous in opto-tagging experiments, because it is less likely that the light will activate multiple cells that are recorded for identification (Roux et al. 2013). Due to its sparse expression, the p038 line may be advantageous for opto-tagging experiments.

Mapping the projections of p038 cells would be important to understand their position in the hippocampal-entorhinal circuit and ultimately understand their role in spatial cognition. Finding the projection targets of p038 cells could be done by injecting a tTA-dependent synaptophysin virus into L5b to label the terminals of p038 cells specifically. Injecting the synaptophysin virus would be more informative than the endogenous mCitrine expression, since it is not clear which of the projections originate from the deep MEC, and which from tTA positive cells in other brain regions. To label cells that send information to the p038 population, a tTA-dependent rabies virus could be injected (Reardon et al. 2016) into the deep MEC.

Spikes by Sarah Tennant and Klára Gerlei.

Chapter III

3 An automated pipeline to analyse extracellular recordings of neuronal activity during behaviour and optogenetic stimulation

3.1 Introduction

When scientific results are not possible to replicate, they carry limited value and may hinder scientific progress when other scientists attempt to build on them (Iqbal et al. 2016; Gilmore et al. 2017; Prinz, Schlange, and Asadullah 2011; Landis et al. 2012). An important step towards achieving replicability is to replace manual analysis methods with computer programs and therefore reduce human error and bias. To be useful for scientific research, code needs to be re-runnable, reproducible and reusable (Benureau and Rougier 2018; Perkel 2018). However, this is rarely the case for workflows analysing spatial firing properties of neurons, and user input is typically required for sorting neural activity as well as later analysis stages.

Since programming languages and packages are continuously developed, to write code that is possible to re-run, the environment in which the code runs needs to be documented in sufficient detail. For example, a simple change such as the version of the operating system after an update may affect whether the code is possible to re-run. Another minimum requirement for scientific code is to be deterministic, or repeatable. This means that when the code is re-run it should give the same result. This is essential for an independent scientist to be able to test that the code can produce the results shown in a paper. To achieve reproducible code, in addition to the previous requirements, one needs to provide all parameter files and inputs that the code uses. Additionally, it is of great use to write code that is reusable and easy to understand. Finally, articles should include a description of the analysis code that

makes it possible for others to write it and replicate the results (Benureau and Rougier 2018). I aimed to apply these ideas when developing analysis software for electrophysiology data.

A major obstacle to reproducibility of experiments that investigate neuronal firing with extracellular electrodes is the allocation of spike waveforms to putatively separate neurons. In principle, spike sorting makes it possible to identify firing events that belong to a single neuron when an extracellular signal is recorded. However, analysis pipelines to sort neuronal data typically contain manual interventions (Lewicki 1998; Rey, Pedreira, and Quian Quiroga 2015), which are error prone and can lead to variability in the results that depend on the person who performs the sorting. Manual curation is also a time consuming task, where the experimenter needs to decide whether to merge, split, accept or exclude clusters. It could take several hours of work to sort data from a day of recordings. This means that the experimenter, and therefore the results, can be affected by decision fatigue or other psychological factors in making decisions on whether to accept or merge clusters similarly to how judges' decisions are affected by the amount of time passed since their previous meal (Danziger, Levav, and Avnaim-Pesso 2011). Therefore, it is advantageous to reduce manual steps in spike sorting pipelines as much as possible for more reproducible data and time efficiency.

Recently, significant progress has been made to implement algorithms (J. E. Chung et al. 2017) that can perform sorting automatically, making experiments more reproducible and removing the bias introduced by manual strategies. However, there are no environments that automate data analysis from recording the data to spike sorting through to quantification of spatial firing characteristics.

My primary aim was to successfully sort tetrode data using MountainSort (J. E. Chung et al. 2017), a fully automated spike sorting program, and test different parameters and noise reduction strategies to optimize the number of high quality clusters detected. My secondary aim was to implement code that can run on a designated computer and can accept sorting tasks that it carries out without user intervention. I wanted this to be possible to use by multiple users simultaneously. Finally, I wanted to set up and validate an open field exploration task combined with electrophysiology recordings and optogenetic stimulation.

While much of this work is methodological, it required considerable development and testing of new code and adaptation of existing code. Given the importance of this work for reproducible and efficient data analysis I have described it here in a dedicated chapter. To achieve my goals for this chapter, I set up an open field exploration task, and analysed spatial properties of recorded neuronal events. I set up and tested all steps of the analysis to run on a computer and implemented a script that monitored files in designated folders on the computer for inputs that users could upload via SSH (secure shell) connections. The main script controlled the queue of recordings to sort, called subsequent stages of the analyses and transferred files for long term storage. I applied modern software development strategies to achieve clean and reusable code and followed clean code principle guidelines (Martin 2008). I will first describe the experimental methods and data acquisition and then the details of the data analysis. I will describe the results and methodology related to data analysis in the order they are performed on the data.

The code is available on GitHub:
(https://github.com/MattNolanLab/in_vivo_ephys_openephys).

3.2 Experimental methods and data acquisition

To identify firing events from single neurons and to enable optogenetic stimulation, I built 16-channel optetrodes that I implanted into the brain of mice in stereotaxic surgeries. I recorded neuronal activity while I tracked the movement of mice as they explored an open field arena.

3.2.1 Optetrode implant

For *in vivo* electrophysiology recordings, I built 16-channel microdrives consisting of 4 tetrodes and an optic fiber. I built the microdrives using the following protocol. I glued a 21 gauge 9 mm long inner cannula to an EIB-16 (Neuralynx) board to the hole next to the ground (G) pin using epoxy (RS components 132-605) and left it to dry overnight. I prepared tetrodes using tetrode wire (18 µm HML-coated 90 % platinum 10 % iridium, Neuralynx) by spinning the wires and then melted the insulation with a heat gun to attach them to each other. The next day I connected two grounding wires (1.5 cm long insulated part) to the reference and ground pins, and threaded 4 tetrodes through the inner cannula. I connected all 16 channels of the four tetrodes to one of the pinholes of the EIB-16 board, fixing them with golden pins (Neuralynx, EIB Pins) to remove the insulation and make an electric connection between the wires and the board. After threading the tetrode wires through the EIB-16 board, I put a 13 mm long optic fibre stub (Plexon, PX.OPT-FS-Flat-200/230-13L) through the inner cannula, in between the tetrodes. I covered the wires on the board and the optic ferrule up to about 2/5th with epoxy. I applied the epoxy layer by layer to make sure that the wires do not break. I glued (RS components, 473-455) the tetrodes to four sides of the optic fibre. The next day I cemented a poor lady frame (Axona) to the side of the board. Finally, I put Vaseline around the base of the inner cannula, put the 17 gauge 7 mm long outer cannula on the inner cannula. I sanded down the tip of the outer cannula diagonally so one side was 6 mm to fit the curvature of the skull better. I trimmed the tetrodes using ceramic scissors (Science Tools, Germany) to be 0.5 mm long from the tip of the optic fibre. This design allows the tips of the recording electrodes to reach about 3.5 mm maximum depth in the brain relative to the brain surface.

I performed gold plating to improve the quality of the recordings by reducing the impedances of the recording electrodes. The evening before, or immediately before surgery, I put the tip of the tetrodes in a gold plating solution (non-cyanide gold plating

solution, Neuralynx), and connected them to a power supply (5 V DC). To clean the tetrodes, I ran three 1 second 4 µA pulses with the tetrodes as an anode. Then, to lower the impedance, I plated the drives with the tetrodes as a cathode by passing 2 µA 1 second pulses through them until the impedance was between 150 and 200 kΩ.

3.2.2 Open field recording system

The open field arena consisted of metal box with removable metal walls and a floor area of 1 m^2 (Figure 3.1), and a metal frame (Frame parts from Kanya UK, C01-1, C20-10, A33-12, B49-75, B48-75, A39-31, ALU3). A camera (Logitech B525, 1280 x 720pixels Webcam, RS components 795-0876) was mounted on the top of the frame for motion tracking. I used a commutator (SPI cable adapter board, Intan Technologies C3430 and 3D printed holder, custom designed by Patrick Spooner, CDBS, University of Edinburgh) to hold the SPI cable (Intan Technologies, RHD2000 6-ft (1.8 m) Ultra-Thin SPI interface cable C3216), and patch cable (Campden Instruments, PlexBright Optogenetic Stimulation System patch cable kit for use with a CompactLED Module. 200/230 µm high performance fibre; LC ferrule with polished tip; 1.5 m length. Patch cable with a mono-coil wrap, LC ceramic sleeves & LC-LC coupling, PX.OPT-PC-LC-L CF-200/230-HP-1 .5L-MC KIT). To make it easier for mice to explore, the cables were supported by elastic strings to make them lighter, and the commutator was held by gimbals (custom designed by Patrick Spooner, University of Edinburgh).

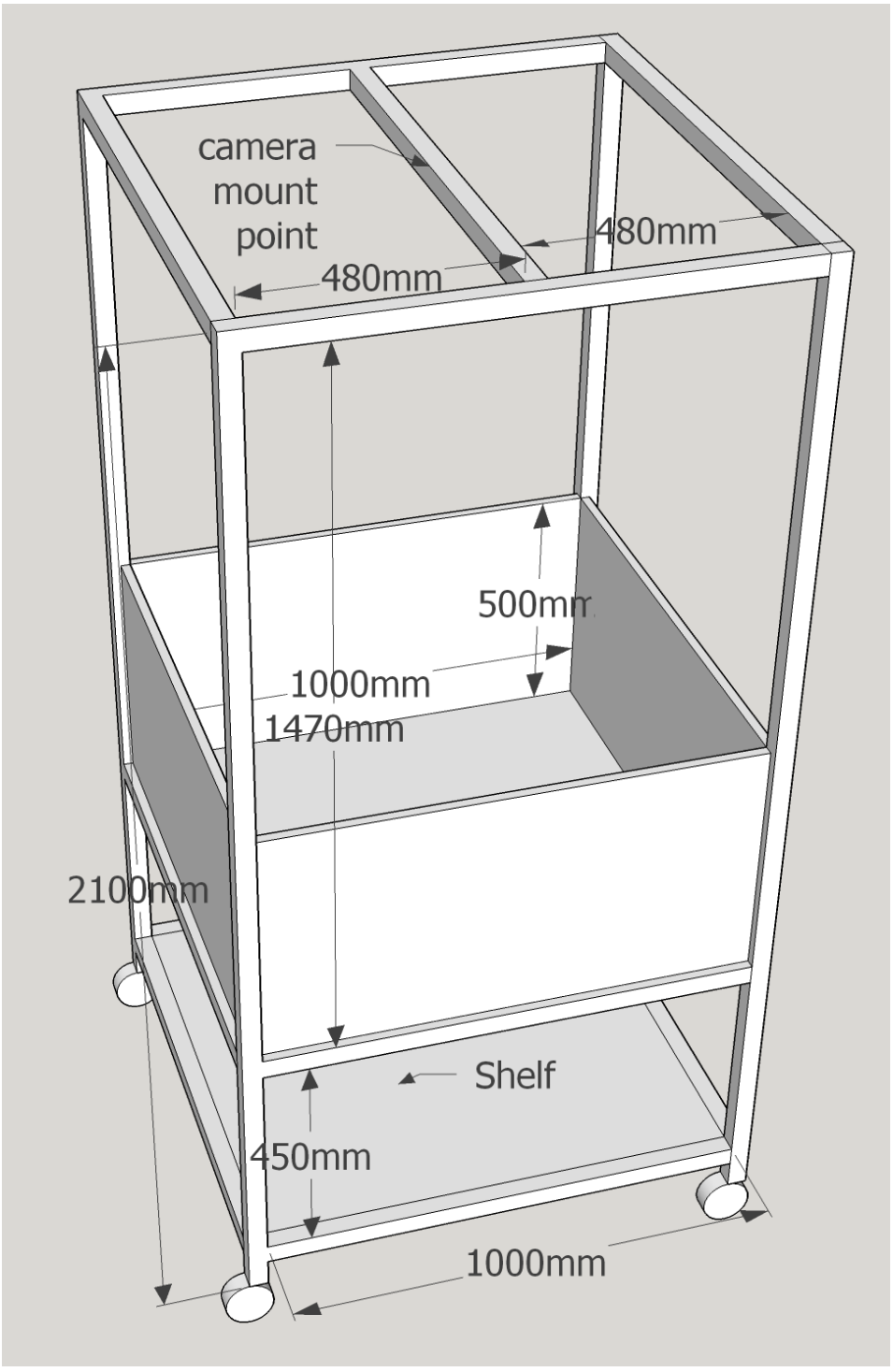

Figure 3.1. Measurements of open field arena frame.

3.2.3 Electrophysiology recording using Open Ephys

I recorded electrophysiology signals using the home-made 16 channel optetrode described above. I used an SPI cable (Intan Technologies, RHD2000 6-ft (1.8 m) Ultra Thin SPI interface cable C3216) to connect the implant to a commutator (SPI cable adapter board, Intan Technologies C3430 and 3D printed holder, custom designed by Patrick Spooner) to allow the mouse to explore without the cables getting tangled. The commutator was connected to an Open Ephys acquisition board (Siegle et al. 2017) that sent the electrophysiology signal to a computer (HP Z440 Tower Workstation i7, 16GB, 512GB SSD, Cat.: J9CO7EA#ABU). The signal was filtered between 2.5 Hz -7603.8 Hz and displayed using the Open Ephys GUI (graphical user interface).

3.2.4 Optogenetic stimulation

I performed optogenetic stimulation using an LED driver (Campden Instruments, PlexBright optogenetic stimulation system single channel LED Driver; includes amplitude modulation control w/ digital read-out, digital and analogue input; for control of PlexBright LED modules) that sent pulses to the commutator and then to the optic fibre stub (PlexBright optogenetic stimulation system fibre stub implants for use with LC ferrule tipped patch cable; 200/230um fibre; flat cleaved) implanted to the brain *via* the patch cable. The stimulation was controlled by an Arduino Uno (arduino.com) using a custom script:

(https://github.com/MattNolanLab/in_vivo_ephys_openephys/blob/master/open_field_optogenetics/open_field_optogenetics.ino).

3.2.5 Motion tracking and synchronization pulses

For motion and head-direction tracking, I attached a camera (30 frames per second) to the frame of the open field and sent the recorded video to the computer. To record head-direction data, I attached a custom made metal pin with a red and a green polystyrene ball on the two sides of the headstage, and used a custom Bonsai script (Lopes et al. 2015) that tracked the polystyrene balls based on their colour:

(https://github.com/MattNolanLab/in_vivo_ephys_openephys/tree/master/Bonsai_tracking_script).

The image taken by the camera was cropped two different ways by Bonsai (Figure 3.2). One selection (top branch on Figure 3.2) included the whole surface of the open field arena that the mouse could explore. The green and red balls were tracked based on thresholds manually calibrated in Hsv (hue, saturation, value) space. I calibrated these values by placing the red and green balls at 16 different locations in the arena, measuring Hsv, and then setting thresholds that distinguish between the two balls the best. The x and y positions of the tracked balls were written into a csv output file along with a timestamp. The other selection area (bottom branch on Figure 3.2) cropped out an LED attached to the side of the open field arena to track its activity. After cropping, intensity was calculated and saved to the same timestamped csv output file as the position data.

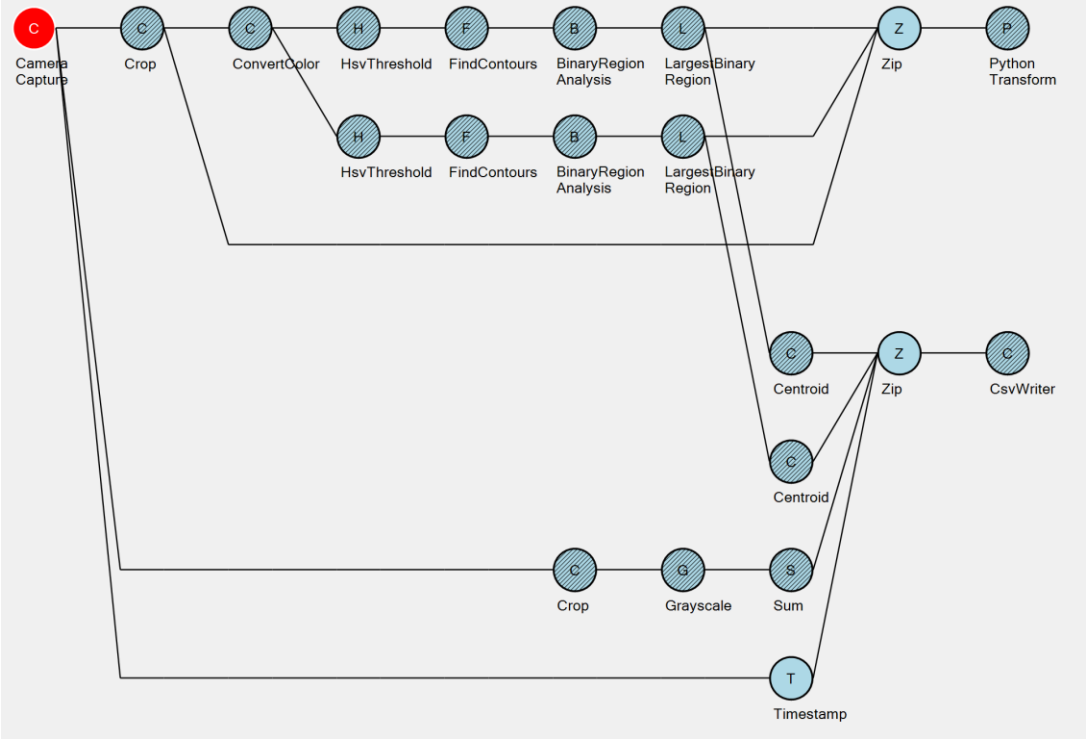

Figure 3.2. Bonsai motion tracking workflow. The image recorded by the camera was cropped to include the whole surface area of the open field arena (top branch) for motion tracking and the LED on the side of the frame (bottom branch) for synchronizing the position data with the electrophysiology data. The Python transformation was implemented by Gonçalo Lopes. Each circle represents an online operation performed by Bonsai on the recorded video.

3.2.6 Synchronizing location and electrophysiology data

To synchronize the position and electrophysiology data, I attached an LED (light-emitting diode) to the side of the open field arena in the field of view of the camera. I wrote an Arduino script that sent pulses to the LED as well as to Open Ephys acquisition board via the I/O (Input/Output) board. The pulses had random generated gaps (20 to 60 seconds) in between them so that the two series could be correlated in the analysis:

(https://github.com/MattNolanLab/in_vivo_ephys_openephys/blob/master/open_field_optogenetics/open_field_optogenetics.ino).

An overview of the connectivity of all components of the system is shown on Figure 3.3.

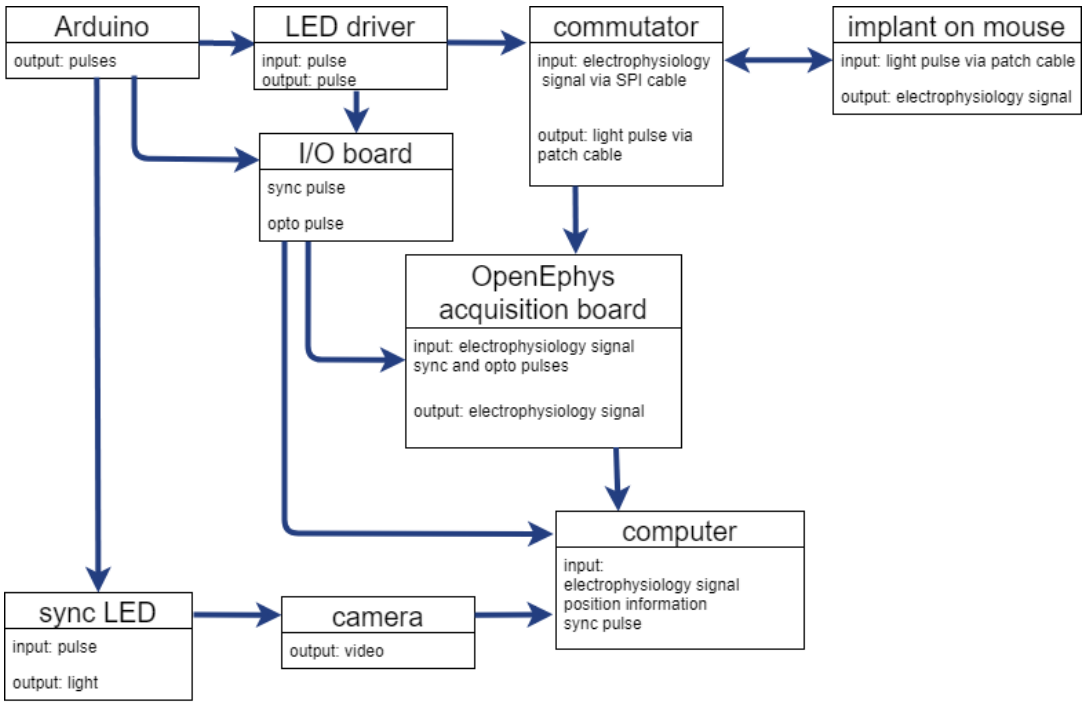

Figure 3.3. Overview of connectivity and flow of information between components of setup.

3.3 Data analysis

I analysed spatial firing properties of neurons recorded in an open field arena. To reduce user intervention in the analysis pipeline, I needed to implement scripts that pre-processed the raw electrophysiology data and then called the spike sorting algorithm and further analysis steps to analyse spatial firing. To analyse the sorted data and create plots of spatial firing and calculate spatial scores, I used a combination of existing MATLAB scripts and scripts I wrote to reproduce parts of these and add to them. I documented the code on GitHub:

(https://github.com/MattNolanLab/in_vivo_ephys_openephys/wiki).

3.3.1 Spike sorting

To perform fully automated analysis and avoid manual clustering, I set up a pipeline using MountainSort (J. E. Chung et al. 2017). I used version 0.11.5 and its dependencies mountainsort-ms3, mountainsort-alg, mountainsort-pyms for all analyses.

After recording data from an animal, I uploaded the recording folder to a designated sorting computer (using Ubuntu 16.04.3 LTS), where the data was pre-processed for spike sorting, sorted, and basic descriptive plots were made and then uploaded to a server for permanent storage (Figure 3.4). I automatically curated the data using MountainSort's cluster quality metrics, and then manually removed any remaining false positive clusters based on autocorrelograms and waveform shapes (Figure 3.4). I use the term false positive cluster to describe clusters identified as neurons by a sorting algorithm that are in fact noise.

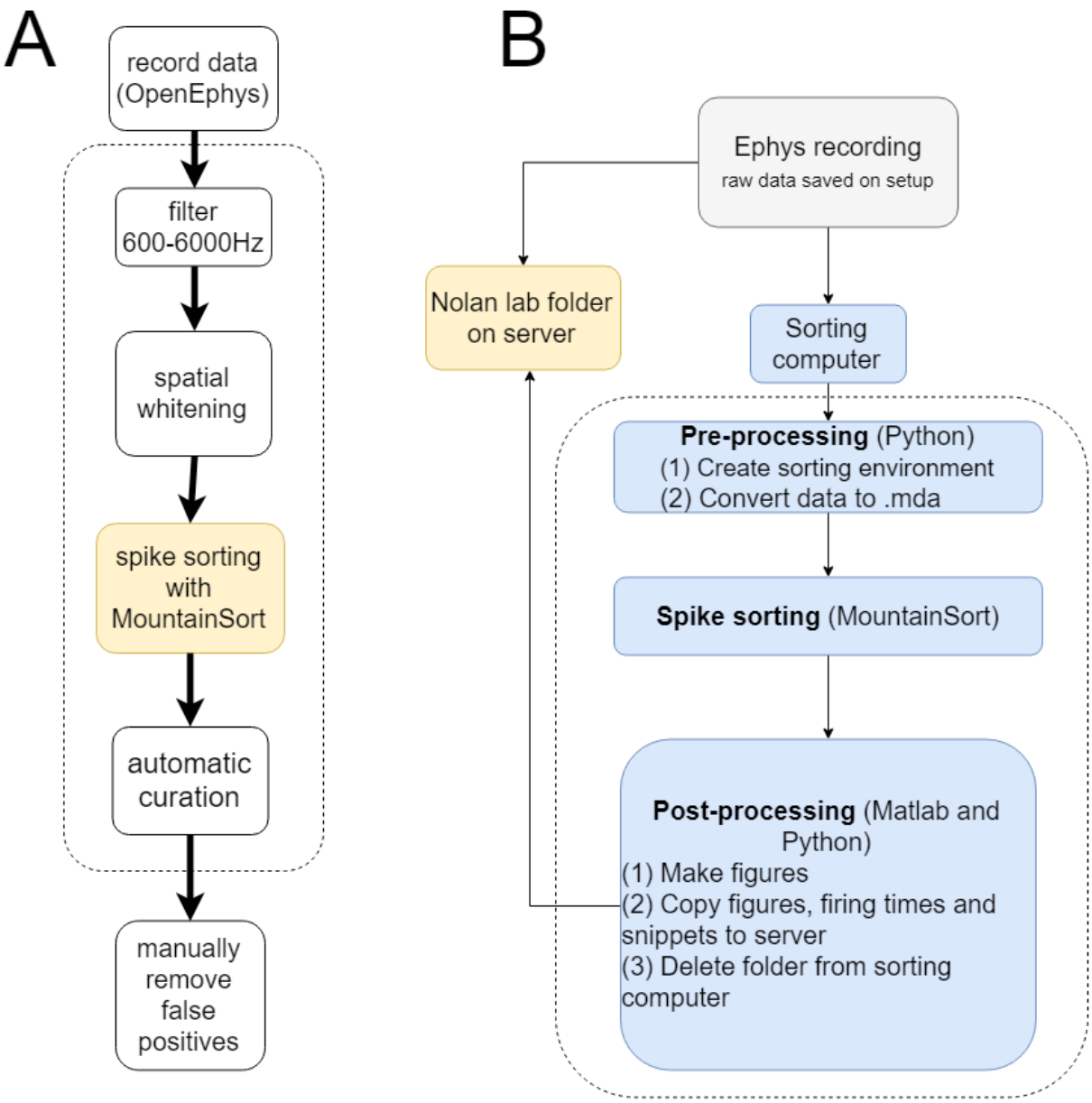

Figure 3.4. Overview of analysis pipeline. (A) Electrophysiology data is recorded using Open Ephys, pre-processed (filtered and whitened) and sorted using MountainSort and curated using automatic and manual methods. (B) To automate data analysis, recordings are uploaded to a designated sorting computer and a server. The data is analysed locally on the sorting computer and the output files (data frames and spatial firing plots) are uploaded to the server in the last step of the pipeline. The analysis steps executed on the sorting computer are surrounded by a dashed line in both A and B.

Automatic file processing pipeline

To make the sorting pipeline available to other members of the lab, I needed to design and implement a robust script that is easy to use and handles unexpected inputs. Additionally, I implemented two different priority levels to make it possible to process urgent recordings immediately (Figure 3.5).

To differentiate between low and high priority recordings, I created two designated sorting folders (to_sort/recordings, to_sort/downtime_sort) and gave users SSH access to these. I wrote a Python script (control_sorting_analysis.py) to monitor these folders and control running analyses. The control script first checks the high priority folder and if it finds recordings in it, it checks whether the recording is fully copied from the user's computer or server. If it was copied, the control script calls analysis scripts to analyse the data. Regardless of whether the analysis was successful, the folder containing the analysed recording is deleted from the high priority folder. This is to ensure that recordings are not analysed multiple times and that the computer's SSD (solid state drive) is not overloaded with recordings. Alternatively, users could put a list of folder paths in txt files in the low priority folder. This folder was only monitored when the high priority folder was empty.

To indicate which recordings were analysed successfully, I created a list of folder names of crashed recordings locally. Reasons for analyses to crash included corrupted and missing files, as well as bugs in the analysis scripts. In addition to the crash list, I wrote a sorting log for all recordings to make debugging easier. The sorting logs contain information on which parts of the analyses were successfully completed. I used Python version 3.5.1 in Anaconda environment 4.0 for all analyses.

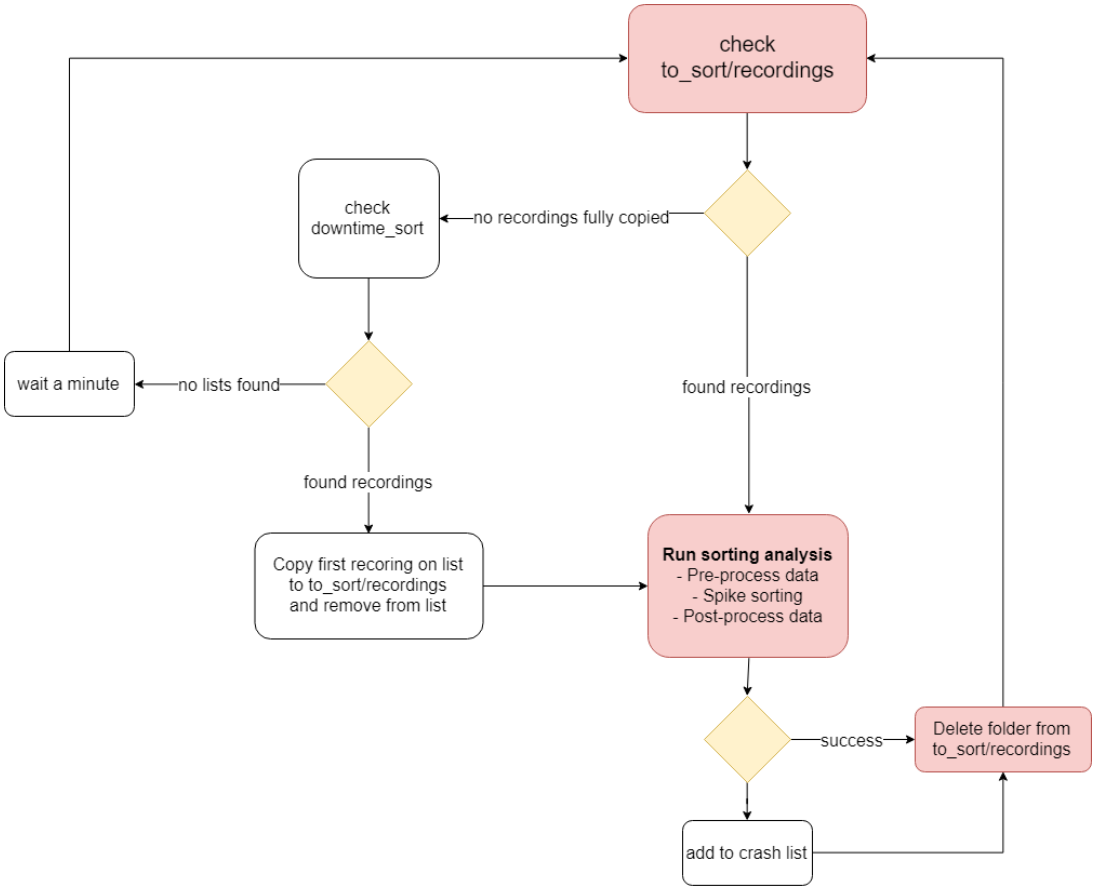

Figure 3.5. Overview of automated analysis on designated sorting computer. The main control script monitors a high and a low priority folder that contains user input that determines the order of analyses. Both successful and failed analyses result in the removal of the data from the local computer.

Pre-processing data for spike sorting

I wrote Python scripts to pre-process the data for sorting. These scripts were called from the main Python script controlling the whole spike sorting analysis.

I read the Open Ephys files using open source analysis tools (github.com/open-ephys/analysis-tools), converted the Open Ephys files to mda format for sorting using MountainSort's mdaio.py, and organized these files together with spike sorting input parameter files. The input files included a file defining the geometry (geom.csv, geom_all_tetrodes.csv) of the recording electrodes, and files to define sorting pipeline parameters for MountainSort (mountainsort3.mlp, params.json). Sorting is performed within electrode neighbourhoods, which include channels that are close to each other

in the brain. I defined the four channels of each tetrode to be in the same sorting neighbourhood to ensure that these are sorted together. I excluded broken channels from the geometry files.

To test whether it is better to do spatial whitening (zero-phase component analysis) to reduce noise on all channels combined and then sort tetrodes separately, or whiten separately tetrode by tetrode, I performed all analyses for all of my data both ways, so I created two sets of input files, and tested which method yields higher quality clusters.

For running MountainSort and later MATLAB, I generated shell scripts (programs to run on a Unix shell, a command line interpreter) so that these scripts could be run by the main control script.

Spike sorting using MountainSort

MountainSort (J. E. Chung et al. 2017) filtered the data from 600 Hz - 6000 Hz using a bandpass filter to remove low frequency oscillations and then performed spatial whitening to remove correlated noise. I selected the default filter option (600 – 6000 Hz). It is possible that choosing a wider band, for example 300 – 6000 Hz would have changed the outcome of the sorting by preserving more information on the shape of the spike. At the same time, this filter setting would have introduced more low frequency noise and could have resulted in more incorrectly split clusters. Optimizing how the data is filtered could increase the number of correctly detected cells. In the next step, events with peaks three standard deviations above average and at least 0.33 ms away from other events on the same channel were detected. The first 10 principal components of the detected waveforms were calculated, creating a 10-dimensional feature space. A spike sorting algorithm, ISO-SPLIT, was applied on the feature space.

The ISO-SPLIT algorithm (J. E. Chung et al. 2017) is based on two assumptions. The first assumption is that each cluster arises from a density function that, when projected onto any line, is unimodal. The second assumption is that any two distinct clusters may be separated by a hyperplane, in the neighbourhood of which there is a relatively lower density. The algorithm first over-clusters the data, and then performs pair-wise checks on clusters to ensure that the two main assumptions are met, and regroups

spikes if necessary. The output of the spike sorting is a file (firings.mda) containing the firing times of each detected event and the assigned cluster ID.

3.3.2 Curation

To evaluate cluster quality, MountainSort calculated three metrics: isolation, noise-overlap, and peak signal to noise ratio. Isolation quantifies how well the given cluster is separated from nearby clusters. Low isolation means a high false positive and false negative ratio, since clusters are mixed up. Noise overlap estimates the fraction of events that do not belong to any cell, but crossed the detection threshold. The fraction of events that do not belong to any cell is calculated by estimating the waveform shape for noise events and then assessing the overlap between the cell and noise in feature space. To automatically exclude events that are not neuronal and originate from other sources such as movement, and therefore are more likely to be variable, the standard deviation of the peak amplitude is calculated on the channel where the peak is highest. The signal to noise ratio for the peak is calculated by dividing the peak amplitude by the standard deviation.

Automatic curation

Output clusters underwent automatic curation based on the cluster quality metrics calculated by MountainSort. Units that had a firing rate higher than 0.5 Hz, isolation more than 0.9, noise overlap less than 0.05, and peak signal to noise ratio more than 1 were accepted for further analyses.

Lower and higher quality thresholds were tested and compared to manual curation results by Elizabeth Allison. Manual curation was performed by an experienced user, Elizabeth Allison, based on visually assessing the position of firing events in principal component space, waveform shapes and autocorrelograms of firing times using data sorted by Klustakwik (https://github.com/klusta-team/klustakwik). Three sets of criteria were tested: C1 [isolation > 0.95, noise overlap < 0.03, peak signal to noise ratio > 1.5], C2 [isolation > 0.9, noise overlap < 0.05, peak signal to noise ratio > 1], and C3 [isolation > 0.9, noise overlap < 0.07, peak signal to noise ratio > 0.75] on two datasets obtained from 11 recording sessions from two mice. In the first dataset, 48 neurons were identified by manual curation, 33 using C1, 41 using C2 and 45 using

C3. Results contained no false positives in C1 and C2 relative to manual curation, and C3 contained 1 false positive. In the second dataset, 105-112 (ranges indicate uncertainty in manual curation) neurons were identified by manual curation, 69 using C1, 91 using C2 and 108 using C3. C1 and C2 contained no false positives and C3 contained 1-6 false positives relative to manual curation results. Hence, C2 identified the highest number of neurons detected by manual curation without introducing noise.

Excluding artefacts

To ensure that no artefacts passed automatic curation after sorting using MountainSort, any units that did not have a refractory period or hyperpolarization on the waveform shape were discarded. These exclusions were based on visually assessing output figures generated for clusters sorted by MountainSort. No manual curation was done to modify the assignment of individual firing events to clusters.

Whitening data over all channels yields more high quality clusters than tetrode by tetrode

To test whether whitening data across all channels of four tetrodes and then sorting tetrode by tetrode yields more high quality clusters than whitening tetrode-by tetrode, I analysed data from 127 recordings from 16 animals in total (Table 3.1, Figure 3.6). I found that overall 425 clusters passed curation when all channels were whitened together, more than when data was whitened tetrode by tetrode. Further, the proportion of false positive clusters was lower when channels were whitened together. Therefore, I decided to use the all-channel-whitened data for further analyses (Table 3.1, Figure 3.6).

Table 3.1. Number of cells that pass curation when all channels are whitened together and tetrode by tetrode, respectively.

	Whitened together	Whitened separately
Passed curation	**425**	**379**
False positives	62	94
Passed isolation	2121	1726
Passed peak SNR	2588	2670
Passed noise overlap	616	738

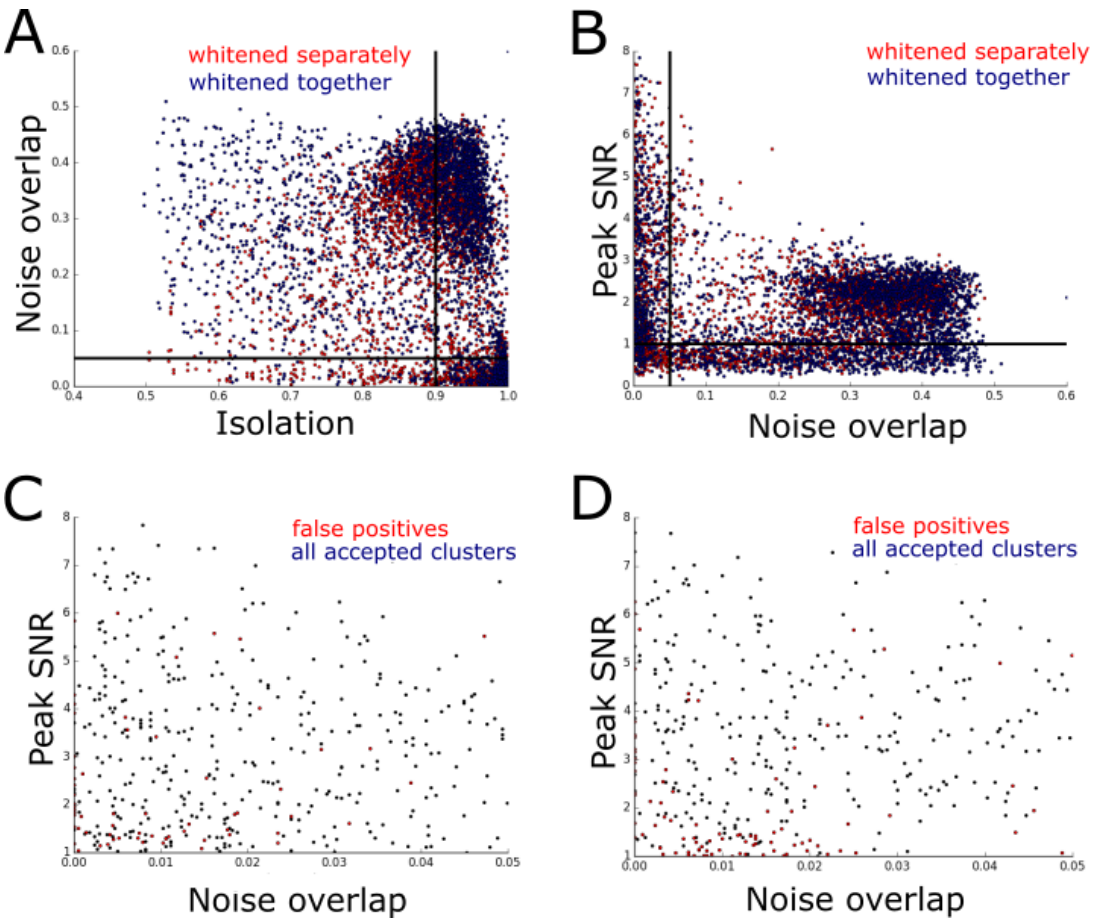

Figure 3.6. The number of high quality sorted units is higher when all channels undergo spatial whitening together. (A, B) Noise overlap, isolation and peak signal to noise ratio of data where whitening was done on all channels (blue) and tetrode by tetrode (red). Vertical and horizontal black lines show the cut-off point for the quality metric displayed on the corresponding axis. (C, D) Noise overlap and peak signal to noise ratio of all clusters that passed curation when tetrodes are whitened together (C) and separately (D). False positives (red) were manually removed from clusters that passed curation (C, D).

3.3.3 Post-clustering analysis

To analyse firing properties after spike sorting, I initially used scripts written by Elizabeth Allison based on scripts from Emma Wood's lab. Briefly, a MATLAB (version: R2016b) script loaded the position data from the Bonsai output file and the synchronization pulses from Open Ephys, and synchronized position and electrophysiology data by correlating the synchronization pulses. It loaded firing times from the MountainSort output, and created plots of firing rates, autocorrelograms, and

spike times relative to light stimulation. Based on the position and spike data, it calculated how well the animal covered the arena, the firing rate, the highest amplitude, spike width, maximum head-direction and position dependent firing rates, spatial coherence, and grid score for each cluster.

Versions of this code were previously implemented and used by multiple students and returned plausible results. Due to the incremental nature of the development of the code, and limited modularity, I found it challenging to test it and add to it. To improve modularity, I first refactored the main code to separate functionally distinct parts into functions. Refactoring the code reduced the scope of variables, and revealed functional modularity, but some functions had more than 30 input and output parameters, making the code difficult to navigate and understand. To reduce the number of parameters, higher level data structures, or object oriented approaches (Gamma et al. 1994) were needed. This means that instead of giving functions variables one by one, they can be grouped on a higher level and accessed in an organized way. For example, the 6 arrays holding the x and y coordinates for the two tracked beads, the head-direction of the animal, and the synchronization pulses could be combined into one data frame.

To begin to address these issues I replicated parts of the original MATLAB scripts in Python (Figure 3.7), and used Pandas (https://pandas.pydata.org/, version 0.23.3), a Python library that provides tools such as data frames for data organization and data manipulation. The main reason for using Python was that the rest of the analysis is implemented in Python and it makes it easier to maintain and modify the scripts if they are all written in the same programming language. Another reason that makes Python an attractive option is that it is a fully open source language. That makes Python more accessible for others who may want to reproduce the experiments or build new experiments on those. Here I will present an example of how the modularity and structure differs between the two implementations and explain why these differences are important.

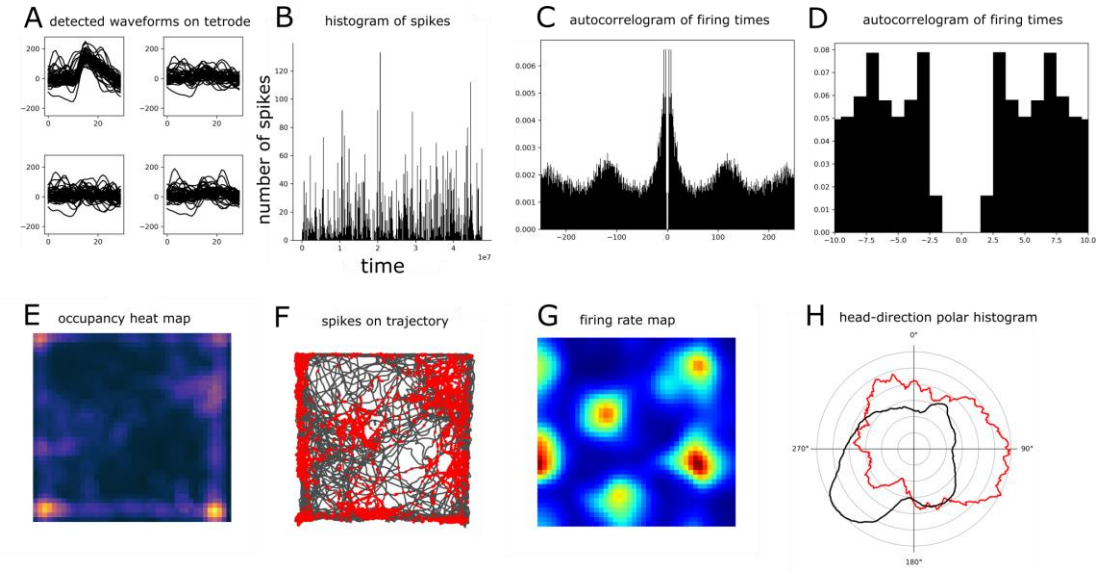

Figure 3.7. Examples of output plots of Python post-sorting script. (A) Randomly selected spike waveforms overlaid from the four channels of the tetrode. (B) Histogram of spikes during the recording. (C and D) Autocorrelograms of firing times. (E) Heat map of the position of the animal to show coverage during exploration. (F) The trajectory of the animal is shown as a black line in the open field arena, and the locations where the cell fired are shown as red dots. (G) The firing rate map was calculated by summing the number of spikes in each location and dividing that by the time the animal spent there and then smoothing the surface with a Gaussian centred on each location bin (Leutgeb et al. 2007). (H) The head direction plot was made by plotting a smoothed (10 degree window) polar histogram of the animal's head direction from the whole session (black, normalized value) and during when the cell fired (red, in Hz).

High level organization of post-sorting code

First, I will compare the structure of the main post-sorting scripts. I will use the version of the MATLAB script before I refactored the code (commit: ff5782ee7f3ec494f178f0281bc9eb5789f11337), and the current version of the Python script (commit: 01258b4f4d3f8e090245e62d6f829d7b52c006c9).

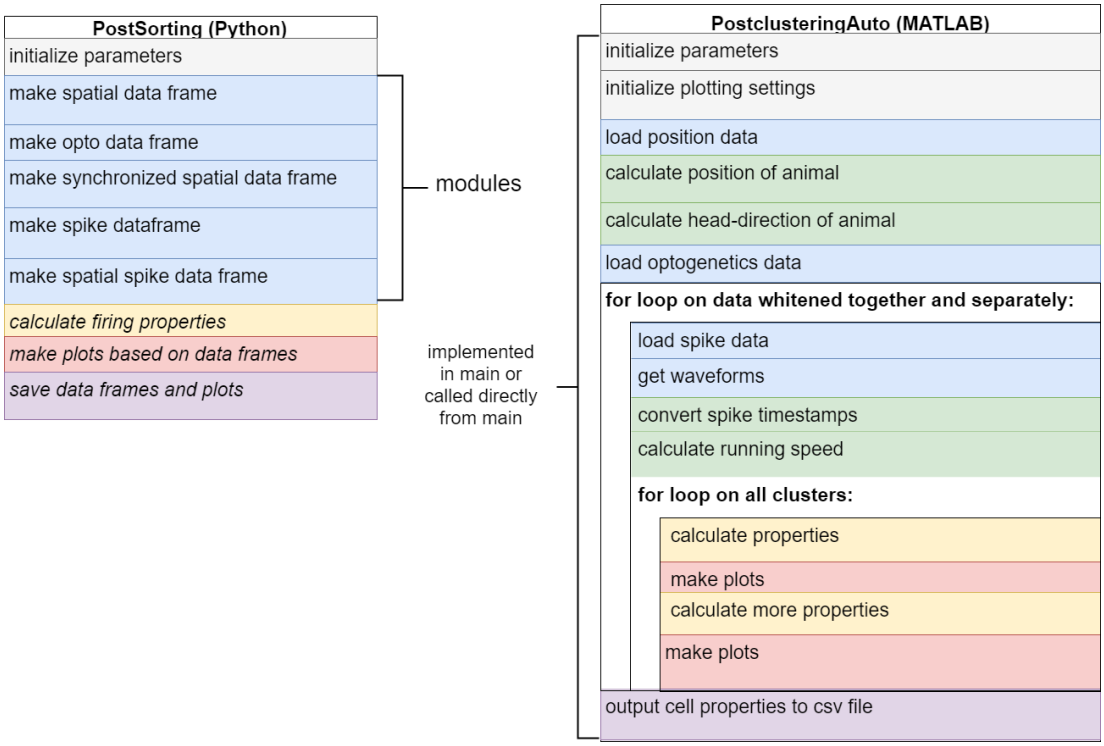

Figure 3.8. Comparison of main functions of Python and MATLAB implementations of post-sorting analysis. The data is processed in a modular way in the Python implementation, each analysis adds its output to combined data frames. Analyses are nested and run sequentially for each cluster in the MATLAB implementation.

One major difference between the two implementations (Figure 3.8) is how variables are handled. In the MATLAB version, global variables are defined in the main function and passed on to specialized functions called directly from the main function. Global variables in the main function have a scope of 438 lines, so they can be accessed from anywhere in the main. The problem with big scopes is that variables clutter the name space, or can lead to code that is difficult to read and add to, especially if variables are redefined. To reduce the scope and number of variables in my Python code I applied an object-oriented approach and implemented a parameters class. Using this class, instead of variables, I can define a parameters object, a programming entity that can contain all parameters that can be passed on to appropriate modules.

For instance, the parameters class contains methods to set and get the sampling rate. Calling `object_name.set_sampling_rate(30000)` will set the sampling rate parameter of the object to 30000. Once this is set, calling `get_sampling_rate()` will return 30000 for this object.

```
def get_sampling_rate(self):
    return Parameters.sampling_rate


def set_sampling_rate(self, sr):
    Parameters.sampling_rate = sr
```

This way, instead of having to pass numerous parameters to functions, it is sufficient to pass a parameters object and use the methods of the class to set and get parameters.

Another difference is structural. In the MATLAB script, the main function contains two embedded for loops that iterate over data (Figure 3.8). The outer loop is on the two types of data obtained with the two different types of whitening strategies, and the inner loop is on clusters. The issue with the outer for loop is that to modify the code to only run analyses using one whitening strategy, the code needs to be altered everywhere the 'stage' data structure is used. The outer for loop in the MATLAB code could be replaced with a solution similar to how the same problem is handled in the pre-processing script, where `boolean` parameters define which parts of the code need to run. The inner for loop iterates over all clusters, and alternates between calculations and making plots for each cluster. This structure is problematic if new features need to be added, because it is difficult to find the place where the desired variables are available, and the function is very long and difficult to read.

In the Python version, instead of having high level loops, modules with functions are used to fill in data frames and perform low level computations. That way, new features, such as another calculated property, can be added to the appropriate data frame as a new column, or a new data frame can be created for a new set of properties.

	synced_time	position_x	position_y	hd	speed
0	0.007091	32.176648	59.083898	138.381042	13.920346
1	0.038630	32.068068	59.065136	134.219527	15.372280
2	0.070822	32.259102	59.018943	131.780320	26.863024
3	0.102912	32.393489	58.942455	128.595982	21.202156
4	0.134579	32.527750	58.898568	126.553803	19.626263
5	0.166873	32.637273	58.767682	126.232870	23.252485
6	0.215078	32.692807	58.675261	127.013365	9.841689
7	0.246413	32.706955	58.681159	126.938080	2.152341
8	0.278387	32.595182	58.622489	124.219470	17.371258
9	0.311654	32.461398	58.672670	127.839117	18.898441
10	0.342605	32.339886	58.862375	135.788091	32.027020

Figure 3.9. Spatial data frame in Python debugger. The spatial data frame contains the timestamps, position, head-direction and speed of the animal from the whole trajectory from a recording session.

Using data frames instead of variables means that the data is labelled, easy to import and export, organized, and high level database functions are available. Data stored in data frames is similar to a spreadsheet with indices and headers, which is helpful when managing big data (Figure 3.9). The rows are indexed and indices do not change after manipulations, so the data will stay aligned unless indices are explicitly changed. Import and export of data is simpler compared to when only arrays are used. When data frames are used it is simple to include the header in the output data. A csv file that does have headers can be read into a data frame directly. In the MATLAB implementation, the output data does not have headers, which makes it more difficult to manage in subsequent steps.

3.3.4 Identifying light responsive cells

To classify cells as light responsive, I compared baseline spike latency histograms from a test epoch to the spike latency histograms of the first spikes after light stimulation. In order to quantitatively assess whether a cell is light responsive, I used a MATLAB implementation of the Stimulus-Associated spike Latency Test (Kvitsiani et al. 2013). This test was developed to statistically compare the baseline firing of cells to firing upon stimuli. Using this method is particularly important for cells that have a high firing rate, and cells that do not respond every time when they are stimulated.

3.3.5 Documentation and clean code implementation

Documenting code by adding comments can be cumbersome and inefficient, since every time the code is changed, the comments need to follow. It is easy to overlook comments that correspond to a previous version of the code, and it can take focus away from implementing changes if comments need to be edited continuously. A better strategy is to name variables and functions in a way that reflects their content and write comprehensive documentation that explain the details of the code. For example, instead of naming a variable `x` and commenting that this is the speed of the animal, the variable could be called `speed_animal` and the comment could be omitted. The documentation could explain how the speed was calculated. Comments are useful and needed in certain situations, for instance to explain why a certain strategy was applied. Explaining coding strategies is important since the code will only reflect the final solution implemented, but not the decisions behind that implementation, which may not be straightforward. I aimed to apply these strategies while commenting and documenting my code.

To help users replicate the environment and run my code, I created a wiki page with instructions (https://github.com/MattNolanLab/in_vivo_ephys_openephys/wiki) linked to the GitHub repository of the code. The GitHub wiki is restricted to explaining how to use the high and low priority options on the sorting computer and brief explanations on what happens in the scripts and what the data frames contain as well as information on the versions of programs used.

3.3.6 Using automated processing is more time efficient

In an experiment where the analysis pipeline is not automated, all subsequent steps of the analysis need to be started by the experimenter before and after curation (Figure 3.10). Using our previous sorting strategy, after recording the data, files needed to be transferred to a server and then pre-processing was manually started for all four tetrodes. The pre-processing step took about 15 minutes, after which the spike sorting needed to be started. Manual curation followed, which could take up to an hour per tetrode depending on the number of cells in the recording and the level of experience of the experimenter. Finally, a post-sorting script had to be started manually to make plots and calculate firing properties, which would take another 15-

20 minutes to run. Our previous sorting strategy typically led to workflows where analysis lagged behind acquiring data in some cases by months, which is a problem in experiments where experimental decisions are made based on sorted cells.

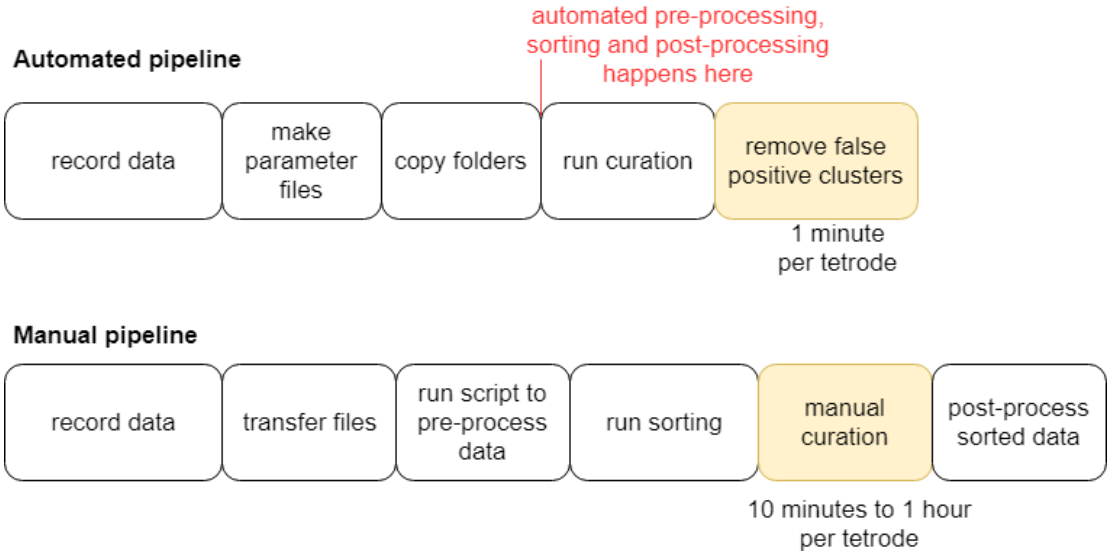

Figure 3.10. Manual analysis steps are reduced in the automated pipeline relative to the manual pipeline. Every box indicates an analysis step initiated by the user that takes less than 1-2 minutes of user time unless indicated otherwise. The yellow boxes indicate manual steps.

When using the automated pipeline (Figure 3.10), most of the analysis can be done while recording from other subjects. The analysis is started by copying the folders to the sorting computer and server along with a parameter file that only contains two lines. The data is automatically processed up to making figures and calculating firing properties for all clusters detected by MountainSort. Automatic curation needs to be started manually, but it is implemented in a way that it can go through all recordings and therefore only needs to be done once per experiment. Removing false positives caused by artefacts takes about 1 minute per tetrode. The user time needed to use our manual method is about 1-4 hours in total depending on the number of clusters, and about 2-4 minutes for the automated method. The computer time for a 30 minute long recording is about an hour in total for the manual and 15 minutes for the automated method.

3.4 Discussion

I set up a new automated and reproducible pipeline to analyse spiking activity recorded from animals during behaviour and during optogenetic stimulation. The pipeline uses MountainSort for spike sorting and requires minimal user intervention. However, it does not fully eliminate detecting noise as clusters and user intervention is required for removing these artefacts based on the spike waveforms and autocorrelograms. I tested two different noise reduction strategies and found that whitening over all channels yields more high quality clusters than whitening tetrode by tetrode. Overall, I implemented a pipeline that is more time efficient for users and is more replicable than our previous manual method. Implementing an automated pipeline allowed me to focus on acquiring data and higher level analyses. In this discussion, I will evaluate to what extent I reached my initial aims and highlight aspects of the analysis that would benefit from further improvement.

My primary aim was to automate analysis of tetrode data using MountainSort and test different noise reduction strategies. I found that sorting was successful with both noise reduction strategies and recorded spatially selective and light-responsive cells (further data presented in Chapter IV and V). Whitening across all channels yielded more clusters that passed curation. One possible reason for the lower success rate when whitening is done tetrode by tetrode is that multiple channels of the same tetrode are likely to record the same cell, so not only correlating noise, but correlating signal will be reduced by whitening within a tetrode. Channels of different tetrodes are unlikely to record from the same cell, and therefore the correlating signal recorded on them more likely originates from noise, so reducing it will increase the signal to noise ratio. For the remainder of the thesis I therefore decided to use the data where I whitened over all channels. However, my data are not sufficient to conclude that this strategy is generally better. For example, because other brain states and areas might have more synchronized firing activity than the MEC, in these areas whitening across all channels may not be a good choice as correlated activity is reduced by the whitening.

My secondary aim was to set up an automated pipeline to pre-process, spike sort and post-process data with minimal user intervention. This system needed to be accessed by multiple users simultaneously and distinguish between high and low priority sorting tasks. My final solution requires users to start the analysis by copying the recorded

data to a computer and to a server along with parameters. The next user intervention is to run a curation script and manually exclude false positive clusters. This pipeline reduced the time spent on analysing data, and also made it easier for inexperienced students to sort data. Further details on testing more manual methods are described in the Appendix. To further improve on the pipeline, the final manual step needs to be removed. The false positives are typically low firing rate events on the border of having acceptable quality metrics. One solution to reduce them could be to further increase quality thresholds. However, increasing quality thresholds would increase the number of false negatives, which would also reduce the overall quality of the dataset. A better option could be to train an artificial neural network (Yang, Wu, and Zeng 2017; Hassoun and H. 1995) to recognise action potential shapes and flag units that pass curation, but have no hyperpolarization. This could be done by creating a database of spike waveforms of real cells for a network to learn features of the possible waveform shapes. Then, this network could be used to recognize waveforms that do not resemble any neuronal waveform shapes. Future work could explore such options and identify properties that distinguish neurons from noise.

My larger aim was to build an open field arena and identify spatially selective and light responsive cells. I did this in collaboration with Elizabeth Allison and based it on setups used by Emma Wood's lab. An improvement we made relative to previous setups was that we built an arena that had metal walls which shielded the recording device and reduced mains noise. We improved how the position and electrophysiology data is synchronized by sending multiple pulses with variable gaps in between them rather than sending one pulse or pulses that are equally spaced. Our approach creates a unique synchronization pulse sequence signature for all corresponding data files which can be correlated to align position and electrophysiology data. Hence, I was able to combine position and electrophysiology data and identify spatially selective cells.

A more advanced solution to synchronizing location information calculated with Bonsai, with electrophysiology data recorded with Open Ephys was recently published as a preprint (Buccino et al. 2018). Using the Open Ephys plugin they implemented, the position data from Bonsai can be channelled straight into Open Ephys, removing the need to synchronize in post-processing. To synchronize the data online, they used a camera that could send TTL (Transistor-Transistor-Logic) pulses

to Bonsai. Thus, using this method, it is possible to integrate the functionality of Bonsai and Open Ephys, and do closed-loop manipulations based on the position of the animal. To perform closed-loop experiments, using my current pipeline, I could use the plugin by Bucciano et al. and change the camera and the processing module that loads the data.

I strived to implement my analysis code in a way that is possible to re-run, repeat, reproduce and reuse (Benureau and Rougier 2018). My code contains no non-deterministic elements and has returned the same results upon re-running. To achieve replicability, I added user instructions and asked fellow lab members to test them. They succeeded in analysing their data while using the system I set up. Two further labs were able to use parts of my code with minimal instructions. The part of the code that performs pre-processing for sorting is highly portable and could be adapted by labs who use Open Ephys to record extracellular tetrode data. The post-sorting module was tested on different enclosure sizes and shapes and could be useful for other labs investigating spatial navigation. To make it easier for new users to set up, it would be useful to move most parameters to configuration files and write documentation specifically for configuring the scripts. Overall, other labs could benefit from using the automated pipeline by reducing time spent on manual analysis and by reducing bias caused by manual curation.

For producing code that follows clean code principles (Martin 2008), I aimed to structure my code to be highly modular. Modularity is useful, because when a new feature is added, or if there is a change in what is required from the program, a well-partitioned non-monolithic code only needs to be modified in the affected modules. Another advantage is that modules can be tested in isolation. I also aimed to write functions that perform one task only and gave meaningful names to variables. Whether these differences in programming style will help other members of the lab or the open source community add to my code remains to be tested.

To further improve on our coding strategy, especially on reporting analyses in a way that others can re-implement the code, programming pipelines could be improved. Writing a specification before implementing code could be helpful, since by the end of the coding process the specification could become the description of what the code does. Another improvement would be to add more unit tests. These tests use dummy

data to test whether a given function returns the expected results. Ideally, an independent programmer should implement unit tests based on specification and without looking at the code to avoid overlooking the same issues as the person who implemented the code.

Testing and optimizing different sorting algorithms can be challenging and time-consuming. Output files of different recording devices differ and so do the inputs required by sorting programs. Implementing all the file conversions and optimizing parameters and comparing output from different programs can take months. Therefore, it would be useful to focus open source effort in developing environments that can be used to run multiple sorting algorithms to evaluate them and push the field to standardise formats. Being able to easily use multiple sorting algorithms on the same data would be invaluable for testing whether higher level conclusions of experiments change when the sorting is different. Performing analyses with multiple sorting algorithms would increase replicability for sorting experiments.

Layers of the medial entorhinal cortex by Komáromy Pongó Terézia.

Chapter IV

4 Optogenetic identification of deep MEC cells

4.1 Introduction

Studies using different recording approaches have reached very different conclusions about the activity of neurons in deep layers of the MEC during behaviour. Recordings using tetrodes from the rat revealed spatially selective firing in all layers of the MEC (Sargolini et al. 2006). Deep layers were found to have an abundance of conjunctive, grid and head-direction cells. Sargolini et al. identified the location of the tetrode recordings based on evaluating the damage the recording electrodes caused in the tissue. Another set of *in vivo* studies applied juxtacellular recordings in rats, a method that allows exact identification of the recorded cell by filling it with a dye. It found that recorded deep MEC cells were silent both in familiar and novel environments (Burgalossi, von Heimendahl, and Brecht 2014). These results suggest sparser coding than reported by Sargolini et al (2006). Burgalossi et al (2014) concluded that sparse firing (Field 1994), which is theorized to be a way of encoding information in the cortex, is a general feature of the deep MEC.

Since the results of extracellular and juxtacellular studies are not in full agreement, I decided to record the firing fields of deep MEC cells in mice and use genetic targeting to specifically identify L5b, a sublayer of the deep MEC with local connectivity (Sürmeli et al. 2015). A potential strategy would be to use opto-tagging methods to identify L5b neurons recorded with tetrodes (Buetfering, Allen, and Monyer 2014; Rowland et al. 2018; Roux et al. 2014). In this approach, recorded neurons can be accessed with a genetic precision using transgenic lines. Briefly, transgenic cell populations can be infected by AAVs that make infected neurons sensitive to light. Light sensitive neurons can be identified based on their response to optical stimulation *via* an implanted fibre optic.

My primary aim was to characterize the firing fields of L5b cells of the deep MEC. I performed tetrode recordings and used the p038 transgenic line to identify cells with optogenetic stimulation. For this, I injected the MEC of p038 mice with a virus that expresses ChR2 conditionally on the presence of tTA (AAV9-tre-ChR2-mCherry). This strategy makes tTA+ cells in p038 mice sensitive to light. Targeting the same region where I injected the virus, I implanted an optetrode, a microdrive that contained tetrodes and an optic fibre. This way, when I sent a light pulse, the infected cells fired action potentials that I could record with the tetrodes. To evaluate whether a cell was light responsive, I needed a statistically robust objective method that is able to evaluate neurons with very high and low firing rates. I used an unsupervised statistical method called Stimulus-Associated spike Latency Test (SALT) that tests the null hypothesis that light stimulation does not change firing latencies (Kvitsiani et al. 2013). The SALT test measures the distance between the distribution of spike latencies after light stimulation and a baseline distribution and does not use arbitrary thresholds or time windows. Using the SALT test allowed me to objectively test whether a neuron was light responsive.

My secondary aim was to find out what type of cells receive input from the tTA+ cell population. Cells that receive direct or indirect input from a stimulated tTA+ cell can consistently fire upon light stimulation. The responses triggered by input from a tTA+ cell have longer latencies than direct responses, since at least two action potentials need to happen for them to be activated. I identified cells that receive input from p038 cells based on the latency of their response to light. Finally, to be able to investigate the role of the deep MEC in spatial cognition in future experiments, I wanted to evaluate whether opto-tagging the tTA+ population is a feasible way of accessing the deep MEC.

Further analyses performed on data from this experiment are presented in Chapter V.

4.2 Methods

4.2.1 Ethical statement

All procedures were performed under a UK Home Office project license (PC198F2A0) in accordance with The University of Edinburgh Animal Welfare committee's guidelines. All procedures complied with the Animals (Scientific Procedures) Act, 1986, and were approved by the Named Veterinary Surgeon.

4.2.2 Animals

Sixteen p038 (mouse line described in Chapter II) mice (8 males and 8 females) 7-13 weeks (mean = 10.6, SD = 1.7 weeks) old at surgery were used in the experiment. Before surgery animals were group housed (3-5 mice per cage) in a standard holding room on a standard 12 hour on/off light cycle (dark from 7PM to 7AM). After surgery, mice were singly housed in a different holding room in otherwise similar conditions. The average temperature in the room was 20°C, and the relative humidity was 50%. Mice were kept in standard IVC cages with the metal food holder removed to avoid implants getting stuck after surgery. The cages contained sawdust, tissues, cardboard tubes and chewing sticks before the experiment. After surgery, the cardboard tube was replaced by a larger cardboard igloo. Two days after the surgery, a training wheel was placed in the cages for environmental enrichment. Standard laboratory chow and water were given *ad libitum* throughout the whole experiment.

4.2.3 Optetrode implant and surgery

I used optetrode implants as described in Chapter III. Briefly, I made microdrives that consisted of an optic fibre and four tetrodes glued to four sides of the fibre. The optic fibre and tetrodes were possible to lower after implantation using a screw mechanism.

4.2.4 Surgery

I washed the tips of the tetrodes before the surgery with ethanol and then with sterile saline by holding them into a drop using a syringe. Before implanting the drive, I injected AAV9-tre-ChR2-mCherry (Gene Therapy Center, University of Massachusetts Medical School) using the injection strategy described in Chapter II. All animals were injected 3.4 mm lateral relative to Bregma. I previously evaluated the

specificity of viral labelling *in vitro* in Chapter II, but I did not have *in vivo* pilot data. Therefore, to evaluate different injection strategies and optimize the injected volume for opto-tagging specifically, I varied the volume of virus injected and number of injection sites across animals (Table 4.1).

To estimate the weight of the implant, I weighed animals before and after the surgery. To keep mice adequately anesthetized, I induced inhalation anaesthesia using 5 % isoflurane / 95 % oxygen, and sustained at 1 – 2 % isoflurane / 98-99 % oxygen throughout the procedure. The oxygen flow was 1 L / minute throughout the procedure. Mice were prepared as follows: the head was shaved (WAHL Pocket Pro Trimmer, Cat.: 34452P) and skin wiped with concentrated Betadine; the eyes were covered with Viscotears; a transparent sterile drape was then used to cover the animal. To expose the skull, I made an incision at the midline from between the eyes to between the ears, removed the skin, and scraped the connective tissue off with a scalpel. To make my injection site accessible, I disconnected the muscles at the left side above the medial entorhinal cortex using a spatula and forceps. To prevent infection, I glued (Vetbond Tissue Adhesive) the sides of the incision to the skull to seal the incision, but leave the skull exposed. I straightened the head using a micropipette to measure depth both medio-laterally and rostro-caudally, and made a craniotomy using a hand drill 3.4 mm lateral from Lambda, on the fissure. For electrical grounding, I drilled two small craniotomies, and implanted M1 x 4 mm screws (AccuGroup SFE-M1-4-A2) on both sides about 3.4 mm lateral, and 1 mm rostral relative to Bregma. Before the last stage of the surgery, I straightened the head again.

Table 4.1. Volume of injected virus and coordinates.

ID	**number of sites**	**injected per site (nl)**	**overall volume (nl)**	**Depth (mm)**
0	3	400	1200	1.8, 2.2, 2.6
1	3	400	1200	1.8, 2.2, 2.6
2	3	400	1200	1.8, 2.2, 2.6
3	4	200	800	1.8, 2.0, 2.2, 2.4
4	4	200	800	1.8, 2.0, 2.2, 2.4
5	3	400	1200	1.8, 2.2, 2.6
6	5	200	1000	1.8, 2.0, 2.2, 2.4, 2.6
7	4	200	800	1.8, 2.0, 2.2, 2.4
8	4	200	800	1.8, 2.0, 2.2, 2.4
9	4	200	800	1.8, 2.0, 2.2, 2.4
10	4	200	800	1.8, 2.0, 2.2, 2.4
11	4	200	800	1.8, 2.0, 2.2, 2.4
12	4	200	800	1.8, 2.0, 2.2, 2.4
13	5	300	1500	1.8, 2.0, 2.2, 2.4, 2.6
14	5	400	2000	1.8, 2.0, 2.2, 2.4, 2.6
15	5	400	2000	1.8, 2.0, 2.2, 2.4, 2.6

To implant the microdrive, I did the following. I attached the microdrive to an Omnetics to Mill-Max adaptor (Axona, HSADPT-NN1) held by a crocodile clip attached to the stereotax. I lowered the tetrodes close to the brain surface around 3.4 mm lateral from Bregma (right hemisphere of two mice, and left hemisphere of 14 mice), between the transverse sinus and fissure, closer to the fissure. I used the stereotax to lower the tetrodes 1.5 mm deep into the brain, targeting the deep medial entorhinal cortex. I sealed the outer cannula with Vaseline by spreading it around the craniotomy, and then lowering the outer cannula to the surface using a forceps. I fixed the implant by putting dental acrylic (Simplex Rapid powder) up to three quarters of the outer cannula, and around the foot of the frame, leaving the grounding screws uncovered. After the cement set, I carefully wrapped the grounding wires around the grounding screws (the reference wire was connected to the right side screw, and the ground wire to the left screw), and fixed the wires with silver paint (RS components 101-5621). After the silver paint dried, I applied another layer of dental acrylic to cover the skull and the grounding screws, but not the insulated part of the grounding wires, or the board, to ensure that the drive is able to move down. I left mice to recover on a heat mat for about 20 minutes, and then I moved them back to the holding room and gave them Vetergesic jelly (0.5 mg / kg of body weight buprenorphine in raspberry jelly) 12 hours after surgery.

During the two days after surgery, I performed health checks at least once a day in addition to the technicians checking on the animals. On these days I did not weigh or handle the animals. After the recovery days, I gave mice a training wheel to encourage active behaviour in addition to their igloo, tissues and chewing sticks.

4.2.5 Open field recording system

I recorded electrophysiology data and performed optogenetic stimulation (see methods described in Chapter III).

4.2.6 Behaviour and timeline of experiment

I allowed mice to recover from surgery for two days. For the following four weeks, I handled mice three times a week for about 5-10 minutes per session and weighed them. To habituate mice to the setup, I allowed them to explore the open field arena for about 5-10 minutes for 3 consecutive days.

For recording sessions, I allowed mice to explore the open field arena until they covered the whole area, or for a maximum of 90 minutes, and recorded extracellular activity. My pilot experiment (data not shown) suggested that animals do not explore more when food deprived and that food rewards can contribute to noise when animals chew it. Animals in this experiment were not rewarded and were only motivated by their natural interest to explore the arena.

At the end of each recording session, I stimulated the neurons by sending 100 pulses of 3 ms duration interleaved by 2 or 5 second intervals using a blue LED to obtain sufficient data for identification of light responsive tTA positive cells (Figure 4.1). I selected the highest light intensity (<=1200 mA with Plexon LED driver). Additionally, I stimulated mice another 100 times, sometimes at a lower light intensity in cases where high intensity stimulation evoked multi-unit responses. Furthermore, during recording from some of the animals, I performed high frequency stimulation. The high frequency stimulation pulses were 50 Hz of 3 ms pulses for 100 ms or 200 ms with 100 ms or 200 ms gaps in between, 5 times.

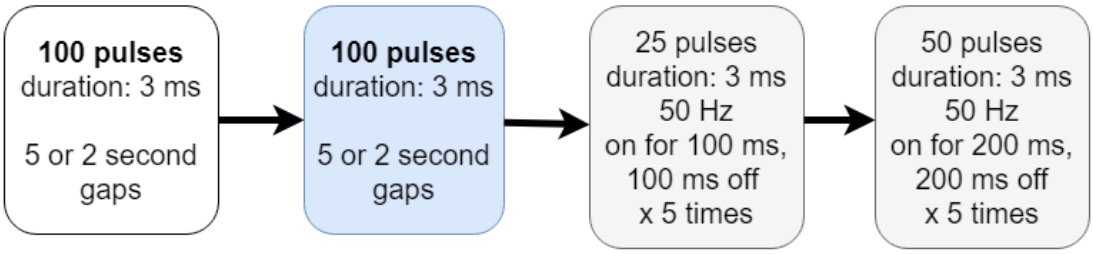

Figure 4.1. Light stimulation protocol. All mice underwent 100 pulses of light stimulation. The following steps of the protocol were introduced as the experiment progressed and were only performed for a subset of the animals. The second optional step was to repeat the 100 pulses using either the same or a lower light intensity. In the last two protocols light stimuli were delivered at 50 Hz. The first one consisted of five trains of twenty-five pulses of duration 3 ms with 100 ms gaps in between each train. The final 50 Hz stimulation was five trains of fifty 3 ms pulses with 200 ms gaps in between.

After the recording session, I performed spike sorting on the data (see methods in Chapter III). To avoid recording from the same location twice, I lowered the tetrodes on the same day by turning the screw on the microdrive by 50 µm. In some cases where there was a multi-unit response, I did not lower the drive and attempted to record the same cells again (Figure 4.2). The first recording day was excluded from the analysis for these recordings.

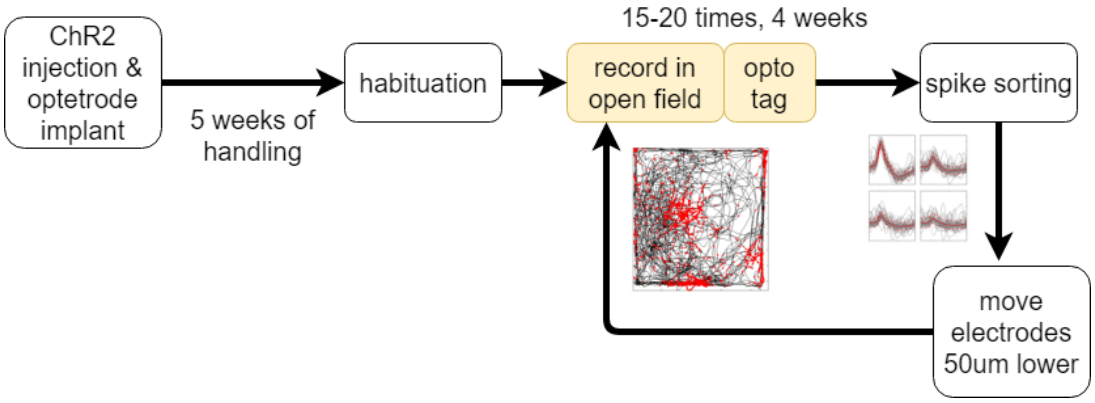

Figure 4.2. Timeline of experiment. AAV9-tre-ChR2-mCherry was injected 5 weeks before the start of the behavioural experiment to allow sufficient expression of the virus. Mice were habituated to the open field arena a week before recordings. In experimental recording sessions, mice were allowed to explore an open field arena for up to 90 minutes or until they covered the whole area while extracellular activity was recorded. At the end of each session, opto-tagging was performed. The data was analysed daily and the microdrive was lowered after spike sorting. I recorded from mice for up to 4 weeks, 15-20 sessions in total per animal.

4.2.7 Histology and imaging

I perfused (see methods in Chapter II) mice after the last recording session either on the same day or within 2 days. Perfused brains were sectioned along the sagittal plane at 50 µm thickness using a freezing microtome. Sections were washed 3 times for 10 minutes in PBS (Sigma Aldrich) and left overnight at 4°C to incubate in rat anti-mCherry antibody (Thermo Fisher M11217, 1:1000 in PBS-Triton (Sigma-Aldrich)). The following day, sections were washed 3 times in PBS for 10 minutes, and then incubated overnight with goat anti-rat Alexa 555 (Thermo Fischer A-21434, 1:1000) and either Neurotrace 640/660 (Thermo Fischer N21483, 1:500) or Neurotrace 435/455 (Thermo Fischer N21479, 1:500) in PBST. Finally, sections were washed three times in PBS and then mounted using Mowiol.

Images were taken on a Zeiss Axio Scan Z1 using a 10x objective. Histology and imaging was performed by Holly Stevens.

4.2.8 Analysis

I did not perform a power calculation before the experiment due to the exploratory nature of my aims. To evaluate and interpret light responses, I needed to quantify the specificity and extent of viral expression. I was blind to the identity of the experimental animals while performing histology analysis.

Quantifying viral expression

To quantify the extent of tre-ChR2-mCherry expression, I selected the section with the highest number of mCherry positive cells for each mouse and counted the cells manually. To assess specificity, I took notes on any off-target expression I observed. Additionally, I counted mCitrine positive cells on the same section.

Spike sorting and identification of light responsive cells

I used the analysis pipeline described in Chapter III to perform spike sorting and the SALT test (Kvitsiani et al. 2013) to determine which cells are light responsive. I accepted cells as responsive that had a p value <= 0.01.

4.3 Results

I recorded neuronal activity in p038 mice that explored an open field arena to obtain the firing fields of deep MEC neurons. I used the opto-tagging strategy outlined above to identify neurons that are tTA positive or that receive input from tTA+ cells. I successfully recorded and isolated single units in 15 out of the 16 animals from 179 recording sessions in total (2 – 16 sessions per animal, mean = 11.19, SD = 4.13 sessions). Three of the animals had broken optic fibres so could not undergo light stimulation. I terminated two animals for health reasons and could not process the tissue. I will first describe light responses that I observed, and then evaluate factors that may have influenced the ability to successfully identify light-responsive units.

4.3.1 Single unit light responses

I evaluated responses to light stimulation in 16 animals and observed single unit responses in 1 animal. From 11 recording sessions recorded from different depths in this animal, I identified light responsive cells five times. Two of the responsive units were from the same session and same tetrode (Figure 4.4 B and C). One of the light responsive units had a response latency shorter than 2 ms which suggests that it was directly modulated by light (Lima et al. 2009). I further identified 4 light responsive cells (out of 27 neurons in total recorded during 11 sessions) in the same animal (Figure 4.4, Table 4.2). No other animal had light responsive single units that were well-isolated (297 isolated neurons from 167 sessions in total). Since this was the first animal I recorded from and the setup was not completely finished, I only recorded position data correctly synchronized with the electrophysiology data for three of the responsive units.

The detected waveforms (Figure 4.3 and Figure 4.4, left panels) of the light responsive neurons were shaped like neuronal action potentials (Bean 2007), similar to the waveforms of the neuron during the open field exploration. The firing autocorrelograms (Figure 4.4, right panel, top plot) of the cells showed a refractory period, further confirming that these neurons were well-isolated from noise and other clusters. Overlaid plots of action potentials of the identified cells differed in amplitudes on different channels of the tetrode, which suggests that none of the neurons were the same cell recorded for a second time on a different session. The position of local maxima on autocorrelograms (Figure 4.4, right panel, bottom plot) of cells A, C, D and

E, but not of B are at theta frequency, which suggest that the firing of A, C, D and E neurons is modulated by theta oscillations (Mitchell and Ranck 1980; Alonso and García-Austt 1987; Dickson et al. 1995).

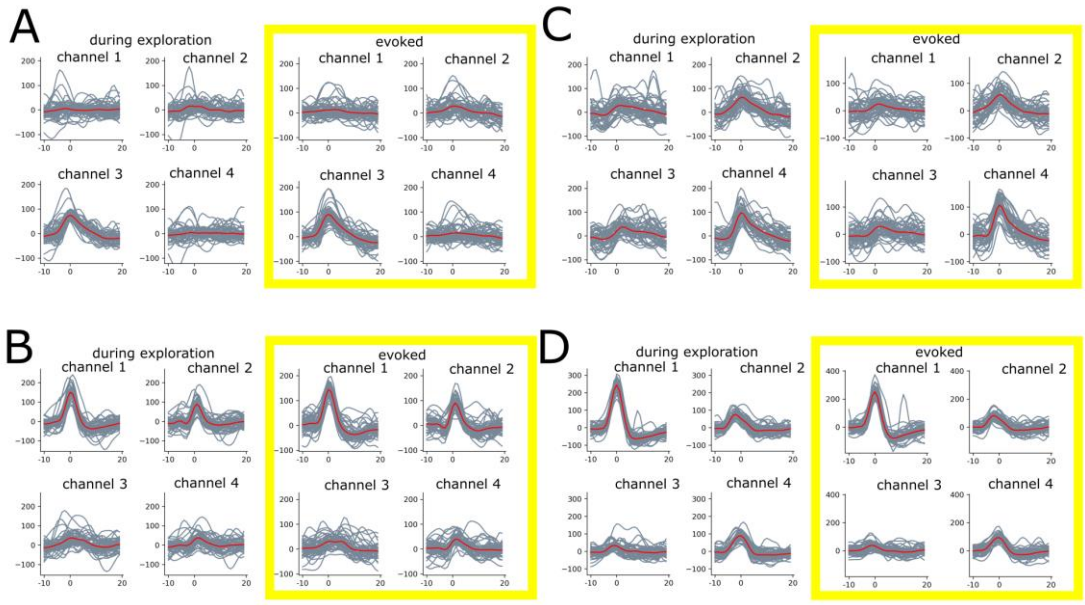

Figure 4.3. Light evoked action potentials were similar to action potentials during open field exploration. Detected spike waveforms for four example cells (A, B, C, D) during open field exploration (left) and light stimulation (right, in yellow rectangles).

To visually assess whether cells were correctly classified as responsive, I made raster plots (Figure 4.4, second panel form left) to show firing events on trials of light stimulation. Light responsive neurons had spikes clustered after the light stimulation (blue band on raster plots) suggesting that they fired as a result of light stimulation. To further illustrate this, I plotted peristimulus time histograms (Figure 4.4, third panel from left) to visualize the distribution of firing frequency around the light stimulation. For four out of five responsive cells (A, C, D, E), peristimulus histograms had one single maximum after the stimulation. The peristimulus histogram of cell B had a local maximum during light stimulation a second maximum shortly after the stimulation ended. The short latencies of the responses suggest that cell B (Figure 4.4 B, Table 4.2 B) is tTA positive (Lima et al. 2009). The other four cells had longer (> 3 ms) latencies, which suggest that they were activated by a stimulated tTA positive cell, possibly *via* multiple synapses (Lima et al. 2009). Light-responsive neurons did not fire upon every stimulation pulse (Table 4.2). Visual inspection of the continuous electrophysiology data during failed trials suggests that lack of firing events on some

trials were not caused by a failure of spike detection (see Appendix A for example cells). I have not identified significant responses to high frequency stimulation in any of the animals.

Table 4.2. Results of SALT test for light responsive cells. All responsive cells were recorded from the same animal, mouse 0 (M0).

cell	p (SALT)	latency (ms)	% of trials when cell responded	mean firing rate (Hz)	max firing rate (Hz)	HD score	spatial coherence
A	< 0.001	3.75	41	4	-	-	-
B	**< 0.001**	**1.25**	**38**	**34**	**41.63**	**0.01**	**97.44**
C	< 0.001	3.25	33	7	10.87	0.02	103.23
D	< 0.001	3.75	80	32	-	-	-
E	< 0.001	3.75	95	35	47.14	0.04	121.81

Two of the recorded neurons, A and C had low firing rates of 4 Hz and 7 Hz, respectively. B, D and E neurons had higher (> 10 Hz) average firing rates (Table 4.2). This suggest that tTA positive cells in p038 mice send information to neurons both with low and high firing rates. Since the curation step of my analysis removed all cells with lower than 0.5 Hz firing rates, the majority of the silent cells in the deep MEC reported previously (Burgalossi, von Heimendahl, and Brecht 2014) were not possible to detect in this experiment. B, C and E cells did not show spatially selective firing or head-direction sensitivity (Figure 4.5) and spatial properties could not be analysed for the remaining two cells.

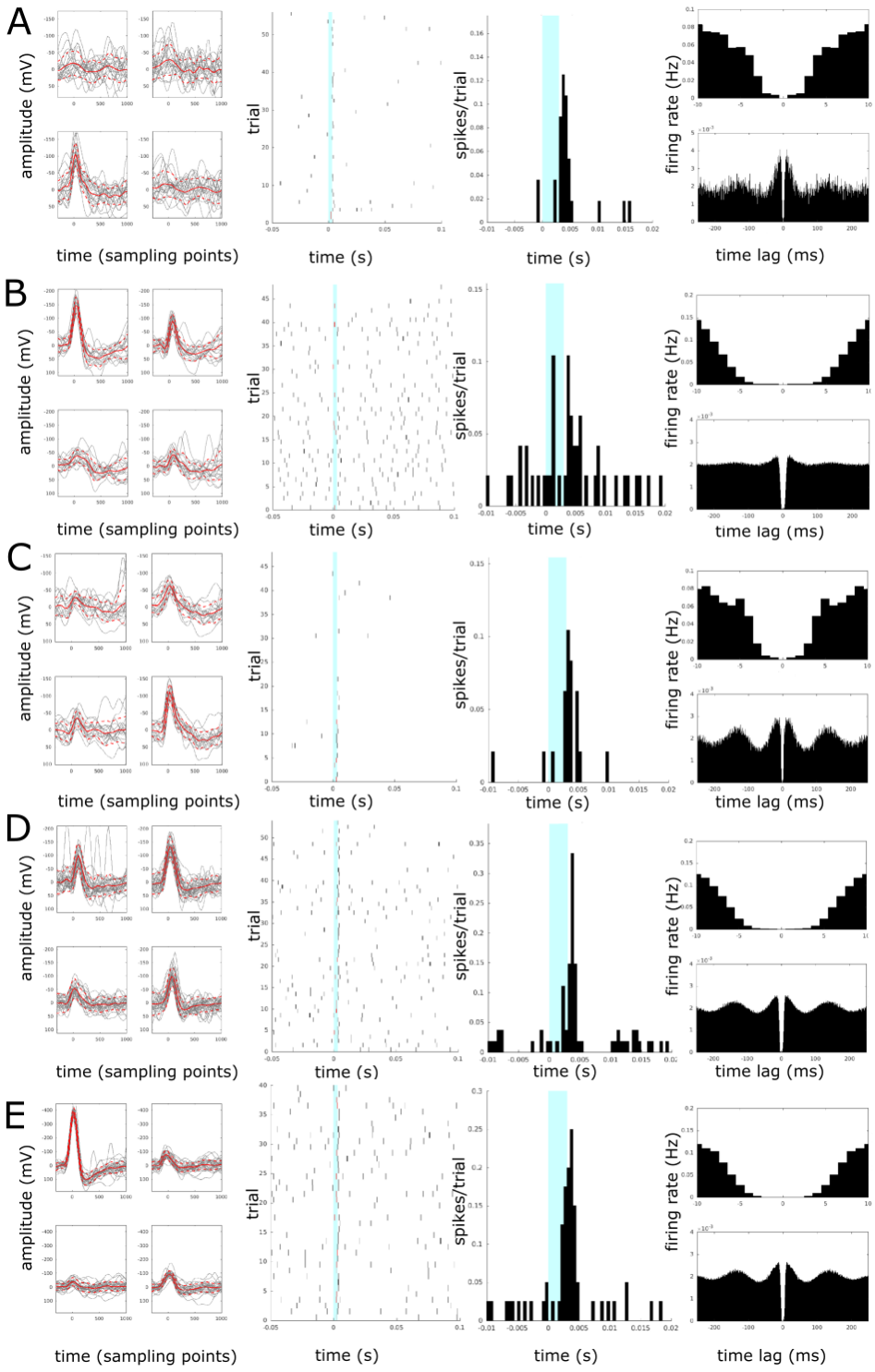

Figure 4.4. Light responsive units recorded from mouse 0. The panels from left to right show: (1) overlaid action potentials from the opto-tagging part of the session for the four channels of the tetrode; (2) a raster plot of action potentials on opto-tagging trials; (3) a histogram of spikes per trial with the blue 3 ms bands showing when the light was on; (4) autocorrelograms of firing. B and C were recorded simultaneously on the same tetrode.

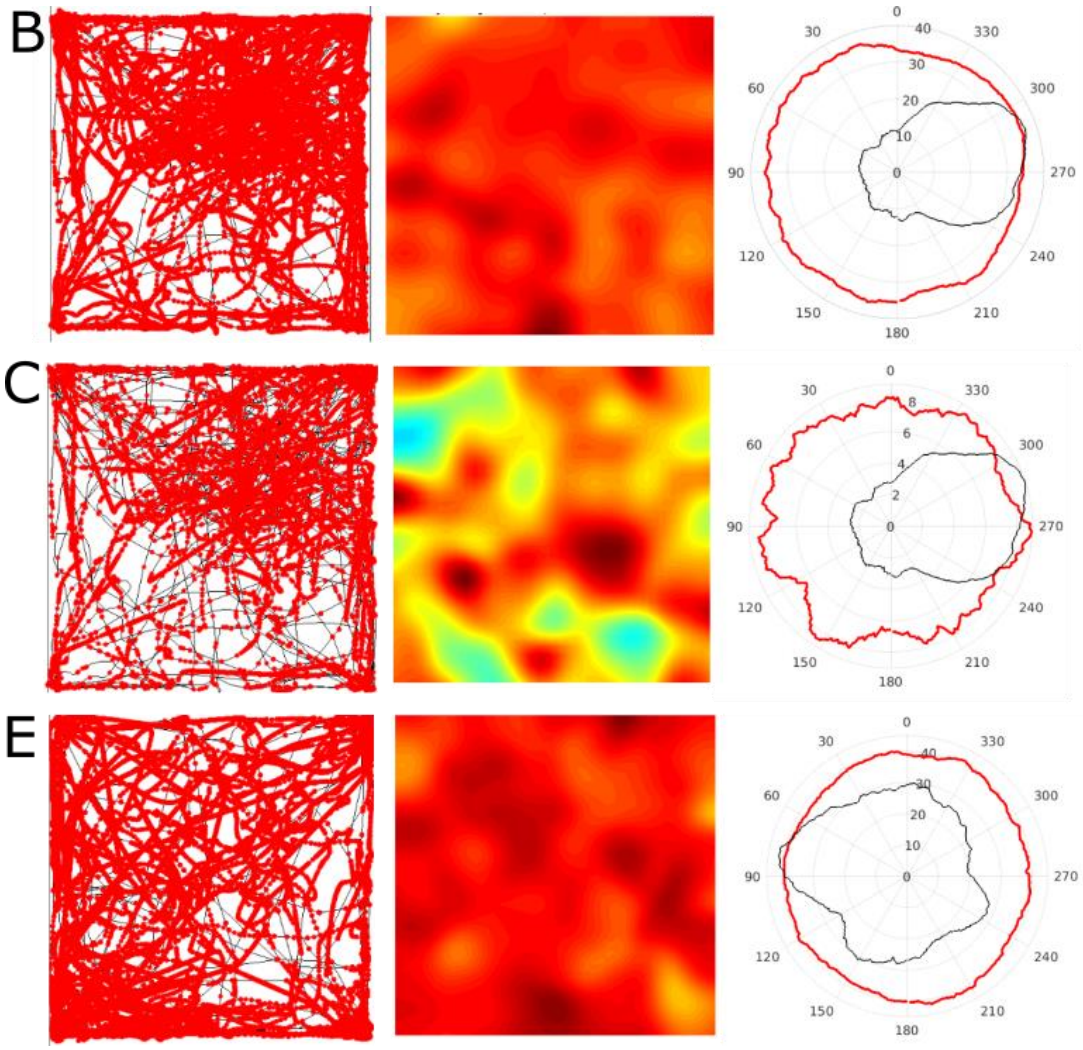

Figure 4.5. Firing properties of cells B, C and E recorded from mouse 0. The identified cells did not have spatially selective firing. The trajectory of the animal is shown as a black line in the open field arena, and the locations where the cell fired are shown as red dots (left panel). The firing rate map (middle) was calculated by summing the number of spikes in each location and dividing that by the time the animal spent there and then smoothing the surface with a Gaussian centred on each location bin (Leutgeb et al. 2007). Blue represents low firing rates and red represents high rates. Head direction plots (right panel) were made by plotting a smoothed (10 degree window) polar histogram of the animal's head direction from the whole session (black, normalized value) and during when the cell fired (red, in Hz).

4.3.2 Multi-unit responses

In addition to single unit responses, I recorded multi-unit responses in further three animals. Raster plots (Figure 4.6 C) and peristimulus histograms (Figure 4.6 D) looked similar to those of the responsive single units, but autocorrelograms (Figure 4.6 B) of these cells showed no refractory period and the overlaid waveforms looked noisy (Figure 4.6 A). These clusters were not well-isolated units and therefore did not pass curation. This was possibly because the recorded neurons were too far away from the tetrode tips, since other non-responsive neurons were isolated from the same animals, suggesting that the noise levels were low enough to detect cells. I also observed multi-unit responses in the animal where I successfully isolated responsive single units.

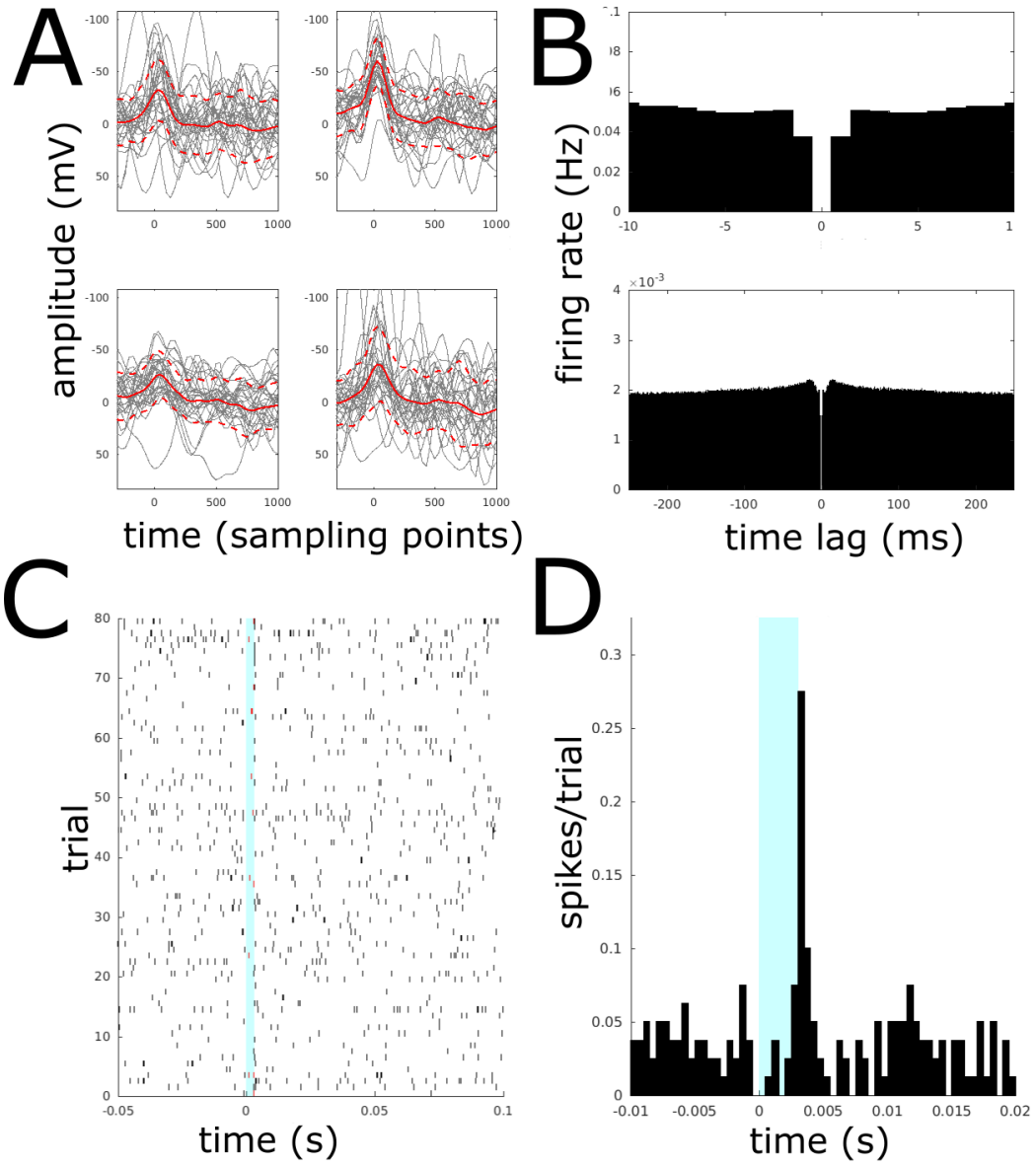

Figure 4.6. Multi-unit response example. The unit shown did not pass sorting quality criteria and is likely noise or a combination of activity from multiple cells that responded to light stimulation. (A) Overlaid waveforms of detected cluster from the opto-tagging part of the recording session for the four channels of the tetrode. (B) Autocorrelograms of firing from the whole session. (C) Raster plot of action potentials on opto-tagging trials. (D) Histogram of spikes per trial with the blue 3 ms bands showing when the light was on.

4.3.3 ChR2 viral expression was low in most animals

To evaluate viral infection in experimental animals, I counted mCherry labelled cells (Table 4.3, Figure 4.7 and Figure 4.8) infected with the AAV9-tre-ChR2-mCherry virus on the slice with the highest number of mCherry labelled cells. Eight out of fourteen analysed animals had no mCherry labelled cells in the MEC. Four of the animals had fewer than 10 mCherry labelled cells and only two mice had more than 10 mCherry labelled cells. The animals with the highest number of labelled cells had mCherry labelled cells over several sections. Three of the animals with little or no mCherry expression in the MEC had mCherry labelled mCitrine negative cells in the hippocampus. The animal in which I recorded single unit responses had the highest number of both mCitrine and mCherry positive cells. In the three animals where I recorded multi-unit responses I found no mCherry labelled cells in the MEC.

Since the numbers of labelled cells were not in line with my expectations based on characterizing the p038 line (Chapter II) and mCitrine expression was visibly variable, I quantified the number of mCitrine positive cells (Table 4.3, Figure 4.7 and Figure 4.8). My previous experiments (Chapter II) suggested that 13 % of Ctip2 positive L5b cells are tTA positive in p038 mice. However, experimental animals in the opto tagging experiment showed a different expression pattern. I found that three of the experimental animals had no or very little mCitrine expression in the MEC, and that only one of the animals had high levels of expression. The number of mCitrine and mCherry labelled cells was correlated (Pearson's correlation coefficient = 0.88, $p = 2.29 * 10^{-5}$).

Table 4.3. Number of mCitrine and mCherry expressing cells in the MEC and light responses recorded. The number of mCitrine labelled cells correlated with the number of mCherry labelled cells. I was able to record single-unit light responses in the animal with the highest number of mCherry labelled cells (mouse 0).

Animal ID	Number of mCitrine positive cells	Number of mCherry positive cells	Light response
0	**556**	**17**	**single unit**
1	96	0	multi-unit
2	92	0	-
3	56	0	multi-unit
4	27	0	-
5	102	0	-
6	67	4	-
7	0	0	-
8	2	1	-
9	1	0	-
12	20	1	-
13	202	5	-
14	223	14	-
15	0	0	multi-unit

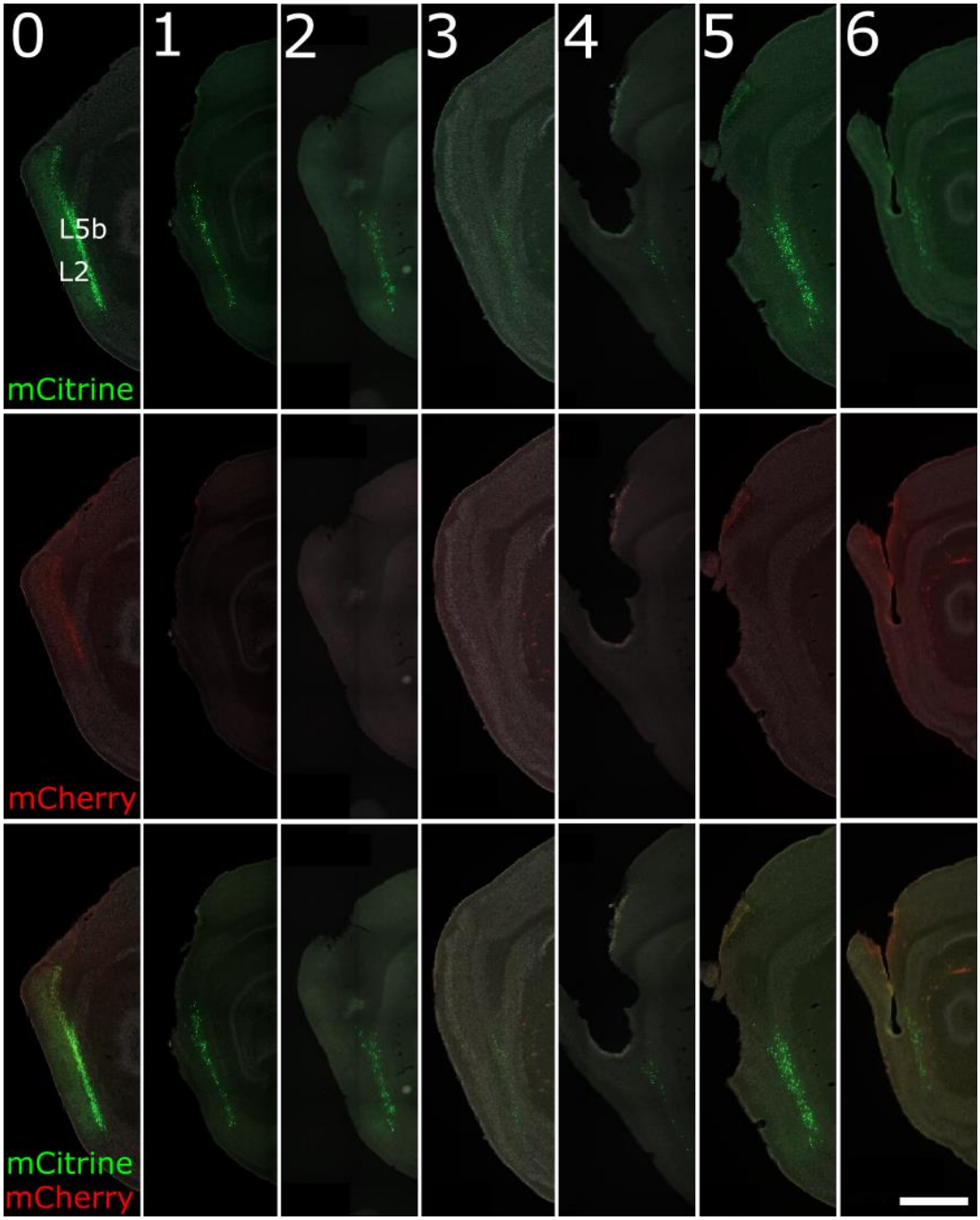

Figure 4.7. Expression of mCitrine and mCherry in the MEC of experimental animals 0 to 6. The number of labelled cells was lower than expected in all animals apart from mouse 0. Endogenous mCitrine expression in p038 positive cells (top), mCherry expression in cells infected with AAV9-tre-ChR2-mCherry (middle) and overlay (bottom) fluorescent image. Sections were stained with Neurotrace and anti-mCherry. Scale bar = 1000 µm.

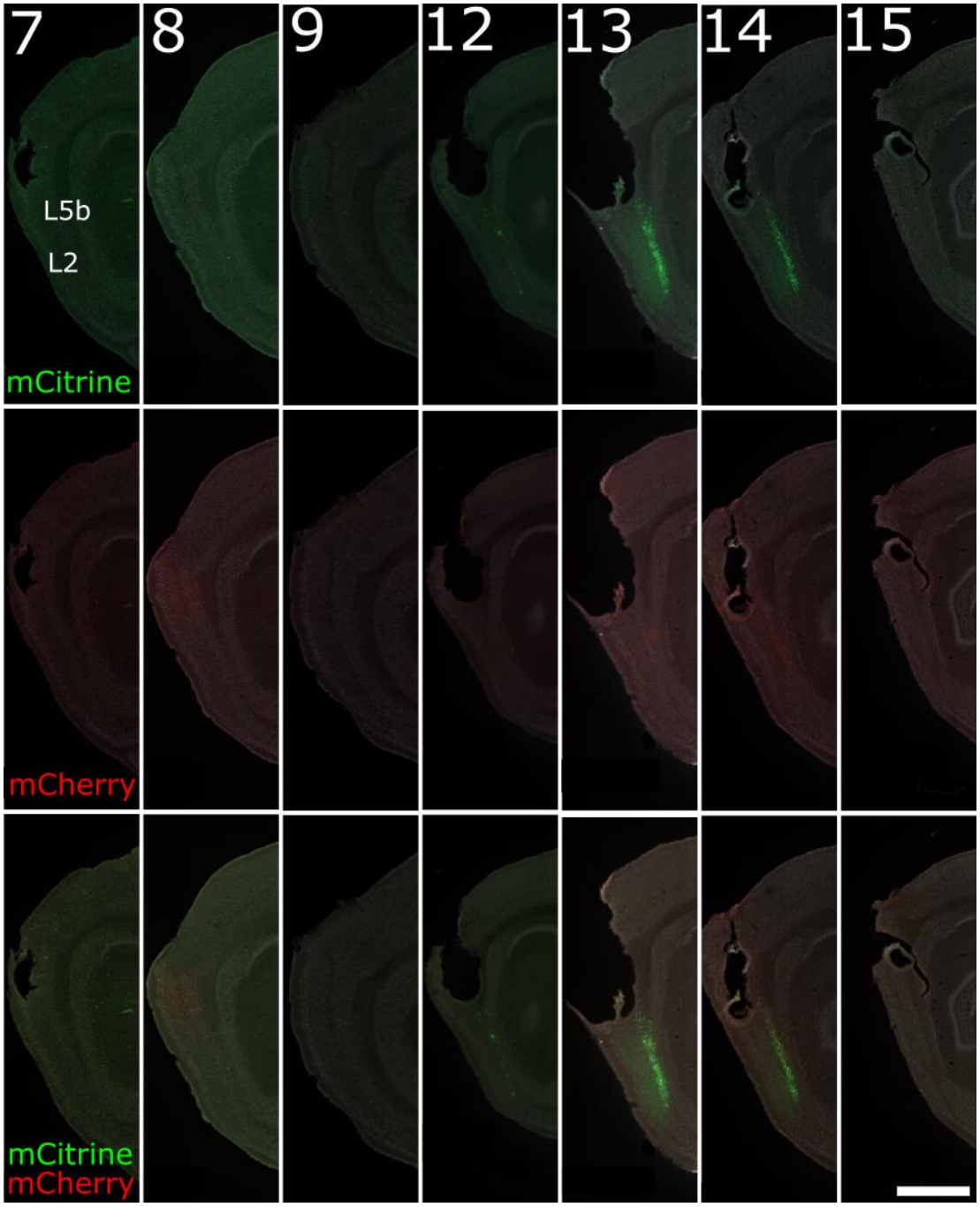

Figure 4.8. Expression of mCitrine and mCherry in the MEC of experimental animals 7, 8, 9, 12, 13, 14 and 15. The number of labelled cells was lower than expected in all animals. Endogenous mCitrine expression in p038 positive cells (top), mCherry expression in cells infected with AAV9-tre-ChR2-mCherry (middle) and overlay (bottom) fluorescent image. Sections were stained with Neurotrace and anti-mCherry. Scale bar = 1000 µm.

4.4 Discussion

The experiments described in this chapter evaluate an optical approach to identification of extracellularly-recorded action potentials fired by layer 5b neurons in freely moving animals. I identified the firing fields of a subpopulation of L5b of the MEC labelled by tTA expression in the p038 mouse line. However, in most animals the tTA expression was unexpectedly low, which resulted in very few light responsive cells. My analysis suggests that more L5b neurons would need to express tTA for successful optical identification, because otherwise the chances of recording from a stimulated tTA positive cell are very low. Furthermore, to identify neurons that are silent or have very low firing rates that were previously reported in the deep MEC (Burgalossi, von Heimendahl, and Brecht 2014), more identification pulses and different sorting strategies might be needed.

4.4.1 Opto-tagging is feasible in p038 mice with ChR2 positive cells

Anatomical characterization of the p038 line (Chapter II) suggested that tTA expression is present in the deep MEC in all p038 positive animals consistently. A possible explanation for the different pattern here, compared to the previous chapter might be that the expression of tTA changed across generations. Loss of expression over generations was not predicted in the p038 line, but variability in between individual animals was reported as well as age related changes in a few other lines (Shima et al. 2016). My previous experiments suggested that 13 % (SD = 3.8, n = 3 mice) of Ctip2 positive L5b cells express tTA in p038 mice (see Chapter II). All but one animal processed in the experiments in this chapter had lower than expected expression with 4 of them having less than 10 cells. Litter mates of animals with low expression used in different *in vitro* patch clamp and immunohistochemistry experiments were found to have high levels of expression, which supports the idea that expression is variable rather than reduced across generations. A possible reason for the variability could be the different housing conditions of the animals in different experiments, for example as a result of doxycycline contamination in the diet of some animals in some of the holding rooms, but not in others.

In mice where mCitrine labelling was present, viral mCherry labelling correlated with the number of mCitrine labelled cells, but the proportion of infected mCitrine labelled cells was very low (less than 10 %). One possibility is that the AAV infected relatively

few cells. This could be addressed by using a different AAV serotype (Shima et al. 2016). Another possibility is that a large proportion of tTA+ cells were infected, but the viral transgene expression was insufficient for fluorescence to be detectable. In experiments where viral expression was detected, mCherry labelling was specific to mCitrine labelled cells in the MEC. However, three animals had mCherry labelling in the hippocampus in mCitrine negative cells. This could be explained by tTA-independent expression when many copies of the Tre construct are injected (Mizuno et al. 2014; P. Zhu et al. 2007; Shima et al. 2016).

In the one animal where I successfully infected tTA positive cells with AAV9-tre-ChR2-mCherry, opto-tagging was successful. I was able to identify one cell with a very short (< 2 ms) latency, which suggests that it was tTA positive. This result suggests that it is possible to identify light responsive tTA positive cells in p038 mice. I identified 4 more light responsive cells that had longer response latencies, suggesting that the activation was indirect, *via* one or more neurons activated by a tTA positive cell. Since the SALT test is not able to distinguish between directly and indirectly activated cells, the above findings are based on the length of the latencies and need to be confirmed by further analyses. A possible way to test which neurons are directly activated could be to analyse the standard deviation of the latencies, since directly activated cells have lower standard deviations. The directly activated cell and one of the longer latency cells were recorded simultaneously on the same tetrode. Since these two clusters were possible to separate and did not overlap in time, this result demonstrated that it is possible to identify two responsive neurons within a tetrode. The recorded light responsive neurons that had correctly recorded position data (n=3) did not show spatially selective or direction selective firing.

In three of the animals (1, 3 and 15) I recorded multi-unit responses, clusters with significant light responses that could not be isolated. I found no AAV-ChR2-mCherry expression in these mice, which suggests that these responses were either caused by photo-electric artefacts (Kozai and Vazquez 2015) or that my histology analysis did not detect all the mCherry signal. Analysing local field potentials could further confirm whether neurons responded to the light stimulation at a population level.

4.4.2 Different approaches to identify L5b cells

Since the success rate of opto-tagging p038 cells is undermined by the variable expression pattern of tTA, I will outline alternative approaches to characterize the firing fields of deep MEC cells.

One approach that does not depend on transgenic lines is to inject a ChR2 virus in CA1 of the hippocampus, an area that projects to L5b cells (Sürmeli et al. 2015) and then stimulate *via* the axon terminals in L5b. Stimulating CA1 axon terminals would make CA1 cells that send input to L5b fire, and 5b cells that are activated by hippocampal input could be identified based on the latency of the response. Characterizing the firing fields of L5b cells as well as downstream MEC cells that receive hippocampal input would be useful for computational models of navigation.

Another possible way to specifically target L5b cells would be to perform juxtacellular recordings (Burgalossi, von Heimendahl, and Brecht 2014; Burgalossi et al. 2011). This would allow the cell to be identified and immunohistochemical staining against Ctip2 could confirm the molecular identity of the recorded cell. The drawback of this approach relative to extracellular recordings is that only one cell per animal could be identified.

Understanding the function and organization of cells in the deep MEC on a population level would require recording multiple neurons simultaneously. A possible way of doing this would be to use calcium imaging (Stosiek et al. 2003) to record neuronal activity in a virtual reality based environment (Gu et al. 2018) or using a miniscope in open field exploration (C. Sun et al. 2015). Such an experiment could use p038 mice to identify the deep MEC and record activity from a part of the deep MEC. However, this approach would likely cause damage either to the superficial entorhinal cortex, or to the perirhinal cortex and parasubiculum, which would confound the results.

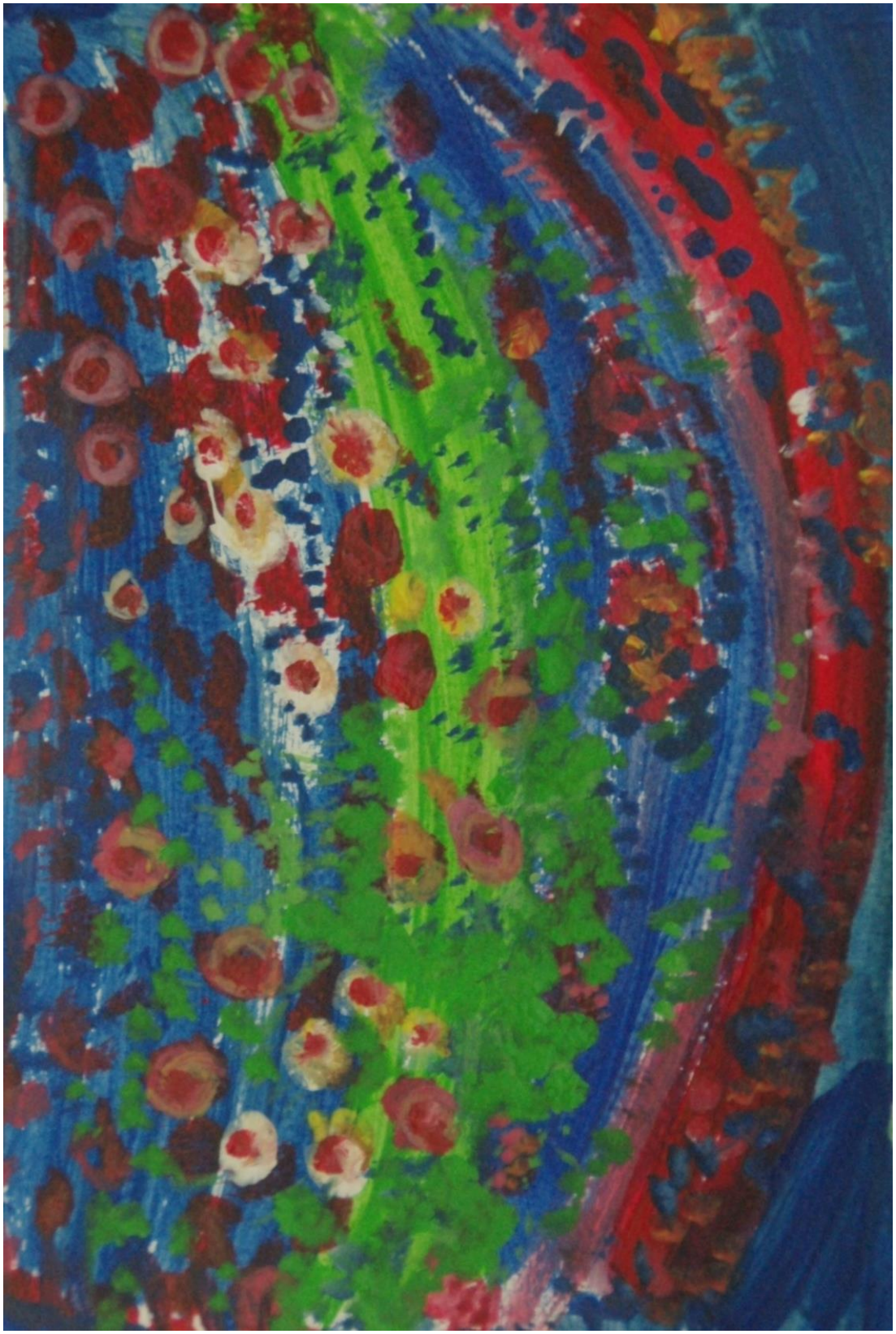

Medial entorhinal ‘rainbow’ by Komáromy Pongó Terézia and Klára Gerlei.

Chapter V

5 Firing properties of neurons of the mouse medial entorhinal cortex

5.1 Introduction

What role do L5b neurons play in spatial computation? A possible approach to address this question is to consider the position of L5b in the spatial circuitry (Figure 5.1). L5b neurons receive projections from CA1 of the hippocampus (Sürmeli et al. 2015), a brain region thought to represent the location of the animal (Wilson and McNaughton 1993). In addition to projections from the hippocampus, L5b receives input from L2 of the MEC from stellate cells (Sürmeli et al. 2015), the group of cells that have the highest proportion of grid cells among them (Gu et al. 2018). Further, the deep MEC was shown to receive input from the retrosplenial cortex (Ohara et al. 2018), a region that has head-direction cells and cells that can represent multiple head-directions depending on context (Jacob et al. 2017). L5b sends projections to L5a of the MEC (Ohara et al. 2018), a layer that sends entorhinal output to multiple regions of the telencephalon (Sürmeli et al. 2015). Further, the loop is closed by L5b projections targeting the superficial layers of the MEC (Ohara et al. 2018). A possible prediction based on the input L5b receives from areas rich in spatial selectivity is that L5b neurons integrate location, head-direction and grid input, and forward the processed information to the telencephalon *via* L5a, and update the superficial MEC using this integrated signal (Figure 5.1). An alternative hypothesis could be that L5b relays information from its input areas to the superficial MEC where it is integrated. A possible way to address these hypotheses is to record neuronal activity in L5b in behaving animals.

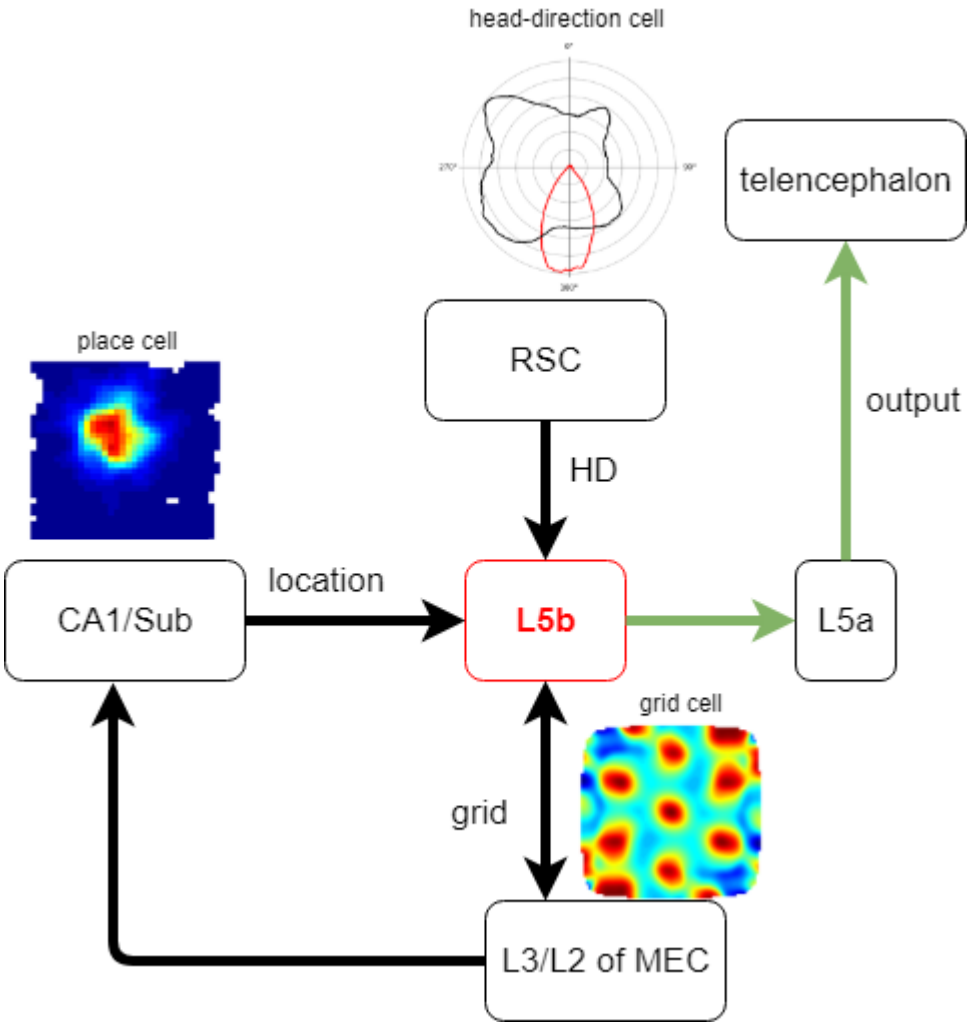

Figure 5.1. L5b neurons are well-placed to integrate location, grid and head-direction information. L5b of the MEC receives input from cornu ammonis 1 (CA1) of the hippocampus, subiculum (Sub), superficial MEC (Sürmeli et al. 2015) and retrosplenial cortex (RSC) (Ohara et al. 2018). L5b neurons project to the superficial layers of the MEC and to L5a of the MEC (Ohara et al. 2018). L5a neurons send information to the telencephalon (Sürmeli et al. 2015). L5b cells may receive location information from place cells (rate map by Brianna Vandrey), head-direction input from the RSC, and grid input from the superficial MEC.

Firing properties of neurons from deep layers of the MEC were previously investigated *in vivo* by recording extracellular activity in rats (Sargolini et al. 2006) and by juxtacellular recordings (Burgalossi, von Heimendahl, and Brecht 2014). Extracellular recordings (Sargolini et al. 2006) suggest that there are spatially selective cells in the deep MEC that are active during open field exploration. Notably, a group of these spatially selective cells, conjunctive cells, have grid and head-direction properties simultaneously, supporting the idea that head-direction and grid properties are integrated in the deep MEC. Results from juxtacellular recordings (Burgalossi, von

Heimendahl, and Brecht 2014) are not in full agreement with this and suggest that deep MEC cells have relatively low firing rates and are not very active. Overall, these results support the idea that the deep MEC plays a role in spatial cognition, but do not reveal specific coding mechanisms.

Could the integrated head-direction and location information be coded within the firing fields of cells? Some models suggest that grid cells might be formed as a combined weighted output of place cell firing (Dordek et al. 2016; Kropff and Treves 2008). A recent study found evidence to support this hypothesis by analysing firing rates of individual firing fields in grid cells. Different grid fields were found to have different firing rates, suggesting that they might code local positional information (Ismakov et al. 2017). Further, it is possible that the different firing rates in the fields are a consequence of increasing projection strength from place cells to grid cells in given regions of the environment. Cells with head-direction sensitivity, such as conjunctive cells of the deep MEC were excluded from these previous analyses and only firing rate was investigated in the fields. Interestingly, depolarizing stellate cells in the superficial MEC using excitatory DREADDs caused hippocampal (CA1) place fields to remap as well as the firing rates to change differentially within grid fields, while the position of the fields remained stable (Kanter et al. 2017).

Given that L5b might integrate grid, place and head-direction input, I reasoned that it would be important to investigate signatures of each signal in the firing of L5b neurons. I was particularly interested to ask if regions of the firing fields of deep layer neurons differ in their spatial or head direction properties. This was partly motivated by the idea that the head-direction system might have an effect on grid firing similar to how place cells might be modulating the firing rate in individual firing fields (Ismakov et al. 2017). This idea is further supported by a recent study that found cells in the retrosplenial cortex that have multiple head-direction preferences depending on the position of the animal in the arena and on context (Jacob et al. 2017). Since the part of the retrosplenial cortex where the bidirectional head-direction cells were found projects to the deep MEC (Sugar et al. 2011), it is possible that deep MEC grid cells could inherit this firing property and have different head-direction modulated firing in different parts of the environment.

My first aim in this chapter was to replicate analyses from the studies above (Sargolini et al. 2006; Burgalossi, von Heimendahl, and Brecht 2014) and investigate whether

their results apply to my extracellular data from the mouse. To achieve this, I identified the locations in the brain I recorded from based on tissue damage and compared firing rates and grid and head-direction properties in deep and superficial layers of the MEC. My second aim was to test whether different regions of firing fields of deep and superficial neurons differ in their spatial and head-direction properties. To perform these analyses I implemented scripts to detect firing fields and analysed head-direction within individual firing fields.

5.2 Methods

The acquisition and basic analysis of the data presented in this chapter is described in Chapters III and IV. The recordings presented in this chapter are from the same experiment that is described in Chapter IV. Briefly, I implanted 16 channel optetrodes (4 tetrodes and optic fibre) in mice targeting the deep MEC and recorded extracellular neuronal activity in an open field arena. I performed automated spike sorting using MountainSort (J. E. Chung et al. 2017) to identify single neurons. I analysed the firing properties of well isolated neurons using scripts described in Chapter III. The first half of the chapter (up to 'Is head-direction selectivity spatially organized?') uses the MATLAB version of the post-processing scripts, and the second half uses the Python implementation (please see Chapter III for more information). This is because although the Python version does not completely replicate the MATLAB version yet, it contains analysis code not implemented previously. In this section, I will detail additional analyses that I did not perform in previous chapters.

5.2.1 Identifying final recording locations

I implanted tetrodes to be above the deep MEC before the recording sessions (Table 5.1). After each recording I lowered the tetrodes by 50 µm using the drive mechanism on the implant. The intended track of the tetrodes was perpendicular to the straightened skull surface. However, histology results suggest that this was not precisely achieved, and some implants entered the brain at different angles (Table 5.1). Consequently, some animals had the tetrodes in the deep MEC at the beginning of the experiment and in the superficial MEC at the end. After the last recording day before perfusing the mice, I applied a current to burn the tissue at the tip of the electrodes (see methods in Chapter III). I identified the final position of the recording

electrodes by visually assessing the burn and physical damage on the tissue. Importantly, implants had the four tetrodes arranged on four sides of the optic fibre. Tetrodes were never in one bundle, making layer specific location identification impossible. This is because different tetrodes of the same drive could have been in different layers, and the identity of individual tetrodes corresponding to the electrophysiology signal is not possible to know. I classified recording sites to be in the deep MEC, superficial MEC, parasubiculum or not possible to determine, based on where the majority of the tissue damage was located. I was blind to the identity of the animals while performing this analysis.

Table 5.1. Estimated position of tips of recording electrodes at the beginning and end of experiments and estimated recording sites in deep and superficial layers of the MEC. Estimated angles are relative to the straightened skull and are based on histology images (see Appendix B for all animals).

animal ID	implanted depth (mm)	final location (mm)	distance travelled (mm)	estimated angle	recording site
0	1.6	2.15	0.55	90	**deep**
1	1.8	2.3	0.5	100	not in MEC
2	1.4	2	0.6	90	not in MEC
3	1.6	2.3	0.7	100	parasubiculum
4	1.5	2	0.5	90	parasubiculum
5	1.6	2.3	0.7	100	**superficial**
6	1.5	2.3	0.8	90	**deep**
7	1.5	1.7	0.2	110	**superficial**
8	1.5	2.3	0.8	100	**superficial**
9	1.5	2.3	0.8	90	not in MEC
12	1.5	2.3	0.8	90	**deep**
13	1.5	2.15	0.65	90	**superficial**
14	1.5	2.2	0.7	90	**superficial**
15	1.5	2	0.5	80	**deep**

5.2.2 Classification of cell types

To identify spatially selective cells, such as head-direction cells, grid cells and conjunctive cells, I calculated grid and head-direction scores. To quantify location-dependent firing, I calculated spatial information scores.

Spatially selective neurons that fire depending on the location of the animal can be described by calculating the amount of information about the location of the animal encoded in each spike. Spatial information scores were calculated the following way (Skaggs, McNaughton, and Gothard 1993; Markus et al. 1994):

$$information\ content = \sum P_i(R_i/R)log_2(R_i/R)$$

Where ***i*** is the bin number, $\boldsymbol{P_i}$ is the probability that the animal is in bin ***i***, $\boldsymbol{R_i}$ is the mean firing rate in bin ***i*** and ***R*** is the overall mean firing rate.

Grid scores (Figure 5.2) were defined as the difference between the minimum correlation coefficient for rate map autocorrelogram rotations of 60 and 120 degrees and the maximum correlation coefficient for autocorrelogram rotations of 30, 90 and 150 degrees (Julija Krupic et al. 2015). Grid scores can have values between -2 and 2. Autocorrelograms were calculated by shifting the binned firing rate map (Leutgeb et al. 2007) into every possible binned position along both horizontal and vertical axes and calculating correlation scores for each of these positions. This rate map was then converted into a binary array using a 20 % threshold on normalized data. If the binary array had more than 7 local maxima, a grid score was calculated. Subsequent parts of the analysis, where correlations between the rotated autocorrelograms were calculated, only included the ring containing 6 local maxima closest to the centre of the binary array, excluding the maximum at the centre. The ring was detected based on the average distance of the 6 fields near the centre of the autocorrelogram (middle border = 1.25* average distance, outer border = 0.25 * average distance).

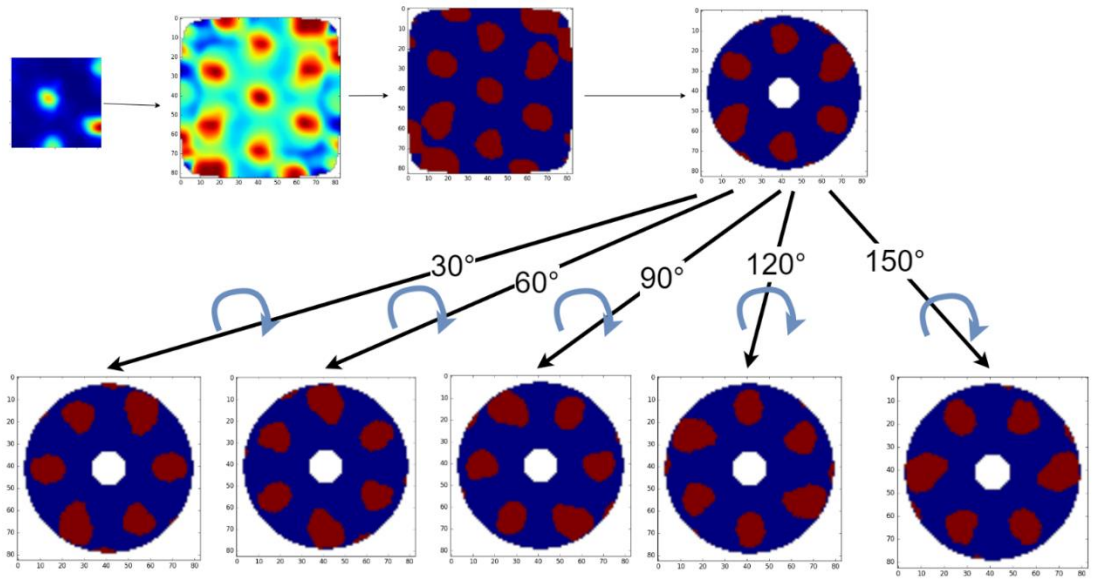

Figure 5.2. Grid score. To obtain grid scores, firing rate maps' autocorrelograms are calculated. Autocorrelograms are converted to binary arrays using a 20 % threshold. Local maxima are identified on the binary maps and used to cut out the inner ring of six fields, excluding the centre. The ring is then rotated by 30, 60, 90, 120 and 150 degrees, and the rotated rings are correlated to the original ring. Grid scores are defines as the difference between the lowest correlation coefficient for rate map autocorrelogram rotations of 60 and 120 degrees and the maximum correlation coefficient for autocorrelogram rotations 30, 90 and 150 degrees (Julija Krupic et al. 2015).

Grid cells are defined in literature as cells whose grid scores are higher than the 95th percentile of a distribution of grid scores for shuffled data from a population of recorded cells (Julija Krupic et al. 2015; Rowland et al. 2018). Since I did not perform analyses on firing data combined from multiple recordings, in this chapter I defined grid cells as cells with a grid score ≥ 0.4.

Head-direction cells were categorized based on head-direction scores (Figure 5.3). To calculate head-direction scores, the head-direction angles corresponding to the firing events of a neuron were first binned into 360 bins between 0 and 2π. The obtained polar histogram was smoothed by calculating a rolling sum over a 10 degree window. Head-direction scores were calculated based on the smoothed polar histogram. Head-direction scores could vary between 0 and 1. To calculate the head-direction score, for angles between -179 and 180 degrees in steps of 1 degree, ***dx*** and ***dy*** was calculated in a unit circle (radius = 1).

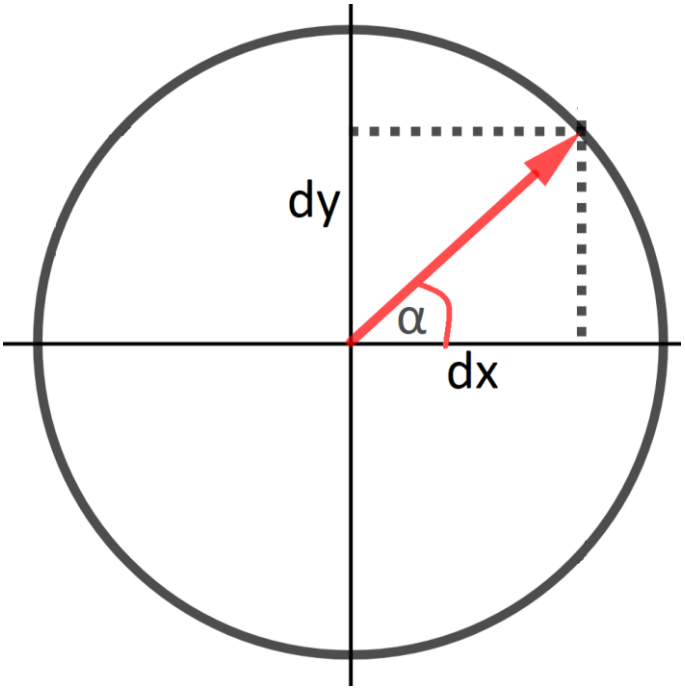

Figure 5.3. Head-direction score. Unit circle with the head-direction vector. The length of the head-direction vector can be obtained based on dx and dy components.

$$dy = \frac{\sin(angle)}{radius}$$

$$dx = \frac{\cos(angle)}{radius}$$

To obtain the x and y components of the head-direction vector, the head-direction polar histogram was multiplied by the ***dx*** and ***dy*** values, respectively, and normalized to the number of observations in the polar head-direction histogram.

$$x_{total} = \frac{\sum(dx \cdot HD_{histogram})}{\sum HD_{histogram}}$$

$$y_{total} = \frac{\sum(dy \cdot HD_{histogram})}{\sum HD_{histogram}}$$

The head-direction score was then calculated using the Pythagorean theorem.

$$hd_{score} = \sqrt{({x_{total}}^2 + {y_{total}}^2)}$$

Head-direction cells can be defined based on shuffled data from the whole population similar to grid cells (Rowland et al. 2018). Similarly to how I defined grid cells in this

chapter, since I did not perform analyses on data combined from multiple recordings, I defined head-direction cells as cells with a head-direction score ≥ 0.5. I defined conjunctive cells as cells that passed both head-direction and grid cell criteria.

I defined putative interneurons and excitatory neurons based on their average firing rates. I categorized cells as excitatory if their firing rate was lower than or equal to 10 Hz, and categorized them as interneurons otherwise (Buetfering, Allen, and Monyer 2014).

5.2.3 Identification and analysis of individual fields

I identified local maxima 'firing fields' on firing rate maps by analysing binned firing rates using methods similar to those used previously to detect place fields (Harvey et al. 2009). The one square meter open field arena was divided into 42 times 42 bins for this analysis, where each bin contained a smoothed firing rate value (please see Chapter III for methods). Smoothed firing rate values were calculated by summing the number of spikes at the locations corresponding to each bin, dividing this by the time the animal spent in the bin and then smoothing the surface with a Gaussian ($e^{\frac{-x^2}{2}}$) centred on each location bin (Leutgeb et al. 2007). I next identified the bin of the rate map with the highest firing rate. If the rate was higher than the average firing rate plus the standard deviation of the rest of the rate map, I collected the bins in the neighbourhood of the bin that had a firing rate higher than 20 % of the local field maximum (bin > local maximum * 0.2). I defined neighbour bins as bins either directly above, below, or next to a bin that is part of the field, and did not include bins as neighbours that only had adjacent corners. I recursively added the whole neighbourhood to the field. I accepted a detected field if it had more than 45 bins, but it was smaller than half of the arena. After successfully detecting a field, I removed it from the rate map by replacing the values with zeros and repeated the analysis to find more fields. I repeated this until I found no more fields.

I saved the detected rate map bin indices for each identified field and extracted the corresponding head-direction data. For head-direction analysis, I compared the distribution of head-directions when the cell fired to the distribution of head-directions when the mouse was in the analysed field. To evaluate whether head direction when the cell fired differed from the head direction of the animal during the time spent in the

field, I performed Watson's two sample test (Fernández-Durán and Domínguez 2010) for homogeneity on the two distributions.

5.3 Results

In the first part of this section, I will present analyses that compare my dataset to those recorded from rats in previous studies (Sargolini et al. 2006; Burgalossi, von Heimendahl, and Brecht 2014). I recorded spatially selective cells in both deep and superficial layers of the MEC of mice and performed analyses to compare head-direction and grid properties as well as firing rates in deep and superficial layers. In the second part, I will present new analyses of intrinsic head-direction sensitivity in grid and conjunctive cells.

5.3.1 Classification of recording locations

In total I recorded 324 units from 15 animals across 179 recording sessions (2 – 16 sessions per animal, mean = 11.19, SD = 4.13 sessions). Comparing firing properties of the deep and superficial layers of the MEC required the recordings to be classified based on the location of the tetrode tips. I visually assessed images of the brains and found that the burned area that marked the recording site was located in the deep MEC in four animals (4, 6, 12 and 15), in the superficial MEC in five animals (5, 7, 8, 13 and 14) and was not in the MEC or could not be ascertained for the rest (Table 5.1.). In mice that I classified to be superficial, it is possible that the tetrodes were in the deep layers at the beginning of the experiment (especially in 7 and 8), due to the angle the tetrodes were implanted at. Animals identified as deep MEC recordings may include recordings from the parasubiculum from the beginning of the experiment and potentially from the superficial MEC on later sessions after some of the electrodes crossed the deep MEC if the recording electrodes were not perpendicular to the brain surface when implanted (see methods for classification). I was not able to classify recordings to specific layers of the MEC due to the extent of the damage and the arrangement of tetrodes in the microdrive (see example on Figure 5.4. and all images in Appendix B). The following analyses where deep and superficial layers are compared are based only on the animals where I successfully identified the recording location.

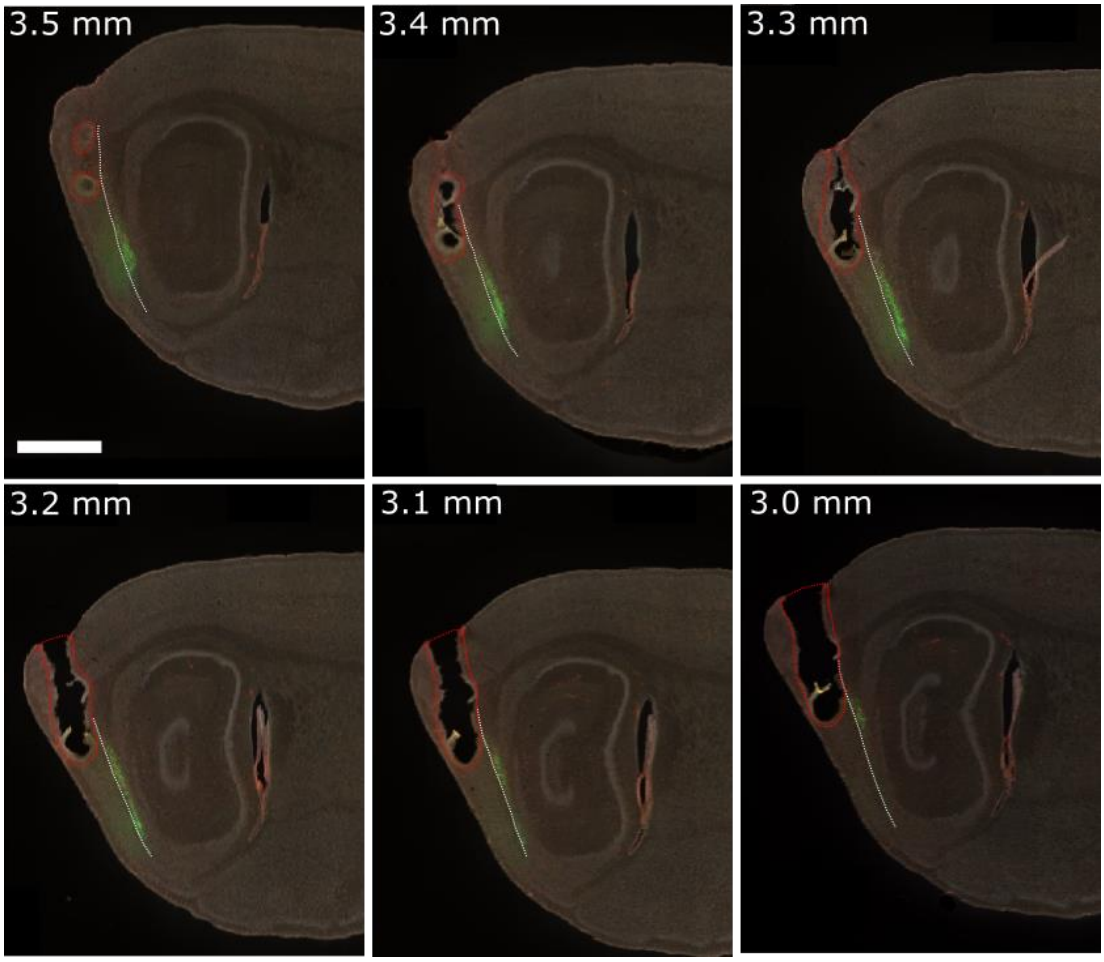

Figure 5.4. Identifying the location of the tetrodes based on the burn holes and damage (animal 14). Sagittal brain sections were stained with Neurotrace and anti-mCherry and imaged using a Zeiss Axio Scan Z1 with a 10x objective, scale bar = 1000 µm. Histology and imaging was performed by Holly Stevens. White dashed lines indicate the border between deep and superficial layers of the MEC. Damage from the recording electrodes and optic fibre are marked with red lines. The recordings from this mouse are identified to be from the superficial MEC. The approximate mediolateral position of the slices relative to the midline is shown in the top left corners.

5.3.2 Firing rates of superficial and deep MEC cells

Juxtacellular recordings from rats found that the average firing rate is lower in the deep MEC relative to superficial layers (Burgalossi, von Heimendahl, and Brecht 2014). To test whether this is the case for my dataset, I calculated average firing rates for the animals where I identified the recording locations. The average firing rate in the deep MEC was 16.9 Hz (sd = 17.5, n = 81 cells) and 13.9 Hz (sd = 17.6, n = 140 cells) in the more superficial recordings (Figure 5.5A). Therefore, I found no significant difference (two-tailed t-test, p=0.2224) between the firing rates of deep and superficial layer neurons. My results from this analysis do not agree with findings from Burgalossi et al (2014), which suggest that deep MEC cells have lower firing rates. A possible reason for this difference is that my dataset included interneurons (Figure 5.5B).

To test whether the difference in results was due to putative interneurons included in the dataset, I repeated the analysis on putative excitatory neurons (Figure 5.5C, firing rate ≤ 10 Hz) and putative interneurons (Figure 5.5D, firing rate > 10 Hz) separately. For putative excitatory neurons, the average firing rate in the deep MEC was 5.2 Hz (sd = 2.3, n = 44 cells) and 4.3 Hz (sd = 2.3, n = 95 cells) in the superficial MEC. The firing rate of neurons in the deep MEC was significantly higher (two-tailed t-test, p=0.03). For putative interneurons, the average firing rate in the deep MEC was 30.8 Hz (sd = 17, n = 37 cells) and 34.1 Hz (sd = 18.9 n = 45 cells) in superficial layers, which is not significantly different (two-tailed t-test, p=0.38). Since separate analysis of excitatory cells showed that firing rates are significantly higher in the deep layers of the MEC relative to superficial layers, I conclude that my results are not in agreement with results from Burgalossi et al (2014), but appear consistent with data from Sargolini et al. (2006). A possible reason for this could be that I was not able to detect neurons with firing rates lower than 0.5 Hz, and therefore would have missed the majority of deep MEC cells reported by Burgalossi et al.

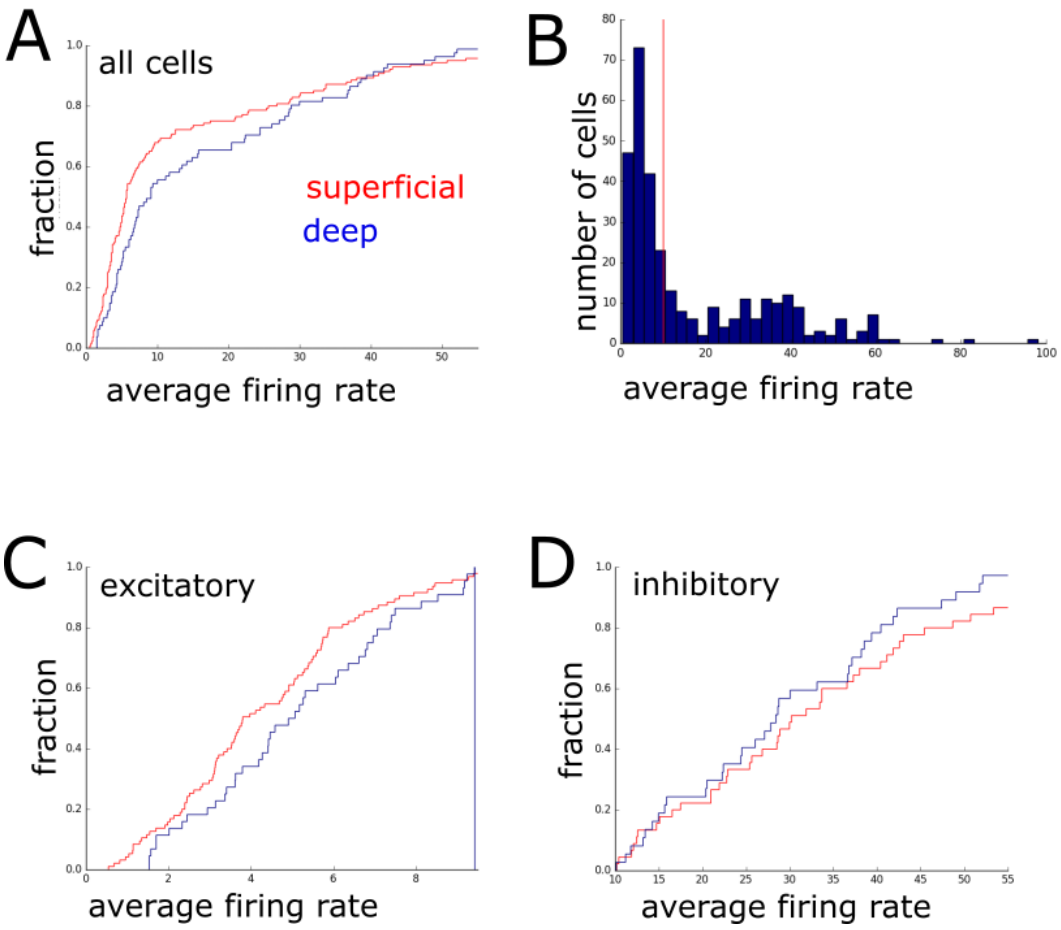

Figure 5.5. Histograms of firing rates in deep (blue) and superficial (red) layers of the MEC. Firing rates of neurons are higher in the deep layers of the MEC of mice relative to superficial layers. (A) Cumulative histograms were generated using 81 neurons from the deep MEC and 140 neurons from the superficial MEC. (B) Histogram of firing rates of all cells shows bimodal distribution. I split data at 10 Hz (red line) for further analysis. (C) Putative excitatory cells from (A) (firing rate ≤ 10 Hz). D. Putative interneurons from (A) (firing rate > 10 Hz).

5.3.3 Grid and head-direction properties of recorded cells in deep and superficial layers

Spatially selective neurons, neurons with firing properties that depend on the position or orientation of the animal, were present in my recordings both in deep layers of the MEC (Figure 5.6) and in superficial layers (Figure 5.7) as previously reported by Sargolini et al. (2006). Recorded cell types included head-direction, grid, conjunctive and border cells. To compare the recorded population of cells to the dataset published by Sargolini et al. (2006), I set out to evaluate grid and head-direction properties for cells in deep and superficial layers.

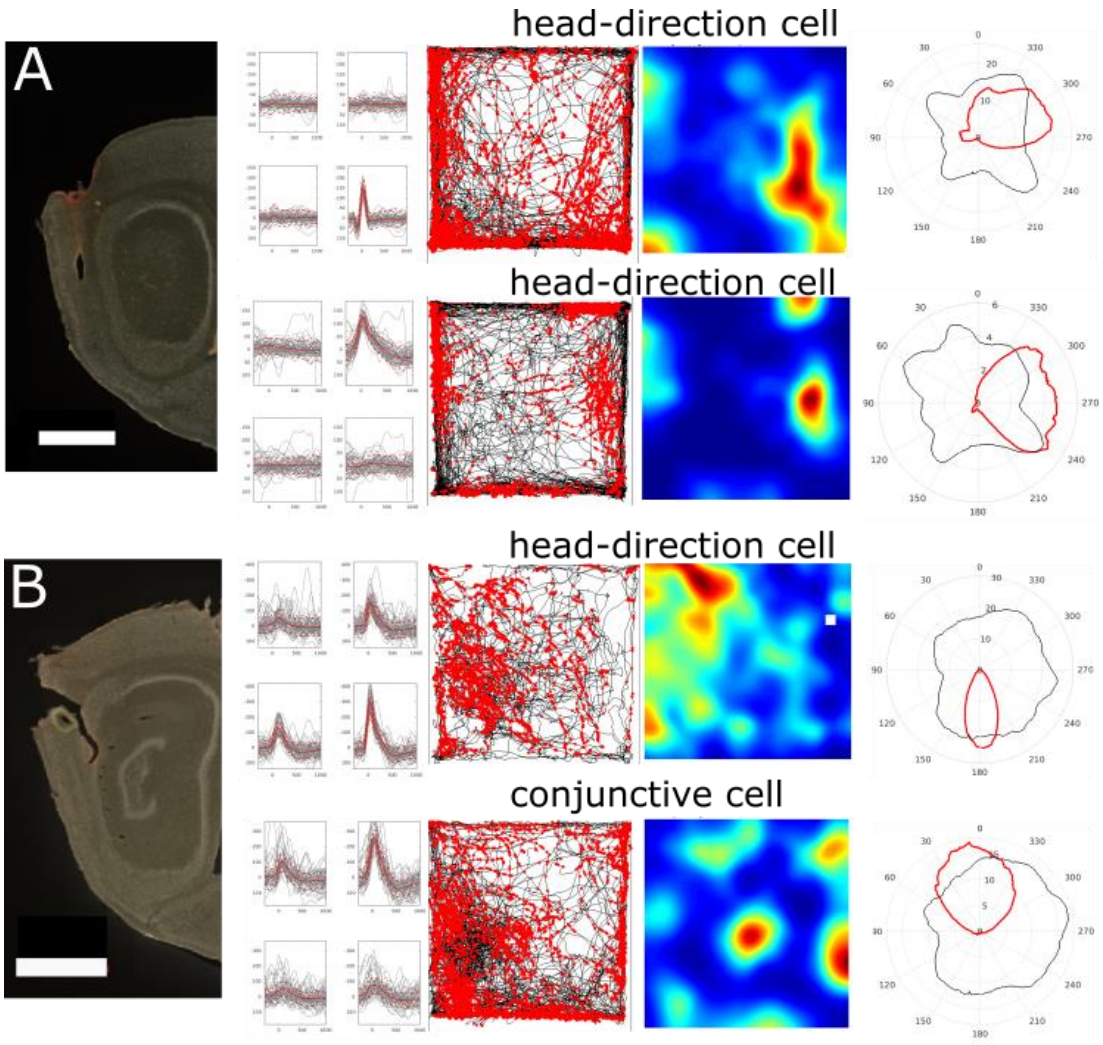

Figure 5.6. Example spatially selective cells recorded from the deep MEC (animals 6 and 15). The examples (top to bottom) include three head-direction cells and a conjunctive cell. Sagittal section of the brain stained with Neurotrace; overlaid waveforms when the cell fired on the four channels of the tetrode, scale bar = 1000 µm; the trajectory of the animal (black) and firing events (red); firing rate map (blue=low firing rate, red=high firing rate) calculated by summing the number of spikes in each location and dividing that by the time the animal spent there and then smoothing the surface with a Gaussian centred on each location bin (Leutgeb et al. 2007); polar head direction histogram generated by plotting a smoothed (10 degree window) polar histogram of the animal's head direction from the whole session (black, normalized value) and during when the cell fired (red, in Hz) normalized to the time spent in the field. Histology and imaging was performed by Holly Stevens.

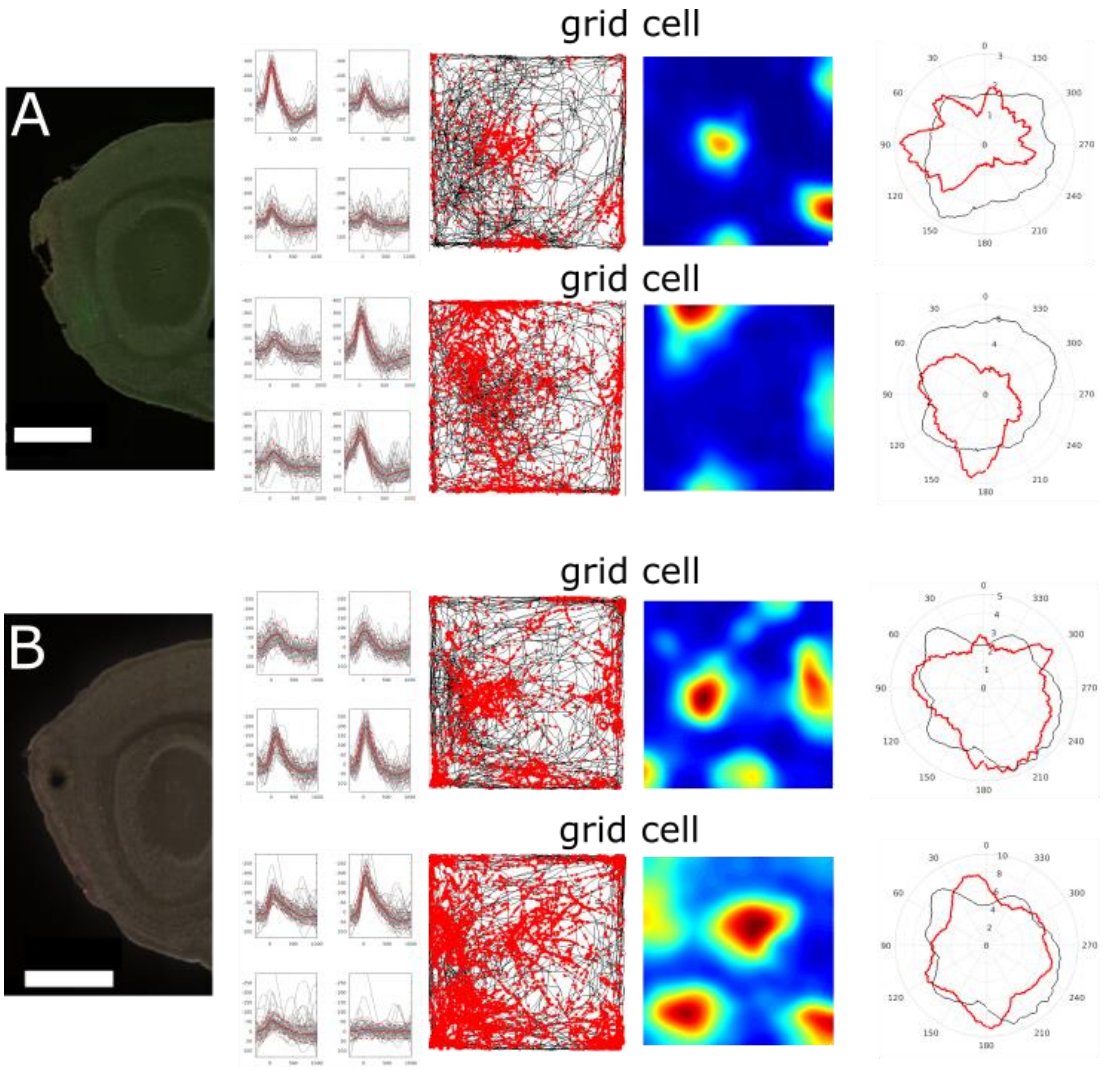

Figure 5.7. Example grid cells recorded from the superficial MEC (animals 5 and 13). Sagittal section of the brain stained with Neurotrace; overlaid waveforms when the cell fired on the four channels of the tetrode, scale bar = 1000 µm; the trajectory of the animal (black) and firing events (red); firing rate map (blue=low firing rate, red=high firing rate) calculated by summing the number of spikes in each location and dividing that by the time the animal spent there and then smoothing the surface with a Gaussian centred on each location bin (Leutgeb et al. 2007); polar head direction histogram generated by plotting a smoothed (10 degree window) polar histogram of the animal's head direction from the whole session (black, normalized value) and during when the cell fired (red, in Hz) normalized to the time spent in the field. Histology and imaging was performed by Holly Stevens.

Deep and superficial layers of the MEC are reported to have differences in spatial properties in the rat with layer 3 and the deep MEC having more head-direction sensitivity and layer 2 more grid cells (Sargolini et al. 2006). To test whether this difference applies to my dataset from the mouse, I analysed grid and head-direction scores including all recorded cells from the animals where I successfully identified the recording location (Table 5.2). The average grid score in the deep layers was -0.04 (sd = 0.4, n = 81 cells, 7 grid cells in total, 8.6 %, 2 conjunctive cells) and 0.11 (sd = 0.4, n = 140 cells, 14 grid cells in total, 10 %, 3 conjunctive cells) in superficial layers. Grid scores were significantly higher (two-tailed t-test, p=0.0078) in the superficial MEC compared to the deep MEC (Figure 5.8). Head-direction scores showed the opposite trend with an average head-direction score of 0.26 (sd = 0.3, n = 81 cells, 15 head-direction cells in total, 18.5 %) in the deep MEC and 0.12 (sd = 0.2, n = 140 cells, 7 head-direction cells in total, 5 %) in the superficial MEC (Figure 5.8). Head-direction scores were significantly higher in the deep MEC compared to superficial layers (two-tailed t-test, p=0.0006). To evaluate whether the presence of outlier cells (Figure 5.8) with high head-direction scores in the superficial MEC could be a consequence of recording from a different layer at the beginning of the experiment, I colour coded cells for recording day, with recordings near the beginning of the experiment coloured lighter than later recordings. I found outliers both from the beginning and end of the experiment to be present in the data. This is in agreement with some of the electrodes crossing multiple layers during the experiment. Due to the size and nature of the damage, and the arrangement of the tetrodes, I could not be more specific about which cells were recorded in which layers.

Overall, my results obtained using mice are in agreement with what was reported by Sargolini et al. (2006) using rats, with the deep layers having higher mean head-direction scores, and the superficial layers higher mean grid scores (Figure 5.8).

Table 5.2. Spatially selective cells and spatial information. Grid cells were defined as cells with grid scores ≥ 0.4 and head-direction cells as cells with head-directions scores ≥ 0.5. Conjunctive cells were defined as cells that passed both grid cell and head-direction cell criteria.

	superficial MEC	deep MEC
number of cells	140	81
spatial information score	0.18 (sd = 0.21)	0.15 (sd = 0.17)
number of grid cells	14	7
% of grid cells	10	8.6
mean grid score of all cells	0.11 (sd = 0.4)	-0.04 (sd = 0.4)
number of HD cells	15	7
% of HD cells	10.7	8.6
mean HD score of all cells	0.12 (sd = 0.2)	0.26 (sd = 0.3)
number of conjunctive cells	3	2
% of conjunctive cells	2.1	2.5

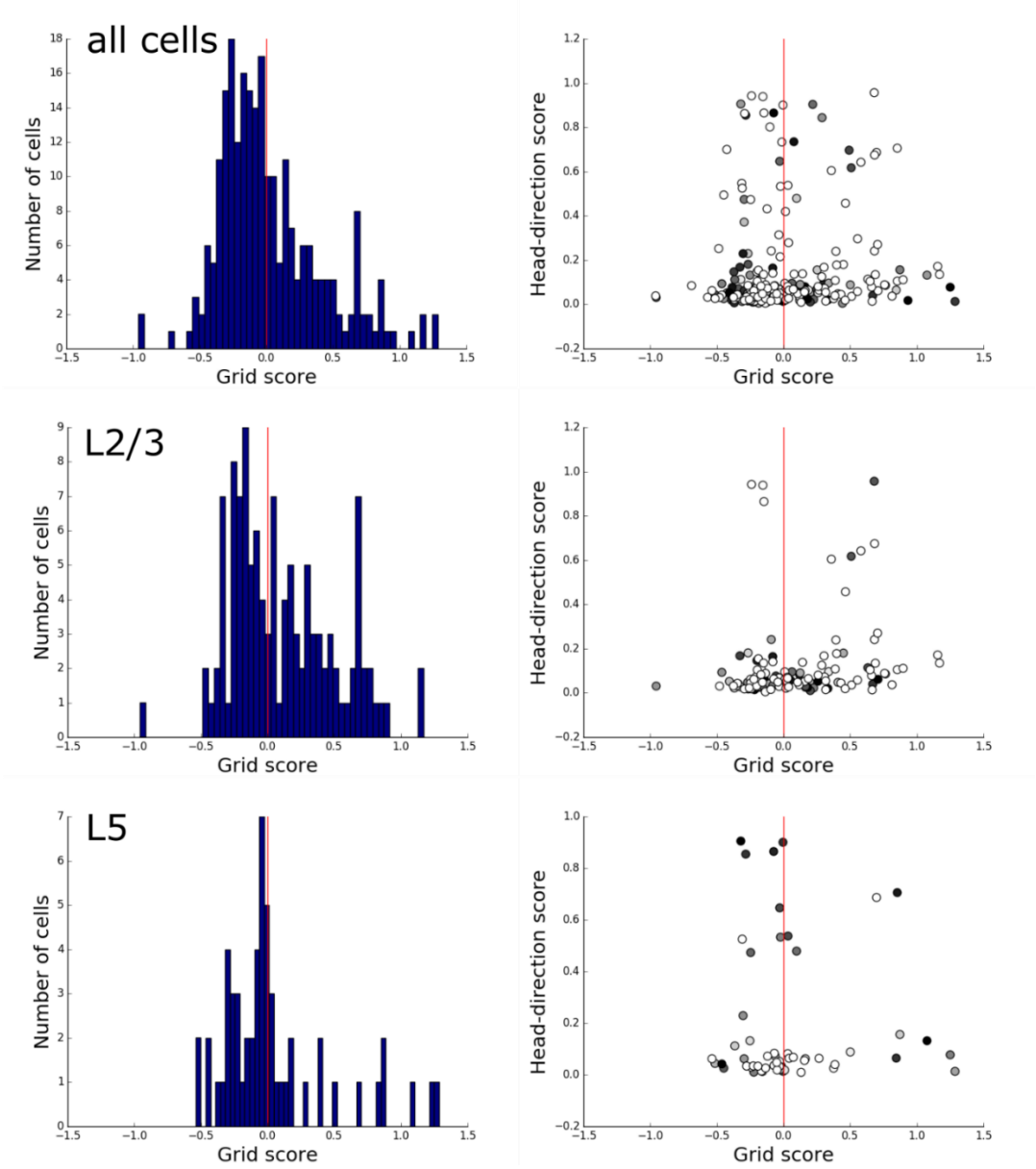

Figure 5.8. Grid and head-direction scores in different layers of the MEC in mice. Grid scores were higher in the superficial layers and head-direction scores were higher in the deep layers of the MEC. Histogram of grid scores (left) recorded from all cells, layer 2/3 and 5 of the MEC. Scatter plot of grid score vs head-direction score (right) for the same layers. The scatter plots are colour coded for the time of the recording with recordings near the beginning of the experiment in white and later recordings in black.

5.3.4 Is head-direction selectivity spatially organized?

While analysing my data I observed that the polar head-direction plots of some cells had unexpectedly complex shapes that are not tuned to a specific head-direction angle (Figure 5.9A). I found that for 257 / 270 excitatory and 55 / 66 inhibitory cells the head-direction distributions for cell firing were different to the distribution of the animal's heading direction (two sample Watson test, $p < 0.001$). A subset of these neurons (49 / 257 excitatory and 1 / 55 inhibitory) passed criteria for being head-direction cells.

To test whether directional firing is stable across the recording sessions, I compared head-direction distributions from the first and second halves of the recordings. I measured the linear relationship between the histograms of head-directions corresponding to firing events from the first and second halves by calculating the Pearson correlation coefficient using Scipy's (Python) stats.pearsonr function. I found positive correlations in most neurons (310 / 312 neurons) both for excitatory and inhibitory neurons (Figure 5.9B).

One possible explanation for the multi-peaked head direction fields is that head-direction preference differs according to location within the arena. I set out to test whether this is the case and investigate the spatial distribution of head-direction sensitive activity.

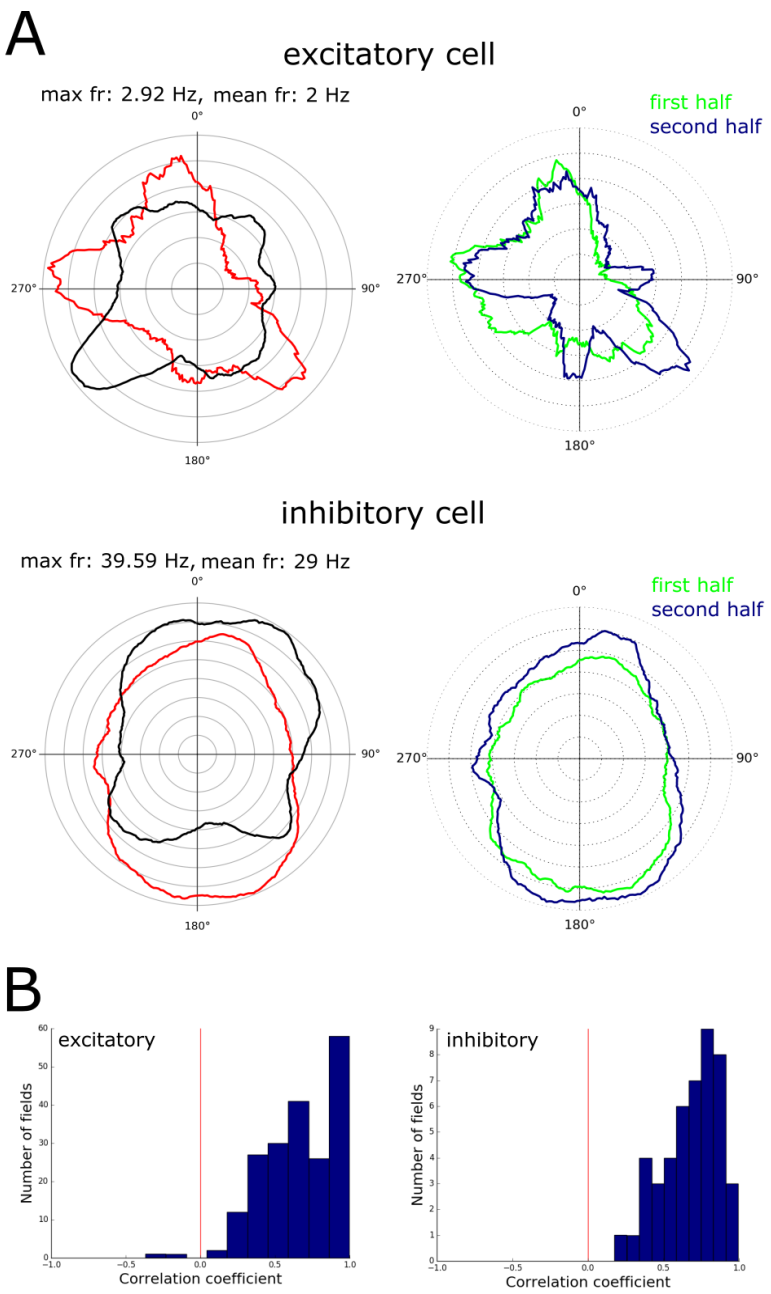

Figure 5.9. Complex head-direction polar plot shapes are stable within the recording session. (A) Head-direction histograms of an excitatory (top) and an inhibitory (bottom) cell were similar in the first and second halves of the recording session. Polar head direction histograms (left panels) were generated by plotting a smoothed (10 degree window) polar histogram of the animal's head direction from the whole session (black, normalized value) and during when the cell fired (red, in Hz) normalized to the time spent in the field. Polar histograms of head-direction when the cell fired are shown for the first (green) and second (navy) half of the recording session (right panels). (B) Histograms of Pearson correlation coefficients calculated for the head-direction histograms from the first and second halves of the recording sessions of excitatory (left, n = 257 neurons) and inhibitory (right, n = 55 neurons) neurons where the two sample Watson test showed a significant ($p < 0.001$) difference between the distribution of head-direction when the cell fired and heading direction. Most cells' histograms correlated between the first and second halves of the session.

To investigate what causes the polar plots to have complex shapes, I analysed the spatial distribution of head-direction sensitivity of 324 cells (this is the total number of cells I was able to perform this analysis on) recorded from 15 animals (Figure 5.10). To visualize the distribution of head-direction specificity, I plotted spikes on the trajectory of the animal and colour coded spikes based on head direction using a circular colour map (Thyng et al. 2016). I visually observed that some cells' head-direction showed spatial organization (Figure 5.9, Figure 5.10A). More specifically, some cells with multiple firing fields, including some grid cells appeared to be sensitive to different head-directions in different fields. As expected, head-direction cells (Figure 5.10B) had uniform head-direction in the whole open field arena, and interneurons (Figure 5.10C) had no visible pattern in their head-direction maps.

To quantify my observation and test whether head-direction sensitivity differs in different firing fields of cells, I extracted data from individual firing fields and compared the distribution of head-direction in the individual field to the distribution of head-direction when the cell fired.

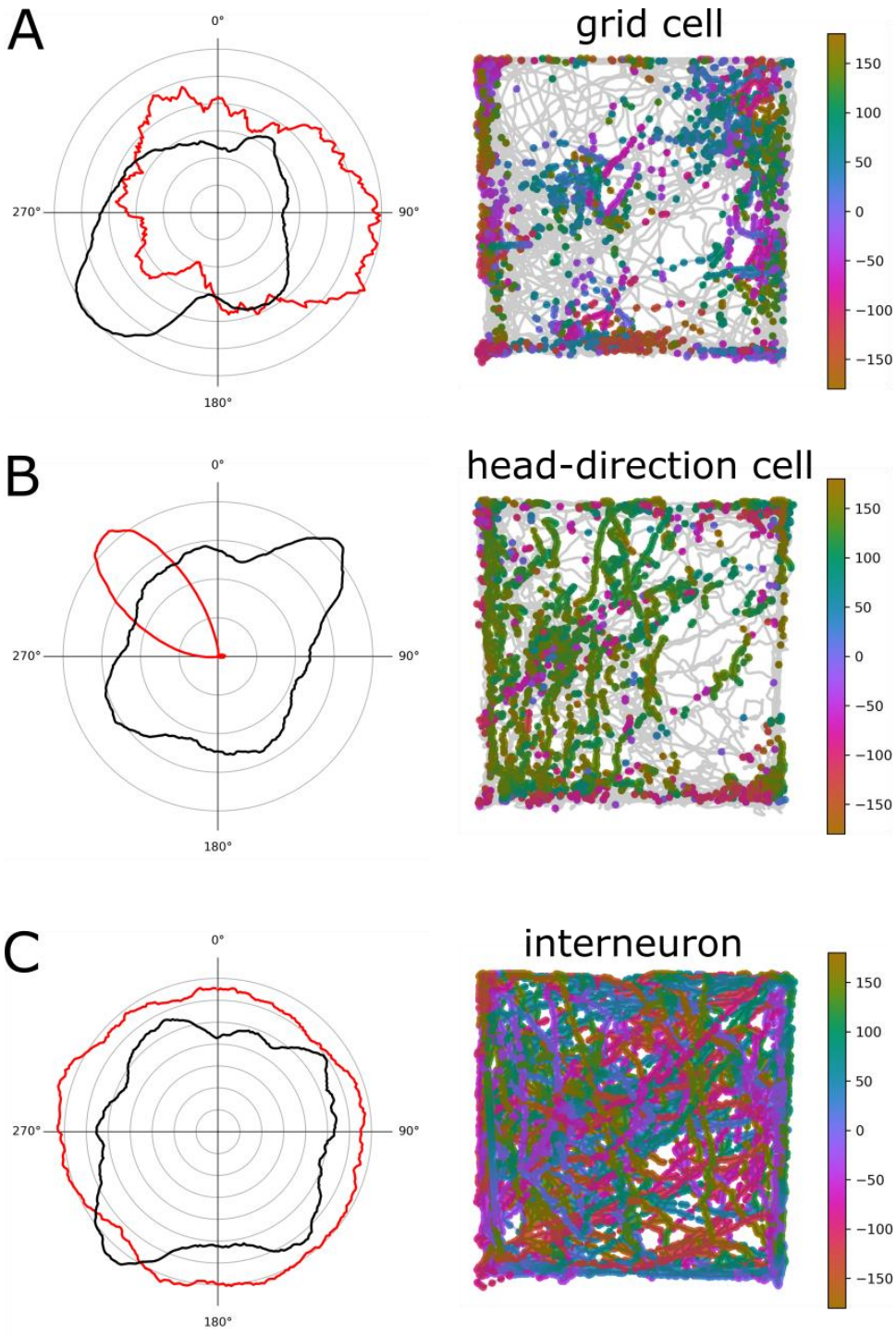

Figure 5.10. Head-direction clusters in some cells. Head-direction in grid cell (A), head-direction cell (B) and interneuron (C). Polar head direction histograms (left) were generated by plotting a smoothed (10 degree window) polar histogram of the animal's head direction from the whole session (black, normalized value) and during when the cell fired (red, in Hz) normalized to the time spent in the field. Spikes (dots) on the trajectory (line) of the animal (right) colour coded for head-direction of grid cell (A), head-direction cell (B) and interneuron (C).

Detecting firing fields on a rate map is equivalent to detecting local maxima and the neighbourhood of these local maxima on a surface. I designed and implemented an algorithm to detect firing fields based on how place fields were detected in previous studies (Harvey et al. 2009). Briefly, I detected the bin of the rate map with the highest firing rate and recursively added its neighbourhood to the field depending on their rate (see Methods). I only accepted fields if the highest bin in the field was above the average rate plus standard deviation in the whole rate map.

After detecting the firing fields, I needed to evaluate how successful the detection was for each cell. To asses this visually, I marked the detected field locations with different colours on the rate map. My script was able to detect fields correctly when they were clearly separated, but not when the local maxima were low and the fields wide (Figure 5.11). I found plots of cells with minor detection errors informative, but I restricted quantitative analyses to correctly detected fields. I was able to analyse data from 11 grid cells, 1 head-direction cell, 1 conjunctive cell and 7 unclassified cells.

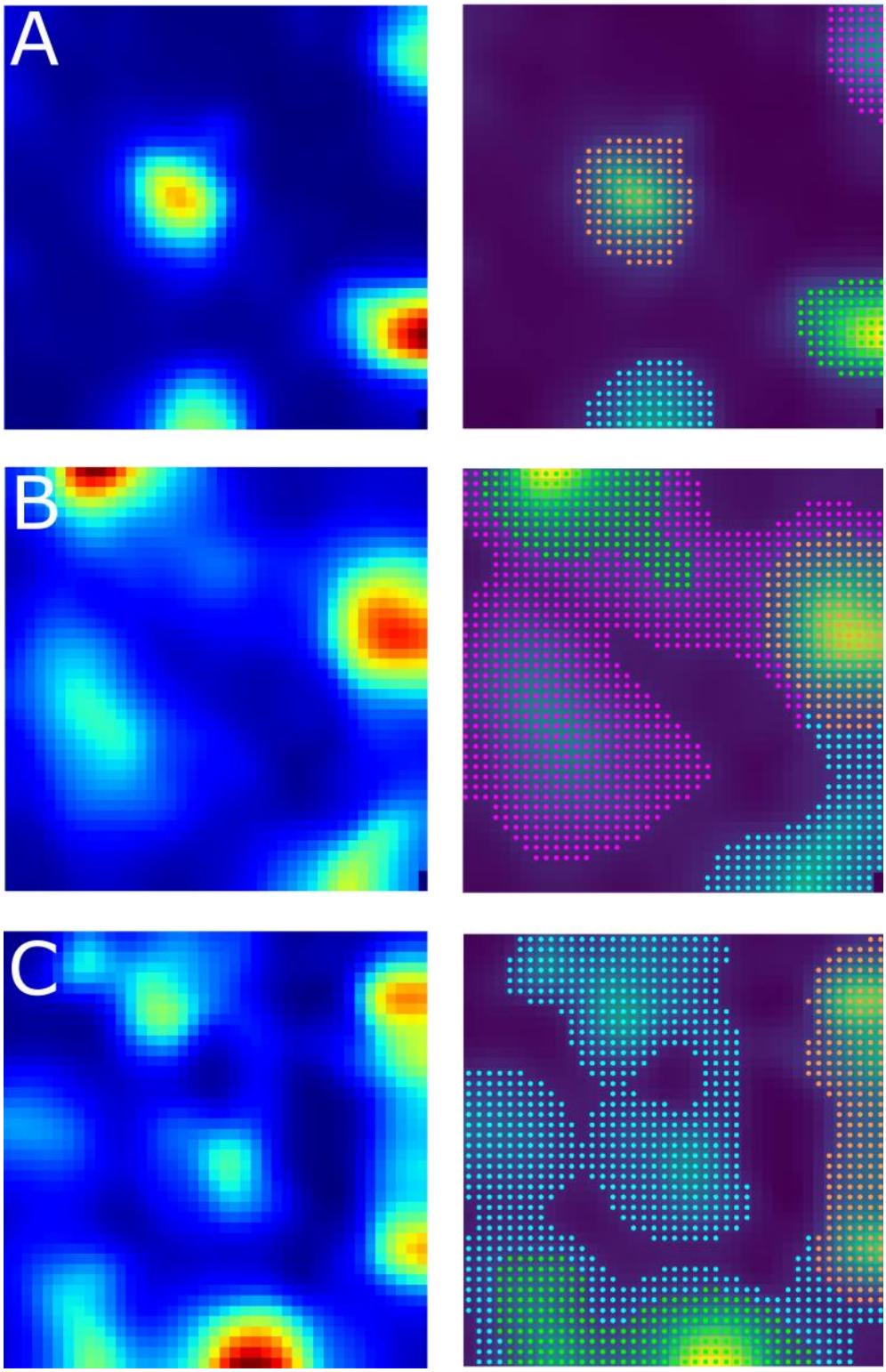

Figure 5.11. Field detection is more successful in cells with fewer and steeper peaks. Rate maps of cells (left panel) and detected fields on rate maps (right panel) are marked with different colours. (A) Fields are successfully detected in grid cells with four peaks. (B) Some fields are detected successfully, but lower peaks are not detected correctly. (C) Detection is unsuccessful in cell with 7 peaks.

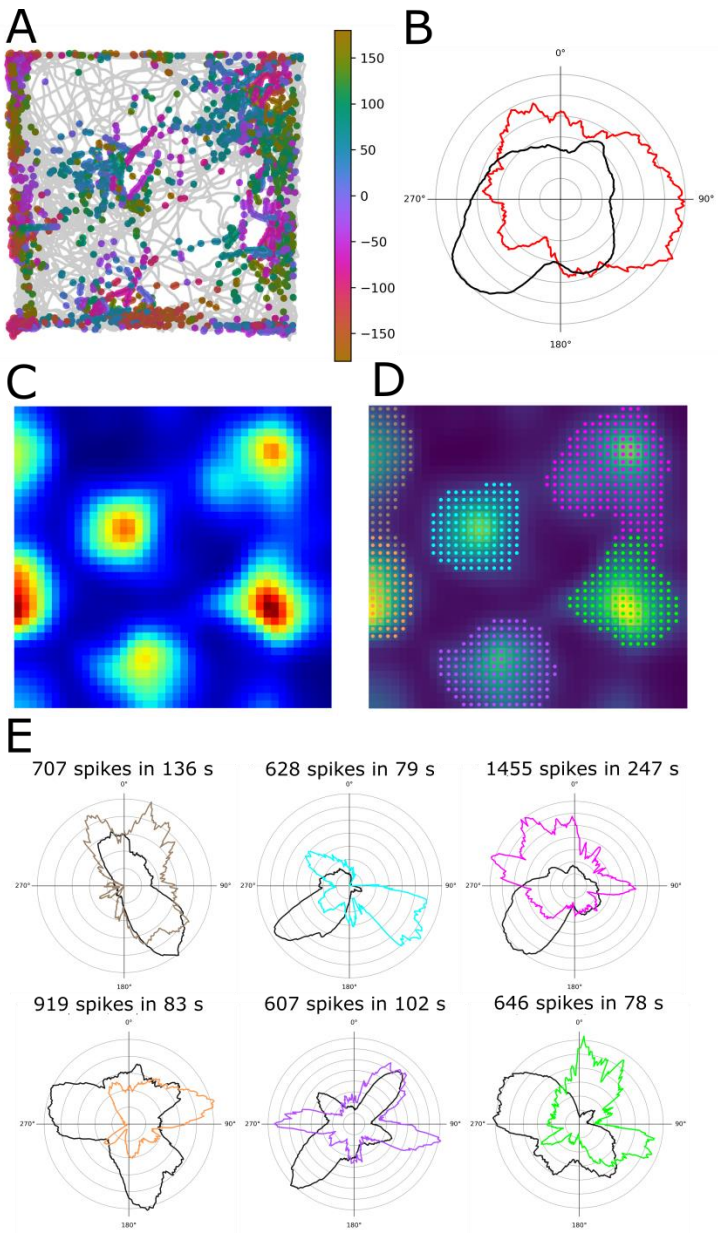

Figure 5.12. Head-direction differs in different firing fields of grid cell. (A) Trajectory of the animal (grey) and firing events (dots) are shown in the open field arena. Firing events are colour coded (Thyng et al. 2016) to show head direction. (B) Polar head direction histogram was generated by plotting a smoothed (10 degree window) polar histogram of the animal's head direction from the whole session (black, normalized value) and during when the cell fired (red, in Hz) normalized to the time spent in the field. Two sample Watson test showed significant ($p < 0.001$) difference between the two distributions. (C) The firing rate map was calculated by summing the number of spikes in each location and dividing that by the time the animal spent there and then smoothing the surface with a Gaussian centred on each location bin (Leutgeb et al. 2007). (D) Detected firing fields are marked on the rate map with coloured dots. (E) Polar head-direction histograms from the whole session when the animal was in the given firing field (black) and when the cell fired (coloured) corresponding to the detected firing fields normalized to the time spent in the field. Two sample Watson test showed that head-direction distributions were significantly different when the cell fired compared to the head-direction of the animal in the field ($p < 0.001$ for all fields except the top left where $p < 0.01$).

Visual inspection of head-direction polar plots generated from the data I extracted suggested that head-direction selectivity was indeed different in different firing fields (Figure 5.12). To rule out that this difference is by chance due to low sample size, I used Watson's two sample test (Fernández-Durán and Domínguez 2010) to compare the total distribution of head-directions when the animal was in a detected field to the distribution of head-direction when the cell fired in the field. Overall, I found 10 superficial and 1 deep MEC grid cells in three animals where I was able to detect individual fields successfully using this algorithm (number of detected fields / cell = 3.6 ± 1.2 (SD), range = 2 to 7). All these cells had directional firing in their individual firing fields that was significantly different to the animal's heading. For all of the grid cells, individual firing fields had head direction preferences that differed from one another.

To see whether other cells with multiple firing fields, such as conjunctive grid cells share this property with grid cells, I analysed all cells where my script was able to detect individual firing fields. Conjunctive cells generally had wider fields than most grid cells in my recordings, and therefore the field detection was rarely successful. The conjunctive cell I successfully analysed had slight differences in its preferred angle in between fields, but the preferred angles were all within the overall preferred direction of the cell (Figure 5.13). As expected, the head-direction when the cell fired was significantly different from the head-direction when the animal was in the field during the whole session ($p < 0.001$ for all fields). Furthermore, I found 1 head-direction cell and 7 unclassified cells with firing fields where field detection was successful. Similar to grid cells, all these cells had directional firing that was significantly different from the heading direction in the fields. Overall, my results suggest that grid cells and other entorhinal cells with non-grid firing code head-direction within their firing fields.

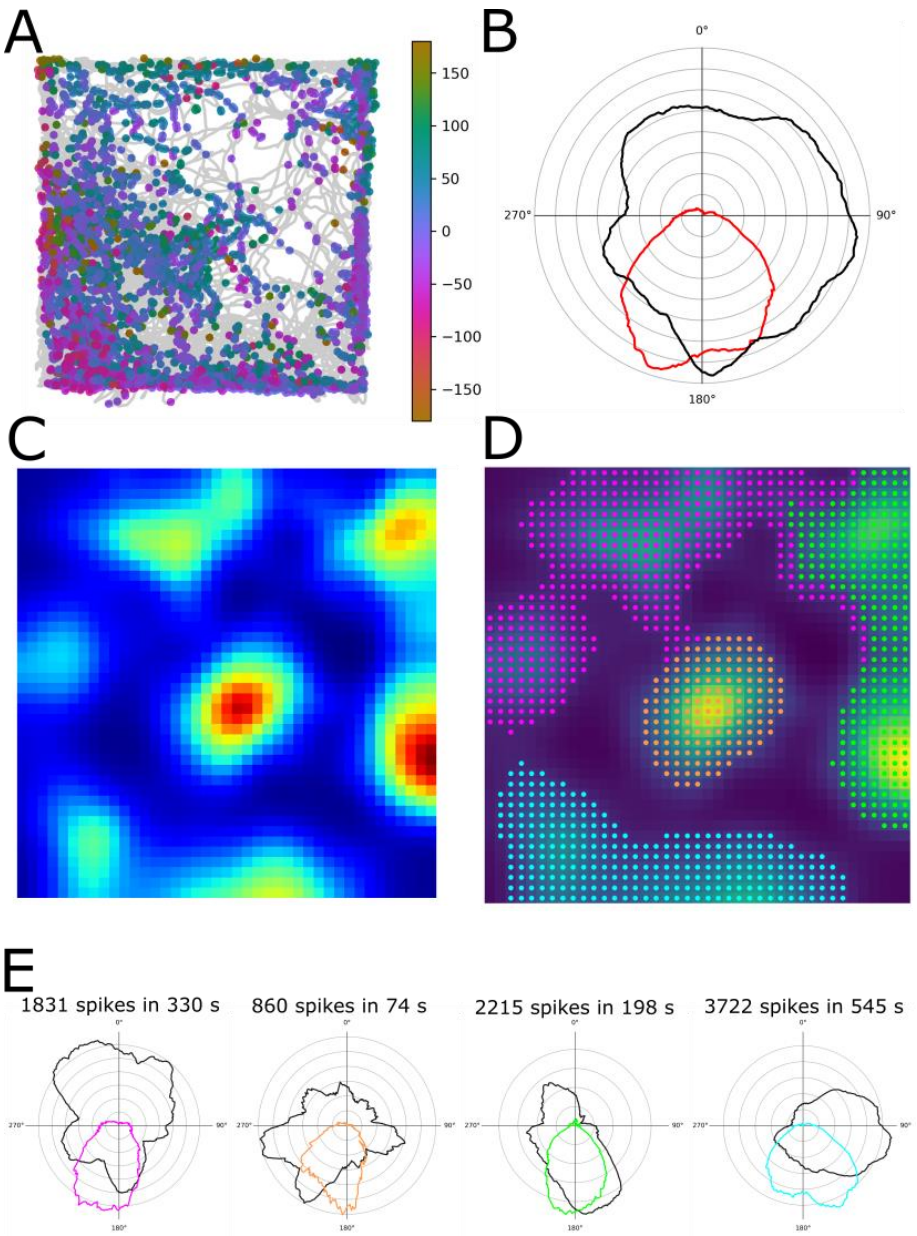

Figure 5.13. Head-direction is different between different firing fields of a conjunctive cell. (A) Trajectory of the animal (grey) and firing events (dots) are shown in the open field arena. Firing events are colour coded (Thyng et al. 2016) to show head direction. (B) Polar head direction histogram was generated by plotting a smoothed (10 degree window) polar histogram of the animal's head direction from the whole session (black, normalized value) and during when the cell fired (red, in Hz) normalized to the time spent in the field. Two sample Watson test showed significant ($p<0.001$) difference between the two distributions. (C) The firing rate map was calculated by summing the number of spikes in each location and dividing that by the time the animal spent there and then smoothing the surface with a Gaussian centred on each location bin (Leutgeb et al. 2007). (D) Detected firing fields are marked on the rate map with coloured dots. (E) Polar head-direction histograms from the whole session when the animal was in the given firing field (black) and when the cell fired (coloured) corresponding to the detected firing fields. Two sample Watson test showed that head-direction distributions were significantly different when the cell fired compared to the head-direction of the animal in the field ($p < 0.001$ for all fields).

Since the heading direction of the animal within each field was not uniformly distributed, I wanted to test whether different head-direction preferences visible on polar head-direction plots are a result of grid cells not being active every time the animal passes through the field or low sampling of some heading directions. A possible way to test whether head-direction preferences are by chance due to low sampling or noise is to compare the first and second half of the recordings and evaluate whether head-direction preferences correlate (Figure 5.14 and Figure 5.15). Out of the 72 fields of 20 cells included in the correlation analysis, 56 fields had significant p values (< 0.001) in the Pearson correlation test. The average Pearson correlation coefficient was 0.5 for all included fields (SD = 0.3), 0.4 (SD = 0.4, 34 fields) for grid cell fields, 0.8 (SD = 0.2, 3 fields) for head-direction cell fields, 0.95 (SD = 0.03) of fields of the conjunctive cell, and 0.6 (SD = 0.2, 15 fields) for fields of unclassified cells. These results suggest that most fields had a positive correlation between head-direction in the first and second half of the recording.

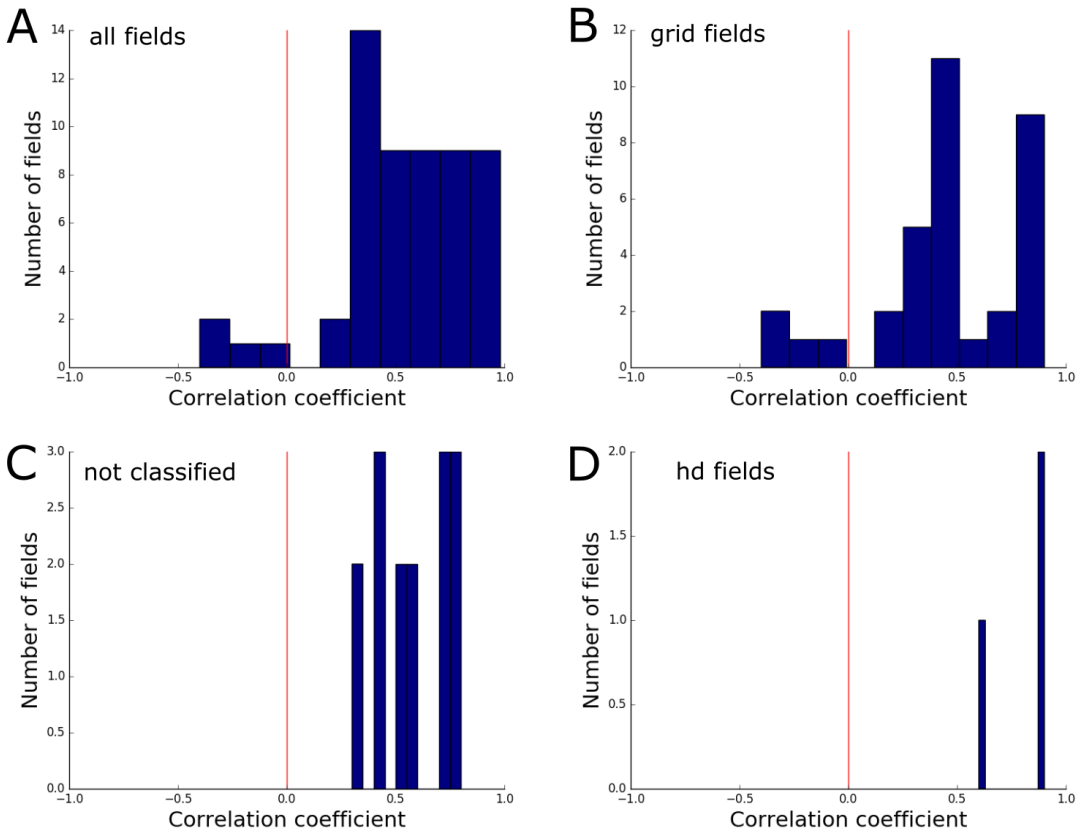

Figure 5.14. Histogram of correlation coefficients of fields from the first and second halves of the recording. Most field histograms were correlated in between the first and second halves of the recording session. (A) Polar histograms of directional firing normalized to the time spent heading directions was correlated between the first and second half of the recordings for successfully identified fields for 72 fields of 20 cells. The histogram only includes Pearson's correlation coefficients of cells with p values < 0.001. Fields of grid cells (B), unclassified cells (C) and head-direction cells (D) are shown for the analysis shown on (A).

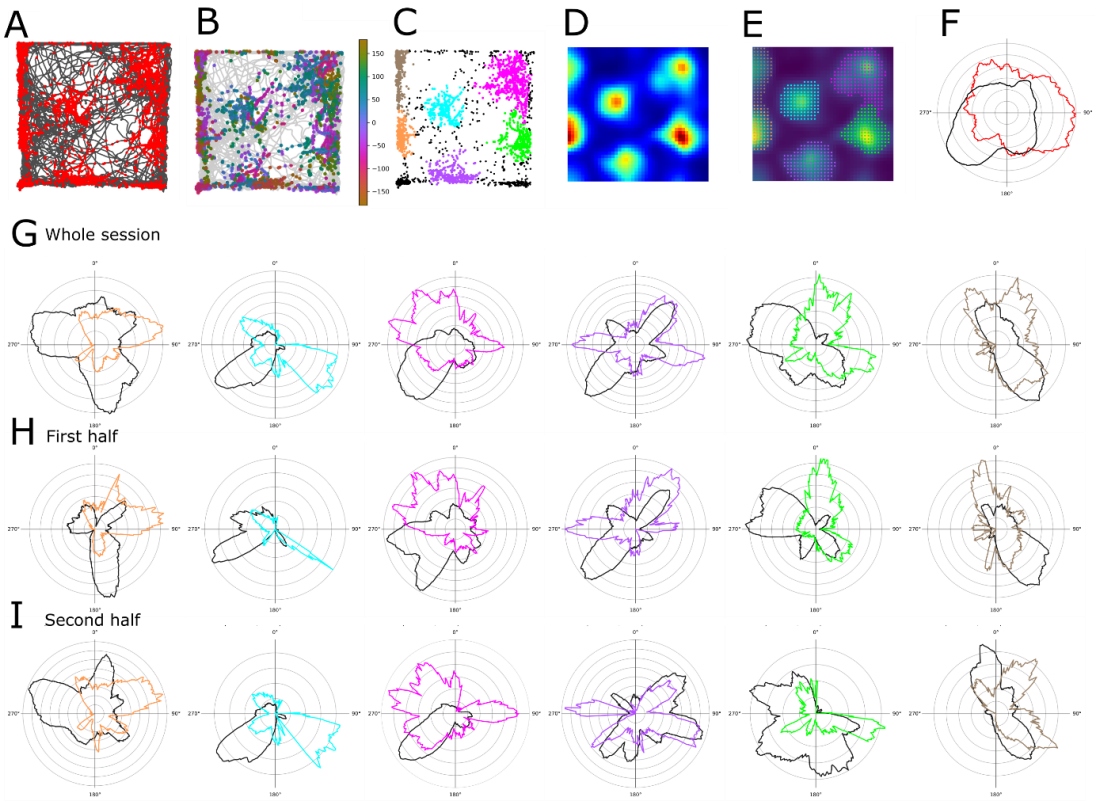

Figure 5.15. Head-direction preferences in the first and second half of the session of grid cell. (A) Spikes (red dots) on trajectory (black line) from the whole session. (B) Spikes on trajectory colour coded for head-direction. (C) Spikes colour coded for gird field identity (black dots are not included in any fields. (D) The firing rate map was calculated by summing the number of spikes in each location and dividing that by the time the animal spent there and then smoothing the surface with a Gaussian centred on each location bin (Leutgeb et al. 2007). (E) Detected fields are marked on the firing rate map. (F) Polar head direction histogram was generated by plotting a smoothed (10 degree window) polar histogram of the animal's head direction from the whole session (black, normalized value) and during when the cell fired (red, in Hz) normalized to the time spent in the field. (G) Polar head-direction plots generated from firing fields during the whole session. Number of spikes and time spent in fields from left to right: 919, 628, 1455, 607, 646, 707 spikes, 83, 79, 247, 102, 78, 136 seconds. (H) Polar plots of head-direction of fields during the first half of the recording. Number of spikes and time spent in fields from left to right: 353, 144, 683, 350, 405, and 395 spikes, 36, 15, 126, 71, 41, 74 seconds. (I) Polar plots of head-direction of fields during the second half of the session. Number of spikes and time spent in fields from left to right: 566, 484, 772, 257, 241, and 312 spikes, 47, 64, 121, 31, 36, 62 seconds. Pearson correlation coefficients were calculated for the field histograms from the first and second half of the recording. Correlation coefficients for pairs of fields from (H) and (I) from left to right are 0.82, 0.34, 0.38, -0.02, -0.09, 0.35. p values for field 4 and 5 were 0.09 and 0.7, respectively, and < 0.0001 for all other fields for the correlation.

5.4 Discussion

The experiments described aimed to replicate previous investigations of spatial firing in deep layers of the MEC and to further investigate relationships between location and head direction codes. I successfully replicated analyses from previous studies (Sargolini et al. 2006; Burgalossi, von Heimendahl, and Brecht 2014) investigating firing properties of the deep MEC. My results using mice were in agreement with findings reported by Sargolini et al (2006), which suggested that in rats, head-direction sensitivity was more prevalent in the deep layers and grid cells more abundant in superficial layers. My findings differed from juxtacellular results by Burgalossi et al. (2014), I found that the average firing rate is higher in deep layers in excitatory cells. Analysing individual firing fields from my data suggested that grid cells and some non-grid cells with multiple firing fields have different head-direction preferences in different firing fields.

In the first part of the discussion, I will focus on interpreting my results from replicating previous studies and on technical limitations of my experiment. In the second part, I will discuss my results on firing fields, assess limitations and further control experiments to challenge the findings, and consider their functional implications.

5.4.1 Comparison of recordings from rats and mice from the MEC

Deep MEC cells were previously shown to have lower firing rates compared to the superficial MEC (Burgalossi, von Heimendahl, and Brecht 2014). I compared firing rates of cells in my data from superficial and deep layer recordings to replicate this analysis, but found no significant difference between the firing rates of superficial and deep layer neurons. One reason for this difference in results could be that in the dataset collected by Burgalossi et al (2014) the highest firing rate included was 10 Hz, but my recordings contained several interneurons with high firing rates. I repeated the analysis only including putative excitatory neurons with firing rates lower than 10 Hz and found deep layer neurons to have significantly higher firing rates relative to superficial layers. A further reason for the different results could be that I was not able to detect cells with firing rates lower that 1 Hz, because they did not have enough events for the spike sorting to identify them as clusters. Overall, I concluded that tetrode recordings may systematically overestimate the population firing rate by not detecting cells with very low firing rates. On the other hand, cell-attached methods

used by Burgalossi et al. (2014) may have systematic biases caused by the sizes of the glass pipettes used to record from single cells, in particular with this approach smaller neurons may have been overlooked. Longer tetrode recordings where more firing events are recorded could improve detection of neurons with low firing rates.

Previously, extracellular recordings from the rat showed that head-direction and grid properties are layer dependent in the MEC with deep layers having more head-direction sensitive cells and superficial layers having more grid cells (Sargolini et al. 2006). Specific layers were identified in this study based on the damage caused by the implanted tetrode bundle. In my recordings, I implanted the four tetrodes separated, rather than in a bundle. Consequently, my different tetrodes could potentially record from different layers of the MEC. Furthermore, I applied a current to mark the location of the tetrode tips by burning the tissue, which caused extensive tissue damage, and made the identification of the recording location ambiguous. With my experimental approach, I was able to categorize my recordings as superficial or deep, but I was not able to identify specific layers I recorded from. Further, I was only able to estimate the final recording location, which means that in some animals I categorized as superficial recordings, the recording electrodes may have crossed the deep MEC before reaching the superficial position, contaminating the superficial data with deep MEC cells. Misclassifying deep layer recordings as superficial could mean that I might have underestimated the proportion of superficial grid cells and overestimated the proportion of head-direction cells in superficial recordings. Colour-coding my data for recording day (Figure 5.8) did not suggest that outliers are from early recording days exclusively. My results were in line with those reported by Sargolini et al. (2006) in that I found higher average head-direction scores in deep and higher average grid scores in superficial layers.

How can identification of recording location be improved? Identifying the layer of the MEC I recorded from would be crucial for experiments asking questions about the deep MEC. In the experiment presented in this chapter, the original aim was to opto-tag deep MEC cells, and tetrodes were not implanted as a bundle to make it more likely that some tetrodes hit the target area. To improve my success rate of identifying recording locations, in future experiments I could implant tetrodes as a bundle to ensure they all record from the same layer to reduce ambiguity of identifying the recording locations. Further, I could test different protocols for marking the recording

location by applying a current using lower intensities to reduce the tissue damage and have a smaller burned area. Finally, I could perform a Prussian blue reaction (Valerio and Taube 2016) to mark the burned tissue.

5.4.2 Do grid cells code head-direction?

Previous studies have found that firing frequency differs in between fields of grid cells (Ismakov et al. 2017; Kanter et al. 2017), and that the multiple fields of a grid cell operate independently to encode physical space (Reifenstein et al. 2012). Analysing individual firing fields of grid cells in my data suggested that grid cells are sensitive to multiple head-directions in different firing fields.

To compare the head-direction in a given field for the whole duration the animal spent there during the entire recording session, to the head-direction when the animal was in the field and the cell fired, I performed two sample (non-parametric) Watson tests (Fernández-Durán and Domínguez 2010). I decided to use the Watson test for the analysis rather than calculating head-direction scores for the individual fields. This is because many of the head-direction distributions were multi-modal, and head-direction scores only detect direction selective firing if it is unimodal. The results of the Watson test showed for most fields that the two distributions were different, suggesting that the cell's firing was significantly different from what is expected based on the head-direction if the neuron just fired irrespective of head-direction. Further analyses are needed to determine what proportion of the head-direction distributions of individual fields are multi-modal.

If the head direction specific firing within firing fields is a property of a cell then I would expect the distribution of directional firing to be stable over time. To test whether this is the case, I analysed data from the first and second halves of the recordings and looked at whether the histograms of normalized directional firing from the two halves correlated. I found that half of the analysed fields showed moderate correlation (Pearson's coefficient > 0.5), which suggests directional firing in these fields was more stable across the session than by chance. Therefore, my results suggest that some cells with multiple firing fields have head-direction selective firing specific to individual fields. Due to the exploratory nature of my analysis, more data is needed to repeat these tests to confirm this result.

Mechanisms and functional implications for direction modulated grid firing

What are the implications of individual grid fields coding different head-directions? I will consider whether this result is consistent with existing grid cell models and suggest experiments to further characterize this property. I will also outline functional implications regarding how grid cells might code information.

One of the major classes of grid models, continuous attractor network models, suggest that grid firing arises from local network activity, as a result of recurrent connectivity (Giocomo, Moser, and Moser 2011). Attractor network models assume that each grid cell receives input from a speed modulated head-direction cell, or a population of similarly tuned speed modulated head-direction cells, and that the cell's connectivity profile is shifted asymmetrically based on the preferred heading direction of these inputs. Therefore, the neuron drives the attractor's activity bump towards the preferred direction, which is a hard wired property of the circuit (Burak and Fiete 2009). Hence, individual grid cells coding for multiple head-directions would not allow the neuron to favour one direction and would not drive the network as expected. Therefore, my results do not support attractor network models. Oscillatory-interference models propose that the speed and heading direction of the animal is coded in changes in membrane potential oscillations (Giocomo, Moser, and Moser 2011). Since this model does not require network interactions for grid generation, it is possible that location dependent head-direction input could be integrated by neurons using similar mechanisms as proposed by oscillatory-interference models.

Can head-direction sensitivity in individual fields be controlled by cues? A possible way to test this would be to place salient cues in the environment and record neuronal activity before and after rotating the cues relative to the walls of the enclosure. Head-direction cells and grid cells were both shown to follow such rotations and rotate their firing fields accordingly (Hafting et al. 2005; Taube, Muller, and Ranck 1990a, 1990b). Therefore, I would expect head-direction sensitivity in fields to rotate with the cue consistently with the rest of the head-direction and grid cell system.

Grid cells are thought to provide a global metric that contributes to navigation and cognitive processes (Buzsáki and Moser 2013). Experiments where animals explored compartmentalized spaces demonstrated that grid cells first have identical firing patterns in identical compartments, but the representations later shift to tile the whole

environment to include all compartments (Carpenter et al. 2015). Therefore, grid firing can be influenced by local cues and evolve to a global representation, which is not in disagreement with the idea that individual fields may code local information. If head-direction is coded in individual fields that would result in a high capacity code where each grid cell stores the position of the fields as well as the head-direction information. This could be a potential mechanism by which L2 grid cells code head-direction, where head-direction cells are absent (Sargolini et al. 2006).

In conclusion, my data suggests a previously unexpected spatial organization of head-direction selectivity in the MEC. A possible implication of fields of grid cells having different head-direction selectivity could be that the grid cell system could store the heading direction of the animal in addition to its position. A possible explanation for this property could be that it is inherited from the head-direction system, for example by individual grid cells only receiving input from head-direction cells in certain fields. To test this idea, experiments could temporarily manipulate the head-direction system using optogenetic methods while recording grid cells.

What mechanism could individual grid fields having different head-direction preferences support? A possible explanation could be that grid cells compute path integration and need to integrate the position and heading direction to keep track of the location of the animal. To investigate this, grid cells could be recorded during a path integration task, and the head-direction system could be manipulated using an optogenetic approach when an animal is in a specific grid field. If the head-direction specificity in the field is needed for computing path integration, path integration would be impaired and the estimation error in the task might reflect the contribution of head-direction selectivity in the manipulated field.

Chapter VI

6 Discussion

The overarching aim of my thesis was to investigate functional and anatomical properties of the deep MEC. In the first set of experiments I identified three transgenic mouse lines with deep MEC specific transgene expression and characterized the extent of that specificity. The p038 mouse line turned out to be remarkably specific to L5b of the deep MEC. I investigated projection targets of the tTA+ cells in the p038 line and I found that they project to the superficial MEC and that their projections avoid calbindin islands. Further, I found that tTA+ cells do not, but other deep MEC cells do project to the thalamus. For *in vivo* characterization of deep MEC firing properties, I first set up an automated analysis pipeline to process extracellular recordings of neuronal activity during open field exploration and optogenetic stimulation. Using this pipeline, I performed an experiment to opto-tag tTA+ cells in p038 mice and identify their firing fields. The success rate of this experiment was low due to unexplained variable transgenic expression in these experiments. Finally, I analysed extracellular data recorded from the mouse MEC during open field exploration acquired for the opto-tagging experiment and compared my results to existing findings from the rat. I found that deep MEC cells have more head-direction selective cells among them and superficial cells have more grid cells which is in agreement with extracellular recordings from the rat (Sargolini et al. 2006). Deep MEC cells in my recordings had higher firing rates than superficial MEC cells, which is not in agreement with juxtacellular results (Burgalossi, von Heimendahl, and Brecht 2014). Analysis of individual firing fields of grid cells and non-grid cells with firing fields in my recordings suggests that head-direction differs in between firing fields, revealing an unexpected organization of head-direction in the MEC. Overall, my findings support the idea that the deep layers of the MEC have an influence on superficial layers and play a role in spatial cognition. In the following discussion I will outline the implications and

limitations of the above results and propose experiments to address remaining questions.

6.1 Genetic access to sublayers of the deep MEC

Sürmeli et al. (2015) recently demonstrated that L5 of the MEC is divided into two sublayers with distinct connectivity and molecular markers. One of the sublayers, L5b, was shown to have cells positive to the molecular marker Ctip2, and receive input from brain areas rich in spatially selective cells (Sürmeli et al. 2015). Such connectivity suggests that L5b might play a role in spatial cognition. However, to test this hypothesis and specifically manipulate L5b without affecting the adjacent layers of the deep MEC, genetic tools need to be applied. I characterized the extent of specificity of transgenic expression to L5b in three transgenic mouse lines. Both in the rasgrp and trib2CreER lines I found that transgenic expression was not consistently specific to L5b. However, in some animals, expression appeared to be specific to the deep MEC, and most L5b cells were infected in areas where the virus spread. It might be possible to adjust the experimental conditions to achieve higher specificity in these lines and access a high percentage of L5b cells. In p038 mice I found that transgenic expression is highly restricted to a small subpopulation (13 %) of L5b cells. Such specific labelling allowed me to design experiments and ask further questions about the anatomical and functional properties of L5b.

6.2 Where do p038 cells project to and receive input from?

Describing which areas of the brain receive input from L5b of the MEC is crucial to understand its potential influence and role in spatial cognition. To address this question, I first mapped the projections of tTA+ neurons in p038 mice in the whole brain based on the endogenous mCitrine signal. I found abundant projections in superficial layers of the MEC that avoided calbindin islands, groups of pyramidal cells that are strongly speed modulated (C. Sun et al. 2015). Further, I observed terminals of tTA+ cells in the anterodorsal and lateral dorsal nuclei of the thalamus. To test whether these terminals belong to L5b cells, I injected fast blue, a retrograde tracer in the thalamus, specifically targeting the terminals. I found labelled cell bodies in L5b, but the fast blue positive cells only overlapped with the p038 population at the border

of the deep MEC and parasubiculum. Therefore, I concluded that the tTA+ cell population in L5b does not project to the thalamus, but other deep MEC cells possibly do.

My experiments above suggest that the tTA+ population influences superficial layers, but I did not demonstrate functional connectivity or specifically identity the target of projections. Future experiments could identify the molecular identity of the superficial cells that receive input from L5b by stimulating tTA+ cells using an optogenetic approach and recording from superficial cells. Furthermore, to identify all targets of tTA+ L5b cells, a tTA-dependent synaptophysin virus could be injected to label all cells that receive input from tTA+ cells. L5b cells were shown to receive input from CA1 of the hippocampus and the superficial MEC (Sürmeli et al. 2015), but whether this applies to all tTA+ cells and whether there are more input regions is not yet known. To find all input regions of tTA+ cells, a tTA-dependent rabies virus (Reardon et al. 2016) could be injected to the deep MEC to label cells that send input to tTA+ cells.

Performing the experiments proposed above would map the input and output connectivity of tTA+ cells of L5b of p038 mice. However, they would not be able to access other L5b cells which may have different connectivity. Furthermore, to understand the role of tTA+ cells in spatial cognition, *in vivo* experiments are needed.

6.3 What are the spatial properties of L5b neurons?

Spatially selective cells such as head-direction cells, grid cells and conjunctive cells were found in the deep MEC of rats (Sargolini et al. 2006). To find out whether the tTA+ cell population in p038 mice has spatially selective cells among them, I set out to characterize their firing fields in the open field by letting mice explore a rectangular arena and then opto tag cells at the end of the session to identify them as tTA positive. My secondary aim in this experiment was to identify cells that receive input from tTA+ cells. I could identify cells that receive input from tTA+ cells based on the latency of the light response in responsive cells.

Due to variable transgenic expression in p038 mice in this experiment, tTA-dependent channelrhodopsin expression and identified light responsive cells were present in only 1 mouse. From the 5 cells I identified as light responsive, one was p038 positive, and four received input from a p038 cell. Three of the responsive cells, including the p038

positive cell had high firing rates (mean = 33.7 Hz, std = 1.2 Hz), and two had low rates (4 Hz and 7 Hz). I was only able to analyse spatial properties of three of the cells due to technical difficulties, but none of the analysed cells showed spatial or head-direction properties. To conclusively characterize spatial properties of the p038 population, a repeat experiment is needed.

6.4 Is the p038 population a random or a functionally distinct population within L5b?

The above experiments propose ways to investigate the functional connectivity of L5b p038 cells with other brain regions and *in vivo* properties of p038 cells, but do not target other L5b cells. To assess whether experiments on the p038 population represent all L5b cells, experiments need to test whether the p038 population is a random subset of L5b cells. Comparisons between p038 positive and negative cells could be made *in vitro* by comparing morphology and electrophysiological properties. If the p038 population is a distinct subpopulation of Ctip2 positive L5b cells, further experiments will need to find access to the rest of the Ctip2 population to investigate their function to understand the role of L5 in spatial cognition.

6.5 How is interlayer connectivity involving L5b organized?

How does L5b process hippocampal and superficial input? Receiving information from CA1 and the superficial MEC, L5b cells are in a unique position to integrate signal originating from areas rich in place and grid cells. How these inputs are processed and then sent back to superficial layers could be crucial to understanding how spatial information is integrated. One possibility is that the L5b population is homogenous and they all receive input from both the hippocampus and superficial MEC and then relay the processed output back. However, preliminary data from our lab (Martyna Rakowska, unpublished) suggests that this is not the case. To test the internal connectivity of L5b, I injected p038 mice with a Tre-dependent channelrhodopsin virus targeting the deep MEC. Infected L5b cells were optogenetically stimulated, while other L5b cells were recorded *in vitro* (Martyna Rakowska, unpublished). The results of these recordings indicated that L5b cells that receive p038 input had different morphology relative to cells that do not receive input, with interconnected cells

extending their apical dendrites to L2. However, the number of cells reconstructed in this study was not enough to draw conclusions and repeat experiments are needed. Connectivity between L6, L5b and L5a is not known yet. However, preliminary data suggests that L5b projects to L5a (Witter et al. 2017).

Do superficial spatial cells receive input from tTA positive L5b cells in p038 mice? Identifying the firing fields of superficial cells that receive input from tTA+ cells could reveal functional connections between spatial cells in the MEC. Firing fields of superficial MEC cells that receive input from tTA+ cells could be identified by injecting a Tre-dependent channelrhodopsin virus in the deep MEC of p038 mice and recording superficial cells while p038 cells are stimulated. This experiment would show which superficial spatial cells are influenced by p038 input. Knowing which spatial cell types communicate with each other would be invaluable in the investigation of spatial cognition.

6.6 Analysing extracellular recordings of neuronal activity

Analysing extracellular *in vivo* electrophysiology data involves pre-processing the data to filter out low frequency oscillations and reduce noise, perform spike sorting and analyse firing properties of the sorted neurons (Rey, Pedreira, and Quian Quiroga 2015). This pipeline typically includes manual steps such as curating clusters and starting different stages of the analysis, which takes a considerable amount of time and can bias results. To improve efficiency and replicability of my experiments, I set out to automate my analysis as much as possible. I used MountainSort, a fully automated spike sorter (J. E. Chung et al. 2017) to perform the sorting. I implemented Python scripts that controlled running analyses by calling subsequent stages of analyses for multiple recordings without manual intervention. Eventually, my pipeline would accept folder paths to recordings on the lab's server as an input, perform all analyses and then upload the results to the server.

Implementing this pipeline significantly reduced manual intervention in my analysis but did not completely eliminate it. As a last step, accepted clusters need to be validated manually, since MountainSort accepted some clusters that did not appear to be of neuronal origin. These false positives were usually artefacts from movement or light stimulation. Since the waveforms of such artefacts do not resemble an action

potential, additional analysis could be implemented to recognize and flag them or filter them out. One way of implementing this analysis could be to make a database of neuronal action potentials recorded by tetrodes and a database of artefact waveforms and train a network on this dataset to recognize them. Alternatively, additional criteria could be introduced regarding the shape of action potentials for the cluster to be accepted.

New sorting algorithms are developed and published at a high rate (J. E. Chung et al. 2017; Rossant et al. 2016; Franke et al. 2010; Hilgen et al. 2017; S N Kadir, Goodman, and Harris 2017), but user friendly platforms to test and compare them are lacking. Different spike sorters require the data to be in a certain format and some do not include spike detection (Shabnam N Kadir, Goodman, and Harris 2014). These variable requirements mean that users need to rewrite pre-processing scripts when they test a new algorithm, which takes time and limits how many algorithms are tested. Hence, more open source effort needs to be put in developing platforms for validating different sorting algorithms.

6.7 *In vivo* results on the firing properties of deep MEC cells are not in agreement and are not sublayer specific

Extracellular recordings from rats (Sargolini et al. 2006) revealed the presence of spatially selective cells in all layers of the MEC. Further, deep layers were found to have more head-direction cells and superficial layers more grid cells. I replicated this analysis on my data from the mouse and found a similar trend. However, due to the distribution of my recording electrodes I could not identify which cells I recorded from with layer specific precision. Juxtacellular recordings from rats (Burgalossi, von Heimendahl, and Brecht 2014) were not in full agreement with results by Sargolini et al. (2006) and found that deep MEC cells have very low firing rates relative to superficial cells and are quiet in both novel and familiar environments. I compared superficial and deep firing rates in my results and found the opposite. However, I was not able to detect cells with firing rates below 1 Hz, which is what most deep MEC cells in the juxtacellular study had.

All the above studies are limited in specificity, since the sublayer the cells were recorded from was not determined. As different sublayers of the deep MEC have

distinct connectivity (Sürmeli et al. 2015), to understand their function they need to be distinguished in *in vivo* studies. Sub-layer specific identification could be performed in combination with juxtacellular recordings by staining slices against molecular markers specific to L5a or L5b. Alternatively, opto-tagging can be done in extracellular recordings to identify transgenic cells that belong to one of the sublayers. Considering that extracellular recordings are not able to detect cells with very low firing rates, juxtacellular recordings, or calcium imaging (Stosiek et al. 2003) may be more appropriate methods to investigate deep MEC cells if one of their main features is sparse firing.

6.8 Do grid cells code head-direction?

Analysis of individual grid fields in my extracellular data suggested that individual firing fields have distinct head-directions. This finding is in line with results that demonstrated that firing fields have variable firing frequencies (Ismakov et al. 2017) and are independent elements of encoding physical space (Reifenstein et al. 2012). Comparing head-direction specific firing in firing fields the first and second halves of the recordings showed that in about half of the fields analysed, head-direction specificity showed moderate correlation (> 0.5) in between the two halves, suggesting that this property is stable throughout the recording session for these fields. Future experiments could further extend these results, for example cue rotation experiments could test whether the head-directions in individual fields rotate consistently with the firing fields of the cell.

These results are not in agreement with predictions of continuous attractor models, since multiple head-direction preferences within one cell would not allow the cell to have a head-direction preference and the ‘activity bump’ would not move (see discussion in Chapter V). The results do not contradict oscillatory interference models of path integration. A possible interpretation might be that the grid cell network computes path integration and stores the position and heading direction of the animal. To test this idea, experiments could temporarily disrupt the head-direction system using optical methods when the animal is in a specific field during a path integration task and evaluate whether this causes a location estimation error. An alternative interpretation is that the grid system constructs a high capacity representation of the environment (Klukas, Lewis, and Fiete 2019; Burak and Fiete 2009; Mathis, Herz, and

Stemmler 2012; Fiete, Burak, and Brookings 2008) and stores the animal's position as well as head-direction to aid navigation.

6.9 What do deep MEC cells code?

The experiments discussed and proposed in the above sections aim to dissect the connectivity and characterize firing properties of deep MEC cells. Results of these experiments can give insight into potential functions of deep MEC cells, but do not directly test their function or address what deep MEC cells code in behaving animals. To identify the role of deep MEC cells in spatial cognition, they need to be recorded and manipulated in spatial behaviours. In the following section I will outline the main models that include the deep MEC and propose experiments based on the predictions of the models and on existing data.

The deep MEC was proposed to play a role in working memory based on *in vitro* results that found graded persistent firing in deep layers (Egorov et al. 2002; Frank and Brown 2003). Graded persistent firing is when cells fire for a prolonged period after stimulation with a frequency that depends on the input. Such firing could mean that individual cells can hold on to information they receive. However, persistent activity was not found *in vivo* yet. Recording neuronal activity of deep MEC cells during behaviours when animals need to use their working memory could identify persistent firing. Experiments where large populations of L5b neurons are recorded, such as in calcium imaging (Stosiek et al. 2003) would be advantageous for this question. Further, it is possible that persistent firing is dependent on behaviour, and animals would need to perform a task rather than freely explore.

Based on their position in the hippocampal-entorhinal loop, L5b cells are well-placed to play a role in spatial cognition. One of the proposed models that include the deep MEC is based on noise correlation of grid cell pair recordings in superficial and deep layers of the MEC (Tocker, Barak, and Derdikman 2015a). This model suggests that the deep MEC performs path integration. To test this hypothesis, L5b cells could be recorded in the virtual reality based path integration task designed by Tennant et al. (2018). In this task, mice are trained to run on a virtual linear track and stop at a designated location for a reward. The designated location, 'reward zone', is marked with a visual cue on some trials, but is absent on others. On the trials with no visual

cue, animals need to rely on internal self-motion cues and estimate the location based on these. Recording L5b cells while mice execute location estimation trials could reveal correlations between neuronal activity and behaviour, in particular the animal's position on the track and speed of movement. To further test whether L5b cells are needed for this task, their activity could be manipulated during the task. One possibility for this would be to activate or inhibit the p038 population while mice execute location estimation. Alternatively, deep L5b cells that receive CA1 input could be targeted by injecting a channelrhodopsin virus in CA1 and activating axon terminals in L5b with an optic fibre implanted in the deep MEC. Testing the effect of silencing L5b cells during location estimation could reveal whether they are necessary for the task. Targeted manipulation, such as activation or inhibition at certain locations during the task could further reveal how L5b cells contribute to location estimation.

7 Conclusions

How do my experiments move the field forward? I have identified a new genetic tool to access neurons in L5b of the MEC and demonstrated some of its strength and limitations. Using these tools will make it possible to further our understanding on functional and anatomical properties of deep MEC neurons and their connectivity with other regions. I have established new data analysis pipelines in the lab and demonstrated their utility. These pipelines will aid in improving reproducibility and efficiency of analyses. Finally, I have identified a potentially interesting feature of grid firing. I found that head-direction is coded in individual firing fields of some MEC cells. This result requires further validation, but challenges some current models for grid firing and has implications for the information that grid cells may encode.

References

Allen, K., M. Gil, E. Resnik, O. Toader, P. Seeburg, and H. Monyer. 2014. “Impaired Path Integration and Grid Cell Spatial Periodicity in Mice Lacking GluA1-Containing AMPA Receptors.” *Journal of Neuroscience* 34 (18): 6245–59.

Alonso, A., and E. García-Austt. 1987. “Neuronal Sources of Theta Rhythm in the Entorhinal Cortex of the Rat.” *Experimental Brain Research* 67 (3): 493–501.

Alyan, Sofyan, and Rudolf Jander. 1994. “Short-Range Homing in the Mouse Mouse, Mus Musculus: Stages in the Learning of Directions.” *Anim. Behav,* 48: 285–89. https://ac.els-cdn.com/S0003347284712425/1-s2.0-S0003347284712425-main.pdf?_tid=25e0072c-1c2c-4df8-a4ae-5cff9089e209&acdnat=1535475072_11cc8e8bd551184564924967bc50263f.

Aronov, Dmitriy, Rhino Nevers, and David W. Tank. 2017. “Mapping of a Non-Spatial Dimension by the Hippocampal–entorhinal Circuit.” *Nature* 543 (7647): 719–22.

Aronov, Dmitriy, and David W Tank. 2014. “Engagement of Neural Circuits Underlying 2D Spatial Navigation in a Rodent Virtual Reality System.” *Neuron* 84 (2): 1922–2013.

Atasoy, Deniz, Yexica Aponte, Helen Hong Su, and Scott M Sternson. 2008. “A FLEX Switch Targets Channelrhodopsin-2 to Multiple Cell Types for Imaging and Long-Range Circuit Mapping.” *The Journal of Neuroscience : The Official Journal of the Society for Neuroscience* 28 (28): 7025–30.

Barry, Caswell, and Neil Burgess. 2007. “From Grid Cells to Place Cells: A Mathematical Model.” *Hippocampus* 17 (9): 801–12.

Bean, Bruce P. 2007. “The Action Potential in Mammalian Central Neurons.” *Nature Reviews Neuroscience* 8 (6): 451–65.

Benureau, Fabien C. Y., and Nicolas P. Rougier. 2018. “Re-Run, Repeat, Reproduce, Reuse, Replicate: Transforming Code into Scientific Contributions.” *Frontiers in Neuroinformatics* 11 (January): 69.

Blodgett, H. C. 1929. “The Effect of the Introduction of Reward upon the Maze

Performance of Rats.” *University of California Publications in Psychology*. https://psycnet.apa.org/record/1930-01027-001.

Boyden, Edward S., Feng Zhang, Ernst Bamberg, Georg Nagel, and Karl Deisseroth. 2005. “Millisecond-Timescale, Genetically Targeted Optical Control of Neural Activity.” *Nature Neuroscience* 8 (9): 1263–68.

Brun, Vegard Heimly, Trygve Solstad, Kirsten Brun Kjelstrup, Marianne Fyhn, Menno P. Witter, Edvard I. Moser, and May-Britt Moser. 2008. “Progressive Increase in Grid Scale from Dorsal to Ventral Medial Entorhinal Cortex.” *Hippocampus* 18 (12): 1200–1212.

Buccino, Alessio Paolo, Mikkel Elle Lepperod, Svenn-Arne Dragly, Philipp Dominik Hafliger, Marianne Fyhn, and Torkel Hafting. 2018. “Open Source Modules for Tracking Animal Behavior and Closed-Loop Stimulation Based on Open Ephys and Bonsai.” *BioRxiv*, June, 340141.

Buchler, E R, and S B Childs. 1981. “Orientation to Distant Sound by Foraging Big Brown Bats (Eptesicus Fuscus).” *Animal Behaviour* 29: 428–32.

Buetfering, Christina, Kevin Allen, and Hannah Monyer. 2014. “Parvalbumin Interneurons Provide Grid Cell–driven Recurrent Inhibition in the Medial Entorhinal Cortex.” *Nature Neuroscience* 17 (5): 710–18.

Burak, Yoram, and Ila R Fiete. 2009. “Accurate Path Integration in Continuous Attractor Network Models of Grid Cells.” Edited by Olaf Sporns. *PLoS Computational Biology* 5 (2): e1000291.

Burgalossi, Andrea, Moritz von Heimendahl, and Michael Brecht. 2014. “Deep Layer Neurons in the Rat Medial Entorhinal Cortex Fire Sparsely Irrespective of Spatial Novelty.” *Frontiers in Neural Circuits* 8 (July): 74.

Burgalossi, Andrea, Lucas Herfst, Moritz von Heimendahl, Henning Förste, Kurt Haskic, Martin Schmidt, and Michael Brecht. 2011. “Microcircuits of Functionally Identified Neurons in the Rat Medial Entorhinal Cortex.” *Neuron* 70 (4): 773–86.

Burwell, Rebecca D., and David G. Amaral. 1998. “Cortical Afferents of the Perirhinal, Postrhinal, and Entorhinal Cortices of the Rat.” *Journal of Comparative Neurology* 398 (2): 179–205.

Busse, L., A. Ayaz, N. T. Dhruv, S. Katzner, A. B. Saleem, M. L. Scholvinck, A. D.

Zaharia, and M. Carandini. 2011. “The Detection of Visual Contrast in the Behaving Mouse.” *Journal of Neuroscience* 31 (31): 11351–61.

Buzsáki, György, and Edvard I Moser. 2013. “Memory, Navigation and Theta Rhythm in the Hippocampal-Entorhinal System.” *Nature Neuroscience* 16 (2): 130–38.

Buzsáki, György, and David Tingley. 2018. “Space and Time: The Hippocampus as a Sequence Generator.” *Trends in Cognitive Sciences* 22 (10): 853–69.

Canto, Cathrin B., and Menno P. Witter. 2012a. “Cellular Properties of Principal Neurons in the Rat Entorhinal Cortex. I. The Lateral Entorhinal Cortex.” *Hippocampus* 22 (6): 1256–76.

Canto, Cathrin B., Floris G. Wouterlood, and Menno P. Witter. 2008. “What Does the Anatomical Organization of the Entorhinal Cortex Tell Us?” *Neural Plasticity* 2008.

Canto, Cathrin B, and Menno P Witter. 2012b. “Cellular Properties of Principal Neurons in the Rat Entorhinal Cortex. II. The Medial Entorhinal Cortex.” *Hippocampus* 22 (6): 1277–99.

Carpenter, Francis, Daniel Manson, Kate Jeffery, Neil Burgess, and Caswell Barry. 2015. “Grid Cells Form a Global Representation of Connected Environments.” *Current Biology : CB* 25 (9): 1176–82.

Chen, G., J. A. King, N. Burgess, and J. O’Keefe. 2013. “How Vision and Movement Combine in the Hippocampal Place Code.” *Proceedings of the National Academy of Sciences* 110 (1): 378–83.

Christopher D. Harvey, Philip Coen and David W. Tank. 2012. “Choice-Specific Sequences in Parietal Cortex during a Virtual- Navigat” 484 (7392): 62–68.

Chung, Jason E., Jeremy F. Magland, Alex H. Barnett, Vanessa M. Tolosa, Angela C. Tooker, Kye Y. Lee, Kedar G. Shah, Sarah H. Felix, Loren M. Frank, and Leslie F. Greengard. 2017. “A Fully Automated Approach to Spike Sorting.” *Neuron* 95 (6): 1381–1394.e6.

Chung, Kwanghun, Jenelle Wallace, Sung-Yon Kim, Sandhiya Kalyanasundaram, Aaron S. Andalman, Thomas J. Davidson, Julie J. Mirzabekov, et al. 2013. “Structural and Molecular Interrogation of Intact Biological Systems.” *Nature* 497

(7449): 332–37.

Claessen, Michiel H.G., and Ineke J.M. van der Ham. 2017. “Classification of Navigation Impairment: A Systematic Review of Neuropsychological Case Studies.” *Neuroscience & Biobehavioral Reviews* 73 (February): 81–97.

Clark, R E, S M Zola, and L R Squire. 2000. “Impaired Recognition Memory in Rats after Damage to the Hippocampus.” *The Journal of Neuroscience : The Official Journal of the Society for Neuroscience* 20 (23): 8853–60.

Cochran, William W, Henrik Mouritsen, and Martin Wikelski. 2004. “Migrating Songbirds Recalibrate Their Magnetic Compass Daily from Twilight Cues.” *Science (New York, N.Y.)* 304 (5669): 405–8.

Constantinescu, A. O., J. X. OReilly, and T. E. J. Behrens. 2016. “Organizing Conceptual Knowledge in Humans with a Gridlike Code.” *Science* 352 (6292): 1464–68.

Czajkowski, Rafał, Jørgen Sugar, Sheng-Jia Zhang, Jonathan J Couey, Jing Ye, and Menno P Witter. 2013. “Systems/Circuits Superficially Projecting Principal Neurons in Layer V of Medial Entorhinal Cortex in the Rat Receive Excitatory Retrosplenial Input.” *The Journal of Neuroscience* 33 (40): 15778–92.

Danziger, Shai, Jonathan Levav, and Liora Avnaim-Pesso. 2011. “Extraneous Factors in Judicial Decisions.” *Proceedings of the National Academy of Sciences of the United States of America* 108 (17): 6889–92.

Darwin, C. 1873. “Origin of Certain Instincts.” *Nature*, no. 7: 417–18.

Davis, A E, A M Gimenez, and B Therrien. 2001. “Effects of Entorhinal Cortex Lesions on Sensory Integration and Spatial Learning.” *Nursing Research* 50 (2): 77–85. http://www.ncbi.nlm.nih.gov/pubmed/11302296.

Deshmukh, Sachin S, D Yoganarasimha, Horatiu Voicu, and James J Knierim. 2010. “Theta Modulation in the Medial and the Lateral Entorhinal Cortices.” *Journal of Neurophysiology* 104 (May): 994–1006.

Dickson, Clayton T., Ian J. Kirk, Scott D. Oddie, and Brian H. Bland. 1995. “Classification of Theta-Related Cells in the Entorhinal Cortex: Cell Discharges Are Controlled by the Ascending Brainstem Synchronizing Pathway in Parallel with Hippocampal Theta-Related Cells.” *Hippocampus* 5 (4): 306–19.

Domnisoru, Cristina, Amina A Kinkhabwala, and David W Tank. 2013. “Membrane Potential Dynamics of Grid Cells.” *Nature* 495: 199–204.

Dordek, Yedidyah, Daniel Soudry, Ron Meir, and Dori Derdikman. 2016. “Extracting Grid Cell Characteristics from Place Cell Inputs Using Non-Negative Principal Component Analysis.” *ELife* 5 (March).

Dumont, Julie R., and Jeffrey S. Taube. 2015. “The Neural Correlates of Navigation beyond the Hippocampus.” *Progress in Brain Research* 219: 83–102.

Egorov, A V, B N Hamam, E Fransen, M E Hasselmo, and Angel A Alonso. 2002. “Graded Persistent Activity in Entorhinal Cortex Neurons.” *Nature* 420 (6912): 173–78.

Einevoll, Gaute T, Felix Franke, Espen Hagen, Christophe Pouzat, and Kenneth D Harris. 2013. “Towards Reliable Spike-Train Recordings from Thousands of Neurons with Multielectrodes.” *Curr Opin Neurobiol* 22 (1): 11–17.

Ekanadham, Chaitanya, Daniel Tranchina, and Eero P Simoncelli. 2014. “A Unified Framework and Method for Automatic Neural Spike Identification TL - 222.” *Journal of Neuroscience Methods* 222 VN-: 47–55.

Endres, Dominik M, and Johannes E Schindelin. 2003. “A New Metric for Probability Distributions.” *IEEE Transactions on Information Theory* 49 (7): 1858–60.

Etienne, AS, and KJ Jeffery. 2004. “Path Integration in Mammals.” *HIPPOCAMPUS* 14 (2): 180–92.

Faul, Franz, Edgar Erdfelder, A.-G. Lang, and Axel Buchner. 2007. “G*Power: A Flexible Statistical Power Analysis Program for the Social, Behavioral, and Biomedical Sciences.” *Behavior Research Methods* 39 (2): 175–91.

Feil, Susanne, Nadejda Valtcheva, and Robert Feil. 2009. *Inducible Cre Mice*. *Methods in Molecular Biology*. Vol. 530.

Fenton, André A, Hsin-Yi Kao, Samuel A Neymotin, Andrey Olypher, Yevgeniy Vayntrub, William W Lytton, and Nandor Ludvig. 2008. “Unmasking the CA1 Ensemble Place Code by Exposures to Small and Large Environments: More Place Cells and Multiple, Irregularly Arranged, and Expanded Place Fields in the Larger Space.” *The Journal of Neuroscience : The Official Journal of the Society*

for Neuroscience 28 (44): 11250–62.

Ferbinteanu, Janina. 2016. “Contributions of Hippocampus and Striatum to Memory-Guided Behavior Depend on Past Experience.” *The Journal of Neuroscience : The Official Journal of the Society for Neuroscience* 36 (24): 6459–70.

Fernández-Durán, Juan José, and María Mercedes Gregorio- Domínguez. 2010. “A Likelihood Ratio Test for Homogeneity in Circular Data.” *Journal of Biometrics & Biostatistics* 1 (3).

Field, David J. 1994. “Field - 1994 - What Is the Goal of Sensory Coding.Pdf.” *Neural Computation1*.

Fiete, I. R., Y. Burak, and T. Brookings. 2008. “What Grid Cells Convey about Rat Location.” *Journal of Neuroscience* 28 (27): 6858–71.

Frank, Loren M., and Emery N Brown. 2003. “Persistent Activity and Memory in the Entorhinal Cortex.” *Trends in Neurosciences* 26 (8): 397–400.

Franke, Felix, Michal Natora, Clemens Boucsein, Matthias H.J. Munk, and Klaus Obermayer. 2010. “An Online Spike Detection and Spike Classification Algorithm Capable of Instantaneous Resolution of Overlapping Spikes.” *Journal of Computational Neuroscience* 29 (1–2): 127–48.

Fransén, Erik, Babak Tahvildari, Alexei V. Egorov, Michael E. Hasselmo, and Angel A. Alonso. 2006. “Mechanism of Graded Persistent Cellular Activity of Entorhinal Cortex Layer V Neurons.” *Neuron* 49 (5): 735–46.

Fujimaru, Y, and T Kosaka. 1996. “The Distribution of Two Calcium Binding Proteins, Calbindin D-28K and Parvalbumin, in the Entorhinal Cortex of the Adult Mouse.” *Neuroscience Research* 24 (4): 329–43.

Fyhn, Marianne, Sturla Molden, Menno P Witter, Edvard I Moser, and May-Britt Moser. 2004. “Spatial Representation in the Entorhinal Cortex.” *Science (New York, N.Y.)* 305 (5688): 1258–64.

Gamma, Erich, Richard Helm, Ralph Johnson, and John Vlissides. 1994. *Design Patterns - Elements of Reusable Object-Oriented Software*.

Geva-Sagiv, Maya, Liora Las, Yossi Yovel, and Nachum Ulanovsky. 2015. “Spatial Cognition in Bats and Rats: From Sensory Acquisition to Multiscale Maps and Navigation.” *Nature Reviews Neuroscience* 16 (2): 94–108.

Gil, Mariana, Mihai Ancau, Magdalene I. Schlesiger, Angela Neitz, Kevin Allen, Rodrigo J. De Marco, and Hannah Monyer. 2018. “Impaired Path Integration in Mice with Disrupted Grid Cell Firing.” *Nature Neuroscience* 21 (1): 81–93.

Gilmore, Rick O., Michele T. Diaz, Brad A. Wyble, and Tal Yarkoni. 2017. “Progress toward Openness, Transparency, and Reproducibility in Cognitive Neuroscience.” *Annals of the New York Academy of Sciences* 1396 (1): 5–18.

Giocomo, Lisa M, May-Britt Moser, and Edvard I Moser. 2011. “Computational Models of Grid Cells.” *Neuron* 71 (4): 589–603.

Gold, Carl, Darrell A Henze, Christof Koch, and György Buzsáki. 2006. “On the Origin of the Extracellular Action Potential Waveform : A Modeling Study On the Origin of the Extracellular Action Potential Waveform : A Modeling Study.” *J Neurophysiol* 95: 3113–28.

Gray, John R, Vincent Pawlowski, and Mark a Willis. 2002. “A Method for Recording Behavior and Multineuronal CNS Acti v Ity from Tethered Insects Flying in Virtual Space.” *Journal of Neuroscience Methods* 120: 211–23.

Gu, Yi, Sam Lewallen, Amina A. Kinkhabwala, Cristina Domnisoru, Kijung Yoon, Jeffrey L. Gauthier, Ila R. Fiete, and David W. Tank. 2018. “A Map-like Micro-Organization of Grid Cells in the Medial Entorhinal Cortex.” *Cell*, September.

Guanella, ALEXIS, DANIEL Kiper, and PAUL Verschure. 2007. “A Model of Grid Cells Based on a Twisted Torus Topology.” *International Journal of Neural Systems* 17 (04): 231–40.

Hafting, Torkel, Marianne Fyhn, Sturla Molden, May-britt Moser, and Edvard I Moser. 2005. “Microstructure of a Spatial Map in the Entorhinal Cortex.” *Nature* 436 (11): 801–6.

Hartley, Tom, N. Burgess, C. Lever, F. Cacucci, and J. O’Keefe. 2000. “Modeling Place Fields in Terms of the Cortical Inputs to the Hippocampus.” *Hippocampus* 10 (4): 369–79.

Harvey, Christopher D, Forrest Collman, Daniel a Dombeck, and David W Tank. 2009. “Intracellular Dynamics of Hippocampal Place Cells during Virtual Navigation.” *October* 461 (7266): 941–46.

Hassoun, Mohamad H., and Mohamad H. 1995. *Fundamentals of Artificial Neural Networks*. MIT Press. https://dl.acm.org/citation.cfm?id=526717.

Heys, James G, Krsna V Rangarajan, and Daniel A Dombeck. 2015. “The Functional Micro-Organization of Grid Cells Revealed by Cellular-Resolution Imaging.” *Neuron* 84 (5): 1079–90.

Hilgen, Gerrit, Martino Sorbaro, Sahar Pirmoradian, Jens-Oliver Muthmann, Ibolya Edit Kepiro, Simona Ullo, Cesar Juarez Ramirez, et al. 2017. “Unsupervised Spike Sorting for Large-Scale, High-Density Multielectrode Arrays.” *Cell Reports* 18 (10): 2521–32.

Hill, Daniel N, Samar B Mehta, and David Kleinfeld. 2015. “Quality Metrics to Accompany Spike Sorting of Extracellular Signals.” *J Neuroscience* 25 (8): 713–24.

Hodgkin, A. L., and A. F. Huxley. 1952. “A Quantitative Description of Membrane Current and Its Application to Conduction and Excitation in Nerve.” *Bulletin of Mathematical Biology* 117: 500–544.

Holland, Richard A., Joseph L. Kirschvink, Thomas G. Doak, and Martin Wikelski. 2008. “Bats Use Magnetite to Detect the Earth’s Magnetic Field.” Edited by Sarah Frances Brosnan. *PLoS ONE* 3 (2): e1676.

Holscher, C. 2005. “Rats Are Able to Navigate in Virtual Environments.” *Journal of Experimental Biology* 208 (3): 561–69.

Hori, Etsuro, Yoichi Nishio, Kenichi Kazui, Katsumi Umeno, Eiichi Tabuchi, Kazuo Sasaki, Shunro Endo, Taketoshi Ono, and Hisao Nishijo. 2005. “Place-Related Neural Responses in the Monkey Hippocampal Formation in a Virtual Space.” *Hippocampus* 15 (8): 991–96.

Iqbal, Shareen A., Joshua D. Wallach, Muin J. Khoury, Sheri D. Schully, and John P. A. Ioannidis. 2016. “Reproducible Research Practices and Transparency across the Biomedical Literature.” Edited by David L Vaux. *PLOS Biology* 14 (1): e1002333.

Ismakov, Revekka, Omri Barak, Kate Jeffery, and Dori Derdikman. 2017. “Grid Cells Encode Local Positional Information.” *Current Biology* 27: 2337–2343.e3.

Jacob, Pierre-Yves, Giulio Casali, Laure Spieser, Hector Page, Dorothy Overington,

and Kate Jeffery. 2017. “An Independent, Landmark-Dominated Head-Direction Signal in Dysgranular Retrosplenial Cortex.” *Nature Neuroscience* 20 (2): 173–75.

JAX. n.d. “Body Weight Information.” The Jackson Laboratory. Accessed July 17, 2015. http://jaxmice.jax.org/support/weight/000664.html.

Jones, Bethany F., and Menno P. Witter. 2007. “Cingulate Cortex Projections to the Parahippocampal Region and Hippocampal Formation in the Rat.” *Hippocampus* 17 (10): 957–76.

Kadir, S N, D F M Goodman, and K D Harris. 2017. “High-Dimensional Cluster Analysis with the Masked EM Algorithm” 26 (11): 2379–94.

Kadir, Shabnam N, Dan F M Goodman, and Kenneth D Harris. 2014. “High-Dimensional Cluster Analysis with the Masked EM Algorithm.” *Neural Computation* 26 (11): 2379–94.

Kanter, Benjamin R., Christine M. Lykken, Daniel Avesar, Aldis Weible, Jasmine Dickinson, Benjamin Dunn, Nils Z. Borgesius, Yasser Roudi, and Clifford G. Kentros. 2017. “A Novel Mechanism for the Grid-to-Place Cell Transformation Revealed by Transgenic Depolarization of Medial Entorhinal Cortex Layer II.” *Neuron* 93 (6): 1480–1492.e6.

Kautzky, Magdalena, and Kay Thurley. 2016. “Estimation of Self-Motion Duration and Distance in Rodents Subject Category : Subject Areas :”

Keller, Georg B., Tobias Bonhoeffer, and Mark Hübener. 2012. “Sensorimotor Mismatch Signals in Primary Visual Cortex of the Behaving Mouse.” *Neuron* 74 (5): 809–15.

Killian, Nathaniel J., Michael J. Jutras, and Elizabeth A. Buffalo. 2012. “A Map of Visual Space in the Primate Entorhinal Cortex.” *Nature* 491 (7426): 761–64.

Klukas, Mirko, Marcus Lewis, and Ila Fiete. 2019. “Flexible Representation and Memory of Higher-Dimensional Cognitive Variables with Grid Cells.” *BioRxiv*, March, 578641.

Kohara, Keigo, Michele Pignatelli, Alexander J Rivest, Hae-Yoon Jung, Takashi Kitamura, Junghyup Suh, Dominic Frank, et al. 2014. “Cell Type-Specific Genetic

and Optogenetic Tools Reveal Hippocampal CA2 Circuits.” *Nature Neuroscience* 17 (2): 269–79.

Kozai, Takashi D.Y., and Alberto L. Vazquez. 2015. “Photoelectric Artefact from Optogenetics and Imaging on Microelectrodes and Bioelectronics: New Challenges and Opportunities.” *Journal of Materials Chemistry. B, Materials for Biology and Medicine* 3 (25): 4965.

Kravitz, Alexxai V, Scott F Owen, and Anatol C Kreitzer. 2013. “Optogenetic Identification of Striatal Projection Neuron Subtypes during in Vivo Recordings.” *Brain Res* 31 (9): 1713–23.

Kropff, Emilio, and Alessandro Treves. 2008. “The Emergence of Grid Cells: Intelligent Design or Just Adaptation?” *Hippocampus* 18 (12): 1256–69.

Krupic, J., M. Bauza, S. Burton, C. Lever, and J. O’Keefe. 2013. “How Environment Geometry Affects Grid Cell Symmetry and What We Can Learn from It.” *Philosophical Transactions of the Royal Society B: Biological Sciences* 369 (1635): 20130188–20130188.

Krupic, Julija, Marius Bauza, Stephen Burton, Caswell Barry, and John O’Keefe. 2015. “Grid Cell Symmetry Is Shaped by Environmental Geometry.” *Nature* 518 (7538): 232–35.

Kvitsiani, D, S Ranade, B Hangya, H Taniguchi, JZ Huang, and A Kepecs. 2013. “Distinct Behavioural and Network Correlates of Two Interneuron Types in Prefrontla Cortex.” *Nature* 11 (4).

Landis, Story C., Susan G. Amara, Khusru Asadullah, Chris P. Austin, Robi Blumenstein, Eileen W. Bradley, Ronald G. Crystal, et al. 2012. “A Call for Transparent Reporting to Optimize the Predictive Value of Preclinical Research.” *Nature* 490 (7419): 187–91.

Lashley, K S. 1929. *Brain Mechanisms and Intelligence*. Chicago.

Leighty, Katherine A., and Dorothy M. Fragaszy. 2003. “Primates in Cyberspace: Using Interactive Computer Tasks to Study Perception and Action in Nonhuman Animals.” *Animal Cognition* 6 (3): 137–39.

Leutgeb, Jill K, Stefan Leutgeb, May-Britt Moser, and Edvard I Moser. 2007. “Pattern Separation in the Dentate Gyrus and CA3 of the Hippocampus.” *Science (New*

York, N.Y.) 315 (5814): 961–66.

Lever, Colin, Stephen Burton, Ali Jeewajee, John O'Keefe, and Neil Burgess. 2009. "Boundary Vector Cells in the Subiculum of the Hippocampal Formation." *The Journal of Neuroscience : The Official Journal of the Society for Neuroscience* 29 (31): 9771–77.

Lewicki, M S. 1998. "A Review of Methods for Spike Sorting: The Detection and Classification of Neural Action Potentials." *Network (Bristol, England)* 9 (4): R53-78.

Lima, Susana Q., Tomáš Hromádka, Petr Znamenskiy, and Anthony M. Zador. 2009. "PINP: A New Method of Tagging Neuronal Populations for Identification during in Vivo Electrophysiological Recording." *PLoS ONE* 4 (7).

Lipp, Hans-Peter, Alexei L Vyssotski, David P Wolfer, Sophie Renaudineau, Maria Savini, Gerhard Tröster, and Giacomo Dell'Omo. 2004. "Pigeon Homing along Highways and Exits." *Current Biology* 14 (14): 1239–49.

Liske, Holly, Xiang Qian, Polina Anikeeva, Karl Deisseroth, and Scott Delp. 2013. "Optical Control of Neuronal Excitation and Inhibition Using a Single Opsin Protein, ChR2." *Scientific Reports* 3 (January): 3110.

Lithfous, Ségolène, André Dufour, and Olivier Després. 2013. "Spatial Navigation in Normal Aging and the Prodromal Stage of Alzheimer's Disease: Insights from Imaging and Behavioral Studies." *Ageing Research Reviews* 12 (1): 201–13.

Lopes, Goncalo, Niccolo Bonacchi, Joao Frazao, Joana P. Neto, Bassam V. Atallah, Sofia Soares, Luis Moreira, et al. 2015. "Bonsai: An Event-Based Framework for Processing and Controlling Data Streams." *Frontiers in Neuroinformatics* 9 (April): 7.

Markus, Etan J., Carol A. Barnes, Bruce L. McNaughton, Victoria L. Gladden, and William E. Skaggs. 1994. "Spatial Information Content and Reliability of Hippocampal CA1 Neurons: Effects of Visual Input." *Hippocampus* 4 (4): 410–21.

Marre, O., D. Amodei, N. Deshmukh, K. Sadeghi, F. Soo, T. E. Holy, and M. J. Berry. 2012. "Mapping a Complete Neural Population in the Retina." *Journal of*

Neuroscience 32 (43): 14859–73.

Martin, Robert. 2008. *Clean Code: A Handbook of Agile Software Craftsmanship*. Massachusetts.

Martínez, Joan José, Bahar Rahsepar, and John A. White. 2017. “Anatomical and Electrophysiological Clustering of Superficial Medial Entorhinal Cortex Interneurons.” *Eneuro* 4 (5): ENEURO.0263-16.2017.

Mathis, Alexander, Andreas V. M. Herz, and Martin B. Stemmler. 2012. “Resolution of Nested Neuronal Representations Can Be Exponential in the Number of Neurons.” *Physical Review Letters* 109 (1): 018103.

Matsumura, Nobuhisa, Hisao Nishijo, Ryoi Tamura, Satoshi Eifuku, Shunro Endo, and Taketoshi Ono. 1999. “Spatial- and Task-Dependent Neuronal Responses during Real and Virtual Translocation in the Monkey Hippocampal Formation.” *J. Neurosci.* 19 (6): 2381–93. http://www.jneurosci.org.sare.upf.edu/content/19/6/2381.long.

Mattis, Joanna, Kay M Tye, Emily A Ferenczi, Charu Ramakrishnan, Daniel J O’Shea, Rohit Prakash, Lisa A Gunaydin, et al. 2012. “Principles for Applying Optogenetic Tools Derived from Direct Comparative Analysis of Microbial Opsins.” *Nature Methods* 9 (2): 159–72.

McCormick, D. A., B. W. Connors, J. W. Lighthall, and D. A. Prince. 1985. “Comparative Electrophysiology of Pyramidal and Sparsely Spiny Stellate Neurons of the Neocortex.” *Journal of Neurophysiology* 54 (4): 782–806.

Mcnaughton, Bruce L, Francesco P Battaglia, Ole Jensen, and Edvard I Moser. 2006. “Path Integration and the Neural Basis of the ‘ Cognitive Map .’” *Nature Neuroscience* 7: 663–78.

Meliza, C Daniel, and Daniel Margoliash. 2013. “Emergence of Selectivity and Tolerance in the Avian Auditory Cortex” 31 (9): 1713–23.

Menzel, R., U. Greggers, A. Smith, S. Berger, R. Brandt, S. Brunke, G. Bundrock, et al. 2005. “Honey Bees Navigate According to a Map-like Spatial Memory.” *Proceedings of the National Academy of Sciences* 102 (8): 3040–45.

Mitchell, Susan J., and James B. Ranck. 1980. “Generation of Theta Rhythm in Medial Entorhinal Cortex of Freely Moving Rats.” *Brain Research* 189 (1): 49–66.

Mittelstaedt, M.-L., and H. Mittelstaedt. 1980. “Homing by Path Integration in a Mammal.” *Naturwi* 67.

Mizuno, Hidenobu, Wenshu Luo, Etsuko Tarusawa, Yoshikazu M. Saito, Takuya Sato, Yumiko Yoshimura, Shigeyoshi Itohara, and Takuji Iwasato. 2014. “NMDAR-Regulated Dynamics of Layer 4 Neuronal Dendrites during Thalamocortical Reorganization in Neonates.” *Neuron* 82 (2): 365–79.

Morris, Richard G M. 1981. “Spatial Localization Does Not Require the Presence of Local Cues.” *Learning and Motivation* 12 (2): 239–60.

Moser, May-Britt, David C Rowland, and Edvard I Moser. 2015. “Place Cells, Grid Cells, and Memory.” *Cold Spring Harbor Perspectives in Biology* 7 (2): a021808.

Muller, R U, and J L Kubie. 1987. “The Effects of Changes in the Environment on the Spatial Firing of Hippocampal Complex-Spike Cells.” *The Journal of Neuroscience : The Official Journal of the Society for Neuroscience* 7 (7): 1951–68.

O’Keefe, J, and J Dostrovsky. 1971. “The Hippocampus as a Spatial Map . Preliminary Evidence from Unit Activity in the Freely-Moving Rat.” *Brain Research* 34: 171–75.

O’Keefe, John, and Lynn Nadel. 1978. *The Hippocampus as a Cognitive Map*. *Oxford, UK:Clarendon*.

Oh, Seung Wook, Julie A. Harris, Lydia Ng, Brent Winslow, Nicholas Cain, Stefan Mihalas, Quanxin Wang, et al. 2014. “A Mesoscale Connectome of the Mouse Brain.” *Nature* 508 (7495): 207–14.

Ohara, Shinya, Mariko Onodera, Øyvind W Simonsen, Rintaro Yoshino, Hiroyuki Hioki, Toshio Iijima, Ken-Ichiro Tsutsui, and Menno P Witter. 2018. “Intrinsic Projections of Layer Vb Neurons to Layers Va, III, and II in the Lateral and Medial Entorhinal Cortex of the Rat.” *Cell Reports* 24 (1): 107–16.

Olton, David S., and Robert J. Samuelson. 1976. “Remembrance of Places Passed: Spatial Memory in Rats.” *Journal of Experimental Psychology: Animal Behavior Processes* 2 (2): 97–116.

Perkel, Jeffrey M. 2018. “A Toolkit for Data Transparency Takes Shape.” *Nature 2018*

560:7719, August.

Pi, Hyun-Jae, Balazs Hangya, Duda Kvitsiani, Joshua I Sanders, Z Josh Huang, and Adam Kepecs. 2014. “Cortical Interneurons That Specialize in Disinhibitory.Pdf.” *Nature* 503 (7477): 521–24.

“Plexon Offline Sorter.” 2017.

Prinz, Florian, Thomas Schlange, and Khusru Asadullah. 2011. “Believe It or Not: How Much Can We Rely on Published Data on Potential Drug Targets?” *Nature Reviews Drug Discovery* 10 (9): 712–712.

Quilichini, Pascale, Anton Sirota, and György Buzsáki. 2010. “Intrinsic Circuit Organization and Theta-Gamma Oscillation Dynamics in the Entorhinal Cortex of the Rat.” *The Journal of Neuroscience : The Official Journal of the Society for Neuroscience* 30 (33): 11128–42.

Ramirez, Steve, Xu Liu, Pei-Ann Lin, Junghyup Suh, Michele Pignatelli, Roger L Redondo, Tomás J Ryan, and Susumu Tonegawa. 2013. “Creating a False Memory in the Hippocampus.” *Science (New York, N.Y.)* 341 (6144): 387–91.

Ramón Y Cajal, S. 1902. “Sobre Un Ganglio Especial de La Corteza Esfeno-Occipital.” *Trab. Del Lab. de Invest. Biol. Univ. Madrid* 1: 189–206.

Ramsden, Helen L., Gülşen Sürmeli, Steven G. McDonagh, and Matthew F. Nolan. 2015. “Laminar and Dorsoventral Molecular Organization of the Medial Entorhinal Cortex Revealed by Large-Scale Anatomical Analysis of Gene Expression.” *PLOS Computational Biology* 11 (1): e1004032.

Ravassard, Pascal, Ashley Kees, Bernard Willers, David Ho, Daniel A Aharoni, Jesse Cushman, Zahra M Aghajan, and Mayank R Mehta. 2013. “Multi-Sensory Control of Hippocampal Spatiotemporal Selectivity.” *Science* 340 (6138): 1342–46.

Reardon, Thomas R, Andrew J Murray, Gergely F Turi, Christoph Wirblich, Katherine R Croce, Matthias J Schnell, Thomas M Jessell, and Attila Losonczy. 2016. “Rabies Virus CVS-N2c(ΔG) Strain Enhances Retrograde Synaptic Transfer and Neuronal Viability.” *Neuron* 89 (4): 711–24.

Redhead, Edward S., Amanda Roberts, Mark Good, and John M. Pearce. 1997. “Interaction between Piloting and Beacon Homing by Rats in a Swimming Pool.” *Journal of Experimental Psychology: Animal Behavior Processes* 23 (3): 340–

50.

Reifenstein, Eric T, Richard Kempter, Susanne Schreiber, Martin B Stemmler, and Andreas V M Herz. 2012. “Grid Cells in Rat Entorhinal Cortex Encode Physical Space with Independent Firing Fields and Phase Precession at the Single-Trial Level.” *Proceedings of the National Academy of Sciences of the United States of America* 109 (16): 6301–6.

Renier, Nicolas, Zhuhao Wu, David J. Simon, Jing Yang, Pablo Ariel, and Marc Tessier-Lavigne. 2014. “IDISCO: A Simple, Rapid Method to Immunolabel Large Tissue Samples for Volume Imaging.” *Cell* 159 (4): 896–910.

Rey, Hernan Gonzalo, Carlos Pedreira, and Rodrigo Quian Quiroga. 2015. “Past, Present and Future of Spike Sorting Techniques.” *Brain Research Bulletin* 119: 106–17.

Rolston, J.D., R.E. Gross, and S.M. Potter. 2009. “Common Median Referencing for Improved Action Potential Detection with Multielectrode Arrays.” In *2009 Annual International Conference of the IEEE Engineering in Medicine and Biology Society*, 2009:1604–7. IEEE.

Rossant, Cyrille, Shabnam N. Kadir, Dan F.M. Goodman, John Schulman, Maximilian L.D. Hunter, Aman B. Saleem, Andres Grosmark, et al. 2016. “Spike Sorting for Large, Dense Electrode Arrays.” *Nature Neuroscience* 19 (4): 634–41.

Roux, Lisa, Eran Stark, Lucas Sjulson, and György Buzsáki. 2013. “In Vivo Optogenetic Identification and Manipulation of GABAergic Interneuron Subtypes.” *Curr Opin Neurobiol* 31 (9): 1713–23.

———. 2014. “In Vivo Optogenetic Identification and Manipulation of GABAergic Interneuron Subtypes.” *Nature Reviews Cancer* 13 (2): 83–96.

Rowland, David C, Horst A Obenhaus, Emilie R Skytøen, Qiangwei Zhang, Cliff G Kentros, Edvard I Moser, and May-Britt Moser. 2018. “Functional Properties of Stellate Cells in Medial Entorhinal Cortex Layer II.” *ELife* 7 (September).

Sarel, Ayelet, Arseny Finkelstein, Liora Las, and Nachum Ulanovsky. 2017. “Vectorial Representation of Spatial Goals in the Hippocampus of Bats.” *Science* 355 (6321): 176–80.

Sargolini, Francesca, Marianne Fyhn, Torkel Hafting, Bruce L McNaughton, Menno P Witter, May-Britt Moser, and Edvard I Moser. 2006. “Conjunctive Representation of Position, Direction, and Velocity in Entorhinal Cortex.” *Science (New York, N.Y.)* 312 (5774): 758–62.

Schiller, D., H. Eichenbaum, E. A. Buffalo, L. Davachi, D. J. Foster, S. Leutgeb, and C. Ranganath. 2015. “Memory and Space: Towards an Understanding of the Cognitive Map.” *Journal of Neuroscience* 35 (41): 13904–11.

Schindelin, Johannes, Ignacio Arganda-Carreras, Erwin Frise, Verena Kaynig, Mark Longair, Tobias Pietzsch, Stephan Preibisch, et al. 2012. “Fiji: An Open-Source Platform for Biological-Image Analysis.” *Nature Methods* 9 (7): 676–82.

Schmidt-Hieber, Christoph, and Michael Häusser. 2013. “Cellular Mechanisms of Spatial Navigation in the Medial Entorhinal Cortex.” *Nature Neuroscience* 16 (3): 325–31.

Schmitzer-Torbert, N., J. Jackson, D. Henze, K. Harris, and A. D. Redish. 2005. “Quantitative Measures of Cluster Quality for Use in Extracellular Recordings.” *Neuroscience* 131 (1): 1–11.

Séguinot, V., R. Maurer, and A.S. Etienne. 1993. “Dead Reckoning in a Small Mammal: The Evaluation of Distance.” *Journal of Comparative Physiology A* 173 (1).

Shapiro, Matthew L., Heikki Tanila, and Howard Eichenbaum. 1997. “Cues That Hippocampal Place Cells Encode: Dynamic and Hierarchical Representation of Local and Distal Stimuli.” *Hippocampus* 7 (6): 624–42.

Shima, Yasuyuki, Ken Sugino, Chris Martin Hempel, Masami Shima, Praveen Taneja, James B Bullis, Sonam Mehta, Carlos Lois, and Sacha B Nelson. 2016. “A Mammalian Enhancer Trap Resource for Discovering and Manipulating Neuronal Cell Types.” *ELife* 10.7554/eL: 11–13.

Shipston-Sharman, Oliver, Lukas Solanka, and Matthew F Nolan. 2016. “Continuous Attractor Network Models of Grid Cell Firing Based on Excitatory-Inhibitory Interactions.” *The Journal of Physiology* 594 (22): 6547–57.

Siegle, Joshua H., Gregory J. Hale, Jonathan P. Newman, and Jakob Voigts. 2015. “Neural Ensemble Communities: Open-Source Approaches to Hardware for

Large-Scale Electrophysiology.” *Current Opinion in Neurobiology* 32: 53–59.

Siegle, Joshua H., Aaron Cuevas Lopez, Yogi A Pater, Kirill Abramov, Shay Ohayon, and Jakob Voigts. 2017. “Open Ephys : An Open-Source , Plugin-Based Platform for Multichannel Electrophysiology.” *Journal of Neural Engineering* 14.

Skaggs, William E., Bruce L. McNaughton, and Katalin M. Gothard. 1993. “An Information-Theoretic Approach to Deciphering the Hippocampal Code.” https://papers.nips.cc/paper/671-an-information-theoretic-approach-to-deciphering-the-hippocampal-code.

Solstad, Trygve, Charlotte N Boccara, Emilio Kropff, May-Britt Moser, and Edvard I. Moser. 2008. “Representation of Geometric Borders in the Entorhinal Cortex.” *Science (New York, N.Y.)* 1865 (5909): 1–5.

Squire, Larry R. 1992. “Memory and the Hippocampus: A Synthesis from Findings with Rats, Monkeys, and Humans.” *Psychological Review* 99 (2): 195–231.

Stosiek, Christoph, Olga Garaschuk, Knut Holthoff, and Arthur Konnerth. 2003. “In Vivo Two-Photon Calcium Imaging of Neuronal Networks.” *Proceedings of the National Academy of Sciences of the United States of America* 100 (12): 7319–24.

Strauss, R, S Schuster, and K G Götz. 1997. “Processing of Artificial Visual Feedback in the Walking Fruit Fly Drosophila Melanogaster.” *The Journal of Experimental Biology* 200 (Pt 9): 1281–96. http://www.ncbi.nlm.nih.gov/pubmed/9172415.

Stujenske, Joseph M, Timothy Spellman, and Joshua A Gordon. 2017. “Modeling the Spatiotemporal Dynamics of Light and Heat Propagation for in Vivo Optogenetics.” *Cell Reports* 155 (1): 3–12.

Sugar, Jørgen, Menno P Witter, Niels M van Strien, and Natalie L M Cappaert. 2011. “The Retrosplenial Cortex: Intrinsic Connectivity and Connections with the (Para)Hippocampal Region in the Rat. An Interactive Connectome.” *Frontiers in Neuroinformatics* 5: 7.

Sun, Chen, Takashi Kitamura, Jun Yamamoto, Jared Martin, Michele Pignatelli, Lacey J. Kitch, Mark J. Schnitzer, and Susumu Tonegawa. 2015. “Distinct Speed Dependence of Entorhinal Island and Ocean Cells, Including Respective Grid

Cells.” *Proceedings of the National Academy of Sciences* 112 (30): 201511668.

Sun, H. J., D. P. Carey, and M. A. Goodale. 1992. “A Mammalian Model of Optic-Flow Utilization in the Control of Locomotion.” *Exp Brain Res* 91 (1): 171–75.

Sürmeli, Gülşen, Daniel Cosmin Marcu, Christina McClure, Derek L.F. Garden, Hugh Pastoll, and Matthew F. Nolan. 2015. “Molecularly Defined Circuitry Reveals Input-Output Segregation in Deep Layers of the Medial Entorhinal Cortex.” *Neuron* 88: 1–14.

Taube, J S, R U Muller, and J B Ranck. 1990a. “Head-Direction Cells Recorded from the Postsubiculum in Freely Moving Rats. I. Description and Quantitative Analysis.” *The Journal of Neuroscience : The Official Journal of the Society for Neuroscience* 10 (2): 420–35.

———. 1990b. “Head-Direction Cells Recorded from the Postsubiculum in Freely Moving Rats. II. Effects of Environmental Manipulations.” *The Journal of Neuroscience : The Official Journal of the Society for Neuroscience* 10 (2): 436–47.

———. 1990c. “Head-Direction Cells Recorded from the Postsubiculum in Freely Moving Rats. II. Effects of Environmental Manipulations.” *The Journal of Neuroscience : The Official Journal of the Society for Neuroscience* 10 (2): 436–47. http://www.ncbi.nlm.nih.gov/pubmed/2303852.

Tennant, Sarah A, Lukas Fischer, Derek L F Garden, Klára Zsófia Gerlei, Cristina Martinez-Gonzalez, Christina Mcclure, Emma R Wood, and Matthew F Nolan. 2018. “Stellate Cells in the Medial Entorhinal Cortex Are Required for Spatial Learning Article Stellate Cells in the Medial Entorhinal Cortex Are Required for Spatial Learning.” *Cell Reports* 22: 1313–24.

Thyng, Kristen M, Chad A Greene, Robert D Hetland, Heather M Zimmerle, and Steven F DiMarco. 2016. “True Colors of Oceanography Guidelines for Effective and Accurate Colormap Selection.” *Oceanography* 29 (3): 9–13.

Tocker, Gilad, Omri Barak, and Dori Derdikman. 2015a. “Grid Cells Correlation Structure Suggests Organized Feedforward Projections into Superficial Layers of the Medial-Entorhinal Cortex.” *Hippocampus* 00 (0–0): 1–14.

———. 2015b. “Grid Cells Correlation Structure Suggests Organized Feedforward

Projections into Superficial Layers of the Medial Entorhinal Cortex." *Hippocampus* 25 (12): 1599–1613.

Tolman, Edward C. 1948. "Cognitive Maps in Rats and Men." *Psychological Review* 55 (4): 189–208.

Tsoar, Asaf, Ran Nathan, Yoav Bartan, Alexei Vyssotski, Giacomo Dell'Omo, and Nachum Ulanovsky. 2011. "Large-Scale Navigational Map in a Mammal." *Proceedings of the National Academy of Sciences of the United States of America* 108 (37): E718-24.

Valerio, S., and J. S. Taube. 2016. "Head Direction Cell Activity Is Absent in Mice without the Horizontal Semicircular Canals." *Journal of Neuroscience* 36 (3): 741–54.

Vertes, Robert P. 2004. "Differential Projections of the Infralimbic and Prelimbic Cortex in the Rat." *Synapse* 51 (1): 32–58.

Wallace, Dg, Bogdan Gorny, and Iq Whishaw. 2002. "Rats Can Track Odors, Other Rats, and Themselves: Implications for the Study of Spatial Behavior." *Behavioural Brain Research* 131 (1–2): 185–92.

Wilson, M., and B. McNaughton. 1993. "Dynamics of the Hippocampal Ensemble Code for Space." *Science* 261 (5124): 1055–58.

Witter, Menno P., Thanh P. Doan, Bente Jacobsen, Eirik S. Nilssen, and Shinya Ohara. 2017. "Architecture of the Entorhinal Cortex A Review of Entorhinal Anatomy in Rodents with Some Comparative Notes." *Frontiers in Systems Neuroscience* 11 (June): 1–12.

Wood, F, M J Black, C Vargas-Irwin, M R Fellows, and J P Donoghue. 2004. "On the Variability of Manual Spike Sorting." *Ieee Transactions On Biomedical Engineering* 51 (6): 912–18.

Wyass, J. Michael, and Thomas Van Groen. 1992. "Connections between the Retrosplenial Cortex and the Hippocampal Formation in the Rat: A Review." *Hippocampus* 2 (1): 1–11.

Yang, Kai, Haifeng Wu, and Yu Zeng. 2017. "A Simple Deep Learning Method for Neuronal Spike Sorting." *Journal of Physics: Conference Series* 910 (1): 012062.

Yoganarasimha, D, Xintian Yu, and James J Knierim. 2006. “Head Direction Cell Representations Maintain Internal Coherence during Conflicting Proximal and Distal Cue Rotations: Comparison with Hippocampal Place Cells.” *The Journal of Neuroscience : The Official Journal of the Society for Neuroscience* 26 (2): 622–31.

Zemelman, Boris V., Georgia A. Lee, Minna Ng, and Gero Miesenböck. 2002. “Selective Photostimulation of Genetically ChARGed Neurons.” *Neuron* 33 (1): 15–22.

Zhu, Hu, and Bryan L. Roth. 2014. “Silencing Synapses with DREADDs.” *Neuron* 82 (4): 723–25.

Zhu, Peixin, M. Isabel Aller, Udo Baron, Sidney Cambridge, Melanie Bausen, Jan Herb, Jürgen Sawinski, et al. 2007. “Silencing and Un-Silencing of Tetracycline-Controlled Genes in Neurons.” Edited by Peter Fraser. *PLoS ONE* 2 (6): e533.

Appendix A

Multi-unit response examples. The following figures were outputted by MATLAB scripts written by Elizabeth Allison. Top row left to right: action potential waveforms overlaid for the four channels of the tetrode, trajectory of the animal (black line) and firing events (red dots), firing rate map, autocorrelation matrix for rate map, coverage heat map based on the position of the animal. Second row from left to right: smoothed polar histogram of head-direction when the cell fired (red, Hz) and from the whole session (black). The following four plots are the same as in the first row, but only include data from when the animal was running. Third row left to right: action potential waveforms overlaid during light stimulation, raster plot of firing events around light stimulation (blue band), histogram of firing during light stimulation (blue band) for opto tagging (bottom) and high frequency stimulations (top), auto-correlograms, firing throughout the session (top) and histogram of firing events corresponding to the speed of the animal (bottom).

M15-2018-04-23-Tetrode-2-Cluster-6

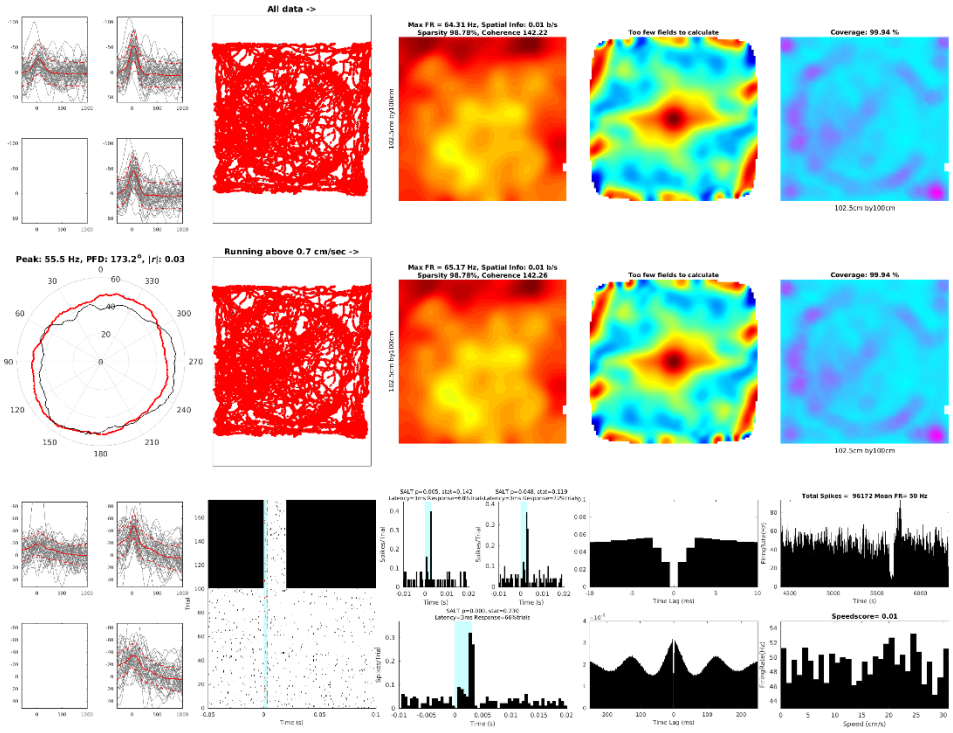

M3-2018-02-19-Tetrode-3-Cluster-11

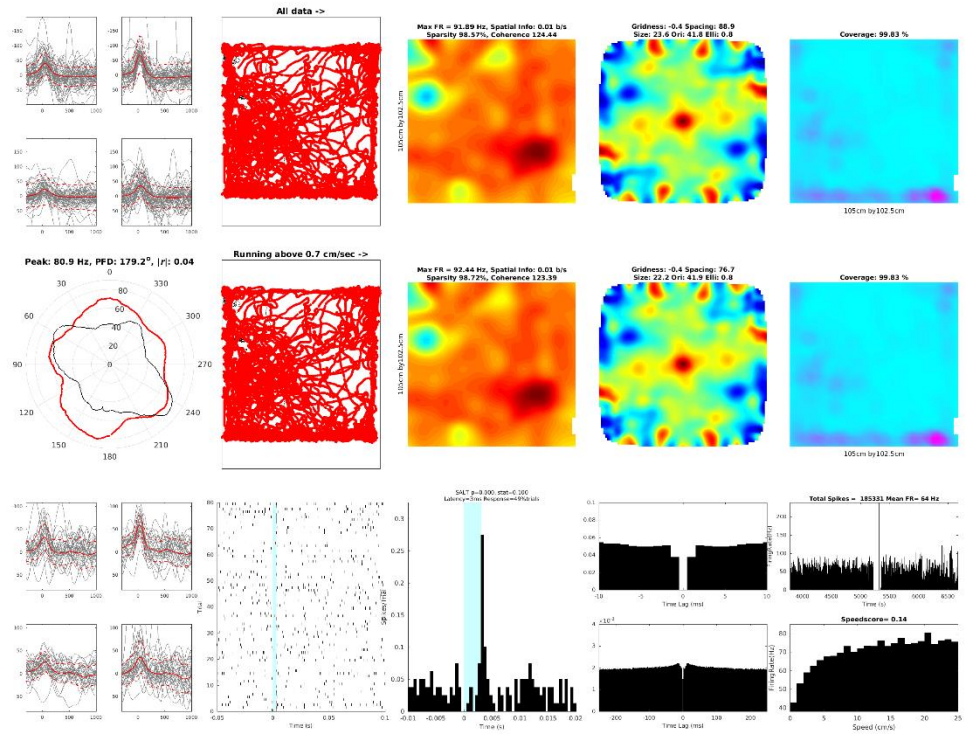

Light responsive cells did not fire during every light pulse. (A) Bandpass filtered traces (600-6000 Hz) of four channels of a tetrode during light stimulation (black lines). (B) Overlaid firing events of two neurons detected on the tetrode. (C) Light stimulation pulses (black line) from (A). Action potentials of cell 1 and cell 2 are visible during some stimulation pulses. Cell 1 fired during pulses 1 and 4. Cell 2 fired during pulses 1, 3 and 4, but did not fire during pulse 2.

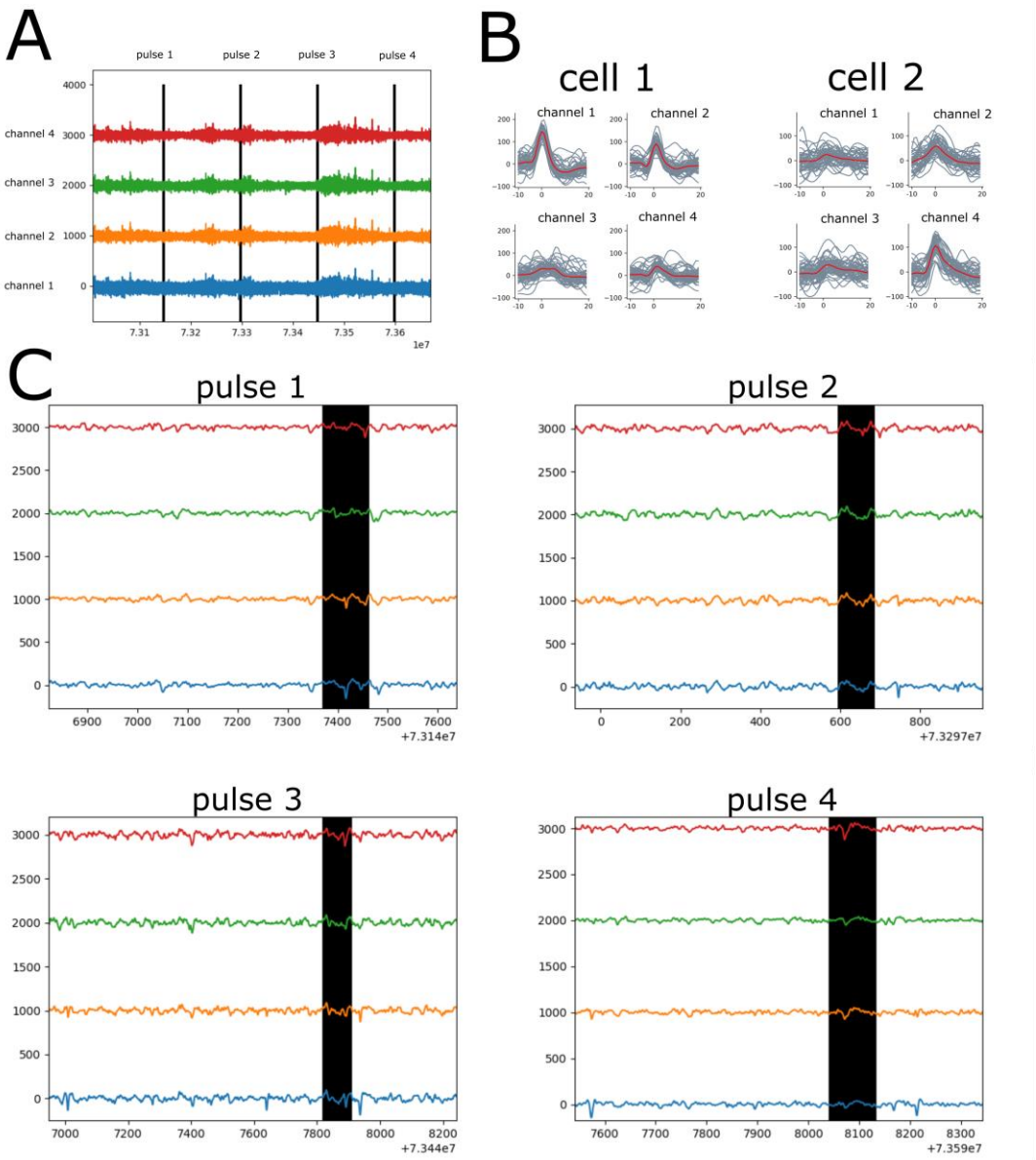

Appendix B

Recording locations for all experimental animals from in vivo open field tetrode recording experiments. Animal IDs are shown on the top left corner for each image. Sagittal brain sections were stained with Neurotrace and anti-mCherry and imaged using a Zeiss Axio Scan Z1 with a 10x objective, scale bar = 1000 µm. Histology and imaging was performed by Holly Stevens.

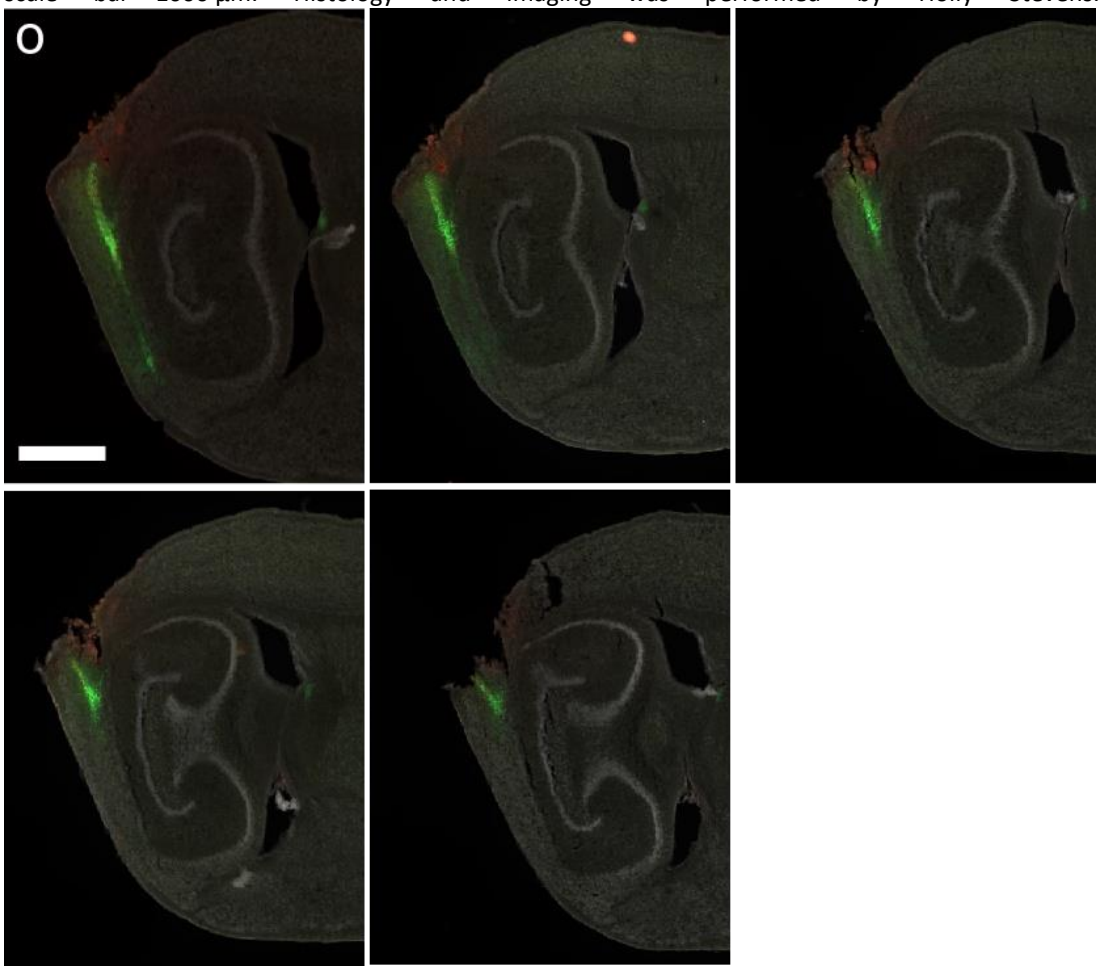

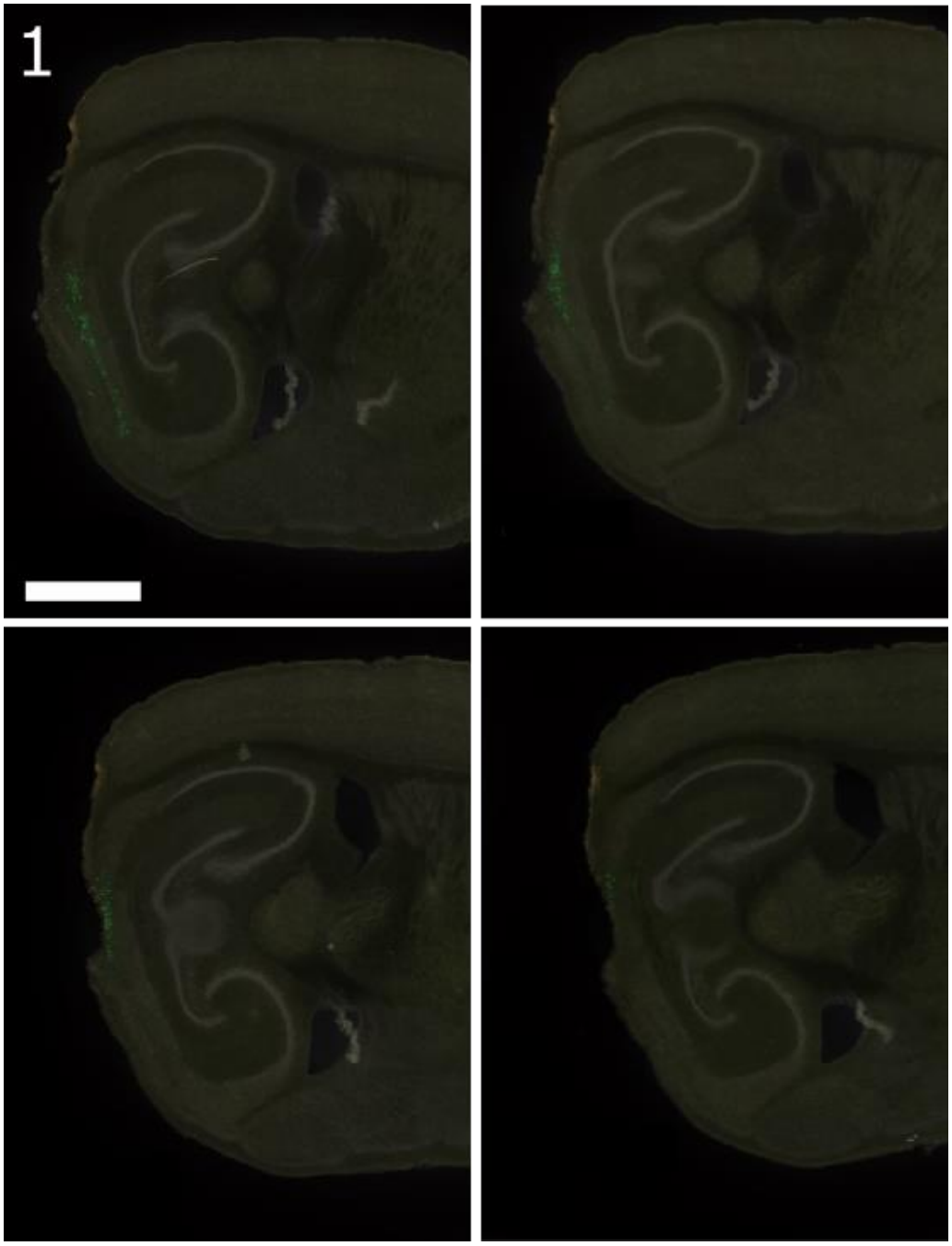
1

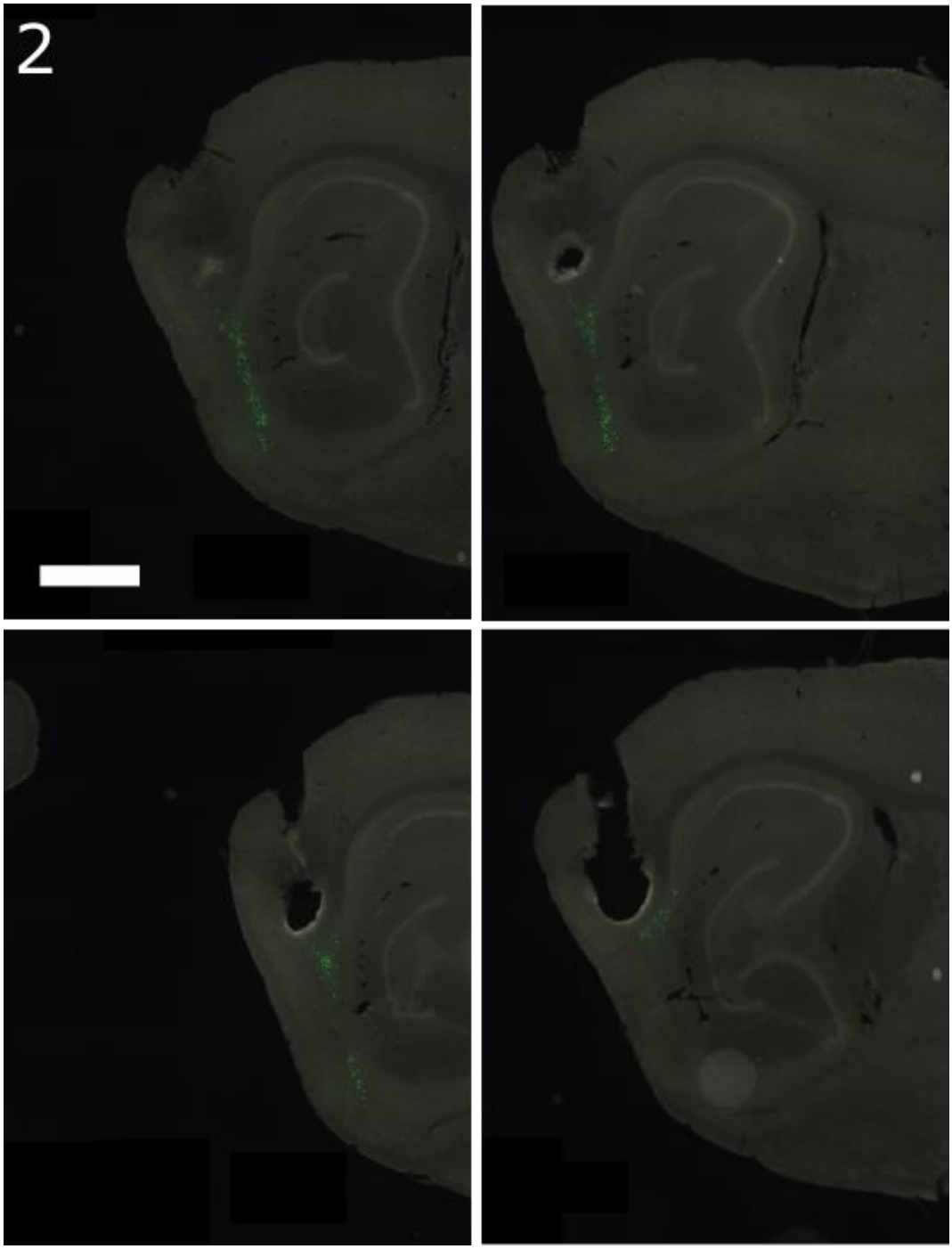
2

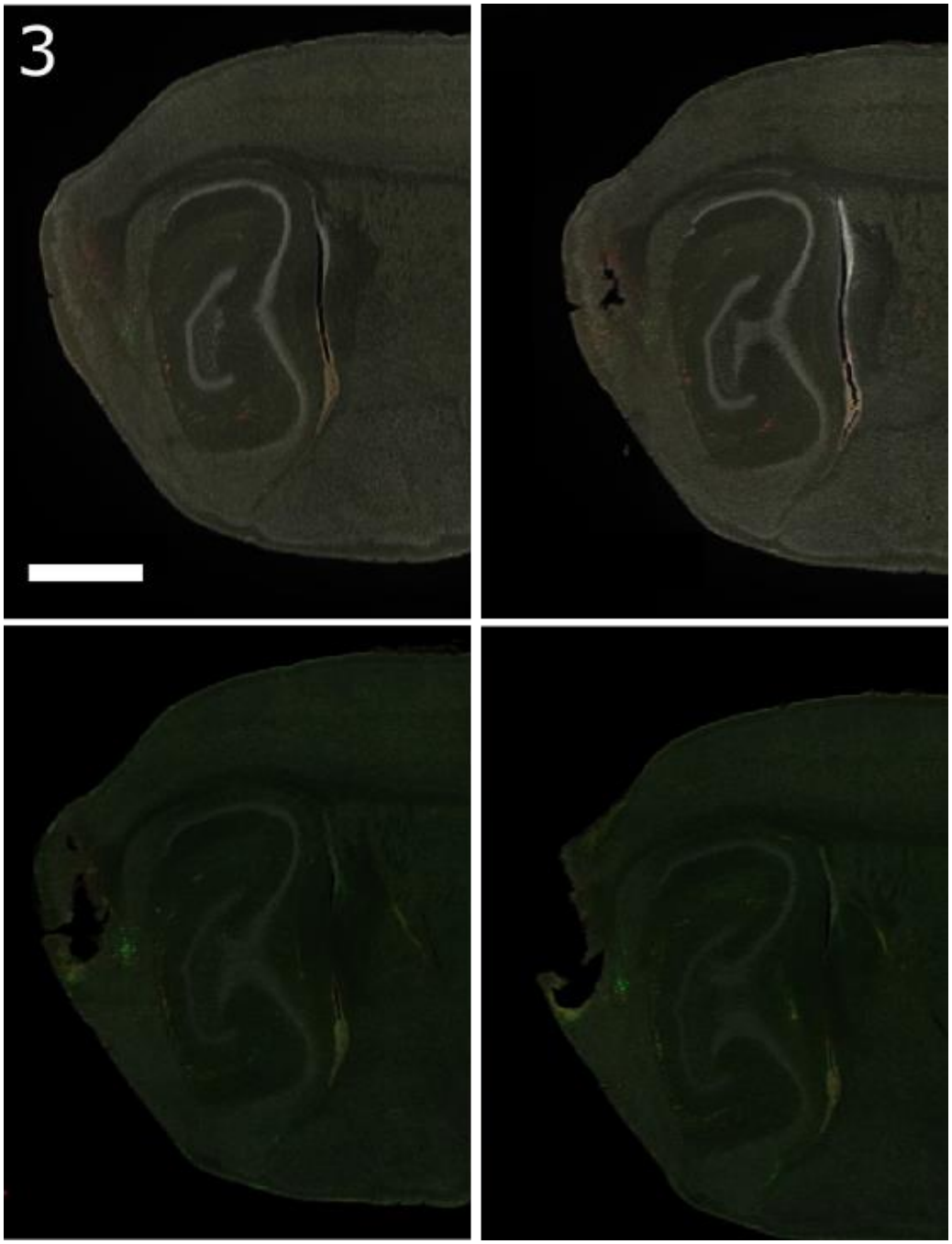
3

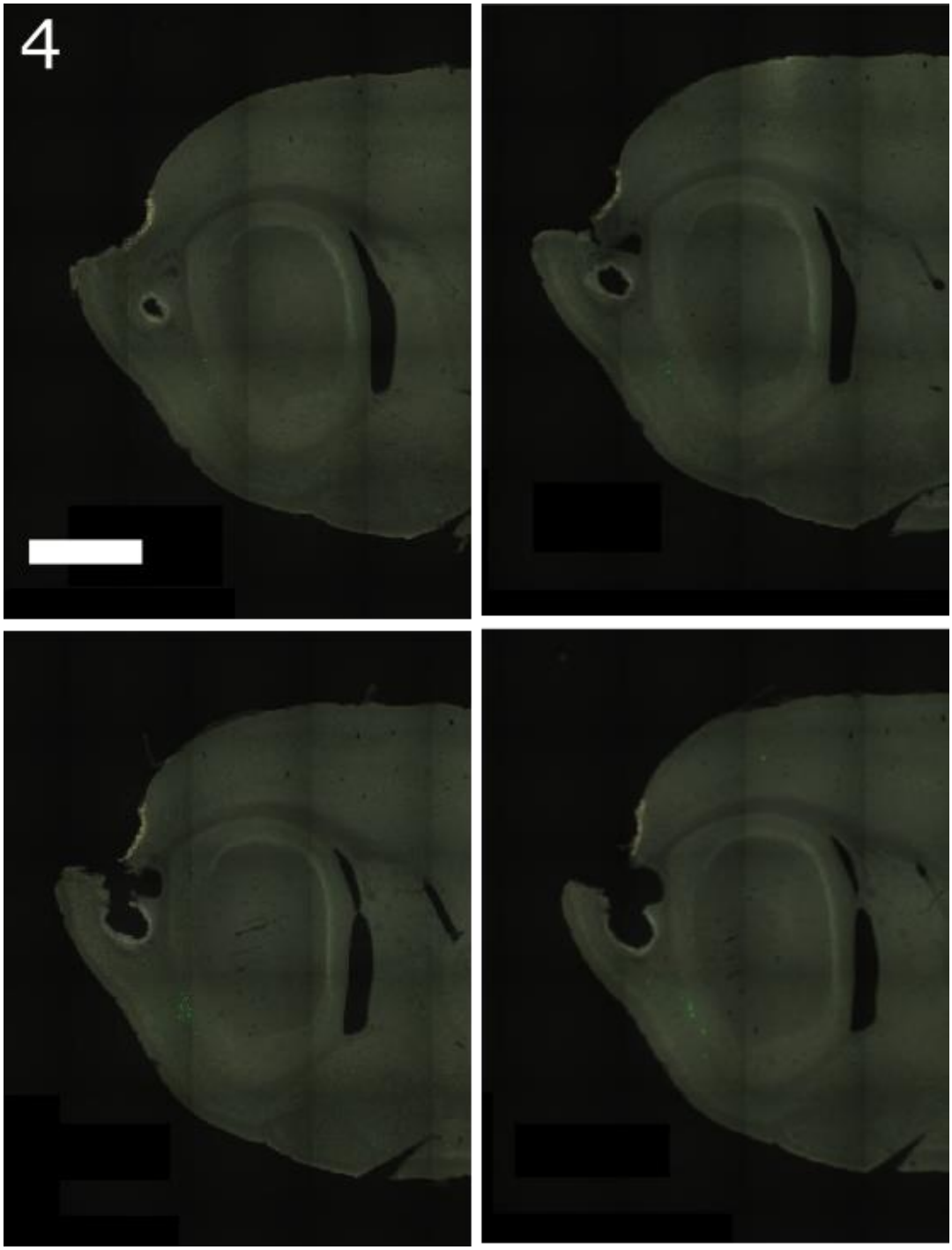
4

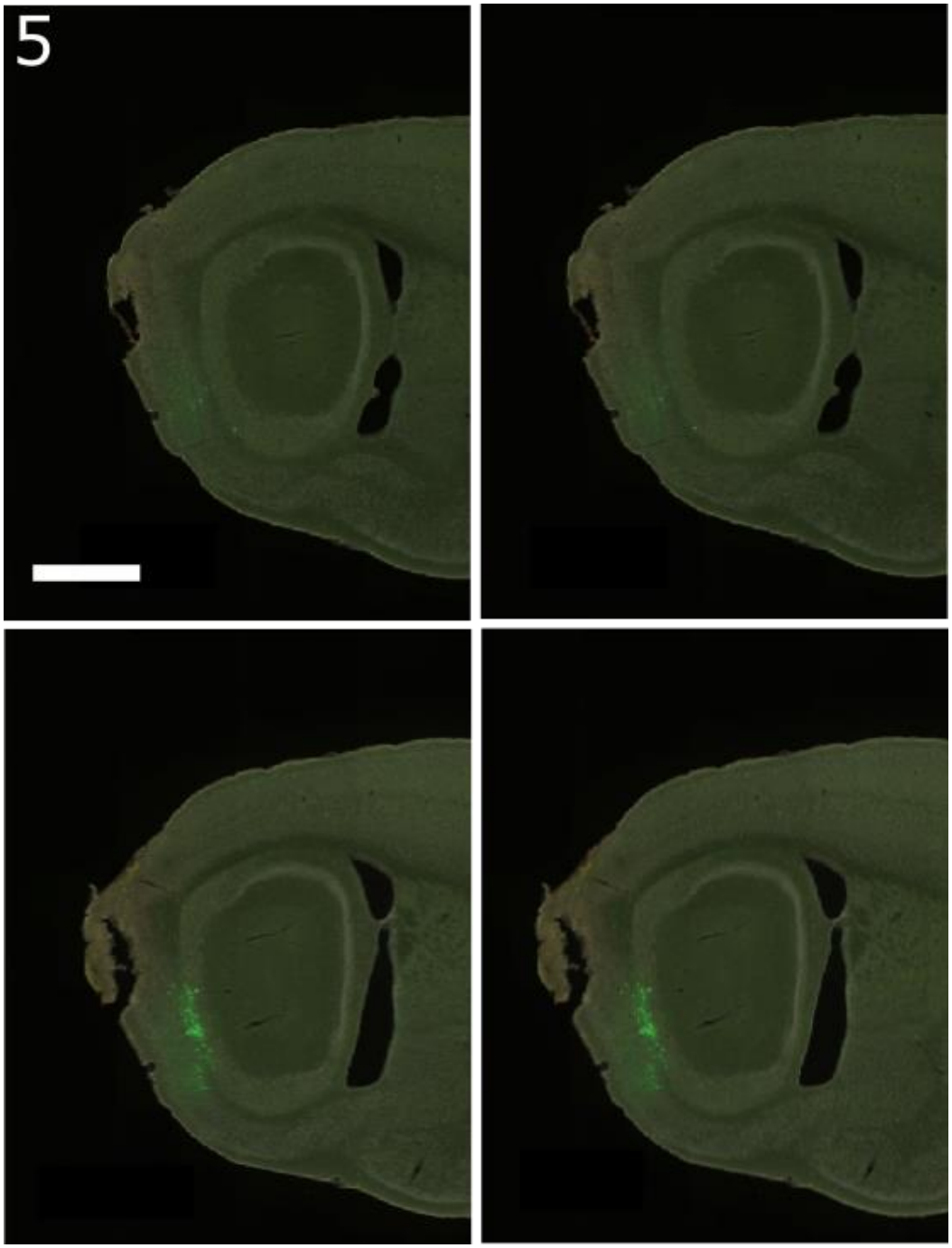
5

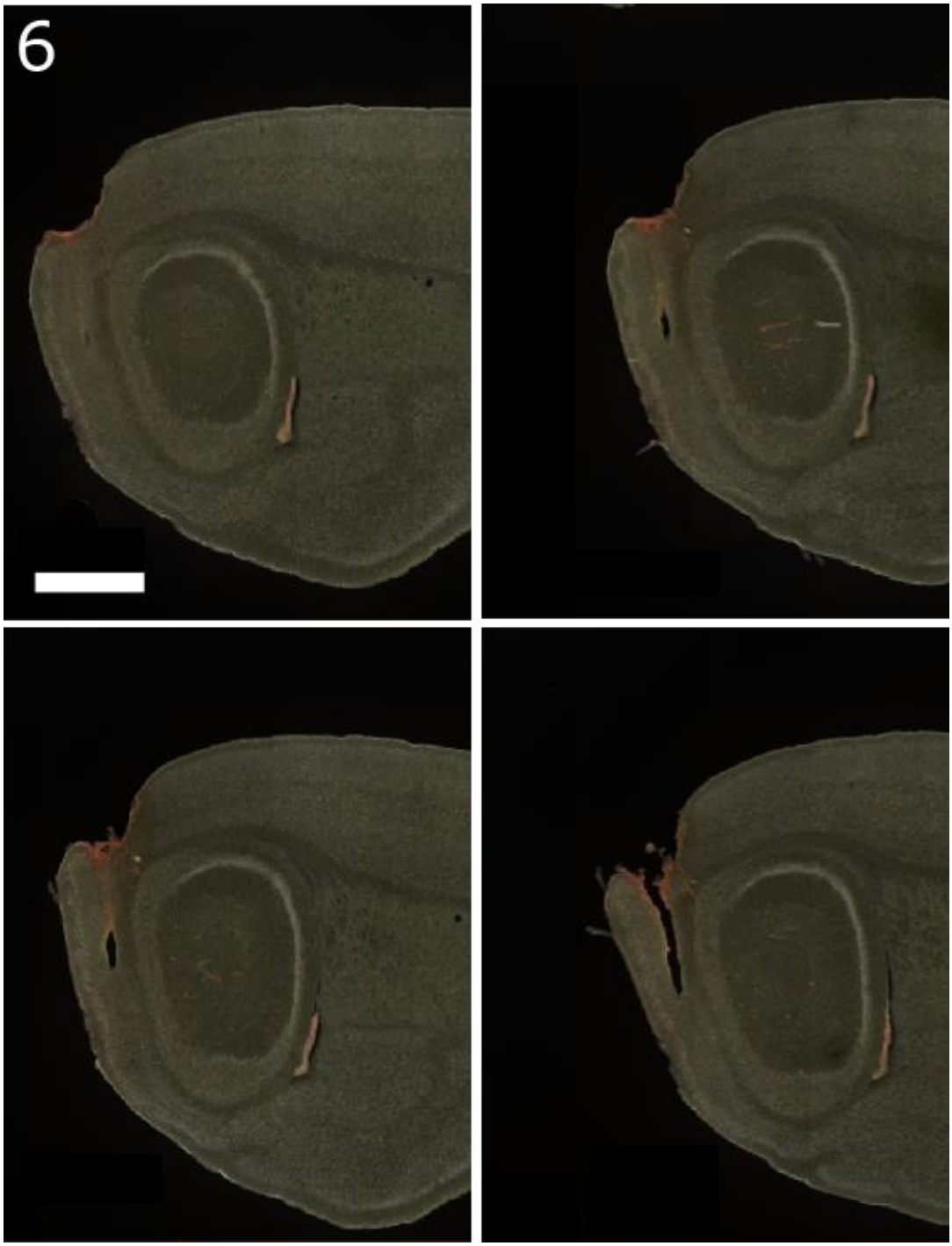
6

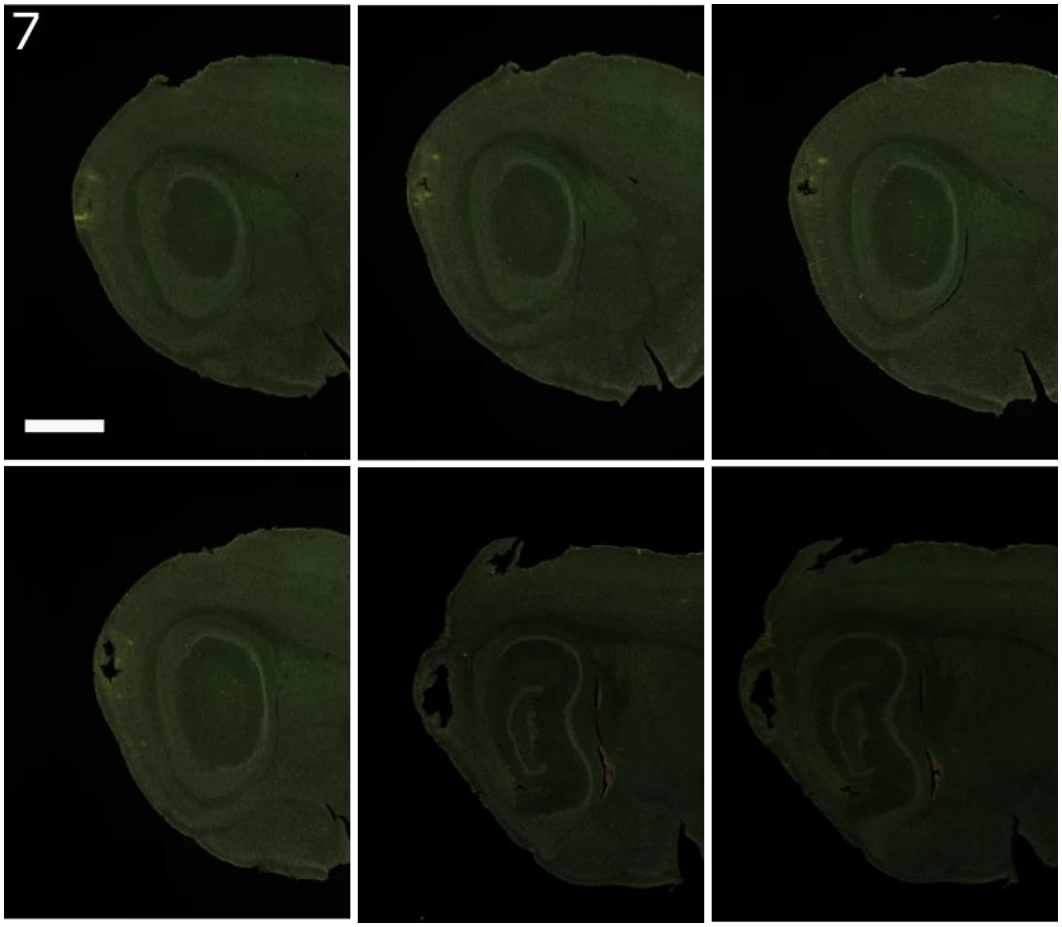
7

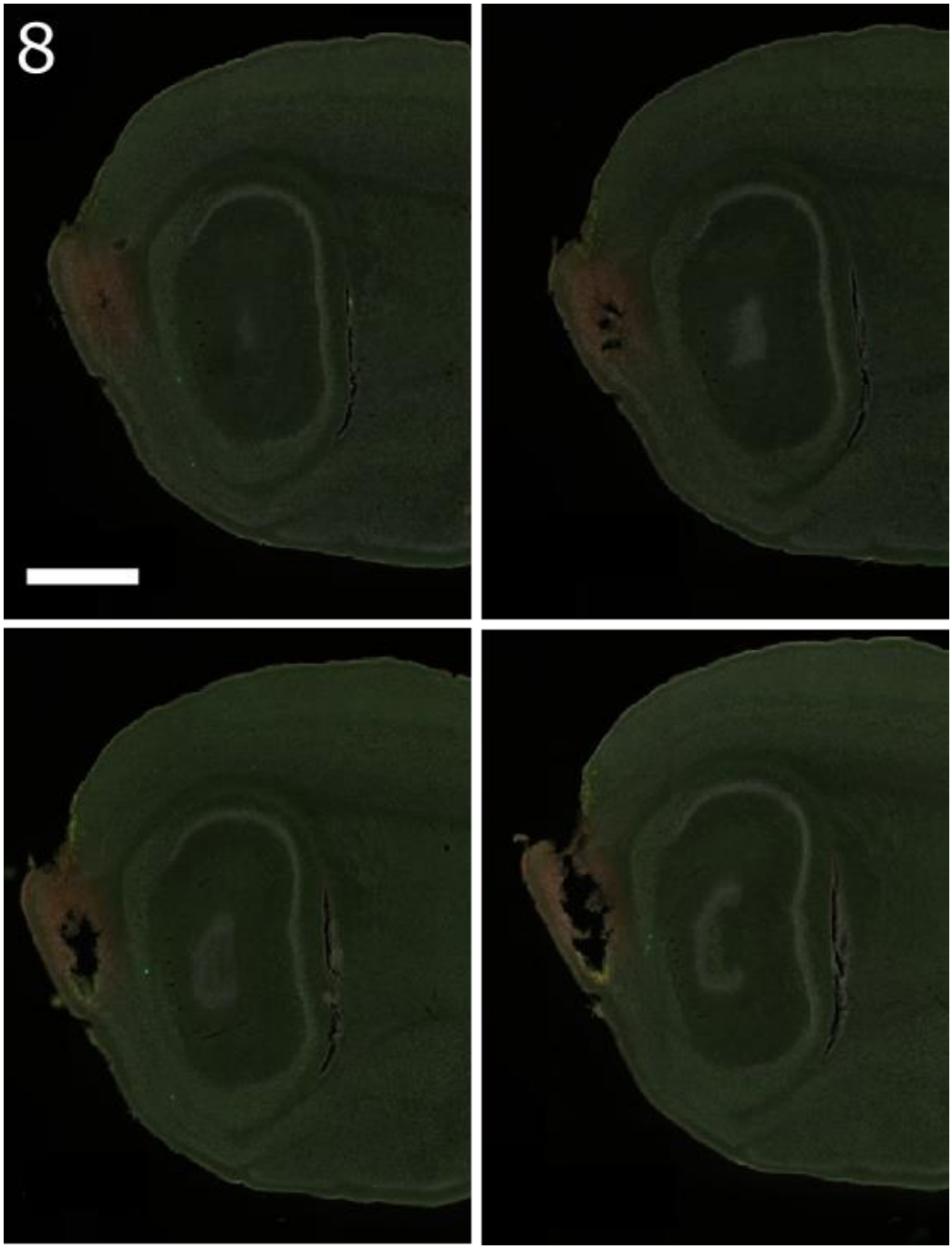
8

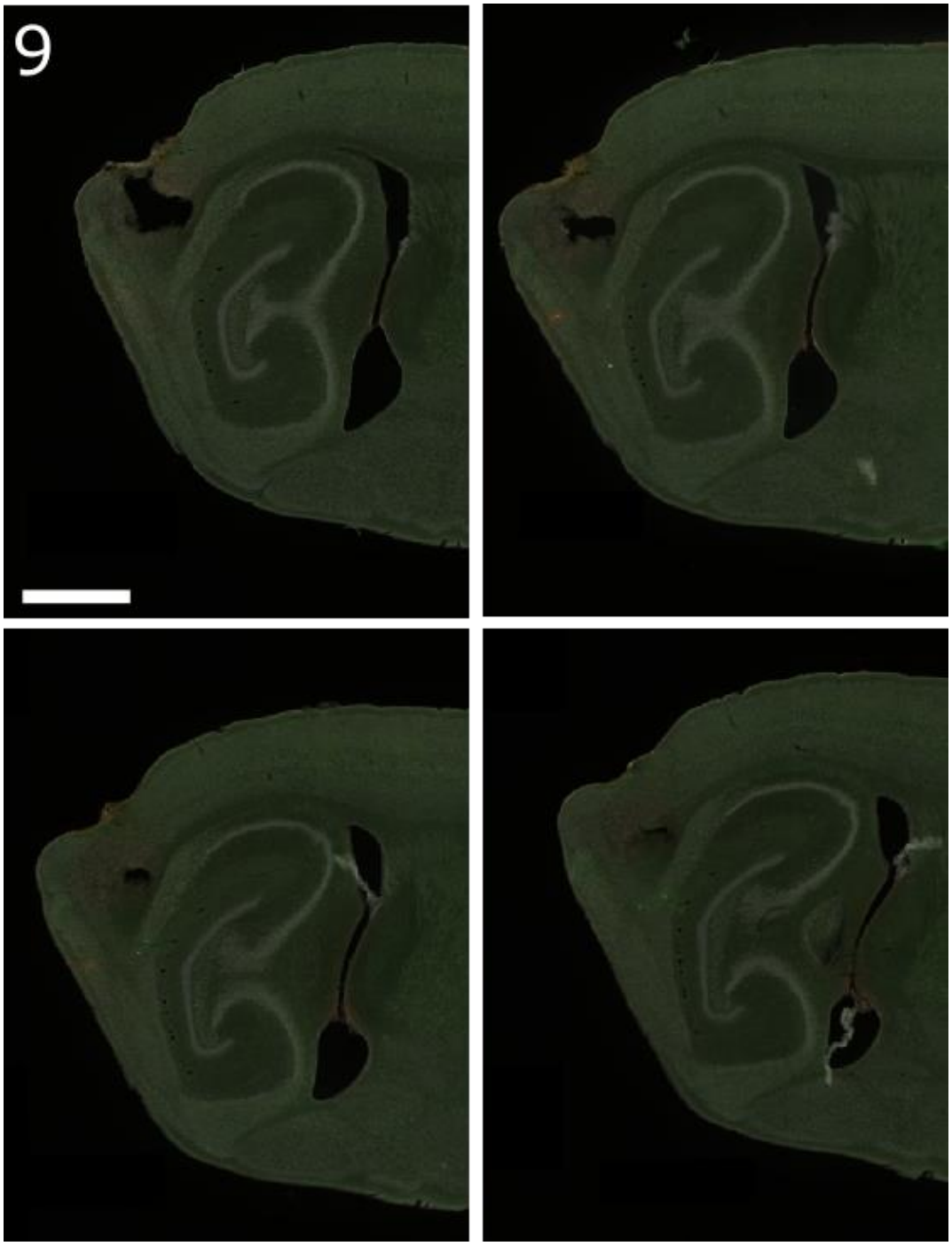
9

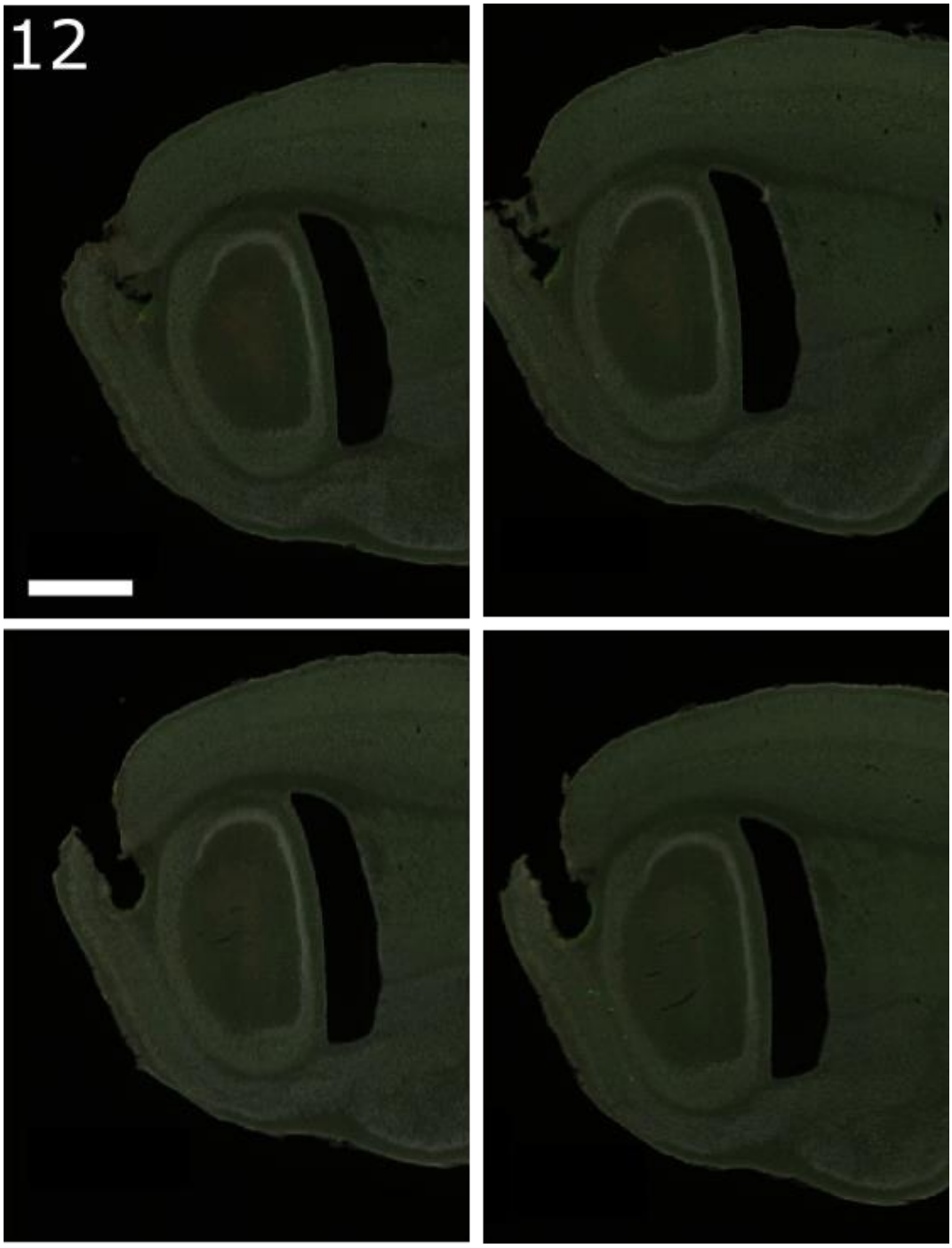
12

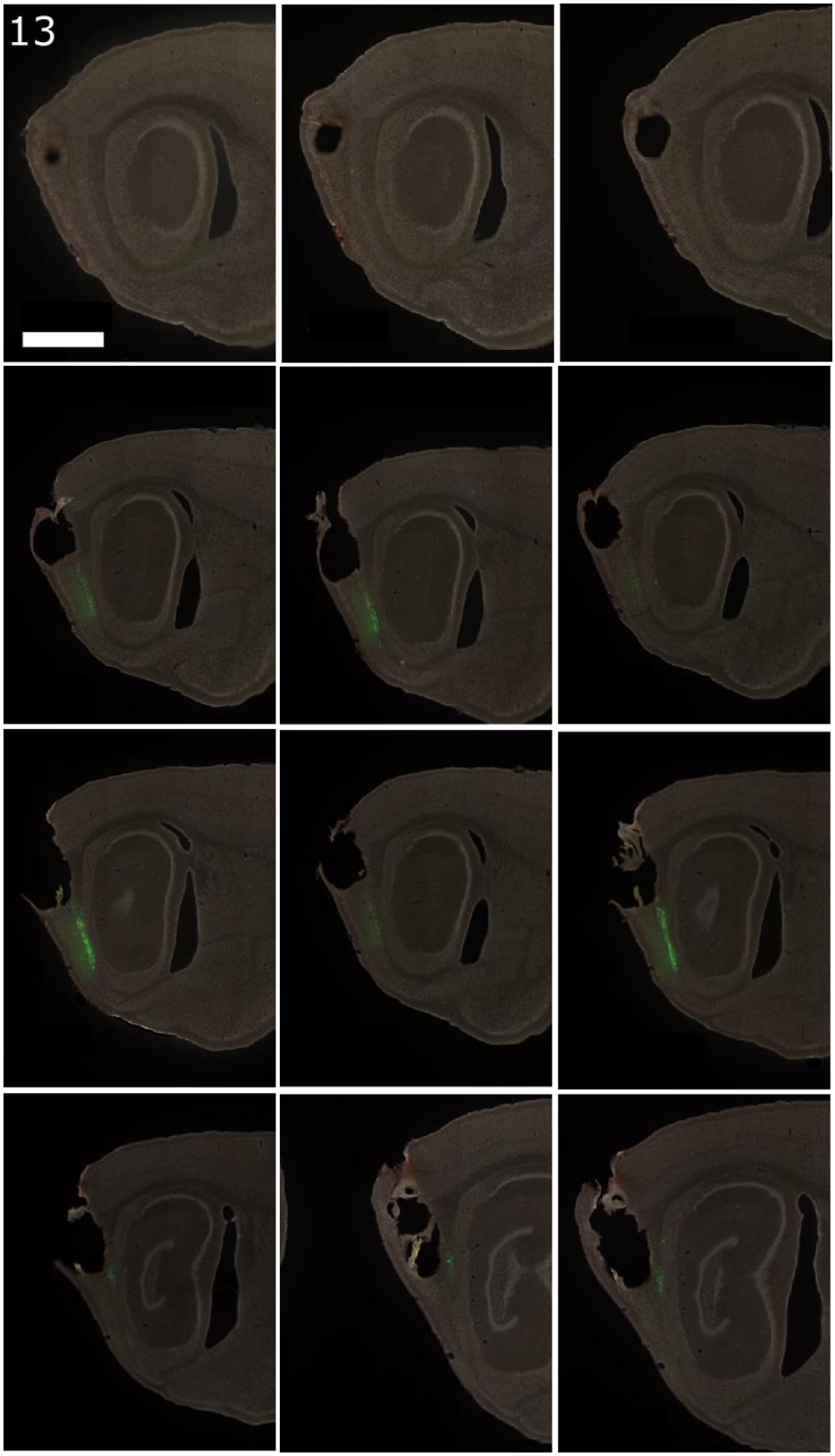
13

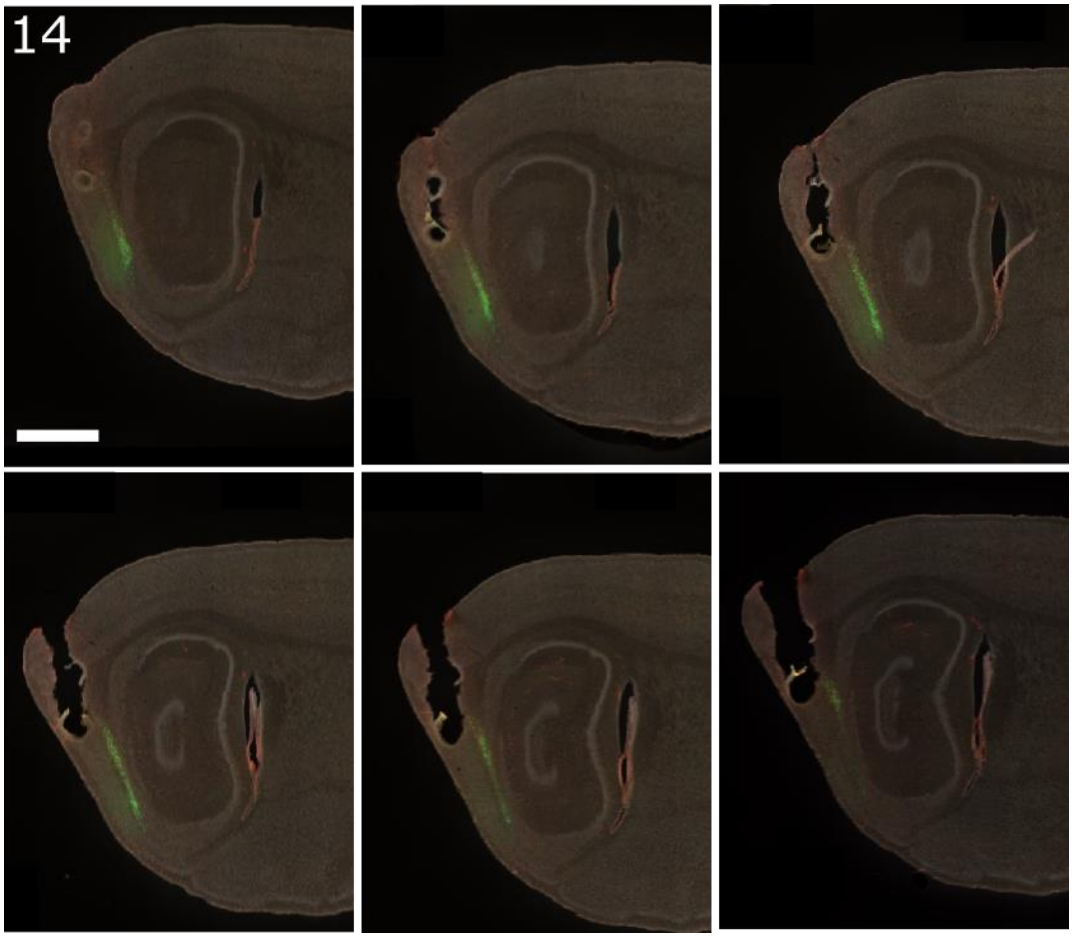
14

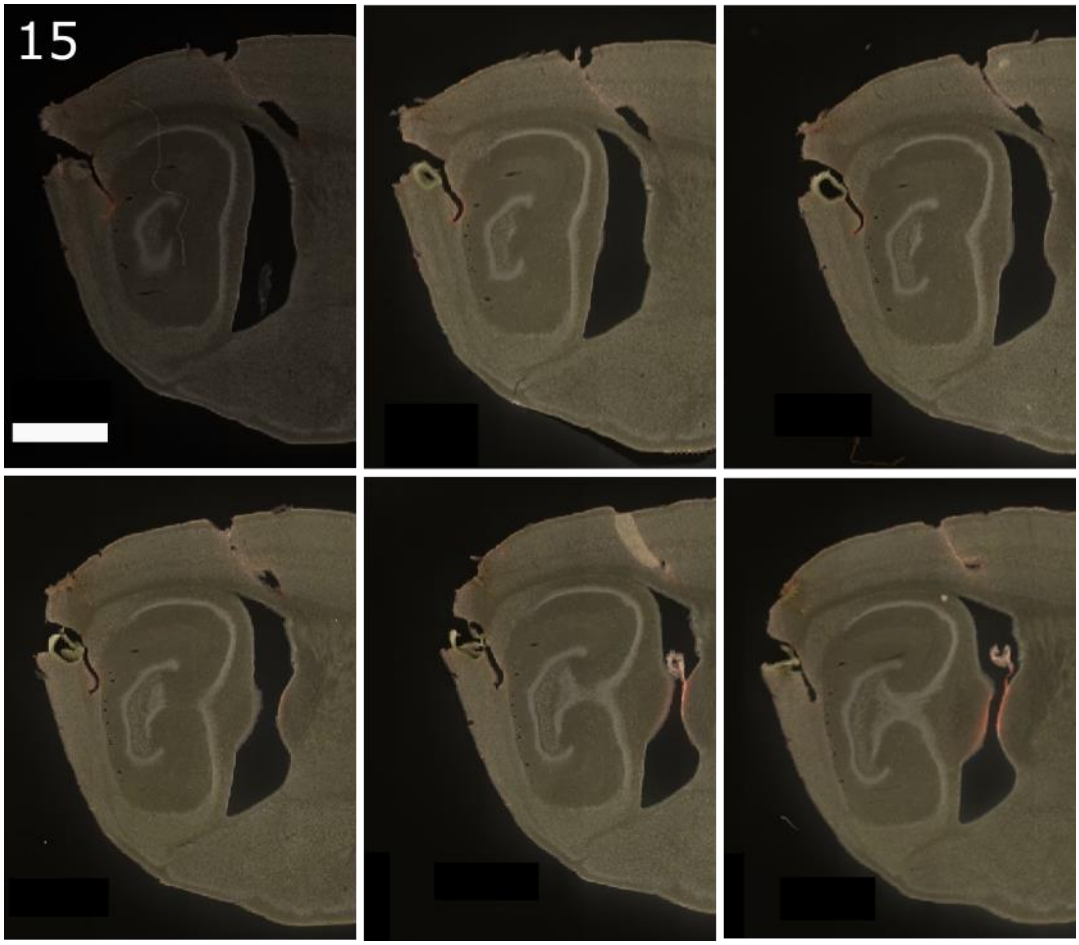
15

Appendix C

The following supplementary chapter presents an experiment where I recorded from the deep MEC of mice in a virtual reality based location estimation task and attempted to silence a subpopulation of L5b cells using DREADDs while mice perform the task. I spent a significant amount of time during my PhD setting up this experiment and improving the behavioural protocol for the virtual reality task. Therefore, the data is presented for completeness.

8 Does L5b play a role in location estimation?

The role of the deep medial entorhinal cortex (MEC) in location estimation has never been tested before, and there is only circumstantial evidence that it may be important in navigation.

One line of evidence that suggests that the deep MEC might play a role in spatial navigation is its position in the hippocampal-entorhinal circuit. The connectivity of the deep MEC was recently investigated by Sürmeli et al. (2015), who found that layer 5 (L5) is subdivided into two sublayers with different projections. One of the sublayers, L5b, was shown to receive projections from *cornu ammonis* 1 (CA1), L2 stellate cells and the subiculum. This connectivity pattern suggests that L5b cells may receive information from both place and grid cells. Receiving such spatial input means that L5b is well situated to integrate these signals.

In addition to anatomical results, modelling data based on noise correlation predicts the deep MEC to be important in location estimation. By reanalysing simultaneously

recorded grid cell firing patterns, Tocker, Barak, & Derdikman (2015) found that pure grid cells can be found in layers 2, 3, and 6 of the MEC, and conjunctive cells reside in layers 2 and 5. The model proposed by Tocker et al. (2015) suggests that the position of the animal may be calculated in the superficial MEC, and that activity bumps in the superficial layers follow the bumps in the deep MEC.

Based on these results, I hypothesized that L5b plays a role in location estimation.

To test this hypothesis, in my first experiment, I silenced a subpopulation of L5b cells in mice that perform a linear location estimation task. I used the p038 transgenic mouse line (Shima et al. 2016) that allowed me to target L5b cells selectively. To manipulate as many cells as possible, I crossed the p038 line with an inhibitory DREADD (designer receptor exclusively activated by designer drugs) line (H. Zhu and Roth 2014). Double heterozygous offspring of this cross expressed hM4Di inhibitory receptors in all Cre positive cells, enabling me to inactivate these cells temporarily by injecting clozapine N-oxide (CNO). Before inactivating the cells, I trained the mice to perform a location estimation task. To be able to see the effect of the manipulation, I needed the animals to perform the task consistently. Therefore, I took a conservative approach, and set strict criteria that the animals' performance had to meet before testing the function of the cells.

To test whether silencing L5b cells impairs location estimation, I looked at the distance between the beginning of the track and the animal's first stop on a given trial. In animals that performed the task well, I expected the animal's first stop to be in the reward zone and have a low standard deviation (< 15 cm). I first predicted that the average estimated location would differ on days when the cells were silenced compared to control days.

In addition to testing the role of L5b cells in location estimation, I combined this task with extracellular tetrode recordings, and investigated neuronal activity in the deep MEC while mice performed the task. I predicted that spiking activity would correlate with the behavioural task. Furthermore, I expected neuronal activity to be reduced on days when I silenced the cells. I established the combination of these methods in our lab.

8.1 Using virtual reality to test navigation strategies

Virtual reality is a valuable tool for testing location estimation. One reason for that is the difficulty of controlling or removing external cues, such as olfactory cues from the environment, in the real world. Virtual realities not only allow the removal of such external cues but enable the manipulation of the visual input the animal receives based on its behaviour. Another advantage of using a virtual reality to test linear location estimation is that by head-fixing the animal, vestibular cues can be removed as the mouse traverses the environment. This allows us to dissect the mechanisms needed for linear location estimation from the components related to head-direction.

The first experiment that manipulated optic flow using a computer screen investigated the role of optic flow in locomotion (H. J. Sun, Carey, and Goodale 1992). In this experiment, gerbils ran in a box towards a screen that displayed a high contrast circle. By varying the length of the corridor leading to the screen and the diameter of the circle, Sun et al (1992) investigated how the deceleration of the animal is influenced by these parameters as it slowed down nearing the end of the corridor to avoid collision. Experiments that studied insects flying and walking in virtual space followed (Strauss, Schuster, and Götz 1997; Gray, Pawlowski, and Willis 2002), introducing ideas later applied in experiments on mammals (Matsumura et al. 1999; Leighty and

Fragaszy 2003; Hori et al. 2005). The first virtual reality task for rodents where the environment was manipulated based on the animal's behaviour was implemented by Holscher et al (2005). The main features of this setup were a treadmill that rats ran on, and a toroidal screen that surrounded the animals. The virtual environment projected to the screen was updated based on the movement of the rat on the treadmill. The rats in this experiment were supported by a harness, and therefore could move their heads freely. Holscher et al (2005) demonstrated that not only humans and other primates, but rodents are also capable of navigating in virtual environments.

To extend the utility of virtual realities to experiments that study neural mechanisms that require the animal's brain to be stationary, animals need to be head-fixed. In such experiments it is possible to combine virtual reality tasks with patch clamp recordings (Harvey et al. 2009; Domnisoru, Kinkhabwala, and Tank 2013; Schmidt-Hieber and Häusser 2013) or calcium imaging (Christopher D. Harvey 2012; Keller, Bonhoeffer, and Hübener 2012; Heys, Rangarajan, and Dombeck 2015) to investigate neuronal activity.

A number of studies have used linear virtual reality systems to dissect neural mechanisms underlying spatial navigation strategies in rodents (Busse et al. 2011; Chen et al. 2013; Ravassard et al. 2013). One of the features of virtual reality based tasks that are not possible to implement in real world environments is to put movement and visual information in conflict (Chen et al. 2013; Ravassard et al. 2013), which is an invaluable asset for spatial navigation studies. To demonstrate that the spatial navigation system is engaged in 2D virtual reality tasks, Aronov & Tank (2014) recorded from grid cells, place cells, head-direction cells and border cells. They found that these spatially selective cells showed 2D activity patterns similar to real world

firing patterns. Furthermore, they showed that hippocampal neurons remapped in response to changes in the shape and appearance of the virtual reality. Overall, these findings suggest that the hippocampal-entorhinal navigation system is engaged in 2D virtual environments.

Recently, two virtual reality based tasks were independently developed to study location estimation. To test estimation of self-motion distance and duration in rodents, Kautzky & Thurley (2016) introduced a virtual reality based task in which Mongolian gerbils ran on a linear corridor, and depending on the length of the corridor, they had to turn right or left in a Y maze to receive a reward. The other task, implemented by Tennant et al (2018), aimed to test location estimation by training mice to run on a linear corridor and stop in a designated reward zone to receive a reward. One of the main differences between the two tasks is that the design by Tennant et al does not have a discrete decision point where the animal has to estimate in retrospect, but there is a continuous integration process up to the stop in the reward zone. Therefore, the task by Tennant et al may be better suited for studies that investigate the online computation needed for path integration.

8.2 Methods

8.2.1 Ethical statement

All procedures were performed under a UK Home Office project license (PC198F2A0) in accordance with The University of Edinburgh Animal Welfare committee's guidelines. All procedures complied with the Animals (Scientific Procedures) Act, 1986, and were approved by the Named Veterinary Surgeon.

8.2.2 Animals

Mice were bred by crossing heterozygous R26-LSL-Gi-DREADD females (The Jackson Laboratory, stock number 026219) with heterozygous p038 Cre males (obtained from Sacha Nelson, Brandeis University). The offspring of this cross (Figure 8.1) were genotyped for eGFP (forward primer: CGTCGTCCTTGAAGAAGATGGT, reverse primer: CACATGAAGCAGCACGACTT, reporter: CATGCCCGAAGGCTAC), and for hChrm4 (forward primer: CGCCTGGTCACGTCATCAT, reverse primer: TCACTGTGGCAATGAAGACCAT, reporter: ACCGTCTCATAGCGATTGT). The first 11 (5 male, 6 female) double heterozygous (eGFP+/-, hChrm4+/-) mice born from our breeding pairs were implanted with a microdrive for tetrode recordings. One animal did not recover well from the surgery, and one was injured by its cage lid and terminated. 9 mice (4 male, 5 female, 8.9 +- 0.5 std weeks old, and 22g +-3.9 std before training) underwent behavioural training and *in vivo* electrophysiology recordings.

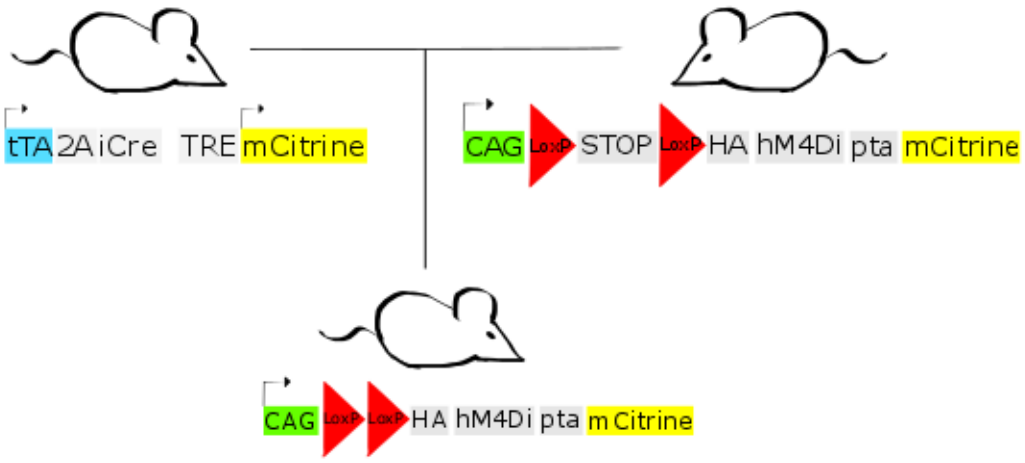

Figure 8.1. Generation of p038xhM4Di mouse line. Mice were generated by crossing p038 (tTA: tet transactivator, 2A:FMDV-2A sequence, TRE: tet response element) heterozygous male mice, and hm4Di (Cre recombinase inducible expression of CAG promoter driven hM4Di-mCitrine expression JAX) heterozygous female mice. The double positive heterozygous offspring of this cross expressed hm4Di and mCitrine in all Cre cells.

The animals were group housed (2-4 cage mates) in a reverse cycle (dark from 7 AM to 7 PM) room for one week before the surgery, and singly housed after surgery. The average temperature in the room was 20°C, and the relative humidity was 50 %. Mice were moved to standard behavioural cages at the beginning of the experiment. The lids of the cages were replaced with safer plastic ones after one of the mice became trapped by the implant and had to be terminated. The cages contained sawdust, tissues, cardboard tubes and chewing sticks before the experiment. After surgery, the cardboard tube was replaced by a bigger cardboard igloo so animals do not get stuck in the tube. Two days after the surgery, a training wheel was placed in the cages for environmental enrichment. Standard laboratory chow was given *ad libitum* up to the habituation stage of the experiment, after which mice were food deprived. The animals had access to water *ad libitum* throughout the experiment.

8.2.3 Microdrive implant

For *in vivo* electrophysiology recordings, I built 16-channel microdrives consisting of 4 tetrodes. I built the microdrives using the following protocol (Figure 8.2). I glued a 23 gauge 6.5 mm long inner cannula to an EIB-16 (Neuralynx) board (Figure 8.2A) to the hole next to the ground (G) pin using epoxy (RS components 132-605) and left it to dry overnight. I prepared tetrodes using tetrode wire (18 µm HML-coated 90 % platinum 10 % iridium, Neuralynx) by spinning the wires and then melted the insulation with a heat gun to attach them to each other. The next day I connected two grounding wires (1.5 cm long insulated part) to the reference and ground pins, and threaded 4 tetrodes through the inner cannula. I connected all 16 channels of the four tetrodes to one of the pinholes of the EIB-16 board, fixing them with golden pins (Neuralynx, EIB Pins) to remove the insulation and make an electric connection between the wires and the board. I used epoxy to cover the wires and pins on the surface of the board, and left it overnight to dry. The next day I cemented a poor lady frame (Axona) to the side of the board (Figure 8.2D). Finally, I put Vaseline around the base of the inner cannula, put the 17 gauge 3.5 mm long outer cannula on the inner cannula, and trimmed the tetrodes using ceramic scissors (Science Tools, Germany) to be 3.5 mm long from the tip of the inner cannula.

The evening before, or immediately before surgery, I put the tip of the tetrodes in a gold plating solution (Non-cyanide gold plating solution, Neuralynx), and connected to a power supply (5V DC). To clean the tetrodes, I ran three 1 second 4 µA pulses with the tetrodes as an anode. Then, to lower the impedance, I plated the drives with the tetrodes as a cathode by passing 2 µA 1 second pulses through them until the impedance was between 150 and 200 kΩ.

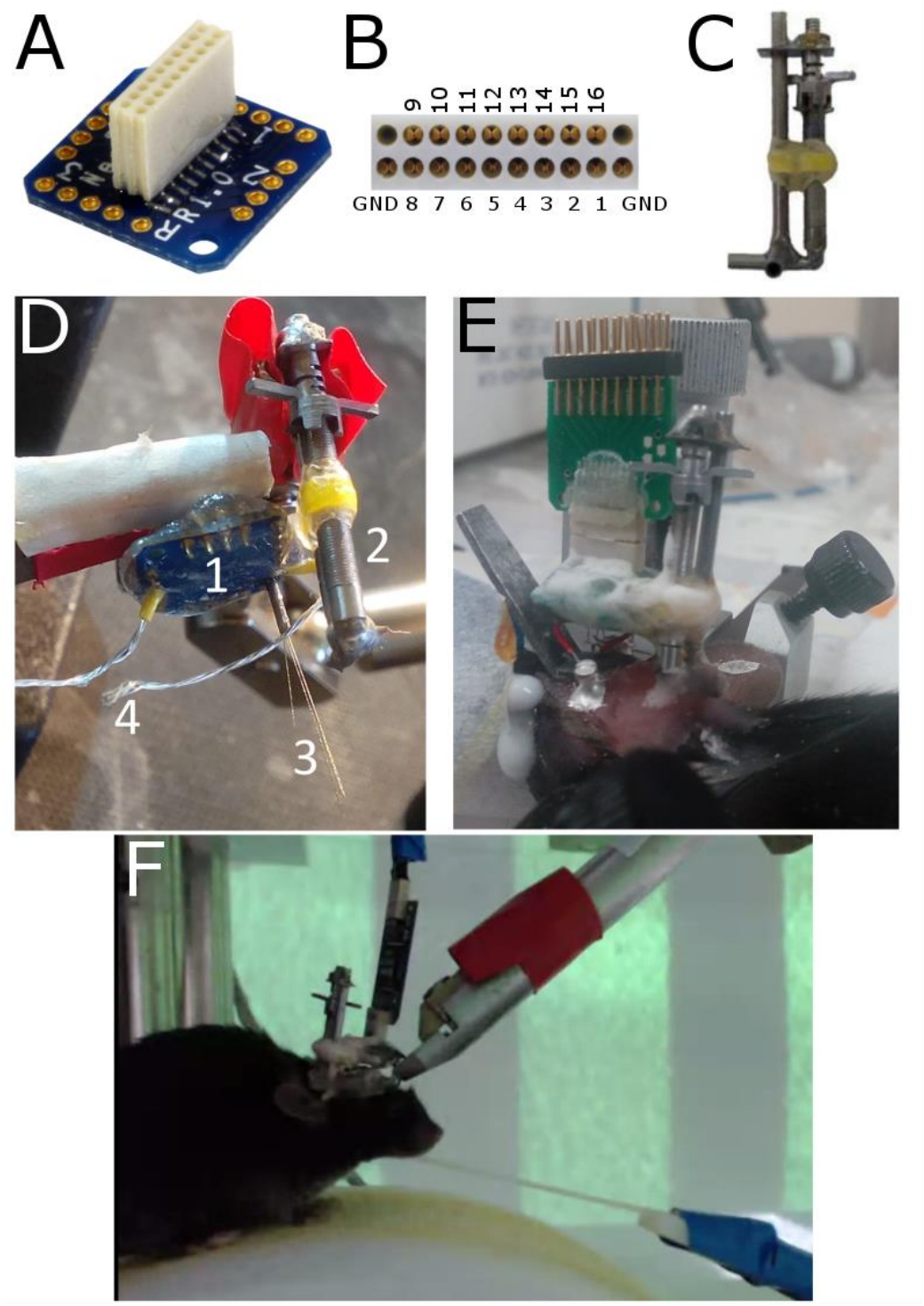

Figure 8.2. Tetrode assembly and attachment. (A) EIB-16 board (B) and its channel map (Neuralynx). (C) Poor lady frame (Axona, bare re-usable frame, 9*6*21mm, 0.71g). (D) A microdrive built from the parts shown above before the tetrodes were cut and plated (1) EIB-16 board, (2) 'poor lady frame' (3) tetrodes, (4) grounding wires. (E) Microdrive during implant surgery, connected to an Omnetics to Mill-Max adaptor (Axona, HSADPT-NN1). (F) Behaving animal implanted with the microdrive performing the virtual reality based linear location estimation task.

8.2.4 Surgical procedure to implant microdrive and head-post

I performed stereotaxic surgeries on 8.9 weeks ± 31 day old mice to implant a microdrive and a head-post. The standard deviation of the ages of the animals was big, because the microdrive appeared to be too heavy for the younger animals I implanted at the beginning of the experiment, and therefore I implanted older mice in subsequent batches. To estimate the weight of the implant, I weighed animals before and after the surgery. To keep mice adequately anesthetized, I induced inhalation anaesthesia using 5 % isoflurane / 95 % oxygen, and sustained at 1 – 2 % isoflurane / 98-99 % oxygen throughout the procedure. The oxygen flow was at 1 L / minute throughout the procedure. To prepare mice for the procedure, I did the following: shaved the head (WAHL Pocket Pro Trimmer, Cat.: 34452P) and wiped the skin with concentrated Betadine; covered the eyes with Viscotears to protect vision; covered the animal with a transparent sterile drape. To expose the skull, I made an incision at the midline from between the eyes to between the ears, removed the skin, and scraped the connective tissue off with a scalpel. To make my injection site accessible, I disconnected the muscles at the left side above the medial entorhinal cortex using a spatula and a forceps. To prevent infection, I glued (Vetbond Tissue Adhesive) the sides of the incision to the skull to seal the incision, but leave the skull exposed. I straightened the head using a micropipette to measure depth both medio-laterally and rostro-caudally, and made a craniotomy using a hand drill 3.5 mm lateral from Lambda, on the fissure. For electrical grounding, I drilled two small craniotomies, and implanted M1 x 4 mm screws (AccuGroup SFE-M1-4-A2) on both sides about 3.4 mm lateral, and 1 mm rostral relative to Bregma. Before the last stage of the surgery, I straightened the head again, and glued (superglue, RS components 473-455) the

head-post (Protolabs, designed in Dr Ian Duguid's lab) to the skull covering Bregma, as rostral as the incision would allow.

To implant the microdrive, I did the following: attached the microdrive to an Omnetics to Mill-Max adaptor (Axona, HSADPT-NN1) held by a crocodile clip attached to the stereotax; lowered the tetrodes close to the brain surface around 3.5 mm lateral from Bregma, slightly caudal relative to the fissure; used the stereotax to lower the tetrodes 1.8 mm +- 0.1 mm SD deep into the brain, targeting the deep MEC; sealed the outer cannula with Vaseline by spreading it around the craniotomy, and then lowering the outer cannula to the surface using a forceps; fixed the implant by putting dental acrylic (Simplex Rapid powder) up to three quarters of the outer cannula, and around foot of the frame, leaving the head-post and the grounding screws uncovered. After the cement set, I carefully wrapped the grounding wires around the grounding screws (the reference wire was connected to the right side screw, and the ground wire to the left screw), and fixed the wires with silver paint (RS components 101-5621). After the silver paint dried, I applied another layer of dental acrylic to cover the bottom of the head-post, and the grounding screws, but not the insulated part of the grounding wires, or the board, to ensure that the drive is able to move down (Figure 8.2E). I left mice to recover on a heat mat for about 20 minutes, and then I moved them back to the reverse light cycle room and gave them Vetergesic jelly (0.5 mg / kg of body weight buprenorphine in raspberry jelly) 12 hours after surgery.

During the two days after surgery, I performed health checks at least once a day in addition to the technicians checking on the animals. On these days I did not weigh or handle the animals. After the recovery days, I gave mice a training wheel to encourage active behaviour in addition to their igloo, tissues and chewing sticks.

8.2.5 Virtual reality setup

I used a virtual reality setup that was designed by Dr Lukas Fischer (Tennant et al. 2018). Briefly, mice are head fixed by the implanted head-post to a head clamp (Thor Labs), and run on top of a polystyrene treadmill (7.5 cm wide, 20 cm diameter, Graham Sweet Studios) (Figure 8.3). All components are mounted on an aluminium breadboard (Thor labs) by M6 screws and clamps (Thor labs), and are surrounded by a frame (CSI products).

Mice are surrounded by a cylindrical screen (extruded PVC, 80 cm diameter, 46cm height, Talbot Designs Limited) that displays a linear corridor and is updated by Blender3D as the mice run based on signal from a rotary encoder (Pewatron E6-2500-471-IE) that is mounted on the central axis of the treadmill. The virtual environment is projected by an InFocus projector (InFocus in3118HD), and the image is transformed and amplified by a mirror system (flat mirror 140 mm diameter, aluminium coated mirror, Knight optical limited, and angular amplification mirror (AAM), amplification factor = 10, 110° vertical coverage, Protolabs UK).

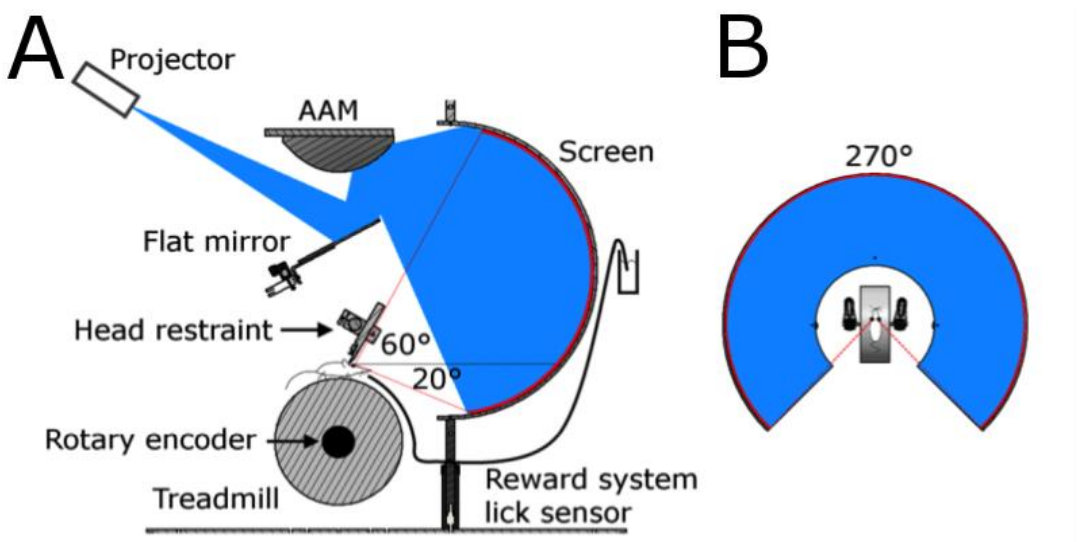

Figure 8.3. Schematic representation of the virtual reality setup. (A) Virtual reality setup shown from the side. Blue represents the path of light, coming from the projector to the mirror system (AAM = angular amplification mirror) to the screen. (B) The path of light in the virtual reality is shown from above. Figure used with permission from Lukas Fischer.

To update the virtual environment, the rotary encoder uses an optical sensor to measure the rotation of the wheel, and sends pulses to an Arduino Uno after a certain amount of rotation. The signal is forwarded to Blender3D. Then, the displacement in the virtual reality is calculated the following way:

$$displacementVR = \frac{track\ length\ in\ VR * circumference\ of\ treadmill}{physical\ tracklength * ppr}$$

Where track length in virtual reality equals 20 units, the circumference of the treadmill is 20 cm, the physical track length 200 cm, and ppr (pulses per rotation) is 5000. After the displacement is calculated by Blender3D, the virtual environment is updated according to the movement of the animal. When the mouse reaches the end of the corridor, the trial is reset to the beginning of the track. In the middle of the linear corridor, there is a designated area (reward zone) that has a distinctly different floor and wall texture.

To deliver soy milk rewards to the animals, there is a plastic feeding tube (Instech, FTP-18-75-50 18 ga (0.7 x 1.2 mm)) placed in front of the animal's mouth, connected to silicone tubing (NResearch, TBGM101) by epoxy (RS components, 132-605). The end of the tube is submerged in a cup of soy milk that is placed above the setup. The tube is filled with soy milk during the experiment, and a valve (full opening pinch valve, NResearch 225PNC1-21) stops the flow by clamping the tube. Blender3D controls when soy milk is released by sending a pulse to the valve via the Arduino Uno, controlled by a custom-made Arduino Script (Lukas Fischer). When the valve opens, the mouse receives about 6 - 12 µl of soy milk reward through a reward tube (Instech, FTP-18-75-50), and a tone is played for 500 ms to encourage the mouse to make an association between the track location and reward. To make sure that the mouse cannot use the end of the track as a landmark, and estimate its self-location based on that landmark instead of using self-motion cues, a virtual black box was put 50 cm ahead of the mouse to restrict its vision.

8.2.6 In vivo electrophysiology recording system

To record extracellular activity from mice performing the virtual reality location estimation task, I used an Open Ephys acquisition board (Siegle et al. 2015) combined with an Intan headstage (RHD2132 16-channel amplifier board), an SPI cable (RHD2000 6-ft (1.8 m) Ultra-Thin SPI interface cable), and a custom-made microdrive described above. I connected the head stage to the Omnetics connector on the EIB-16 board on the implanted microdrive, and connected an SPI cable to the head stage. The SPI cable was plugged into the Open Ephys acquisition board, which was grounded by a BNC (Bayonet Neill–Concelman) cable to the Faraday cage on the setup.

To synchronize the information on the position of the mouse in the corridor with the recording, I connected an Arduino Uno (RS components, 715-4081) to the computer running the virtual reality, and forwarded the information to an I/O board (Open Ephys, I/O board), and then to the Open Ephys acquisition board. This way, the movement information appeared as a 17th channel on the Open Ephys recording system (Siegle et al. 2017) in addition to the electrophysiology data (Figure 8.4).

Even though the analogue-digital conversion happens in the head stage, 50 Hz noise was present in my initial recordings. To overcome this, I built a Faraday cage around the virtual reality setup using aluminium foil and conductive tape, and then I grounded all metal parts in the virtual reality setup that were not on the same potential as the metal base of the cage. These steps reduced noise, but did not eliminate it. Finally, I put a wire mesh (LAIRD TECHNOLOGIES Wire Mesh, Conductive Shielding, Cat.: 1219141) around the SPI cable (from the acquisition board to the head stage), the wire of the rotary encoder (from the Arduino to the rotary encoder of the VR setup in the Faraday cage), and on the reward tube. I threaded the shielded wires through the Faraday cage as they entered, and made sure that they were grounded to the cage. Overall, these steps reduced the 50 Hz noise.

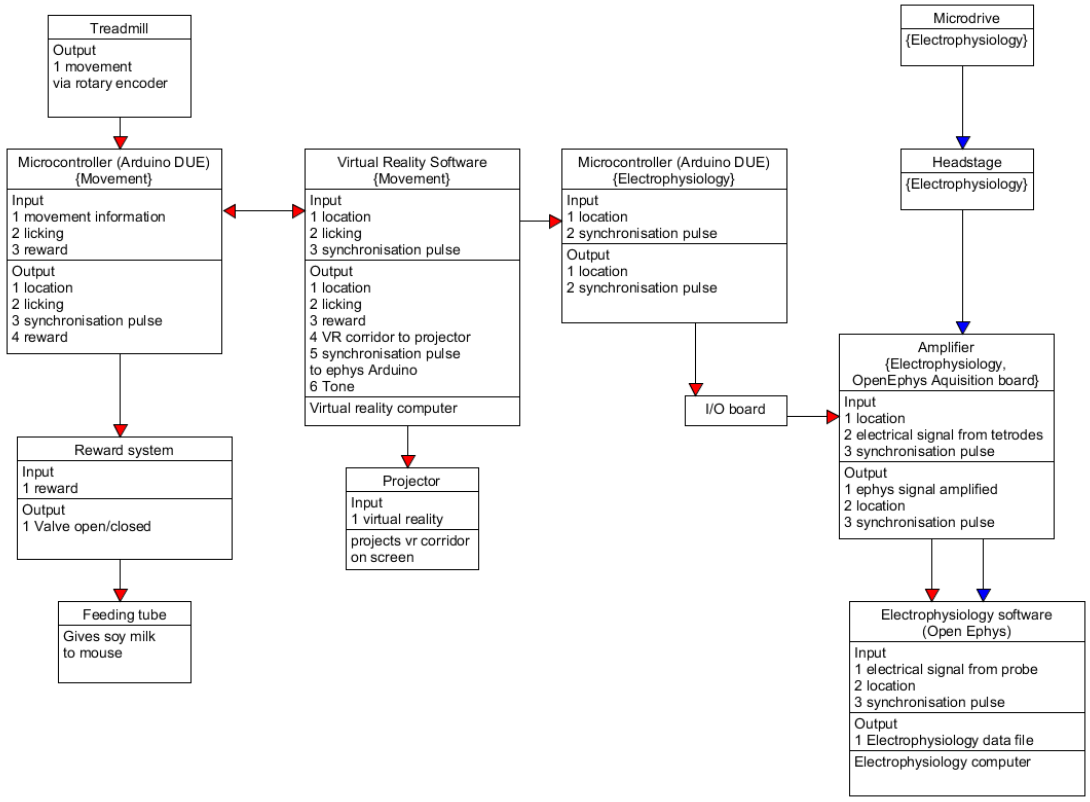

Figure 8.4. Connectivity of components of the virtual reality and electrophysiology setups. Red and blue arrows show the flow of movement and electrophysiology related information respectively.

Open Ephys acquisition protocol

For the in vivo extracellular recordings, each channel was recorded at 30 kHz, and filtered between 0.1 Hz and 10 kHz. Recordings were made simultaneously from 16 channels, and saved as a kwik file. The position of the mouse on the linear track was sent to the Open Ephys GUI (graphical user interface) via an Arduino Due, and was saved as an additional channel in the kwik file simultaneously. Having the location saved simultaneously with the electrophysiology data allowed me to use these aligned data arrays for my analysis.

During training mice to do the location estimation task, I lowered the tetrodes by 50 µm daily if there were no action potentials visible live in the OpenEphys GUI in the recording, and stayed at depths with cells for up to 4 days. The rationale behind recording the same cells for multiple days was to capture neuronal activity on days when mice perform the location activation task well.

8.2.7 Behavioural protocol

I adapted protocols described in Tennant et al. (2018) to include tetrode recordings, and I standardized the food deprivation protocol.

Motivating animals by food deprivation

To motivate mice to do the location estimation task for the soy milk reward, they were food deprived, targeting 85 % of the reference bodyweight. The weight of the animals was calculated by subtracting the weight of the implant measured during the surgery from the measured body weight. To obtain their baseline bodyweight, I weighed the mice before the food deprivation for 5 days and calculated an average. The food deprivation started one day after the mice were habituated to the setup. At the beginning of the food deprivation, I gave a pre-determined amount of food to the animals that was based on previous experiments (Table 8.1).

Table 8.1. The amount of food given to a mouse on the first week of training is determined by the animal's baseline weight.

Baseline weight	Food on first week
< 17 g	3.1 g
17 – 19 g	3.3 g
19 – 21 g	3.5 g
21 - 23 g	3.7 g
23 – 25 g	3.9 g
25 – 26 g	4.0 g
26 - 27 g	4.1 g
27 – 28 g	4.2 g

For five days after the habituation days, I handled and weighed all animals, and habituated them to soy milk. I did this by letting the mice drink maximum 1 ml of soy milk from my hand.

After the first food deprivation week, to determine the amount of food given to the animal, the level of food deprivation and motivation were taken into consideration. To estimate how food deprived the animals were on a given day, I calculated the reference weight. To obtain this value, I first calculated what percentage the mouse's weight was of the population weight (Jackson Laboratories) before the food deprivation started. This was necessary since the animals I used were not fully grown adults and their development had to be considered for food deprivation.

$$\%\, population\ weight = \frac{weight}{population\ weight} * 100$$

I used the % population weight from the last habituation day as an indication for how much the animal's weight differs from average. Using the % population weight I calculated the corrected daily growth.

$$corrected\ daily\ growth = \frac{\%\ population\ weight}{daily\ growth} \div 100$$

By adding the corrected daily growth to the baseline bodyweight that I calculated by averaging five days before food deprivation, I obtained the first deprived baseline. For all following days, I calculated the deprived baseline by adding the daily growth to the previous day's deprived baseline.

Finally, I calculated the reference weight:

$$reference\ weight = \frac{weight}{deprived\ baseline} * 100$$

I scored the level of food deprivation of the animals based on their behaviour the following way.

Severity score 0: reference weight above 95 %, does not start eating immediately after it receives food.

Severity score 1: very active behaviour, runs on its training wheel, nibbles on fingers of experimenter. This is what I was aiming for to motivate the animals.

Severity score 2: even more active than a mildly deprived mouse, might be biting stronger. If an animal is moderately deprived, I increased the amount of food given by 0.1 g daily, until it was not too deprived anymore. If these symptoms were present in combination with a reference body weight that is below 85 %, I increased the amount by 0.2 g.

Severity score 3: slow movement, hunched posture. If an animal showed any of these symptoms, I fed it immediately with at least double the amount of food it was supposed to receive, did not train it on that day, and monitored its behaviour throughout the day.

If the animal was not overly food deprived (> 85 % of reference bodyweight) and it was not motivated (trial number below 40), I reduced the amount of food given by 0.2 g. If an animal appeared overly deprived (< 85 % of reference body weight, scratches the wheel, low trial number (< 40)), I increased the amount of food by 0.2 g. On the following day, if changing the animal's food deprivation made the performance worse, I reduced the amount of food by 0.2 g if the animal's food deprivation score was 0. If an animal did more than 40 trials per day, I kept the amount of food given consistent unless the animal became too deprived. In case of moderate food deprivation symptoms, I added 0.1 g to the amount of food, in case of severe symptoms, I added 0.5 g. In extreme cases, I fed the mouse immediately with wet food and did not train it on that day. If the trial number of an animal was below 20 for 3 consecutive weeks, it was terminated. I fed mice 30 minutes after their training in the holding room to avoid making an association between the behaviour room and food.

To minimise possible long-term adverse effects of food deprivation, I increased the amount of food on days when mice were not trained. On the last training day of the week, I gave 130 % of the amount of food given on the previous day. On the first break day, I gave 115 % of the amount of food given on the day before the last training day. On the second break day, I gave the same amount of food as on the training day before the last training day. I did health checks, and weighed and handled the animals on the break days before feeding them.

Cleaning the cages might make animals food deprived, since they may eat their excrement, or hide food in the bedding that gets replaced. Therefore, to make sure that no food is removed, I cleaned the cages weekly on the fifth training day of the training week, and on the corresponding day of the food deprivation week before the training began. Only the cage and the tissues were changed, not the environmental enrichment.

Location estimation task

Mice were trained during the dark phase of the light cycle to do the location estimation task for 30 minutes per day in 5-day blocks, interleaved with 2-day training breaks. They were trained around the same time of the day to ensure that their feeding time remained consistent.

In the task, mice had to run on a linear corridor, and stop at a designated reward zone to receive a soy milk reward (Figure 8.5). In the first stage of the task, 4 out of 5 trials had a visual cue at the location of the reward zone, and one did not. All trials were rewarded at this stage.

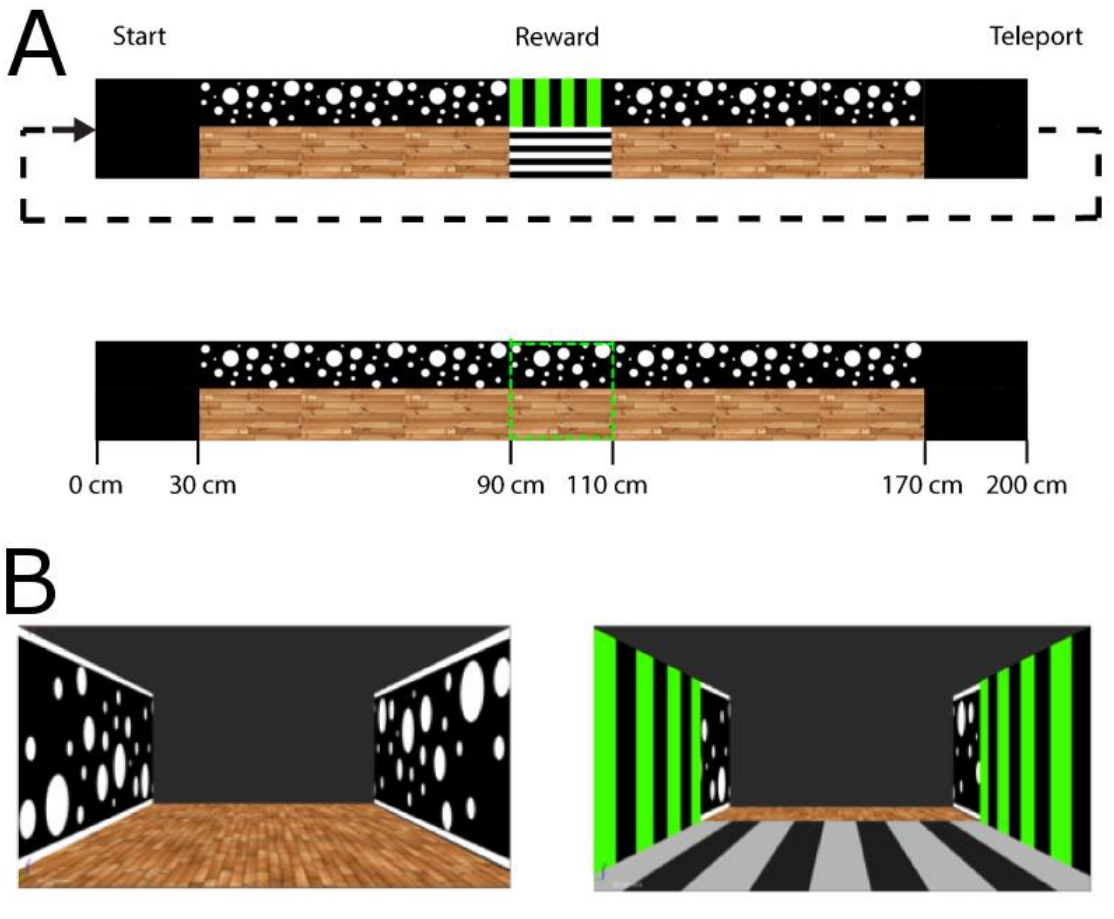

Figure 8.5. Location estimation task. (A) Measurements of the linear corridor on beaconed (top) and non-beaconed (bottom) trials. (B) The virtual corridor from the mouse's perspective in the corridor (left), and in the reward zone (right).

Probe trial and CNO manipulation criteria

When mice completed more than 75 % of the trials successfully for two consecutive days, and they have been trained for at least 6 days, and did more than 40 trials per day, one half of the non-beaconed trials was replaced by probe trials (one in every 10 trials). On probe trials, there was no beaconing cue in the reward zone nor a reward, and the tone was absent as well.

After the mice started probe trials, I calculated the average location and standard deviation of their first stop for each trial. Once the location was in the reward zone

with a standard deviation of 15 cm or less for two consecutive days, I started manipulation (Figure 8.6). Animals that passed this criterion underwent six manipulation days of IP injections, 30 minutes before their training. The injections alternated between 0.1 ml 5 mg / kg CNO in saline (HelloBio, HB1807), and 0.1 ml saline. I was blind to the solution, and the first solution to inject was randomized using a true random number generator (random.org) for each animal.

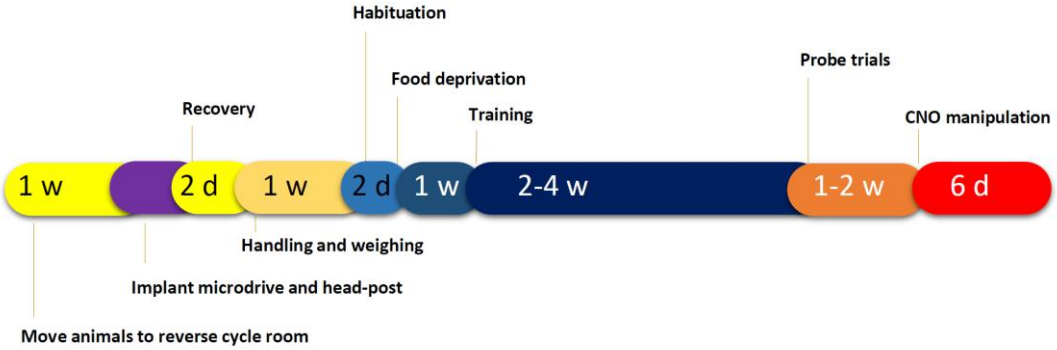

Figure 8.6. Timeline of location estimation experiment. Mice were moved to the reverse light cycle room one week (w) before the experiment. A microdrive and a head-post was implanted in a stereotaxic surgery. Mice were allowed to recover for at least 2 days (d) after the surgery. One week of handling followed, and then habituation to the experimental setup for two days (for 5 and 10 minutes respectively). Food deprivation started after the second habituation day, and continued until the end of the experiment. Mice were trained for 2 - 4 weeks until they reached criteria, and started probe trials, and finally underwent CNO manipulation.

8.2.8 Marking the recording location and histology

After their last training day, I induced inhalation anaesthesia in mice by putting them in a box with a tissue that had drops of isoflurane, and injected them with 0.1 ml of pentobarbital. Once mice were non-responsive, I applied a 2 second long 25 mA pulse through each tetrode via all four channels to burn a small hole at the tip of each tetrode to mark the recording location. I achieved this by connecting pairs of channels to each other by soldering the corresponding wires on an Omnetics to Mill-Max

connector (Axona, HSADPT-NN1), and connecting two pairs of wires tetrode by tetrode to the REF and GND connectors of a pulse generator (Digimeter Ltd). Immediately after, I perfused mice intracardially with phosphate buffered saline (PBS; Invitrogen) until the liquids cleared, and then 4 % paraformaldehyde (PFA; Sigma Aldrich) in 1 M PB for 4 minutes with a flow rate of approximately 10 ml per minute.

After perfusion, brains were removed and left in 4 % PFA in 1 M PB overnight, and moved to 30 % sucrose (Sigma Aldrich) in PB for at least a day. Once the brains sank, I sliced 50 µm sagittal slices using a freezing microtome. I incubated the floating sections in 1 : 500 neurotrace 640 / 660 (Invitrogen, Cat.: N21483) in PBS-T (0.3 % Triton X-100, Sigma Aldrich in PBS, ThermoFisher Cat.: 10010023) for 2 hours on a shaker at room temperature, and then did three 20 minute washes in PBS, and mounted the slices on glass slides. I coverslipped with Mowiol when the slices dried.

8.2.9 Imaging

Sections were imaged using a Nikon A1 confocal microscope with a pinhole diameter of 1 airy unit, and an excitation wavelength of 488 nm, recorded at 525 nm emission wavelength to confirm mCitrine expression in L5b.

8.2.10 Analysis

Power calculation

I estimated the number of mice needed using G power (Faul et al. 2007). I wanted to detect a 30 cm shift in the average first stop location, and estimated the standard deviation of change to be 20 cm. For a two-tailed t-test, I needed 8 animals to undergo

manipulation. I pooled the data from all three CNO, and all three saline days for each mouse.

Exclusion criteria

Some stress is expected from head-fixed animals, but if an animal showed extreme distress for more than one minute during habituation, such as scratching the wheel, or vocalizing, it was put back in its home cage, and habituation was attempted two more times before the animal was excluded from the experiment.

Animals that ran fewer than 20 trials for three consecutive weeks, or did not reach probe trials within 4 training weeks were terminated and excluded from the experiment. Mice that showed severe food deprivation symptoms on manipulation days were excluded. These exclusion criteria were predetermined.

In addition to predetermined exclusion criteria, I excluded the last two manipulation days for one animal, because the reward system stopped working, and therefore the animal was not rewarded and lost motivation.

Data processing pipeline

For the behavioural analysis, local field potential analysis, and pre-processing electrophysiology data for spike sorting, I wrote all analysis software in Python 3 (www.python.org). I adapted some scripts originally written by Dr Marlies Oostland, Dr Alfredo Gonzalez-Sulser, Dr Sarah Tennant, and Alex Kirillov. I implemented an object-oriented approach for handling the files and parameters of the task and animals. For the rest of the code I divided the script into modules. For spike sorting, I used Plexon's Offline Sorter (Plexon Offline sorter, 2017). I decided to split the Python

code into two main functions, one for the processing that took place before spike sorting, and one for the sorted data.

In the first main function, the parameters of the recording are initialized. Parameters, such as file name, properties of the track, location of the reward zone, number of electrophysiology channels, and the speed threshold for detecting stops were defined in the Parameters class. This allowed me to write methods in the Parameters class for setting and getting these parameters that can be called from any part of the script, helping me avoid hardcoding parameters into functions.

After initializing the parameters, I called functions from the first main function to pre-process the data and saved numpy arrays containing information related to the movement of the animal for further processing, and a nex5 (Neuroexplorer) file for spike sorting.

After I performed spike detection and sorting in Plexon's Offline sorter, I exported the cluster IDs and corresponding time stamps to a .txt file. In the second main function, I read the .txt file containing the sorted units, and the numpy arrays with the movement information I saved in the pre-processing step, and plotted firing fields for each cell (Figure 8.7).

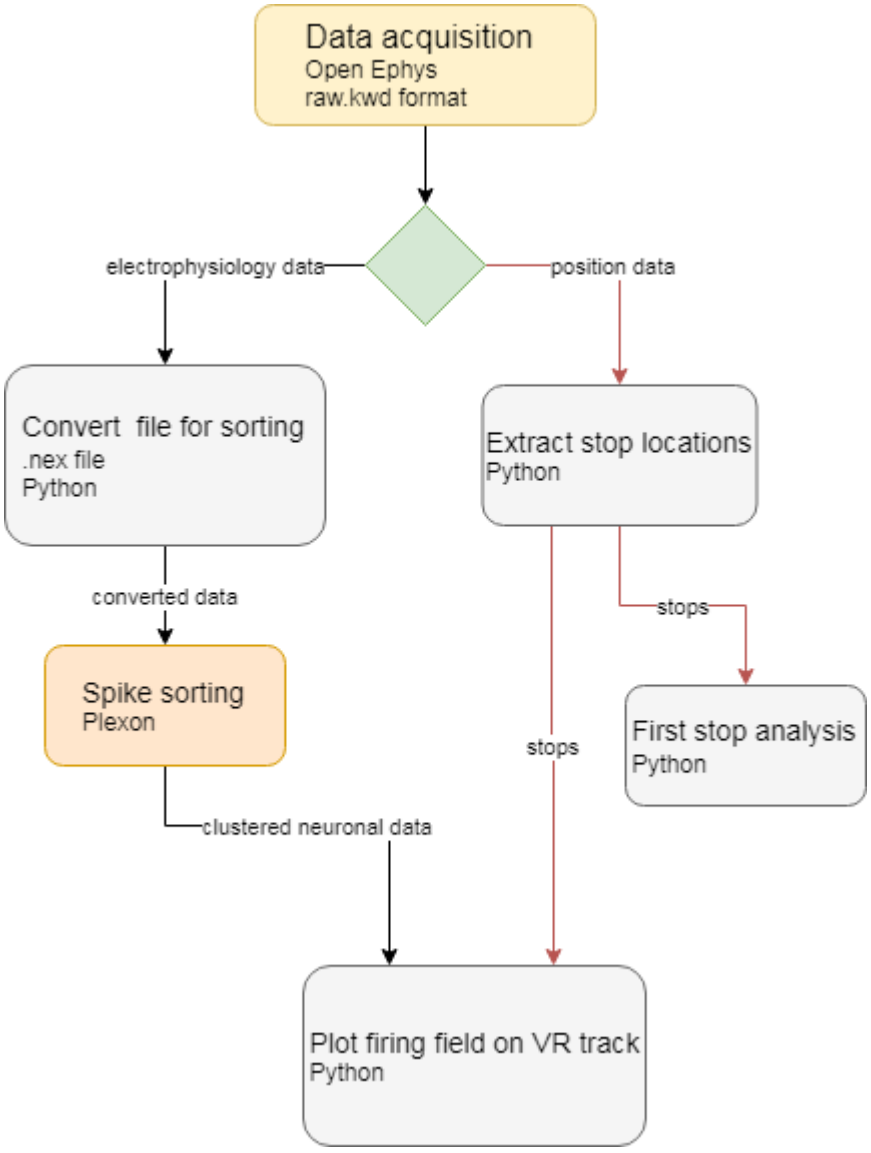

Figure 8.7. Data analysis pipeline. The electrophysiology (black arrows) and position information (red arrows) was saved by the Open Ephys system. Position data was analysed in Python for the first stop analysis. The electrophysiology signal was processed in Python, and converted to a .nex file, and the spike sorting was done using Plexon's Offline Sorter. Firing fields were plotted in Python.

Pre-processing behavioural data

Based on the signal recorded by the rotary encoder, I calculated the location of the mouse on the track, its velocity, average speed, and whether it was stationary. To obtain the location, I first converted the location data to centimetres. I implemented

this by first calculating the virtual units / cm value by finding the minimum and maximum values recorded by the rotary encoder, and dividing the difference of these by the length of the track. Then, I divided the location recorded by the encoder by the units / cm value. For calculating an instantaneous velocity, I subtracted the location of the mouse from the location it reached 200 ms later. When the mouse ran between the end and beginning of the track, subtracting these values from each other yielded incorrect negative speed values. To the values that were bigger than (-1) * track length + maximum velocity and smaller than maximum velocity * (-1), I added track length (200 cm). I calculated the average speed by calculating a rolling average on 200 ms of instant velocity.

I defined a stop as when the treadmill velocity was < 0.7 cm / s, which is the threshold used by Blender for releasing the soy milk reward when the mouse stops in the reward zone. Using this threshold, I separated the data into when the mouse moves and when it is stationary and saved the corresponding indices in numpy arrays.

To extract stops, I first found all indices in the average speed array where the speed was below the stop threshold. This array contained intervals where the mouse was still. To get the location where the animal stopped, I needed to find the first index from each interval. To do this, I added 1 to the indices of the array that contained the intervals with low speed. The indices that were only present in the low speed array, but not in the shifted array were the beginnings of the intervals when the mouse was slower than the threshold, and I considered these indices the stops. I defined a ‘first stop’ as the first location where the mouse stopped from the end of the first back box within a given trial. I extracted first stops and used them for the behavioural analysis.

Pre-processing electrophysiology data

For pre-processing the electrophysiology signal, I read the raw.kwd (Open Ephys) files in Python and extracted the data where the position of the mouse was between the end of the first black box and the reward zone. I did this to remove data that may be noisy due to the mouse drinking the reward. To reduce correlated noise, I did the following for all four tetrodes. For each sampling point, I calculated the median value (Rolston, Gross, and Potter 2009) of the electrophysiology signal from the 12 channels of the other three tetrodes, and then subtracted this value from the channels of the analysed tetrode. I used this method because different tetrodes are less likely to record action potentials from the same cells, so using them as a reference is less likely to reduce the signal. I wrote the data I extracted that had no drinking noise to a .nex5 (Neuroexplorer) file that is compatible with Plexon's Offline Sorter. I adapted the Neuroexplorer writer function provided by Alex Kirillov.

Behavioural analysis

To evaluate how well mice estimated distance in the location estimation task, I looked at how close to the reward zone they ran before stopping for the first time on each trial. I calculated the average first stop location for each training session, and the standard deviation of the first stops pooled from all trials. For analysing days when the mice were injected with saline or CNO, I pooled all trials for the three days of each type of manipulation, respectively.

Electrophysiology analysis

In order to separate single units from the LFP recordings, I performed spike sorting using Plexon's Offline Sorter. First, I opened the .nex5 file containing the recorded data from the outbound journey in the Offline Sorter, and saved it as a .plx file. In the .plx file, I selected 'tetrode' in the channel map tab. I performed the following steps for each tetrode separately. I selected the tetrode, and filtered the data using a 4-pole Bessel low-cut filter. I manually selected thresholds for each tetrode separately (> 70 µV), and detected spikes (waveform length = 4.2 µs). At this point, if the units in my recording were well-separated enough for sorting, it was possible to see the clusters by plotting the first and second principal components. For the sorting I performed a Valley Seeking scan in 3D feature space, using all channels of the given tetrode. I scanned the Parzen Multiplier from 0.5 to 1.5 (step size = 0.2). To determine the quality of the clusters, the isolation distances and L-ratio (isolation quality) were calculated in 2D and 3D feature space for all units (Schmitzer-Torbert et al. 2005). After calculating the quality of the clusters, I exported the timestamps with the corresponding unit ID to a text file. Finally, I plotted the firing locations on each trial of each successfully sorted cell to obtain their firing fields.

8.3 Results

To test whether p038 Cre positive L5b cells play a role in location estimation, I trained mice to perform a virtual reality based location estimation task, and when their performance reached pre-determined criteria, I silenced Cre positive cells by injecting CNO intraperitoneally. Mice ran on a treadmill and over time developed a spatially selective strategy to stop in a reward zone. Three out of the nine mice I trained reached criteria and were tested. One of the other animals was terminated due to health reasons, and the rest of the animals' performance was not high enough to undergo manipulation. Further, I recorded extracellular activity in the deep MEC to test whether neuronal activity correlates with the task. Neurons fired as the animals ran on the track.

8.3.1 Behavioural results

Training mice to learn a location estimation task

The number of mice to reach the test stage of the experiment was in line with previous experiments performed in the lab. Possible reasons for mice not to progress to a subsequent stage are loss of motivation due to inadequate food deprivation, the position of the microdrive, which was not standardized, and the relative body weight, as heavier animals tended to progress further.

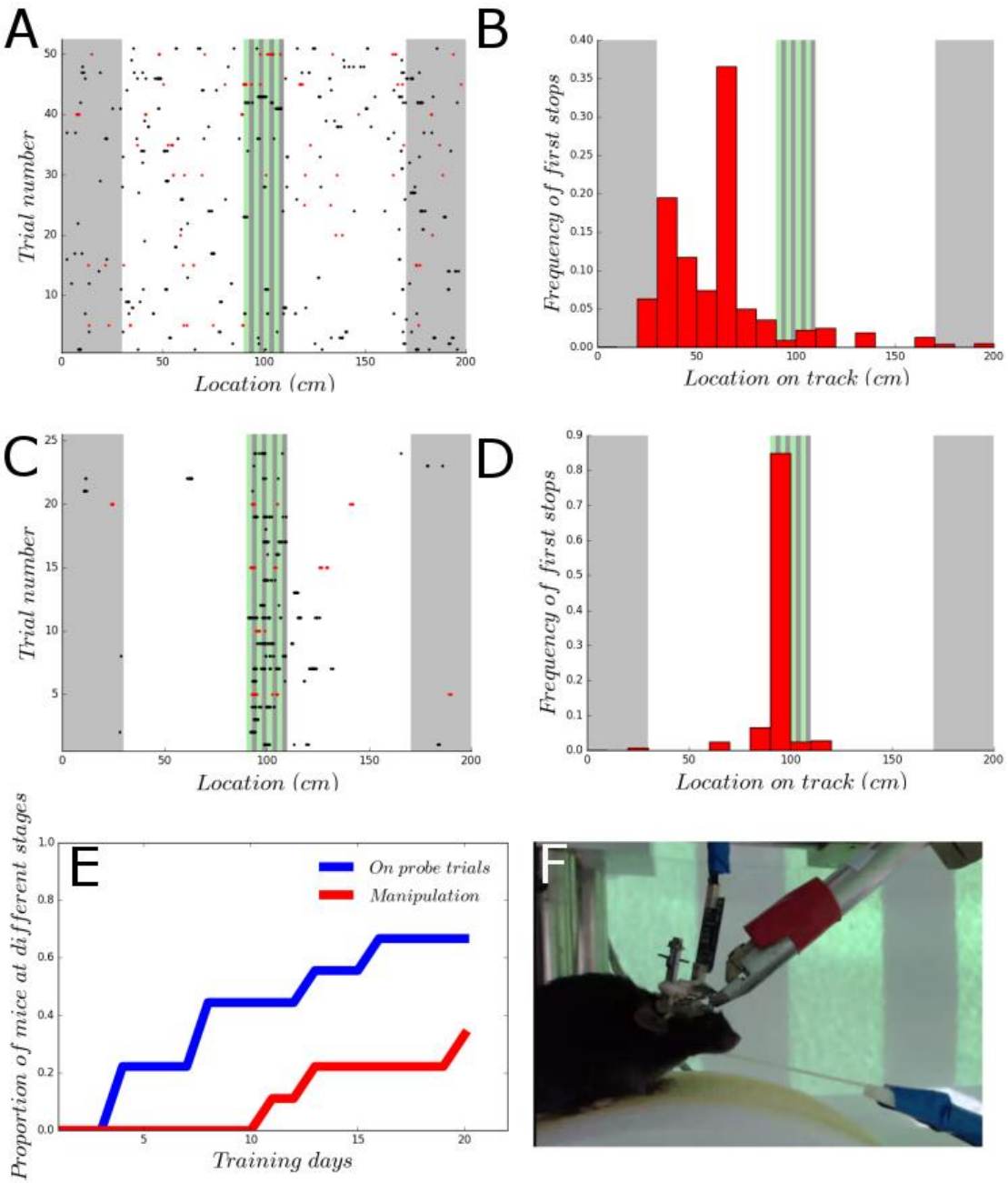

Figure 8.8. Learning the virtual reality location estimation task. A and C show the locations of the stops of a mouse on the first training day, and the day before manipulation, respectively. The red dots represent stops on non-beaconed trials, and the black dots all other trials. Every second non-beaconed trial is a probe trial on C. B and D show the histogram of the locations where the mouse stopped for the first time on the first training day (B) and on the last day before the manipulation (D). The grey areas on the plots show the position of the black box on the virtual corridor, and the green and grey stripes represent the reward zone on A, B, C and D. (E) Proportion of mice on probe trials (blue) and undergoing DREADD manipulation (red) on training days (n=9 mice, 5 males and 4 females). (F) Animal performing the location estimation task.

Naïve mice did not show a spatially selective stopping strategy (Figure 8.8A-B), but after training mice stopped selectively inside the reward zone, or just ahead of the reward zone (Figure 8.8C-D). The fraction of mice meeting the criterion for introduction of probe trials increased to an apparent asymptote of 5 / 9 mice by day 16. The criterion for testing animals with the DREADD manipulation was reached later and in a smaller proportion of mice (n = 3 / 9 by day 21) (Figure 8.8E). Overall, half of the animals reached probe trials within the first two training weeks, and the three mice that reached the manipulation criteria achieved this during the first four training weeks. Three of the animals that reached probe trials performed a high number of trials daily (> 100), suggesting that they stayed motivated, but never reached the manipulation stage (Figure 8.9).

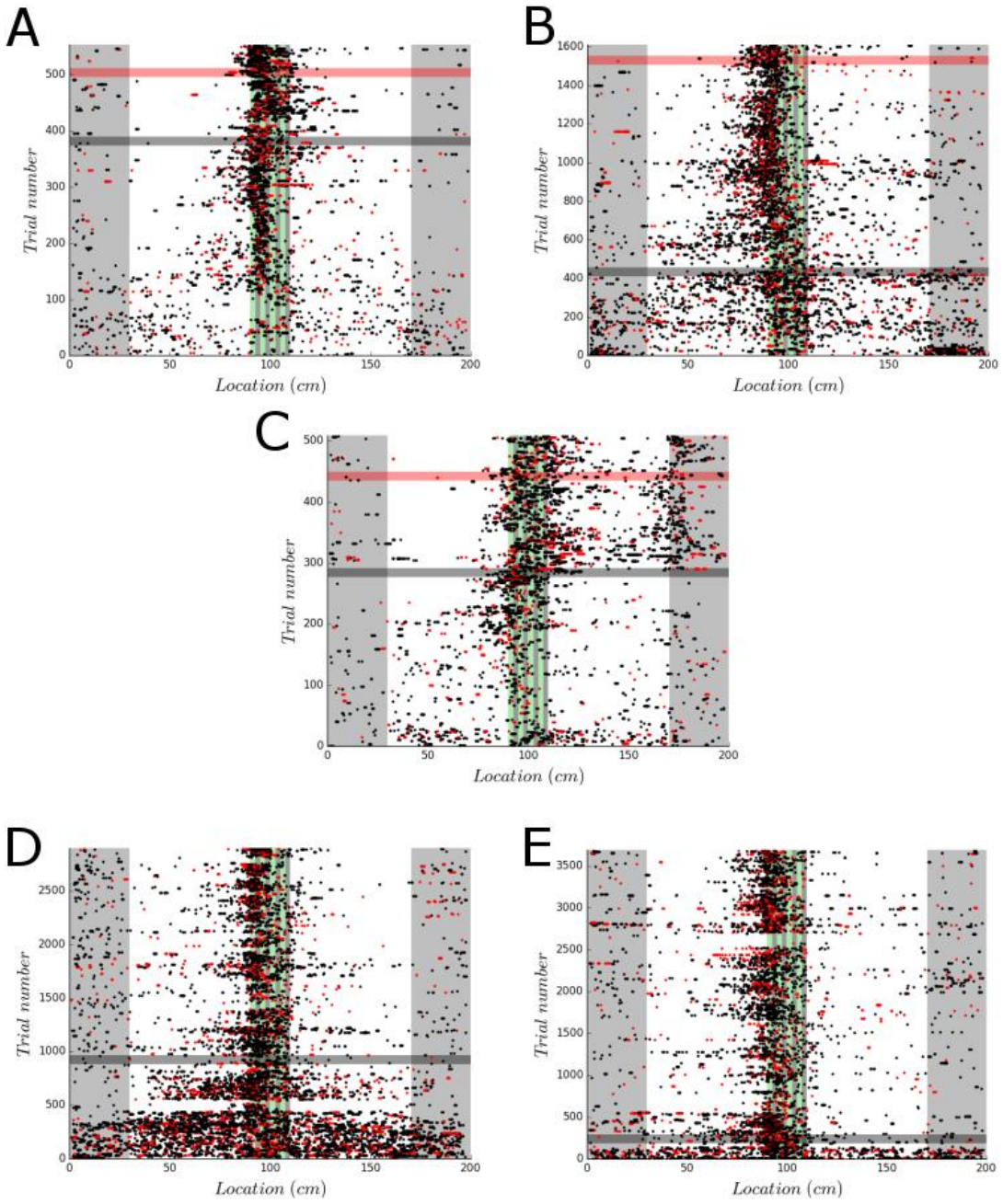

Figure 8.9. Stopping patterns in different stages of learning the location estimation task. (A-C) Data from the three mice that reached the manipulation stage of the experiment. Data from trials across all days of the experiment ordered by trial number. (D-E) Similar plots for data from two mice that reached probe trials, but did not reach the manipulation criteria. Data was pooled for all training days. The horizontal black lines represent when the mouse reached probe trials, and the horizontal red lines show when mice reached the manipulation criteria.

Spatial stopping behaviour is maintained during inhibition of hM4Di expressing neurons

To test whether activation of hMD4i receptors with CNO influences location estimation on the task, I injected CNO and saline on alternate days for 6 days in total. Two animals passed performance criteria and reached the DREADD manipulation stage of the experiment. In addition to these mice I injected 7 more animals that did not pass criteria after they dropped out from the experiment. Overall, out of the 9 animals that received a CNO injection, 4 showed adverse effects and were terminated. These animals were active for a few minutes after the injection, then they became passive, and then completely lethargic, and did not respond to pinch tests. The other five mice did not show any adverse effects and were active shortly after the injection. The animals that did not show adverse effects and underwent manipulation did not have impaired location estimation.

I aimed to evaluate the effects of CNO using a paired t-test, using the saline days as an internal control. Since only two animals completed this stage of the experiment, I was unable to do this test, therefore I performed a within mouse comparison on those two animals to test whether the CNO had an effect on their behaviour (Figure 8.10).

I performed a two tailed t-test (unequal variances) to compare the pooled data from all CNO and all saline days for both mice that completed the experiment. There was no significant difference between the first stop locations on trials ($t = 0.748$, $p = 0.457$ for one of the mice, and $t = -0.325$, $p = 0.746$ for the other mouse). I used the scipy.stat f-test to determine whether variances are equal (alpha = 0.05).

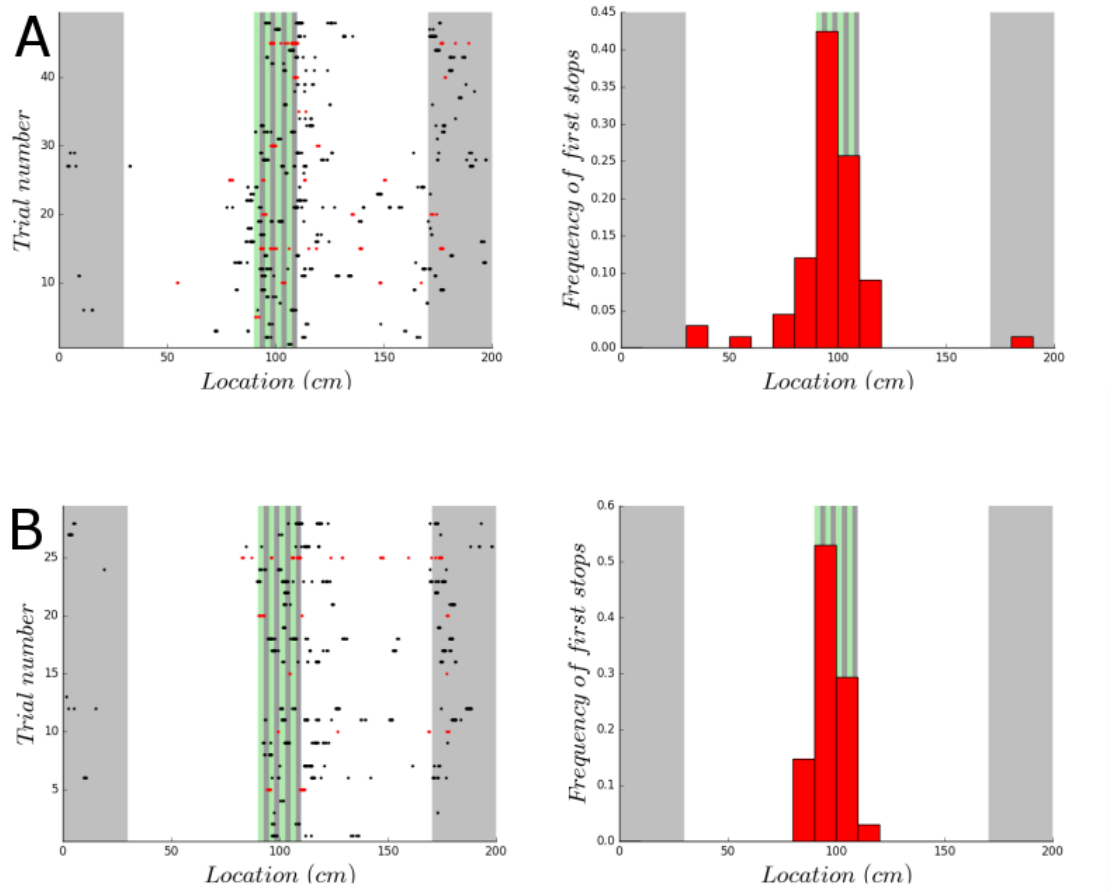

Figure 8.10. Location estimation was not impaired on DREADD manipulation days. Locations of stops on the virtual corridor (left), and the histogram of first stops on trials (right) for an example mouse on pooled data from three days when the mouse was injected with saline (A), and with CNO (B).

8.3.2 Does neuronal activity in L5b correlate with location estimation?

To test whether neuronal activity in layer 5b correlates with location estimation, and to verify that the cells are silenced when CNO is injected, I implanted a 16 channel microdrive targeting the deep MEC to perform extracellular recordings. Unfortunately, from three of the animals that underwent manipulation, I could not record extracellular activity, most likely due to the tetrodes breaking in surgery. Out of the animals I recorded from, only three mice had recordings, where action potentials were visible

on the LFP signal, but due to the high levels of multi-unit activity, and sometimes movement artefacts, I only managed to perform successful spike sorting on data from one animal that dropped out from the behavioural task. In the successful recording (Figure 8.11), the sorted units were well-separated in feature space (L-ratio: 1.39, 0.93, 7.44, and isolation distance: 205.03, 121.77, 194.27 for the three sorted unis respectively). The firing pattern of the sorted cells did not show spatial selectivity, and the animal did not perform the task well. Since I did not manage to acquire electrophysiology data from animals performing the task well, I could not test whether location estimation correlated with neuronal activity, and could not confirm that the cells were silenced during the DREADD manipulation.

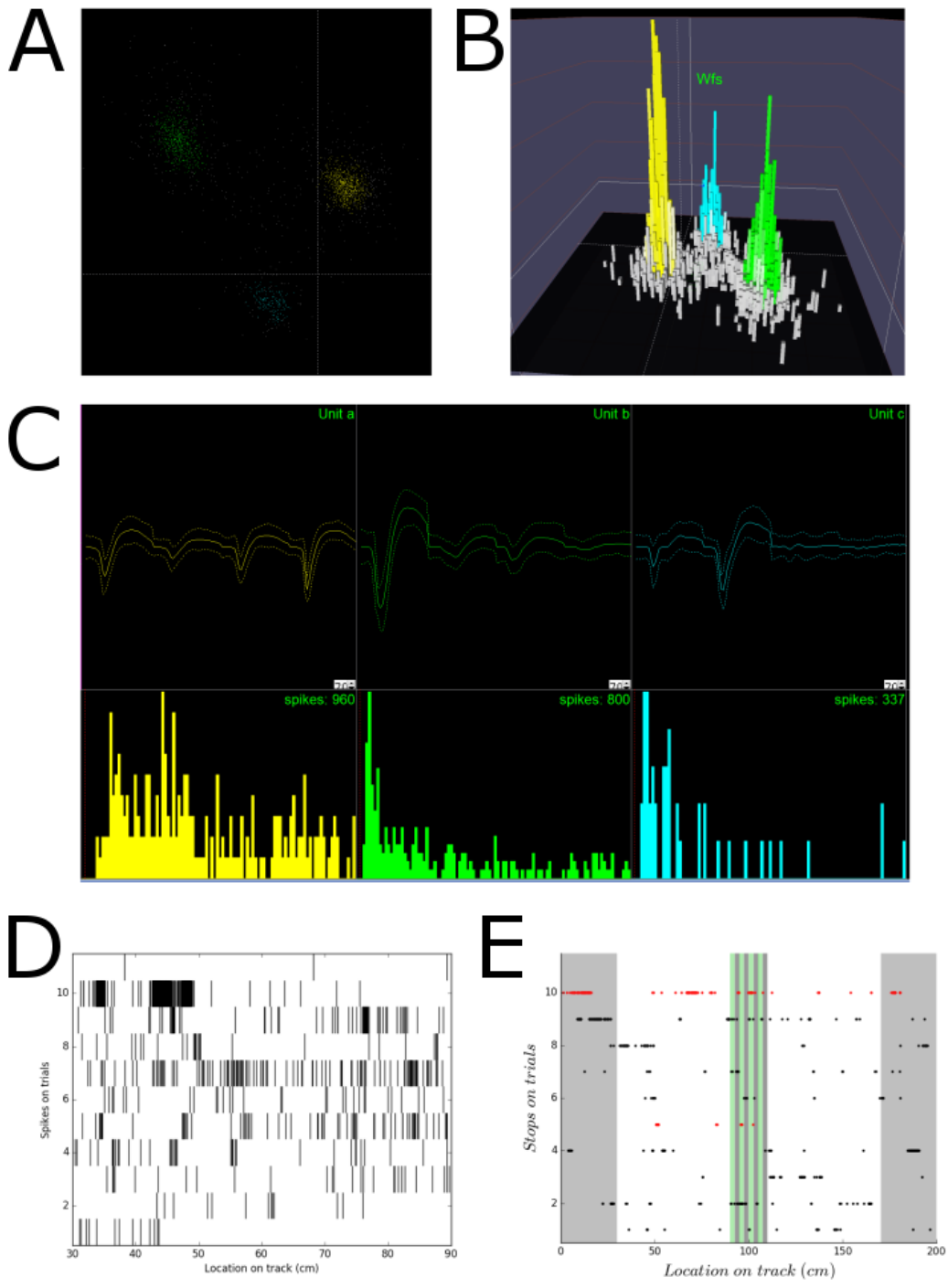

Figure 8.11. Spike sorting and firing field analysis. (A) Spikes in feature space (x= first principal component, y= second principal component). (B) Histogram of waveforms in principal component space (first and second principal components). (C) The shape of waveforms on 4 channels for three sorted units, autocorrelograms of the same units. (D) Firing field of an example cell (plotted in yellow on A, B, and C) in the outbound journey. (E) Stops on the track of the mouse during the recording for the whole virtual track.

8.3.3 hM4Di receptors were not expressed in all animals

Shortly after the animals finished the task I perfused them transcardially, sliced the brains, and labelled neurons using Neurotrace. To verify that hM4Di receptors were present when CNO was injected, I looked at the sections from the mice that completed the task to quantify fluorescence from the mCitrine tag to confirm that they expressed hM4Di receptors. None of the brains had mCitrine labelled cells, and therefore they had no hm4Di receptors.

8.3.4 Cre expression is not specific to L5b in p038 mice

To confirm that Cre is co-expressed with the L5b specific endogenous mCitrine fluorescence in p038 mice, I injected a Cre dependent ChR2 virus (AAV2-fl-ChR2-mCherry, Addgene number: 18916, homemade, 9.84E+12 Cps/ml) into the deep MEC of two mice. I found that the mCherry was not co-expressed with the endogenous mCitrine (Figure 8.12). This indicates that Cre expression is not as specific to L5b as tTA, and that there are Cre positive cells in this line that do not have the mCitrine tag.

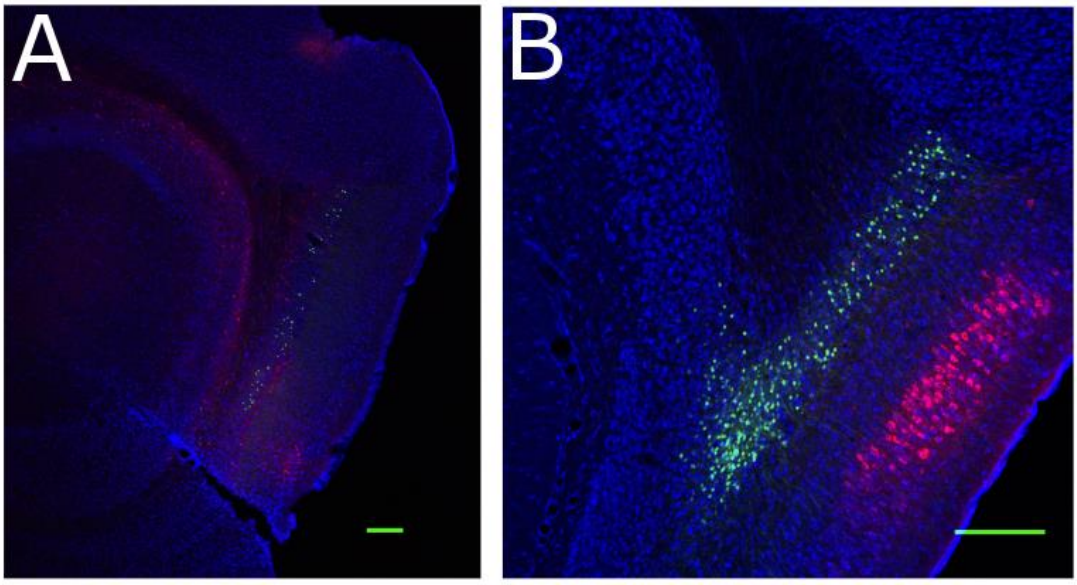

Figure 8.12. Cre expression is not specific to L5b in p038 mice. Histology results on sections from mouse injected with AAV2-fl-ChR2-mCherry (red), stained with neurotrace 640/660 (blue). Green is the endogenous mCitrine fluorescence in p038 mice in the deep MEC. Scale bars are 200 µm. Images were taken using a Nikon A1 microscope using 4x (A), and 10x (B) magnifications with a pinhole diameter of 1 airy unit.

8.4 Discussion

To test whether L5b of the deep MEC in required in location estimation, I trained mice to learn a virtual reality based location estimation task. Once mice learned the task, I silenced L5b cells and tested whether location estimation was impaired. Three out of 9 mice I trained reached pre-determined criteria based on their performance, underwent manipulation, and showed no impairment. Histology analysis revealed that the cells were not silenced in these animals. This was my first attempt at recording neuronal activity in behaving animals, and the signal to noise ratio of my data and technical problems with the microdrive implants and the surgeries did not allow me to perform successful spike sorting analysis on most of the data. The results were not sufficient to test the hypotheses proposed, but I learned about *in vivo* electrophysiology from a technical point of view, and I was able to identify several of

the flaws in my experiment. My results led to observations that can improve on future experiments and this is what I will focus on in the discussion.

8.4.1 Mice learned to estimate location in virtual reality

Using this behavioural protocol enabled me to train mice to learn the virtual reality based location estimation task. To be able to detect subtle changes in behaviour, I needed mice to have consistent performance over the manipulation days, and therefore I set conservative criteria for CNO manipulation. Consequently, very few animals met these criteria. Some animals failed to reach this level of performance, because their first stops were consistently around 5-10 cm before the reward zone. These animals still had a spatially selective stopping strategy and could have had their neural activity manipulated to test whether location estimation is impaired. For this reason, in future experiments I would use more lenient criteria, and I would do manipulations on animals that have an average first stop distance that is either before, or in the reward zone, and train more animals to be able to detect the same effect size.

One reason why some mice did not learn the task could be the position of the microdrive implant, making it uncomfortable for them to run in the virtual reality. Mice that run less will likely receive fewer rewards, and therefore lose motivation. To improve on this, in future experiments I will standardize the location of the grounding screws and the head-post using specific stereotaxic locations. Another potential problem is the weight of the implant relative to the body weight of the animals. The heavier the drive, the more uncomfortable and passive the animal might become. To address this, I will explore options for miniaturizing the microdrive.

8.4.2 Possible ways to improve recordings

To test the prediction that the activity of neurons in L5b of the MEC correlates with behaviour during the location estimation task, I implanted microdrives targeting the deep MEC to record electrophysiological signals while mice perform the task. Most of the electrophysiology recordings in the experiment were unsuccessful. In the majority of recordings, the signal to noise ratio was too low to perform spike sorting. In most cases, the problem was that there were no action potentials present in the recordings, or they had very low amplitudes. In some cases, this was likely because I damaged the tetrodes during surgery, possibly by moving them while fixing the implant with dental cement. To improve on that, in future experiments, I will replace the grounding wires with thinner ones to make sure that accidentally touching them in the surgery cannot move the drive and damage the tetrodes. Another possibility is that if the tetrodes were not perpendicular to the board, lowering the board may have broken or bent them. Lastly, the tetrodes could have been in regions of sparse to no neuronal activity. In some recordings it is possible that the spike sorting did not work because of overlapping waveforms, and low signal to noise ratio.

The presence of 50 Hz noise in most recordings implied that a metal Faraday cage instead of tin foil and conductive tape would be optimal in future experiments. To further increase signal to noise ratio, I will wash the tetrodes with saline after plating to make sure the tips are not blocked by the gold plating solution and are not stuck together. In addition to that, I will use grounding wires that are insulated between the board and ground screw and cover all exposed metal parts with dental cement. Since many cells in the MEC are theta modulated (Deshmukh et al. 2010), they often fire

close to each other in time, making it less useful to use a reference electrode that is in the MEC. To address this difficulty, I could implant a reference electrode to V1.

To perform spike sorting on the data I tested Klusta (Rossant et al. 2016), Klustakwik (S N Kadir, Goodman, and Harris 2017), and Plexon's Offline Sorter. Klusta and Klustakwik use high-dimensional clustering algorithms and take a semi-automatic approach to clustering. Both Klusta and Klustakwik over-cluster the data and then allow the user to do manual curation using a graphical interface. Since most of my data had high frequency noise, possibly due to ground loops in the setup, these noise events were detected as spikes, and resulted in a high number of noise clusters. It is possible that these clusters contained neuronal spikes but they were not possible to isolate using the programs I tested. An additional problem was that Klustakwik required the spike waveforms as an input for clustering, rather than the continuous data, and I had difficulties detecting the spikes and aligning the waveforms correctly. To address this issue, I tested quickspikes (Meliza and Margoliash 2013) for spike detection, which was more successful than my initial attempts, but did not fully eliminate the alignment errors. Eventually, I tested Plexon's Offline Sorter. The main disadvantage of the Plexon program is that it is only able to use two features at the time, which is not sufficient for clustering tetrode data. All these programs have the disadvantage that the data needs to be manually curated after the automatic step, which makes the analysis biased, and not necessarily repeatable. To improve on the spike sorting analysis, I will test other software in future experiments, and aim for a pipeline that is more automatic.

To make targeting the deep MEC easier, in the next experiment, I will inject a tTA-dependent ChR2 virus to p038 mice and implant an optic fibre as well as tetrodes. This way, when I shine the light, if the optic fibre is close enough to the cells infected

by the ChR2 virus, the cells will fire action potentials. This will enable me to identify L5b cells, and if they fire action potentials during the experiment I will be able to characterize their firing fields in the VR task. Even if the cells only give a population level response, the response will help estimate the distance of the recording electrodes from the infected L5b cells. Furthermore, this method will also make it possible to quantify cells that are silent during the recordings.

8.4.3 Interpretation of results and limitations

The results of this experiment are not conclusive, since I did not have enough animals completing the task and I could not prove that the cells were silenced.

Since the two mice that completed the task did not have any fluorescent cells in the MEC, they were genotyped again. The genotyping results showed that these mice were double heterozygous p038 +/-, hm4Di +/- animals, in accordance with the genotyping results prior to the experiment, making mishandling of the samples unlikely. This genotype was unexpected, since our preliminary test showed that double heterozygous mice have fluorescence in the deep MEC. After inspecting the sequences that were used for genotyping, I discovered that the primers used to detect p038 positive mice (primers for eGFP) also bind to the mCitrine sequence found in hm4Di mice. Therefore, some of my hm4Di +/- experimental mice could have been negative for p038 (-/-), but still detected as heterozygous p038 +/-, hm4Di +/- animals. Having both genotypes in my experimental group would explain why some animals showed adverse effects after CNO injection and others did not. This is because the p038 (-/-) mice had no hM4Di receptors, so CNO did not affect them.

Further investigation of Cre specificity in p038 mice showed that expression of Cre in this line is not as specific as expression of tTA. This lack of specificity suggests that the fluorescent tag, that is restricted to L5b, which is linked to a Tet Responsive Element (TRE) promoter, is not present in all Cre positive cells (Shima et al. 2016). The leaky Cre expression, possibly present in other organs, is a potential explanation for some animals showing adverse effects, since all Cre expressing cells were silenced. However, I did not carry out histological analysis in other parts of the brain or in other organs, so I could not confirm whether they had Cre expression.

8.4.4 Future experiments

One way of testing whether the location estimation task requires L5b neurons would be to inject a tTA-dependent inhibitory DREADD virus (hM4Di) into the deep MEC of p038 mice and silence the cells during the virtual reality location estimation task. The main disadvantage of this approach is that based on my histology results, the tTA positive population in p038 mice is only a subset of layer 5b cells, so silencing only the cells infected by the virus may not be enough to impair location estimation even if the layer does contribute to the process. Additionally, further experiments would need to investigate whether p038 cells are a random subpopulation of L5b neurons, or if they are a functional subtype to be able to interpret such an experiment. Another reason why this experiment is likely to yield an inconclusive or negative result is that it was shown by Burgalossi, von Heimendahl, & Brecht (2014) that neuronal firing is sparse in the deep MEC, suggesting that it may be insufficient to silence a small subpopulation for a behavioural test. However, it is possible that deep MEC cells are more active when animals perform a task relative to open field exploration, but this was not tested previously.

Another approach to manipulate p038 cells would be to inject a tTA-dependent excitatory DREADD virus (hM3Dq) into the deep MEC. This approach would test whether the manipulation impairs location estimation. Additionally, by recording neuronal activity in the superficial MEC, it could be tested whether grid fields change when the deep MEC is activated. By recording in CA1 of the hippocampus, it could also be tested whether place cells remap when L5b of the MEC is manipulated. These tests would complement the findings of Kanter et al. (2017), who showed that depolarizing the superficial MEC causes hippocampal place fields to remap, and indicate whether L5b cells influence grid firing fields. The main disadvantage of this approach is that activating p038 cells could influence behaviour even if the cells are not needed for location estimation.

Another way to investigate the contribution of deep MEC cells to location estimation is to record from them and analyse the correlation of neuronal activity and behaviour. For this approach, I could inject a tTA-dependent ChR2 virus to make p038 cells light responsive, and identify them by shining a light via an implanted optic fibre. Infected p038 cells would fire upon light stimulations, allowing me to identify them and see when they are active during the task. Knowing where L5b cells fire during the location estimation task could inform specific manipulation strategies in future experiments.

Appendix references

Allen, K., M. Gil, E. Resnik, O. Toader, P. Seeburg, and H. Monyer. 2014. “Impaired Path Integration and Grid Cell Spatial Periodicity in Mice Lacking GluA1-Containing AMPA Receptors.” *Journal of Neuroscience* 34 (18): 6245–59.

Alonso, A., and E. García-Austt. 1987. “Neuronal Sources of Theta Rhythm in the Entorhinal Cortex of the Rat.” *Experimental Brain Research* 67 (3): 493–501.

Alyan, Sofyan, and Rudolf Jander. 1994. “Short-Range Homing in the Mouse Mouse, Mus Musculus: Stages in the Learning of Directions.” *Anim. Behav,* 48: 285–89. https://ac.els-cdn.com/S0003347284712425/1-s2.0-S0003347284712425-main.pdf?_tid=25e0072c-1c2c-4df8-a4ae-5cff9089e209&acdnat=1535475072_11cc8e8bd551184564924967bc50263f.

Aronov, Dmitriy, Rhino Nevers, and David W. Tank. 2017. “Mapping of a Non-Spatial Dimension by the Hippocampal–entorhinal Circuit.” *Nature* 543 (7647): 719–22.

Aronov, Dmitriy, and David W Tank. 2014. “Engagement of Neural Circuits Underlying 2D Spatial Navigation in a Rodent Virtual Reality System.” *Neuron* 84 (2): 1922–2013.

Atasoy, Deniz, Yexica Aponte, Helen Hong Su, and Scott M Sternson. 2008. “A FLEX Switch Targets Channelrhodopsin-2 to Multiple Cell Types for Imaging and Long-Range Circuit Mapping.” *The Journal of Neuroscience : The Official Journal of the Society for Neuroscience* 28 (28): 7025–30.

Barry, Caswell, and Neil Burgess. 2007. “From Grid Cells to Place Cells: A Mathematical Model.” *Hippocampus* 17 (9): 801–12.

Bean, Bruce P. 2007. “The Action Potential in Mammalian Central Neurons.” *Nature Reviews Neuroscience* 8 (6): 451–65.

Benureau, Fabien C. Y., and Nicolas P. Rougier. 2018. “Re-Run, Repeat, Reproduce, Reuse, Replicate: Transforming Code into Scientific Contributions.” *Frontiers in Neuroinformatics* 11 (January): 69.

Blodgett, H. C. 1929. “The Effect of the Introduction of Reward upon the Maze Performance of Rats.” *University of California Publications in Psychology*. https://psycnet.apa.org/record/1930-01027-001.

Boyden, Edward S., Feng Zhang, Ernst Bamberg, Georg Nagel, and Karl Deisseroth. 2005. “Millisecond-Timescale, Genetically Targeted Optical Control of Neural Activity.” *Nature Neuroscience* 8 (9): 1263–68.

Brun, Vegard Heimly, Trygve Solstad, Kirsten Brun Kjelstrup, Marianne Fyhn, Menno P. Witter, Edvard I. Moser, and May-Britt Moser. 2008. “Progressive Increase in Grid Scale from Dorsal to Ventral Medial Entorhinal Cortex.” *Hippocampus* 18 (12): 1200–1212.

Buccino, Alessio Paolo, Mikkel Elle Lepperod, Svenn-Arne Dragly, Philipp Dominik Hafliger, Marianne Fyhn, and Torkel Hafting. 2018. “Open Source Modules for Tracking Animal

Behavior and Closed-Loop Stimulation Based on Open Ephys and Bonsai." *BioRxiv*, June, 340141.

Buchler, E R, and S B Childs. 1981. "Orientation to Distant Sound by Foraging Big Brown Bats (Eptesicus Fuscus)." *Animal Behaviour* 29: 428–32.

Buetfering, Christina, Kevin Allen, and Hannah Monyer. 2014. "Parvalbumin Interneurons Provide Grid Cell–driven Recurrent Inhibition in the Medial Entorhinal Cortex." *Nature Neuroscience* 17 (5): 710–18.

Burak, Yoram, and Ila R Fiete. 2009. "Accurate Path Integration in Continuous Attractor Network Models of Grid Cells." Edited by Olaf Sporns. *PLoS Computational Biology* 5 (2): e1000291.

Burgalossi, Andrea, Moritz von Heimendahl, and Michael Brecht. 2014. "Deep Layer Neurons in the Rat Medial Entorhinal Cortex Fire Sparsely Irrespective of Spatial Novelty." *Frontiers in Neural Circuits* 8 (July): 74.

Burgalossi, Andrea, Lucas Herfst, Moritz von Heimendahl, Henning Förste, Kurt Haskic, Martin Schmidt, and Michael Brecht. 2011. "Microcircuits of Functionally Identified Neurons in the Rat Medial Entorhinal Cortex." *Neuron* 70 (4): 773–86.

Burwell, Rebecca D., and David G. Amaral. 1998. "Cortical Afferents of the Perirhinal, Postrhinal, and Entorhinal Cortices of the Rat." *Journal of Comparative Neurology* 398 (2): 179–205.

Busse, L., A. Ayaz, N. T. Dhruv, S. Katzner, A. B. Saleem, M. L. Scholvinck, A. D. Zaharia, and M. Carandini. 2011. "The Detection of Visual Contrast in the Behaving Mouse." *Journal of Neuroscience* 31 (31): 11351–61.

Buzsáki, György, and Edvard I Moser. 2013. "Memory, Navigation and Theta Rhythm in the Hippocampal-Entorhinal System." *Nature Neuroscience* 16 (2): 130–38.

Buzsáki, György, and David Tingley. 2018. "Space and Time: The Hippocampus as a Sequence Generator." *Trends in Cognitive Sciences* 22 (10): 853–69.

Canto, Cathrin B., and Menno P. Witter. 2012a. "Cellular Properties of Principal Neurons in the Rat Entorhinal Cortex. I. The Lateral Entorhinal Cortex." *Hippocampus* 22 (6): 1256–76.

Canto, Cathrin B., Floris G. Wouterlood, and Menno P. Witter. 2008. "What Does the Anatomical Organization of the Entorhinal Cortex Tell Us?" *Neural Plasticity* 2008.

Canto, Cathrin B, and Menno P Witter. 2012b. "Cellular Properties of Principal Neurons in the Rat Entorhinal Cortex. II. The Medial Entorhinal Cortex." *Hippocampus* 22 (6): 1277–99.

Carpenter, Francis, Daniel Manson, Kate Jeffery, Neil Burgess, and Caswell Barry. 2015. "Grid Cells Form a Global Representation of Connected Environments." *Current Biology : CB* 25 (9): 1176–82.

Chen, G., J. A. King, N. Burgess, and J. O'Keefe. 2013. "How Vision and Movement Combine in the Hippocampal Place Code." *Proceedings of the National Academy of Sciences* 110 (1): 378–83.

Christopher D. Harvey, Philip Coen and David W. Tank. 2012. “Choice-Specific Sequences in Parietal Cortex during a Virtual- Navigat” 484 (7392): 62–68.

Chung, Jason E., Jeremy F. Magland, Alex H. Barnett, Vanessa M. Tolosa, Angela C. Tooker, Kye Y. Lee, Kedar G. Shah, Sarah H. Felix, Loren M. Frank, and Leslie F. Greengard. 2017. “A Fully Automated Approach to Spike Sorting.” *Neuron* 95 (6): 1381–1394.e6.

Chung, Kwanghun, Jenelle Wallace, Sung-Yon Kim, Sandhiya Kalyanasundaram, Aaron S. Andalman, Thomas J. Davidson, Julie J. Mirzabekov, et al. 2013. “Structural and Molecular Interrogation of Intact Biological Systems.” *Nature* 497 (7449): 332–37.

Claessen, Michiel H.G., and Ineke J.M. van der Ham. 2017. “Classification of Navigation Impairment: A Systematic Review of Neuropsychological Case Studies.” *Neuroscience & Biobehavioral Reviews* 73 (February): 81–97.

Clark, R E, S M Zola, and L R Squire. 2000. “Impaired Recognition Memory in Rats after Damage to the Hippocampus.” *The Journal of Neuroscience : The Official Journal of the Society for Neuroscience* 20 (23): 8853–60.

Cochran, William W, Henrik Mouritsen, and Martin Wikelski. 2004. “Migrating Songbirds Recalibrate Their Magnetic Compass Daily from Twilight Cues.” *Science (New York, N.Y.)* 304 (5669): 405–8.

Constantinescu, A. O., J. X. OReilly, and T. E. J. Behrens. 2016. “Organizing Conceptual Knowledge in Humans with a Gridlike Code.” *Science* 352 (6292): 1464–68.

Czajkowski, Rafał, Jørgen Sugar, Sheng-Jia Zhang, Jonathan J Couey, Jing Ye, and Menno P Witter. 2013. “Systems/Circuits Superficially Projecting Principal Neurons in Layer V of Medial Entorhinal Cortex in the Rat Receive Excitatory Retrosplenial Input.” *The Journal of Neuroscience* 33 (40): 15778–92.

Danziger, Shai, Jonathan Levav, and Liora Avnaim-Pesso. 2011. “Extraneous Factors in Judicial Decisions.” *Proceedings of the National Academy of Sciences of the United States of America* 108 (17): 6889–92.

Darwin, C. 1873. “Origin of Certain Instincts.” *Nature*, no. 7: 417–18.

Davis, A E, A M Gimenez, and B Therrien. 2001. “Effects of Entorhinal Cortex Lesions on Sensory Integration and Spatial Learning.” *Nursing Research* 50 (2): 77–85. http://www.ncbi.nlm.nih.gov/pubmed/11302296.

Deshmukh, Sachin S, D Yoganarasimha, Horatiu Voicu, and James J Knierim. 2010. “Theta Modulation in the Medial and the Lateral Entorhinal Cortices.” *Journal of Neurophysiology* 104 (May): 994–1006.

Dickson, Clayton T., Ian J. Kirk, Scott D. Oddie, and Brian H. Bland. 1995. “Classification of Theta-Related Cells in the Entorhinal Cortex: Cell Discharges Are Controlled by the Ascending Brainstem Synchronizing Pathway in Parallel with Hippocampal Theta-Related Cells.” *Hippocampus* 5 (4): 306–19.

Domnisoru, Cristina, Amina A Kinkhabwala, and David W Tank. 2013. “Membrane Potential Dynamics of Grid Cells.” *Nature* 495: 199–204.

Dordek, Yedidyah, Daniel Soudry, Ron Meir, and Dori Derdikman. 2016. “Extracting Grid Cell

Characteristics from Place Cell Inputs Using Non-Negative Principal Component Analysis." *ELife* 5 (March).

Dumont, Julie R., and Jeffrey S. Taube. 2015. "The Neural Correlates of Navigation beyond the Hippocampus." *Progress in Brain Research* 219: 83–102.

Egorov, A V, B N Hamam, E Fransen, M E Hasselmo, and Angel A Alonso. 2002. "Graded Persistent Activity in Entorhinal Cortex Neurons." *Nature* 420 (6912): 173–78.

Einevoll, Gaute T, Felix Franke, Espen Hagen, Christophe Pouzat, and Kenneth D Harris. 2013. "Towards Reliable Spike-Train Recordings from Thousands of Neurons with Multielectrodes." *Curr Opin Neurobiol* 22 (1): 11–17.

Ekanadham, Chaitanya, Daniel Tranchina, and Eero P Simoncelli. 2014. "A Unified Framework and Method for Automatic Neural Spike Identification TL - 222." *Journal of Neuroscience Methods* 222 VN-: 47–55.

Endres, Dominik M, and Johannes E Schindelin. 2003. "A New Metric for Probability Distributions." *IEEE Transactions on Information Theory* 49 (7): 1858–60.

Etienne, AS, and KJ Jeffery. 2004. "Path Integration in Mammals." *HIPPOCAMPUS* 14 (2): 180–92.

Faul, Franz, Edgar Erdfelder, A.-G. Lang, and Axel Buchner. 2007. "G*Power: A Flexible Statistical Power Analysis Program for the Social, Behavioral, and Biomedical Sciences." *Behavior Research Methods* 39 (2): 175–91.

Feil, Susanne, Nadejda Valtcheva, and Robert Feil. 2009. *Inducible Cre Mice*. *Methods in Molecular Biology*. Vol. 530.

Fenton, André A, Hsin-Yi Kao, Samuel A Neymotin, Andrey Olypher, Yevgeniy Vayntrub, William W Lytton, and Nandor Ludvig. 2008. "Unmasking the CA1 Ensemble Place Code by Exposures to Small and Large Environments: More Place Cells and Multiple, Irregularly Arranged, and Expanded Place Fields in the Larger Space." *The Journal of Neuroscience : The Official Journal of the Society for Neuroscience* 28 (44): 11250–62.

Ferbinteanu, Janina. 2016. "Contributions of Hippocampus and Striatum to Memory-Guided Behavior Depend on Past Experience." *The Journal of Neuroscience : The Official Journal of the Society for Neuroscience* 36 (24): 6459–70.

Fernández-Durán, Juan José, and María Mercedes Gregorio- Domínguez. 2010. "A Likelihood Ratio Test for Homogeneity in Circular Data." *Journal of Biometrics & Biostatistics* 1 (3).

Field, David J. 1994. "Field - 1994 - What Is the Goal of Sensory Coding.Pdf." *Neural Computation1*.

Fiete, I. R., Y. Burak, and T. Brookings. 2008. "What Grid Cells Convey about Rat Location." *Journal of Neuroscience* 28 (27): 6858–71.

Frank, Loren M., and Emery N Brown. 2003. "Persistent Activity and Memory in the Entorhinal Cortex." *Trends in Neurosciences* 26 (8): 397–400.

Franke, Felix, Michal Natora, Clemens Boucsein, Matthias H.J. Munk, and Klaus Obermayer.

2010. “An Online Spike Detection and Spike Classification Algorithm Capable of Instantaneous Resolution of Overlapping Spikes.” *Journal of Computational Neuroscience* 29 (1–2): 127–48.

Fransén, Erik, Babak Tahvildari, Alexei V. Egorov, Michael E. Hasselmo, and Angel A. Alonso. 2006. “Mechanism of Graded Persistent Cellular Activity of Entorhinal Cortex Layer V Neurons.” *Neuron* 49 (5): 735–46.

Fujimaru, Y, and T Kosaka. 1996. “The Distribution of Two Calcium Binding Proteins, Calbindin D-28K and Parvalbumin, in the Entorhinal Cortex of the Adult Mouse.” *Neuroscience Research* 24 (4): 329–43.

Fyhn, Marianne, Sturla Molden, Menno P Witter, Edvard I Moser, and May-Britt Moser. 2004. “Spatial Representation in the Entorhinal Cortex.” *Science (New York, N.Y.)* 305 (5688): 1258–64.

Gamma, Erich, Richard Helm, Ralph Johnson, and John Vlissides. 1994. *Design Patterns - Elements of Reusable Object-Oriented Software*.

Geva-Sagiv, Maya, Liora Las, Yossi Yovel, and Nachum Ulanovsky. 2015. “Spatial Cognition in Bats and Rats: From Sensory Acquisition to Multiscale Maps and Navigation.” *Nature Reviews Neuroscience* 16 (2): 94–108.

Gil, Mariana, Mihai Ancau, Magdalene I. Schlesiger, Angela Neitz, Kevin Allen, Rodrigo J. De Marco, and Hannah Monyer. 2018. “Impaired Path Integration in Mice with Disrupted Grid Cell Firing.” *Nature Neuroscience* 21 (1): 81–93.

Gilmore, Rick O., Michele T. Diaz, Brad A. Wyble, and Tal Yarkoni. 2017. “Progress toward Openness, Transparency, and Reproducibility in Cognitive Neuroscience.” *Annals of the New York Academy of Sciences* 1396 (1): 5–18.

Giocomo, Lisa M, May-Britt Moser, and Edvard I Moser. 2011. “Computational Models of Grid Cells.” *Neuron* 71 (4): 589–603.

Gold, Carl, Darrell A Henze, Christof Koch, and György Buzsáki. 2006. “On the Origin of the Extracellular Action Potential Waveform : A Modeling Study On the Origin of the Extracellular Action Potential Waveform : A Modeling Study.” *J Neurophysiol* 95: 3113–28.

Gray, John R, Vincent Pawlowski, and Mark a Willis. 2002. “A Method for Recording Behavior and Multineuronal CNS Acti v Ity from Tethered Insects Flying in Virtual Space.” *Journal of Neuroscience Methods* 120: 211–23.

Gu, Yi, Sam Lewallen, Amina A. Kinkhabwala, Cristina Domnisoru, Kijung Yoon, Jeffrey L. Gauthier, Ila R. Fiete, and David W. Tank. 2018. “A Map-like Micro-Organization of Grid Cells in the Medial Entorhinal Cortex.” *Cell*, September.

Guanella, ALEXIS, DANIEL Kiper, and PAUL Verschure. 2007. “A Model of Grid Cells Based on a Twisted Torus Topology.” *International Journal of Neural Systems* 17 (04): 231–40.

Hafting, Torkel, Marianne Fyhn, Sturla Molden, May-britt Moser, and Edvard I Moser. 2005. “Microstructure of a Spatial Map in the Entorhinal Cortex.” *Nature* 436 (11): 801–6.

Hartley, Tom, N. Burgess, C. Lever, F. Cacucci, and J. O’Keefe. 2000. “Modeling Place Fields in

Terms of the Cortical Inputs to the Hippocampus." *Hippocampus* 10 (4): 369–79.

Harvey, Christopher D, Forrest Collman, Daniel a Dombeck, and David W Tank. 2009. "Intracellular Dynamics of Hippocampal Place Cells during Virtual Navigation." *October* 461 (7266): 941–46.

Hassoun, Mohamad H., and Mohamad H. 1995. *Fundamentals of Artificial Neural Networks*. MIT Press. https://dl.acm.org/citation.cfm?id=526717.

Heys, James G, Krsna V Rangarajan, and Daniel A Dombeck. 2015. "The Functional Micro-Organization of Grid Cells Revealed by Cellular-Resolution Imaging." *Neuron* 84 (5): 1079–90.

Hilgen, Gerrit, Martino Sorbaro, Sahar Pirmoradian, Jens-Oliver Muthmann, Ibolya Edit Kepiro, Simona Ullo, Cesar Juarez Ramirez, et al. 2017. "Unsupervised Spike Sorting for Large-Scale, High-Density Multielectrode Arrays." *Cell Reports* 18 (10): 2521–32.

Hill, Daniel N, Samar B Mehta, and David Kleinfeld. 2015. "Quality Metrics to Accompany Spike Sorting of Extracellular Signals." *J Neuroscience* 25 (8): 713–24.

Hodgkin, A. L., and A. F. Huxley. 1952. "A Quantitative Description of Membrane Current and Its Application to Conduction and Excitation in Nerve." *Bulletin of Mathematical Biology* 117: 500–544.

Holland, Richard A., Joseph L. Kirschvink, Thomas G. Doak, and Martin Wikelski. 2008. "Bats Use Magnetite to Detect the Earth's Magnetic Field." Edited by Sarah Frances Brosnan. *PLoS ONE* 3 (2): e1676.

Holscher, C. 2005. "Rats Are Able to Navigate in Virtual Environments." *Journal of Experimental Biology* 208 (3): 561–69.

Hori, Etsuro, Yoichi Nishio, Kenichi Kazui, Katsumi Umeno, Eiichi Tabuchi, Kazuo Sasaki, Shunro Endo, Taketoshi Ono, and Hisao Nishijo. 2005. "Place-Related Neural Responses in the Monkey Hippocampal Formation in a Virtual Space." *Hippocampus* 15 (8): 991–96.

Iqbal, Shareen A., Joshua D. Wallach, Muin J. Khoury, Sheri D. Schully, and John P. A. Ioannidis. 2016. "Reproducible Research Practices and Transparency across the Biomedical Literature." Edited by David L Vaux. *PLOS Biology* 14 (1): e1002333.

Ismakov, Revekka, Omri Barak, Kate Jeffery, and Dori Derdikman. 2017. "Grid Cells Encode Local Positional Information." *Current Biology* 27: 2337–2343.e3.

Jacob, Pierre-Yves, Giulio Casali, Laure Spieser, Hector Page, Dorothy Overington, and Kate Jeffery. 2017. "An Independent, Landmark-Dominated Head-Direction Signal in Dysgranular Retrosplenial Cortex." *Nature Neuroscience* 20 (2): 173–75.

JAX. n.d. "Body Weight Information." The Jackson Laboratory. Accessed July 17, 2015. http://jaxmice.jax.org/support/weight/000664.html.

Jones, Bethany F., and Menno P. Witter. 2007. "Cingulate Cortex Projections to the Parahippocampal Region and Hippocampal Formation in the Rat." *Hippocampus* 17 (10): 957–76.

Kadir, S N, D F M Goodman, and K D Harris. 2017. “High-Dimensional Cluster Analysis with the Masked EM Algorithm” 26 (11): 2379–94.

Kadir, Shabnam N, Dan F M Goodman, and Kenneth D Harris. 2014. “High-Dimensional Cluster Analysis with the Masked EM Algorithm.” *Neural Computation* 26 (11): 2379–94.

Kanter, Benjamin R., Christine M. Lykken, Daniel Avesar, Aldis Weible, Jasmine Dickinson, Benjamin Dunn, Nils Z. Borgesius, Yasser Roudi, and Clifford G. Kentros. 2017. “A Novel Mechanism for the Grid-to-Place Cell Transformation Revealed by Transgenic Depolarization of Medial Entorhinal Cortex Layer II.” *Neuron* 93 (6): 1480–1492.e6.

Kautzky, Magdalena, and Kay Thurley. 2016. “Estimation of Self-Motion Duration and Distance in Rodents Subject Category : Subject Areas :”

Keller, Georg B., Tobias Bonhoeffer, and Mark Hübener. 2012. “Sensorimotor Mismatch Signals in Primary Visual Cortex of the Behaving Mouse.” *Neuron* 74 (5): 809–15.

Killian, Nathaniel J., Michael J. Jutras, and Elizabeth A. Buffalo. 2012. “A Map of Visual Space in the Primate Entorhinal Cortex.” *Nature* 491 (7426): 761–64.

Klukas, Mirko, Marcus Lewis, and Ila Fiete. 2019. “Flexible Representation and Memory of Higher-Dimensional Cognitive Variables with Grid Cells.” *BioRxiv*, March, 578641.

Kohara, Keigo, Michele Pignatelli, Alexander J Rivest, Hae-Yoon Jung, Takashi Kitamura, Junghyup Suh, Dominic Frank, et al. 2014. “Cell Type-Specific Genetic and Optogenetic Tools Reveal Hippocampal CA2 Circuits.” *Nature Neuroscience* 17 (2): 269–79.

Kozai, Takashi D.Y., and Alberto L. Vazquez. 2015. “Photoelectric Artefact from Optogenetics and Imaging on Microelectrodes and Bioelectronics: New Challenges and Opportunities.” *Journal of Materials Chemistry. B, Materials for Biology and Medicine* 3 (25): 4965.

Kravitz, Alexxai V, Scott F Owen, and Anatol C Kreitzer. 2013. “Optogenetic Identification of Striatal Projection Neuron Subtypes during in Vivo Recordings.” *Brain Res* 31 (9): 1713–23.

Kropff, Emilio, and Alessandro Treves. 2008. “The Emergence of Grid Cells: Intelligent Design or Just Adaptation?” *Hippocampus* 18 (12): 1256–69.

Krupic, J., M. Bauza, S. Burton, C. Lever, and J. O’Keefe. 2013. “How Environment Geometry Affects Grid Cell Symmetry and What We Can Learn from It.” *Philosophical Transactions of the Royal Society B: Biological Sciences* 369 (1635): 20130188–20130188.

Krupic, Julija, Marius Bauza, Stephen Burton, Caswell Barry, and John O’Keefe. 2015. “Grid Cell Symmetry Is Shaped by Environmental Geometry.” *Nature* 518 (7538): 232–35.

Kvitsiani, D, S Ranade, B Hangya, H Taniguchi, JZ Huang, and A Kepecs. 2013. “Distinct Behavioural and Network Correlates of Two Interneuron Types in Prefrontla Cortex.” *Nature* 11 (4).

Landis, Story C., Susan G. Amara, Khusru Asadullah, Chris P. Austin, Robi Blumenstein, Eileen W. Bradley, Ronald G. Crystal, et al. 2012. “A Call for Transparent Reporting to Optimize the Predictive Value of Preclinical Research.” *Nature* 490 (7419): 187–91.

Lashley, K S. 1929. *Brain Mechanisms and Intelligence*. Chicago.

Leighty, Katherine A., and Dorothy M. Fragaszy. 2003. “Primates in Cyberspace: Using Interactive Computer Tasks to Study Perception and Action in Nonhuman Animals.” *Animal Cognition* 6 (3): 137–39.

Leutgeb, Jill K, Stefan Leutgeb, May-Britt Moser, and Edvard I Moser. 2007. “Pattern Separation in the Dentate Gyrus and CA3 of the Hippocampus.” *Science (New York, N.Y.)* 315 (5814): 961–66.

Lever, Colin, Stephen Burton, Ali Jeewajee, John O’Keefe, and Neil Burgess. 2009. “Boundary Vector Cells in the Subiculum of the Hippocampal Formation.” *The Journal of Neuroscience : The Official Journal of the Society for Neuroscience* 29 (31): 9771–77.

Lewicki, M S. 1998. “A Review of Methods for Spike Sorting: The Detection and Classification of Neural Action Potentials.” *Network (Bristol, England)* 9 (4): R53-78.

Lima, Susana Q., Tomáš Hromádka, Petr Znamenskiy, and Anthony M. Zador. 2009. “PINP: A New Method of Tagging Neuronal Populations for Identification during in Vivo Electrophysiological Recording.” *PLoS ONE* 4 (7).

Lipp, Hans-Peter, Alexei L Vyssotski, David P Wolfer, Sophie Renaudineau, Maria Savini, Gerhard Tröster, and Giacomo Dell’Omo. 2004. “Pigeon Homing along Highways and Exits.” *Current Biology* 14 (14): 1239–49.

Liske, Holly, Xiang Qian, Polina Anikeeva, Karl Deisseroth, and Scott Delp. 2013. “Optical Control of Neuronal Excitation and Inhibition Using a Single Opsin Protein, ChR2.” *Scientific Reports* 3 (January): 3110.

Lithfous, Ségolène, André Dufour, and Olivier Després. 2013. “Spatial Navigation in Normal Aging and the Prodromal Stage of Alzheimer’s Disease: Insights from Imaging and Behavioral Studies.” *Ageing Research Reviews* 12 (1): 201–13.

Lopes, Goncalo, Niccolo Bonacchi, Joao Frazao, Joana P. Neto, Bassam V. Atallah, Sofia Soares, Luis Moreira, et al. 2015. “Bonsai: An Event-Based Framework for Processing and Controlling Data Streams.” *Frontiers in Neuroinformatics* 9 (April): 7.

Markus, Etan J., Carol A. Barnes, Bruce L. McNaughton, Victoria L. Gladden, and William E. Skaggs. 1994. “Spatial Information Content and Reliability of Hippocampal CA1 Neurons: Effects of Visual Input.” *Hippocampus* 4 (4): 410–21.

Marre, O., D. Amodei, N. Deshmukh, K. Sadeghi, F. Soo, T. E. Holy, and M. J. Berry. 2012. “Mapping a Complete Neural Population in the Retina.” *Journal of Neuroscience* 32 (43): 14859–73.

Martin, Robert. 2008. *Clean Code: A Handbook of Agile Software Craftsmanship*. Massachusetts.

Martínez, Joan José, Bahar Rahsepar, and John A. White. 2017. “Anatomical and Electrophysiological Clustering of Superficial Medial Entorhinal Cortex Interneurons.” *Eneuro* 4 (5): ENEURO.0263-16.2017.

Mathis, Alexander, Andreas V. M. Herz, and Martin B. Stemmler. 2012. “Resolution of Nested

Neuronal Representations Can Be Exponential in the Number of Neurons." *Physical Review Letters* 109 (1): 018103.

Matsumura, Nobuhisa, Hisao Nishijo, Ryoi Tamura, Satoshi Eifuku, Shunro Endo, and Taketoshi Ono. 1999. "Spatial- and Task-Dependent Neuronal Responses during Real and Virtual Translocation in the Monkey Hippocampal Formation." *J. Neurosci.* 19 (6): 2381–93. http://www.jneurosci.org.sare.upf.edu/content/19/6/2381.long.

Mattis, Joanna, Kay M Tye, Emily A Ferenczi, Charu Ramakrishnan, Daniel J O'Shea, Rohit Prakash, Lisa A Gunaydin, et al. 2012. "Principles for Applying Optogenetic Tools Derived from Direct Comparative Analysis of Microbial Opsins." *Nature Methods* 9 (2): 159–72.

McCormick, D. A., B. W. Connors, J. W. Lighthall, and D. A. Prince. 1985. "Comparative Electrophysiology of Pyramidal and Sparsely Spiny Stellate Neurons of the Neocortex." *Journal of Neurophysiology* 54 (4): 782–806.

Mcnaughton, Bruce L, Francesco P Battaglia, Ole Jensen, and Edvard I Moser. 2006. "Path Integration and the Neural Basis of the ' Cognitive Map .'" *Nature Neuroscience* 7: 663–78.

Meliza, C Daniel, and Daniel Margoliash. 2013. "Emergence of Selectivity and Tolerance in the Avian Auditory Cortex" 31 (9): 1713–23.

Menzel, R., U. Greggers, A. Smith, S. Berger, R. Brandt, S. Brunke, G. Bundrock, et al. 2005. "Honey Bees Navigate According to a Map-like Spatial Memory." *Proceedings of the National Academy of Sciences* 102 (8): 3040–45.

Mitchell, Susan J., and James B. Ranck. 1980. "Generation of Theta Rhythm in Medial Entorhinal Cortex of Freely Moving Rats." *Brain Research* 189 (1): 49–66.

Mittelstaedt, M.-L., and H. Mittelstaedt. 1980. "Homing by Path Integration in a Mammal." *Naturwi* 67.

Mizuno, Hidenobu, Wenshu Luo, Etsuko Tarusawa, Yoshikazu M. Saito, Takuya Sato, Yumiko Yoshimura, Shigeyoshi Itohara, and Takuji Iwasato. 2014. "NMDAR-Regulated Dynamics of Layer 4 Neuronal Dendrites during Thalamocortical Reorganization in Neonates." *Neuron* 82 (2): 365–79.

Morris, Richard G M. 1981. "Spatial Localization Does Not Require the Presence of Local Cues." *Learning and Motivation* 12 (2): 239–60.

Moser, May-Britt, David C Rowland, and Edvard I Moser. 2015. "Place Cells, Grid Cells, and Memory." *Cold Spring Harbor Perspectives in Biology* 7 (2): a021808.

Muller, R U, and J L Kubie. 1987. "The Effects of Changes in the Environment on the Spatial Firing of Hippocampal Complex-Spike Cells." *The Journal of Neuroscience : The Official Journal of the Society for Neuroscience* 7 (7): 1951–68.

O'Keefe, J, and J Dostrovsky. 1971. "The Hippocampus as a Spatial Map . Preliminary Evidence from Unit Activity in the Freely-Moving Rat." *Brain Research* 34: 171–75.

O'Keefe, John, and Lynn Nadel. 1978. *The Hippocampus as a Cognitive Map*. *Oxford, UK:Clarendon*.

Oh, Seung Wook, Julie A. Harris, Lydia Ng, Brent Winslow, Nicholas Cain, Stefan Mihalas, Quanxin Wang, et al. 2014. “A Mesoscale Connectome of the Mouse Brain.” *Nature* 508 (7495): 207–14.

Ohara, Shinya, Mariko Onodera, Øyvind W Simonsen, Rintaro Yoshino, Hiroyuki Hioki, Toshio Iijima, Ken-Ichiro Tsutsui, and Menno P Witter. 2018. “Intrinsic Projections of Layer Vb Neurons to Layers Va, III, and II in the Lateral and Medial Entorhinal Cortex of the Rat.” *Cell Reports* 24 (1): 107–16.

Olton, David S., and Robert J. Samuelson. 1976. “Remembrance of Places Passed: Spatial Memory in Rats.” *Journal of Experimental Psychology: Animal Behavior Processes* 2 (2): 97–116.

Perkel, Jeffrey M. 2018. “A Toolkit for Data Transparency Takes Shape.” *Nature 2018 560:7719*, August.

Pi, Hyun-Jae, Balazs Hangya, Duda Kvitsiani, Joshua I Sanders, Z Josh Huang, and Adam Kepecs. 2014. “Cortical Interneurons That Specialize in Disinhibitory.Pdf.” *Nature* 503 (7477): 521–24.

“Plexon Offline Sorter.” 2017.

Prinz, Florian, Thomas Schlange, and Khusru Asadullah. 2011. “Believe It or Not: How Much Can We Rely on Published Data on Potential Drug Targets?” *Nature Reviews Drug Discovery* 10 (9): 712–712.

Quilichini, Pascale, Anton Sirota, and György Buzsáki. 2010. “Intrinsic Circuit Organization and Theta-Gamma Oscillation Dynamics in the Entorhinal Cortex of the Rat.” *The Journal of Neuroscience : The Official Journal of the Society for Neuroscience* 30 (33): 11128–42.

Ramirez, Steve, Xu Liu, Pei-Ann Lin, Junghyup Suh, Michele Pignatelli, Roger L Redondo, Tomás J Ryan, and Susumu Tonegawa. 2013. “Creating a False Memory in the Hippocampus.” *Science (New York, N.Y.)* 341 (6144): 387–91.

Ramón Y Cajal, S. 1902. “Sobre Un Ganglio Especial de La Corteza Esfeno-Occipital.” *Trab. Del Lab. de Invest. Biol. Univ. Madrid* 1: 189–206.

Ramsden, Helen L., Gülşen Sürmeli, Steven G. McDonagh, and Matthew F. Nolan. 2015. “Laminar and Dorsoventral Molecular Organization of the Medial Entorhinal Cortex Revealed by Large-Scale Anatomical Analysis of Gene Expression.” *PLOS Computational Biology* 11 (1): e1004032.

Ravassard, Pascal, Ashley Kees, Bernard Willers, David Ho, Daniel A Aharoni, Jesse Cushman, Zahra M Aghajan, and Mayank R Mehta. 2013. “Multi-Sensory Control of Hippocampal Spatiotemporal Selectivity.” *Science* 340 (6138): 1342–46.

Reardon, Thomas R, Andrew J Murray, Gergely F Turi, Christoph Wirblich, Katherine R Croce, Matthias J Schnell, Thomas M Jessell, and Attila Losonczy. 2016. “Rabies Virus CVS-N2c(ΔG) Strain Enhances Retrograde Synaptic Transfer and Neuronal Viability.” *Neuron* 89 (4): 711–24.

Redhead, Edward S., Amanda Roberts, Mark Good, and John M. Pearce. 1997. “Interaction

between Piloting and Beacon Homing by Rats in a Swimming Pool." *Journal of Experimental Psychology: Animal Behavior Processes* 23 (3): 340–50.

Reifenstein, Eric T, Richard Kempter, Susanne Schreiber, Martin B Stemmler, and Andreas V M Herz. 2012. "Grid Cells in Rat Entorhinal Cortex Encode Physical Space with Independent Firing Fields and Phase Precession at the Single-Trial Level." *Proceedings of the National Academy of Sciences of the United States of America* 109 (16): 6301–6.

Renier, Nicolas, Zhuhao Wu, David J. Simon, Jing Yang, Pablo Ariel, and Marc Tessier-Lavigne. 2014. "IDISCO: A Simple, Rapid Method to Immunolabel Large Tissue Samples for Volume Imaging." *Cell* 159 (4): 896–910.

Rey, Hernan Gonzalo, Carlos Pedreira, and Rodrigo Quian Quiroga. 2015. "Past, Present and Future of Spike Sorting Techniques." *Brain Research Bulletin* 119: 106–17.

Rolston, J.D., R.E. Gross, and S.M. Potter. 2009. "Common Median Referencing for Improved Action Potential Detection with Multielectrode Arrays." In *2009 Annual International Conference of the IEEE Engineering in Medicine and Biology Society*, 2009:1604–7. IEEE.

Rossant, Cyrille, Shabnam N. Kadir, Dan F.M. Goodman, John Schulman, Maximilian L.D. Hunter, Aman B. Saleem, Andres Grosmark, et al. 2016. "Spike Sorting for Large, Dense Electrode Arrays." *Nature Neuroscience* 19 (4): 634–41.

Roux, Lisa, Eran Stark, Lucas Sjulson, and György Buzsáki. 2013. "In Vivo Optogenetic Identification and Manipulation of GABAergic Interneuron Subtypes." *Curr Opin Neurobiol* 31 (9): 1713–23.

———. 2014. "In Vivo Optogenetic Identification and Manipulation of GABAergic Interneuron Subtypes." *Nature Reviews Cancer* 13 (2): 83–96.

Rowland, David C, Horst A Obenhaus, Emilie R Skytøen, Qiangwei Zhang, Cliff G Kentros, Edvard I Moser, and May-Britt Moser. 2018. "Functional Properties of Stellate Cells in Medial Entorhinal Cortex Layer II." *ELife* 7 (September).

Sarel, Ayelet, Arseny Finkelstein, Liora Las, and Nachum Ulanovsky. 2017. "Vectorial Representation of Spatial Goals in the Hippocampus of Bats." *Science* 355 (6321): 176–80.

Sargolini, Francesca, Marianne Fyhn, Torkel Hafting, Bruce L McNaughton, Menno P Witter, May-Britt Moser, and Edvard I Moser. 2006. "Conjunctive Representation of Position, Direction, and Velocity in Entorhinal Cortex." *Science (New York, N.Y.)* 312 (5774): 758–62.

Schiller, D., H. Eichenbaum, E. A. Buffalo, L. Davachi, D. J. Foster, S. Leutgeb, and C. Ranganath. 2015. "Memory and Space: Towards an Understanding of the Cognitive Map." *Journal of Neuroscience* 35 (41): 13904–11.

Schindelin, Johannes, Ignacio Arganda-Carreras, Erwin Frise, Verena Kaynig, Mark Longair, Tobias Pietzsch, Stephan Preibisch, et al. 2012. "Fiji: An Open-Source Platform for Biological-Image Analysis." *Nature Methods* 9 (7): 676–82.

Schmidt-Hieber, Christoph, and Michael Häusser. 2013. "Cellular Mechanisms of Spatial Navigation in the Medial Entorhinal Cortex." *Nature Neuroscience* 16 (3): 325–31.

Schmitzer-Torbert, N., J. Jackson, D. Henze, K. Harris, and A. D. Redish. 2005. “Quantitative Measures of Cluster Quality for Use in Extracellular Recordings.” *Neuroscience* 131 (1): 1–11.

Séguinot, V., R. Maurer, and A.S. Etienne. 1993. “Dead Reckoning in a Small Mammal: The Evaluation of Distance.” *Journal of Comparative Physiology A* 173 (1).

Shapiro, Matthew L., Heikki Tanila, and Howard Eichenbaum. 1997. “Cues That Hippocampal Place Cells Encode: Dynamic and Hierarchical Representation of Local and Distal Stimuli.” *Hippocampus* 7 (6): 624–42.

Shima, Yasuyuki, Ken Sugino, Chris Martin Hempel, Masami Shima, Praveen Taneja, James B Bullis, Sonam Mehta, Carlos Lois, and Sacha B Nelson. 2016. “A Mammalian Enhancer Trap Resource for Discovering and Manipulating Neuronal Cell Types.” *ELife* 10.7554/eL: 11–13.

Shipston-Sharman, Oliver, Lukas Solanka, and Matthew F Nolan. 2016. “Continuous Attractor Network Models of Grid Cell Firing Based on Excitatory-Inhibitory Interactions.” *The Journal of Physiology* 594 (22): 6547–57.

Siegle, Joshua H., Gregory J. Hale, Jonathan P. Newman, and Jakob Voigts. 2015. “Neural Ensemble Communities: Open-Source Approaches to Hardware for Large-Scale Electrophysiology.” *Current Opinion in Neurobiology* 32: 53–59.

Siegle, Joshua H., Aaron Cuevas Lopez, Yogi A Pater, Kirill Abramov, Shay Ohayon, and Jakob Voigts. 2017. “Open Ephys : An Open-Source , Plugin-Based Platform for Multichannel Electrophysiology.” *Journal of Neural Engineering* 14.

Skaggs, William E., Bruce L. McNaughton, and Katalin M. Gothard. 1993. “An Information-Theoretic Approach to Deciphering the Hippocampal Code.” https://papers.nips.cc/paper/671-an-information-theoretic-approach-to-deciphering-the-hippocampal-code.

Solstad, Trygve, Charlotte N Boccara, Emilio Kropff, May-Britt Moser, and Edvard I. Moser. 2008. “Representation of Geometric Borders in the Entorhinal Cortex.” *Science (New York, N.Y.)* 1865 (5909): 1–5.

Squire, Larry R. 1992. “Memory and the Hippocampus: A Synthesis from Findings with Rats, Monkeys, and Humans.” *Psychological Review* 99 (2): 195–231.

Stosiek, Christoph, Olga Garaschuk, Knut Holthoff, and Arthur Konnerth. 2003. “In Vivo Two-Photon Calcium Imaging of Neuronal Networks.” *Proceedings of the National Academy of Sciences of the United States of America* 100 (12): 7319–24.

Strauss, R, S Schuster, and K G Götz. 1997. “Processing of Artificial Visual Feedback in the Walking Fruit Fly Drosophila Melanogaster.” *The Journal of Experimental Biology* 200 (Pt 9): 1281–96. http://www.ncbi.nlm.nih.gov/pubmed/9172415.

Stujenske, Joseph M, Timothy Spellman, and Joshua A Gordon. 2017. “Modeling the Spatiotemporal Dynamics of Light and Heat Propagation for in Vivo Optogenetics.” *Cell Reports* 155 (1): 3–12.

Sugar, Jørgen, Menno P Witter, Niels M van Strien, and Natalie L M Cappaert. 2011. "The Retrosplenial Cortex: Intrinsic Connectivity and Connections with the (Para)Hippocampal Region in the Rat. An Interactive Connectome." *Frontiers in Neuroinformatics* 5: 7.

Sun, Chen, Takashi Kitamura, Jun Yamamoto, Jared Martin, Michele Pignatelli, Lacey J. Kitch, Mark J. Schnitzer, and Susumu Tonegawa. 2015. "Distinct Speed Dependence of Entorhinal Island and Ocean Cells, Including Respective Grid Cells." *Proceedings of the National Academy of Sciences* 112 (30): 201511668.

Sun, H. J., D. P. Carey, and M. A. Goodale. 1992. "A Mammalian Model of Optic-Flow Utilization in the Control of Locomotion." *Exp Brain Res* 91 (1): 171–75.

Sürmeli, Gülşen, Daniel Cosmin Marcu, Christina McClure, Derek L.F. Garden, Hugh Pastoll, and Matthew F. Nolan. 2015. "Molecularly Defined Circuitry Reveals Input-Output Segregation in Deep Layers of the Medial Entorhinal Cortex." *Neuron* 88: 1–14.

Taube, J S, R U Muller, and J B Ranck. 1990a. "Head-Direction Cells Recorded from the Postsubiculum in Freely Moving Rats. I. Description and Quantitative Analysis." *The Journal of Neuroscience : The Official Journal of the Society for Neuroscience* 10 (2): 420–35.

———. 1990b. "Head-Direction Cells Recorded from the Postsubiculum in Freely Moving Rats. II. Effects of Environmental Manipulations." *The Journal of Neuroscience : The Official Journal of the Society for Neuroscience* 10 (2): 436–47.

———. 1990c. "Head-Direction Cells Recorded from the Postsubiculum in Freely Moving Rats. II. Effects of Environmental Manipulations." *The Journal of Neuroscience : The Official Journal of the Society for Neuroscience* 10 (2): 436–47. http://www.ncbi.nlm.nih.gov/pubmed/2303852.

Tennant, Sarah A, Lukas Fischer, Derek L F Garden, Klára Zsófia Gerlei, Cristina Martinez-Gonzalez, Christina Mcclure, Emma R Wood, and Matthew F Nolan. 2018. "Stellate Cells in the Medial Entorhinal Cortex Are Required for Spatial Learning Article Stellate Cells in the Medial Entorhinal Cortex Are Required for Spatial Learning." *Cell Reports* 22: 1313–24.

Thyng, Kristen M, Chad A Greene, Robert D Hetland, Heather M Zimmerle, and Steven F DiMarco. 2016. "True Colors of Oceanography Guidelines for Effective and Accurate Colormap Selection." *Oceanography* 29 (3): 9–13.

Tocker, Gilad, Omri Barak, and Dori Derdikman. 2015a. "Grid Cells Correlation Structure Suggests Organized Feedforward Projections into Superficial Layers of the Medial-Entorhinal Cortex." *Hippocampus* 00 (0–0): 1–14.

———. 2015b. "Grid Cells Correlation Structure Suggests Organized Feedforward Projections into Superficial Layers of the Medial Entorhinal Cortex." *Hippocampus* 25 (12): 1599–1613.

Tolman, Edward C. 1948. "Cognitive Maps in Rats and Men." *Psychological Review* 55 (4): 189–208.

Tsoar, Asaf, Ran Nathan, Yoav Bartan, Alexei Vyssotski, Giacomo Dell'Omo, and Nachum

Ulanovsky. 2011. “Large-Scale Navigational Map in a Mammal.” *Proceedings of the National Academy of Sciences of the United States of America* 108 (37): E718-24.

Valerio, S., and J. S. Taube. 2016. “Head Direction Cell Activity Is Absent in Mice without the Horizontal Semicircular Canals.” *Journal of Neuroscience* 36 (3): 741–54.

Vertes, Robert P. 2004. “Differential Projections of the Infralimbic and Prelimbic Cortex in the Rat.” *Synapse* 51 (1): 32–58.

Wallace, Dg, Bogdan Gorny, and Iq Whishaw. 2002. “Rats Can Track Odors, Other Rats, and Themselves: Implications for the Study of Spatial Behavior.” *Behavioural Brain Research* 131 (1–2): 185–92.

Wilson, M., and B. McNaughton. 1993. “Dynamics of the Hippocampal Ensemble Code for Space.” *Science* 261 (5124): 1055–58.

Witter, Menno P., Thanh P. Doan, Bente Jacobsen, Eirik S. Nilssen, and Shinya Ohara. 2017. “Architecture of the Entorhinal Cortex A Review of Entorhinal Anatomy in Rodents with Some Comparative Notes.” *Frontiers in Systems Neuroscience* 11 (June): 1–12.

Wood, F, M J Black, C Vargas-Irwin, M R Fellows, and J P Donoghue. 2004. “On the Variability of Manual Spike Sorting.” *Ieee Transactions On Biomedical Engineering* 51 (6): 912–18.

Wyass, J. Michael, and Thomas Van Groen. 1992. “Connections between the Retrosplenial Cortex and the Hippocampal Formation in the Rat: A Review.” *Hippocampus* 2 (1): 1–11.

Yang, Kai, Haifeng Wu, and Yu Zeng. 2017. “A Simple Deep Learning Method for Neuronal Spike Sorting.” *Journal of Physics: Conference Series* 910 (1): 012062.

Yoganarasimha, D, Xintian Yu, and James J Knierim. 2006. “Head Direction Cell Representations Maintain Internal Coherence during Conflicting Proximal and Distal Cue Rotations: Comparison with Hippocampal Place Cells.” *The Journal of Neuroscience : The Official Journal of the Society for Neuroscience* 26 (2): 622–31.

Zemelman, Boris V., Georgia A. Lee, Minna Ng, and Gero Miesenböck. 2002. “Selective Photostimulation of Genetically ChARGed Neurons.” *Neuron* 33 (1): 15–22.

Zhu, Hu, and Bryan L. Roth. 2014. “Silencing Synapses with DREADDs.” *Neuron* 82 (4): 723–25.

Zhu, Peixin, M. Isabel Aller, Udo Baron, Sidney Cambridge, Melanie Bausen, Jan Herb, Jürgen Sawinski, et al. 2007. “Silencing and Un-Silencing of Tetracycline-Controlled Genes in Neurons.” Edited by Peter Fraser. *PLoS ONE* 2 (6): e533.